

A THREE AXIS CAPACITIVE MEMS ACCELEROMETER
ON A MULTI-STACK SUBSTRATE

A THESIS SUBMITTED TO
THE GRADUATE SCHOOL OF NATURAL AND APPLIED SCIENCES
OF
MIDDLE EAST TECHNICAL UNIVERSITY



BY

SERDAR TEZ

IN PARTIAL FULFILLMENT OF THE REQUIREMENTS
FOR
THE DEGREE OF DOCTOR OF PHILOSOPHY
IN
MICRO AND NANO TECHNOLOGY

JANUARY 2014

Approval of the thesis:

**A THREE AXIS CAPACITIVE MEMS ACCELEROMETER
ON A MULTI-STACK SUBSTRATE**

submitted by **SERDAR TEZ** in partial fulfillment of the requirements for the degree of **Doctor of Philosophy in Micro and Nano Technology Program, Middle East Technical University** by,

Prof. Dr. Canan Özgen _____
Dean, Graduate School of **Natural and Applied Sciences**

Prof. Dr. Tayfun Akın _____
Head of Department, **Micro and Nano Technology**

Prof. Dr. Tayfun Akın _____
Supervisor, **Electrical and Electronics Eng. Dept., METU**

Prof. Dr. Mehmet Ali Sahir Arıkan _____
Co-Supervisor, **Mechanical Eng. Dept., METU**

Examining Committee Members

Prof. Dr. Raşit Turan _____
Physics Dept., METU

Prof. Dr. Tayfun Akın _____
Electrical and Electronics Eng. Dept., METU

Assoc. Prof. Dr. Haluk Külah _____
Electrical and Electronics Eng. Dept., METU

Assist. Prof. Dr. Yakup Özkanç _____
Electrical and Electronics Eng. Dept., Hacettepe University

Assist. Prof. Dr. Kıvanç Azgın _____
Mechanical Eng. Dept., METU

Date: 22.01.2014



I hereby declare that all information in this document has been obtained and presented in accordance with academic rules and ethical conduct. I also declare that, as required by these rules and conduct, I have fully cited and referenced all referenced material and results that are not original to this work.

Name, Surname: Serdar Tez

Signature:

ABSTRACT

A THREE AXIS CAPACITIVE MEMS ACCELEROMETER ON A MULTI-STACK SUBSTRATE

Tez, Serdar

Ph. D., Micro and Nanotechnology Program

Supervisor: Prof.Dr. Tayfun Akin

January 2014, 235 pages

Micro-Electro-Mechanical Systems (MEMS) having capacitive sensing mechanism have been recently gaining interest as a result of low-cost, small-size, and high-reliability sensors applications. Today micromachined capacitive sensors find different places in many areas. Especially, MEMS capacitive accelerometers have been using in many military and industrial applications such as inertial navigation, vibration monitoring, and robotics control. Three-axial acceleration sensing is a must for most of these applications. Hence, single or dual axis accelerometers are assembled to provide three dimensional sensing. However, this leads to increase not only packaging size but also cost. Furthermore, the misalignment of individual accelerometers is a major problem causing cross-axis sensitivity. Therefore, there is a need for the fabrication of a monolithic three-axis accelerometer. The aim of the study is to develop a process for the fabrication of a monolithic three-axis accelerometer.

The proposed three-axis accelerometer is considered implementing both differential lateral and differential vertical accelerometers in the same die by using a glass-silicon-glass multi-stack. The glass-silicon-glass multi-stack is formed by a fabrication process called the double glass modified silicon on glass process

(DGM-SOG), where the structural layer is selected to be 35 μm thick $<111>$ silicon. The fabrication process uses the anodic bonding as well as the Au-Si eutectic bonding in the last step of the formation of the glass-silicon-glass multi-stack, allowing implementing 2 μm capacitive gaps for the vertical accelerometers. The top glass wafer allows implementing not only a top electrode for the vertical accelerometer, but also an inherent cap for the entire structure. The three-axis accelerometer is fabricated, for the first time in literature, by using the glass-silicon-glass multi-stack. The fabricated three-axis MEMS capacitive accelerometer die is $12 \times 7 \times 1 \text{ mm}^3$. The best system level results obtained for the vertical accelerometers are $10.5 \mu\text{g}/\sqrt{\text{Hz}}$ noise floor, $12 \mu\text{g}$ bias instability and 122 dB dynamic range. On the other hand, the best system level result obtained for the lateral accelerometers are $4.3 \mu\text{g}/\sqrt{\text{Hz}}$ noise floor, $3.3 \mu\text{g}$ and 125 dB dynamic range.

Keywords: MEMS capacitive three-axis accelerometer, MEMS capacitive lateral accelerometer, MEMS capacitive vertical accelerometer, SiGeB, SOI, glass-silicon-glass, inherent cap.

ÖZ

ÇOKLU TABAN ÜZERİNDE ÜÇ EKSENLİ KAPASİTİF MEMS İVMEÖLÇER

Tez, Serdar

Doktora, Mikro ve Nanoteknoloji Programı

Tez Yöneticisi: Prof.Dr. Tayfun Akın

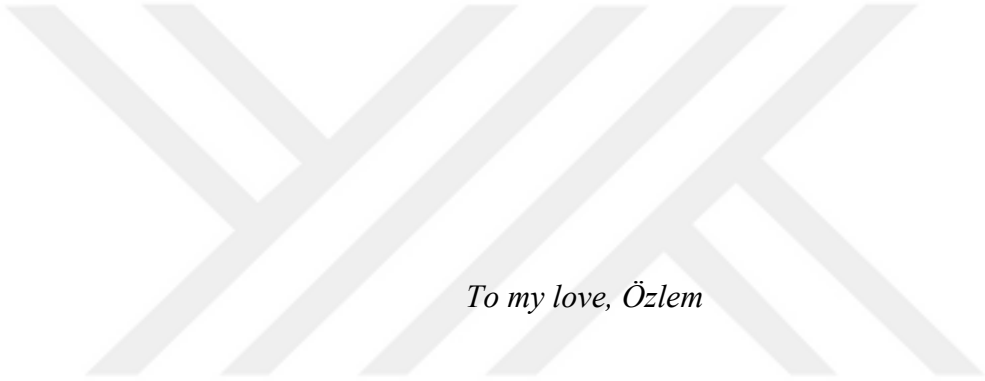
Ocak 2014, 235 sayfa

Küçük boyut, düşük fiyat ve yüksek güvenilirlikli duyarga uygulamalarının bir sonucu olarak kapasitif algılama mekanizmasına sahip mikro-elektro-mekanik sistemler (MEMS) ilgi kazanmaktadır. Bugün mikro imalat kapasitif duyargalar çeşitli alanlarda farklı yerler bulmaktadır. Özellikle, MEMS kapasitif ivmeölçerler ataletsel navigasyon, titreşim izleme ve robotik kontrol gibi birçok asgari ve endüstriyel alanlarda kullanılmaktadır. Bu uygulamaların çoğu için üç boyutlu ivme algılama bir gereklilikdir. Bu yüzden tek veya çift eksenli ivmeölçerler bir araya getirilerek üç eksenli algılama sağlanmıştır. Ancak, bu sadece paket boyutu değil aynı zamanda maliyetin artmasına neden olmaktadır. Buna ek olarak, bireysel ivmeölçerlerin hizalanamaması çapraz eksen hassasiyetine sebep olan başlıca sorundur. Bu yüzden, bu tezin amacı yekpare üç eksenli ivmeölçer üretimi için bir sürecin geliştirilmesidir.

Önerilen üç eksenli ivmeölçer cam-silisyum-cam çoklu yiğini kullanarak diferansiyel yatay ve diferansiyel dikey ivmeölçerlerin aynı kalıpta uygulanması ile düşünüldü. Cam-silisyum-cam çoklu yiğini çift camlı modifiye cam üzerine silisyum üretim süreci ile oluşturuldu, burada yapısal kalınlık $<111>$ doğrultusunda $35 \mu\text{m}$ silisyum olarak seçildi. Üretim yöntemi cam-silisyum-cam çoklu yiğininin oluşturulmasında son adımda anodik yapıştırma ve Au-Si ötektik yapıştırma kullanarak, dikey

ivmeölçer için $2 \mu\text{m}$ 'lik kapasitif açılığın oluşturulmasına izin verir. Üst cam dikey ivmeölçer için sadece bir üst elektrot değil aynı zamanda bütün yapı için bir kapaktır. Üç eksenli ivmeölçer literatürde ilk defa cam-silisyum-cam çoklu yiğinını kullanarak üretilmiştir. Üretilen ivmeölçer kalıpları $12 \times 7 \times 1 \text{ mm}^3$ tür. Dikey ivmeölçer için elde edilen en iyi sistem seviye sonuçlar $10.5 \mu\text{g}/\sqrt{\text{Hz}}$ gürültü seviyesi, $12 \mu\text{g}$ kayma kararsızlığı, ve 122 dB dinamik aralıktır. Diğer taraftan, yatay ivmeölçer için elde edilen en iyi sistem seviye sonuçlar $4.3 \mu\text{g}/\sqrt{\text{Hz}}$ gürültü seviyesi, $3.3 \mu\text{g}$ kayma kararsızlığı, ve 125 dB dinamik aralıktır.

Anahtar Kelimeler: MEMS kapasitif üç eksenli ivmeölçer, MEMS kapasitif yanal ivmeölçer, MEMS kapasitif dikey ivmeölçer, SiGeB, SOI, cam-silisyum-cam, kendinden kapaklı.



To my love, Özlem

ACKNOWLEDGEMENTS

I would like thank to my supervisor, Prof. Dr. Tayfun Akın for his support, guidance, and encouragement. Especially, I am very grateful for his financial support to my thesis project. I feel lucky to work with such a distinguished and an exceptional professor. I also would like to acknowledge my co-supervisor Prof. Dr. M. A. Sahir Arıkan for his guidance and motivation.

I wish thank to my thesis committee members Assoc. Prof. Dr. Haluk Külah and Assist. Prof.Dr. Yakup Özkazanç for their valuable discussions and feedback.

I am also very thankful to Dr. Akın Aydemir, Orhan Ş. Akar, and Dr. Said Emre Alper for their valuable contributions and advices.

I am indebted my many colleagues who helped me during my studies even most hopeless times and I am especially very thankful to M. Mert Torunbalcı, Ulaş Aykutlu, Osman Aydın, Selçuk Keskin, Kaan Demirel and Yunus Terzioğlu for their unique contributions on the fabrication of three-axis accelerometer and readout electronics studies. I also would like to thank to Evren Erdil, Gülşah Demirhan, Hasan Doğan Gavcar, Ferhat Yeşil, Onur Yalçın, Eren Canga, Başak Kebabçı, Ozan Ertürk, Özgecan Dervişoğlu, Taylan Toral, Ebru Sağıroğlu Topallı for a stimulating and fun environment.

I also would like to appreciate to Melek Karahan, Ayşegül Nadar, Şebnem Taş Ebru Uğur Aslan, Yusuf Murat, Fatih Aykut Bakırçı, Levent Abat, and Ali Aytekin.

I would like to appreciate to my family for their endless trust and support during my education. I am also grateful to my wife for her self-sacrifice.

TABLE OF CONTENTS

| | |
|--|-----|
| ABSTRACT | v |
| ÖZ | vii |
| ACKNOWLEDGEMENTS | x |
| TABLE OF CONTENTS | xi |
| LIST OF TABLES | xv |
| LIST OF FIGURES | xx |
| CHAPTERS | |
| 1. INTRODUCTION | 1 |
| 1.1. MEMS Accelerometers..... | 3 |
| 1.2. Classification of MEMS Accelerometers | 7 |
| 1.3. Three Axis Accelerometers Reported in Literature..... | 9 |
| 1.3.1. Post CMOS-MEMS Three Axis Accelerometers..... | 9 |
| 1.3.2. Bulk Micromachined Three-Axis Accelerometers..... | 15 |
| 1.3.3. Vertical Accelerometers Reported in the Literature..... | 22 |
| 1.4. Objectives of This Study..... | 27 |
| 1.5. Outline of the Thesis..... | 32 |
| 2. THEORETICAL BACKGROUND | 33 |
| 2.1. Basic Operation Principles of the Accelerometer..... | 33 |
| 2.2. Spring Constant Estimation | 35 |
| 2.3. Damping Coefficient Estimation | 39 |
| 2.4. Sensitivity | 41 |
| 2.5. Operation Range of the Accelerometer | 42 |

| | |
|--|-----|
| 2.6. Brownian Noise | 44 |
| 2.7. Summary of the Chapter | 44 |
| 3. DESIGN CONCEPT OF THE THREE AXIS ACCELEROMETER | 45 |
| 3.1. Design of Three Axis Accelerometer | 45 |
| 3.2. Three Axis Accelerometer Designs | 51 |
| 3.2.1. Three-Axis Accelerometer Design Mask Set-1 | 51 |
| 3.2.1.1. Lateral Accelerometer Design-1 | 51 |
| 3.2.1.2. Vertical Accelerometer Design-1 | 55 |
| 3.2.1.3. Vertical Accelerometer Design-1 with Perforation Holes.. | 59 |
| 3.2.1.4. Vertical Accelerometer Design-2 | 62 |
| 3.2.1.5. Vertical Accelerometer Design-2 with Perforation Holes.. | 65 |
| 3.2.1.6. Vertical Accelerometer Design-3 | 68 |
| 3.2.1.7. Vertical Accelerometer Design-3 with Perforation Holes.. | 71 |
| 3.2.2. Three Axis Accelerometer Design Mask set-2 | 74 |
| 3.2.2.1. Lateral Accelerometer Design-1 | 75 |
| 3.2.2.2. Lateral Accelerometer Design-2 | 78 |
| 3.2.2.3. Lateral Accelerometer Design-3 | 79 |
| 3.2.2.4. Vertical Accelerometer Design-1 | 82 |
| 3.2.2.5. Vertical Accelerometer Design-2 | 85 |
| 3.2.2.6. Vertical Accelerometer Design-3 | 88 |
| 3.2.2.7. Vertical Accelerometer Design-4 | 91 |
| 3.2.2.8. Vertical Accelerometer Design-5 | 94 |
| 3.3. Three Axis Accelerometer Design | 97 |
| 3.4. Summary of the Chapter | 97 |
| 4. FABRICATION PROCESS..... | 101 |
| 4.1. Double Glass Modified Dissolved Wafer (DGM-DWP) Fabrication Process and Optimization..... | 104 |

| | | |
|----------|--|-----|
| 4.1.1. | Definition of Process Steps | 104 |
| 4.1.2. | Vertical Capacitive Gap Optimization | 112 |
| 4.1.3. | Silicon Wafer Fabrication | 115 |
| 4.1.3.1. | Deposition of an Insulator Layer on Silicon Wafer | 115 |
| 4.1.3.2. | DRIE Optimization..... | 116 |
| 4.1.4. | The First Anodic Bonding Recipe Optimization..... | 117 |
| 4.1.5. | Thinning of the Bottom Glass-SiGeB Stack | 117 |
| 4.1.6. | Two-Electrode Anodic Bonding Optimization | 118 |
| 4.1.7. | Two-Step Dicing Process | 121 |
| 4.1.8. | Die Level Test Result and Further Observation | 124 |
| 4.2. | Double Glass Modified Silicon on Glass (DGM-SOG) Fabrication Process and Optimization..... | 130 |
| 4.2.1. | Definition of Process Steps | 130 |
| 4.2.2. | Fabrication of Glass Wafers | 139 |
| 4.2.3. | Structural DRIE | 142 |
| 4.2.4. | Bonding Optimization | 142 |
| 4.2.5. | The First Anodic Bonding | 143 |
| 4.2.6. | Handle Layer Removing | 145 |
| 4.2.7. | Three-Electrode Anodic Bonding Optimization | 147 |
| 4.2.8. | Anodic and then Au-Si Eutectic Bonding Optimization | 155 |
| 4.2.9. | Two-Step Dicing Process | 165 |
| 4.3. | Summary of the Chapter | 167 |
| 5. | THE DIE LEVEL AND SYSTEM LEVEL TEST | 171 |
| 5.1. | Die Level C-V Test..... | 171 |
| 5.1.1. | C-V Measurement Test | 171 |
| 5.1.2. | The Resonance Frequency Test..... | 173 |
| 5.2. | The System Level Test | 173 |

| | |
|---|-----|
| 5.2.1. Allan-Variance Noise and Bias Instability Measurement Technique | 177 |
| 5.2.1.1. Quantization Noise | 178 |
| 5.2.1.2. Angle (Velocity) Random Walk..... | 178 |
| 5.2.1.3. Bias Instability | 178 |
| 5.2.1.4. Rate Random Walk..... | 179 |
| 5.2.1.5. Rate Ramp | 179 |
| 5.2.1.6. Exponentially Correlated (Markov) Noise | 179 |
| 5.2.2. System Level Test Procedure | 179 |
| 5.2.3. Non-Linearity Measurement..... | 181 |
| 5.3. Test Performed on Sensors Fabricated by Using Mask Set-1..... | 181 |
| 5.4. Test Performed on Sensors Fabricated by Using Mask Set-2..... | 184 |
| 5.4.1. C-V Test Results..... | 185 |
| 5.4.1.1. Sensors Fabricated by Using the Three-Electrode Anodic Bonding Method..... | 185 |
| 5.4.1.2. Sensors Fabricated the Anodic Bonding and then the Au-Si Eutectic Bonding | 188 |
| 5.4.2. Resonance Frequency Measurement Test Results..... | 194 |
| 5.4.3. System Level Test Result | 197 |
| 5.4.3.1. System Level Results For Sensors by Two-Step Anodic Bonding | |
| 197 | |
| 5.4.3.2. System Level Results For Sensors by The Anodic Bonding and then Au-Si Eutectic Bonding | 206 |
| 5.4.4. The Non-Linearity Test Result | 216 |
| 5.5. Summary of the Chapter | 219 |
| 6. CONCLUSION AND FUTURE WORK..... | 221 |
| REFERENCES | 227 |
| CURRICULUM VITAE | 235 |

LIST OF TABLES

TABLES

| | |
|--|----|
| Table 1.1: The performance parameters of the reported accelerometer [20]..... | 18 |
| Table 1.2: The comparison of the performance parameter of the three axis accelerometer with respect to the reported accelerometer in the literature..... | 29 |
| Table 3.1: Constants used during the calculation of the design parameter of the three axis accelerometer..... | 47 |
| Table 3.2: Abbreviations of electrical design parameters of the three axis accelerometer | 47 |
| Table 3.3: Abbreviations of mechanical design parameters of the three axis accelerometer | 48 |
| Table 3.4: Abbreviations of physical design parameters of the three axis accelerometer | 48 |
| Table 3.5: Design parameters of the lateral accelerometer..... | 49 |
| Table 3.6: Design parameters of the vertical accelerometer | 50 |
| Table 3.7: Design and performance parameters of the lateral accelerometer design-1..... | 52 |
| Table 3.8: The comparison of the hand calculation and the simulation result for the lateral accelerometer design-1..... | 55 |
| Table 3.9: Simulation mod analysis results of the lateral accelerometer design-1.... | 55 |
| Table 3.10: Design and performance parameters of vertical accelerometer design-1..... | 56 |
| Table 3.11: The comparison of the hand calculation and the simulation result for the vertical accelerometer design-1..... | 59 |
| Table 3.12: Simulation mod analysis results of the vertical accelerometer design-1.59 | |
| Table 3.13: Design and performance parameters of the vertical accelerometer design-1 with perforation holes. | 60 |
| Table 3.14: The comparison of the hand calculation and the simulation result for the vertical accelerometer design-1 with perforation holes. | 62 |

| | |
|---|----|
| Table 3.15: Simulation mode analysis results of the vertical accelerometer design-1 with perforation holes..... | 62 |
| Table 3.16: Design and performance parameters of the vertical accelerometer design-2..... | 63 |
| Table 3.17: The comparison of the hand calculation and the simulation result for the vertical accelerometer design-2..... | 65 |
| Table 3.18: Simulation mode analysis results of the vertical accelerometer design-2. | 65 |
| Table 3.19: Design and performance parameters of the vertical accelerometer design 2 with perforation holes..... | 66 |
| Table 3.20: The comparison of the hand calculation and the simulation result for the vertical accelerometer design-2 with perforation holes. | 68 |
| Table 3.21: Simulation mode analysis results of the vertical accelerometer design-2 with perforation holes..... | 68 |
| Table 3.22: Design and performance parameters of the vertical accelerometer design-3. | 69 |
| Table 3.23: The comparison of the hand calculation and the simulation result for the vertical accelerometer design-3..... | 71 |
| Table 3.24: Simulation mode analysis results of the vertical accelerometer design-3. | 71 |
| Table 3.25: Design and performance parameters of the vertical accelerometer design-3 with perforation holes..... | 72 |
| Table 3.26: The comparison of the hand calculation and the simulation result for the vertical accelerometer design 3 with perforation holes..... | 74 |
| Table 3.27: Simulation mode analysis results of the vertical accelerometer design 3 with perforation holes..... | 74 |
| Table 3.28: Performance parameters of the lateral accelerometer design-1. | 76 |
| Table 3.29: The comparison of the hand calculation and the simulation result for the lateral accelerometer design-1..... | 76 |
| Table 3.30: Simulation mode analysis results of the lateral accelerometer design-1. | 76 |
| Table 3.31: Performance Parameters of the lateral accelerometer design-2. | 78 |
| Table 3.32: The comparison of the hand calculation and the simulation result for the lateral accelerometer design-2..... | 78 |

| | |
|---|----|
| Table 3.33: Simulation mode analysis results of the lateral accelerometer design-2. | 78 |
| Table 3.34: Design and performance parameters of lateral accelerometer desing-3. | 80 |
| Table 3.35: The comparison of the hand calculation and the simulation result for the lateral accelerometer design-3..... | 80 |
| Table 3.36: Simulation mode analysis results of the lateral accelerometer design-3. | 80 |
| Table 3.37: Design and performance parameters of vertical accelerometer design-1. | |
| | 83 |
| Table 3.38: The comparison of the hand calculation and the simulation result for the vertical accelerometer design-1..... | 83 |
| Table 3.39: Simulation mode analysis results of the vertical accelerometer design-1. | |
| | 83 |
| Table 3.40: Design and performance parameters of the vertical accelerometer design-2. | |
| | 86 |
| Table 3.41: The comparison of the hand calculation and the simulation result for the vertical accelerometer design-2..... | 86 |
| Table 3.42: Simulation mode analysis results of the vertical accelerometer design-2. | |
| | 86 |
| Table 3.43: Design and performance parameters of vertical accelerometer design-3. | |
| | 89 |
| Table 3.44: The comparison of the hand calculation and the simulation result for the vertical accelerometer design-3..... | 89 |
| Table 3.45: Simulation mode analysis results of the vertical accelerometer design-3. | |
| | 89 |
| Table 3.46: Design and performance parameters of vertical accelerometer design-4. | |
| | 92 |
| Table 3.47: The comparison of the hand calculation and the simulation result for the vertical accelerometer design-4..... | 92 |
| Table 3.48: Simulation mode analysis results of the vertical accelerometer design-4. | |
| | 92 |
| Table 3.49: Design and performance parameters of vertical accelerometer design-5. | |
| | 95 |
| Table 3.50: The comparison of the hand calculation and the simulation result for the vertical accelerometer design-5..... | 95 |

| | |
|---|-----|
| Table 3.51: Simulation mode analysis results of the vertical accelerometer design-5. | 95 |
| Table 3.52: Summarization of design and performance parameters of the lateral accelerometer and the vertical accelerometer for mask set1..... | 98 |
| Table 3.53: Summarization of design and performance parameters of the lateral accelerometer and the vertical accelerometer for mask set 2..... | 99 |
| Table 4.1: The DRIE recipe used during the fabrication of three axis accelerometer. | 116 |
| Table 4.2: The rest capacitance and the C-V characteristics of lateral and vertical accelerometers..... | 125 |
| Table 4.3: The DRIE recipe used for the handle layer removing. | 146 |
| Table 4.4: Temperature and piston values used during the optimization of the Au-Si eutectic bonding recipe..... | 159 |
| Table 5.1: The lateral and the vertical accelerometer test result for the fabrication mask set-1..... | 184 |
| Table 5.2: Test results of the three axis accelerometer designed for the fabrication mask set-2 fabricated by two-step anodic bonding. | 188 |
| Table 5.3: The rest capacitance value for the vertical accelerometer design 5 fabricated in the first attempt of the anodic bonding and then the Au-Si shown in Figure 4.76. | 189 |
| Table 5.4: Sensors test results for the fabrication run#5 shown in Figure 4.81 (b). . | 190 |
| Table 5.5: The comparison of design and test values of the resonance frequency. . | 194 |
| Table 5.6: The system level test results for three-axis accelerometer fabricated by using the two-step anodic boding..... | 197 |
| Table 5.7: The system level test results for three-axis accelerometers fabricated by using the anodic and then the Au-Si eutectic bonding. | 206 |
| Table 5.8: Non-linearity test result of the C09 accelerometer for different measurement ranges. Output range is extracted as +16.1 g, -7.5 g from the linearity test. | 216 |
| Table 5.9: Non-linearity test result of the B04 accelerometer for different measurement ranges. Output range is extracted as +13.6 g, -9.4 g from the linearity test. | 216 |

| | |
|--|-----|
| Table 5.10: Non-linearity of the B06 accelerometer for different measurement ranges. Output range was extracted as +13.8 g, -9.6 g from the linearity test..... | 217 |
| Table 5.11: Non-linearity of the A06 accelerometer for different measurement ranges. Output range is extracted as +21.9 g, -16.5 g from the linearity test. | 217 |
| Table 5.12: Non-linearity of the A04 accelerometer for different measurement ranges. Output range was extracted as +12.0 g, -12.4 g from the linearity test..... | 217 |
| Table 5.13: Non-linearity of the B07 accelerometer for different measurement ranges. Output range is extracted as +12.1 g, -12.8 g from the linearity test. | 218 |
| Table 6.1: The comparison of fabrication results of accelerometers for two-different fabrication process. | 223 |
| Table 6.2: The three-axis accelerometer sensor A06 system level test results fabricated by using the Au-Si eutectic bonding. | 223 |
| Table 6.3: The three-axis accelerometer sensor A01 system level test results fabricated by using the two-step anodic bonding..... | 224 |

LIST OF FIGURES

FIGURES

| | |
|--|----|
| Figure 1.1: Different applications and performance requirements of the accelerometers [5]. | 2 |
| Figure 1.2: Historical genealogy of MEMS sensors and actuators in 1954-1990 [9].. | 5 |
| Figure 1.3: Die size versus year [10]..... | 6 |
| Figure 1.4: The estimation of the compounded annual growth rate (GAGR) for MEMS sensors [11]..... | 6 |
| Figure 1.5: The illustration of the tri-axis CMOS-MEMS accelerometer design [16]. | 9 |
| Figure 1.6: The post-CMOS fabrication process for tri-axis accelerometer reported in [16]. | 10 |
| Figure 1.7: The illustration of the design concept for the three-axis accelerometer (a). The cross sectional view of the three axis accelerometer showing the sensing electrodes on the proof mass [17]. | 11 |
| Figure 1.8: The post-CMOS process for the three axis accelerometer reported in [17]. | 12 |
| Figure 1.9: The illustration of the design of the tri-axis accelerometer reported in [18]. | 14 |
| Figure 1.10: The fabrication process for the tri-axis accelerometer reported in [18]. | 14 |
| Figure 1.11: The illustration of the proposed tri-axis accelerometer reported in [19]. | 16 |
| Figure 1.12: Cross-sectional view of the tri-axis accelerometer reported in [19]..... | 16 |
| Figure 1.13: The illustration of the three axis accelerometer design reported in [20]. | 17 |
| Figure 1.14: The fabrication steps of the tri-axial accelerometer reported in [20]. ... | 18 |
| Figure 1.15: The illustration of the three axis accelerometer structure reported in [21]. | 20 |
| Figure 1.16: The fabrication process flows for the three axis accelerometer reported in [21]. | 20 |

| | |
|--|----|
| Figure 1.17. The schematic representation of the three axis accelerometer reported in [22]. | 21 |
| Figure 1.18: The fabrication process steps for the three axis accelerometer reported in [22]. | 22 |
| Figure 1.19: The schematic of the vertical accelerometer reported [23]. | 23 |
| Figure 1.20: The fabrication process steps for the reported vertical accelerometer [23]. | 23 |
| Figure 1.21: The schematic view of the reported device in [24]. | 25 |
| Figure 1.22: The fabrication process flow for the fabricated devices [24]. | 25 |
| Figure 1.23: The schematic demonstration of the vertical accelerometer reported in [25]. | 26 |
| Figure 1.24: The fabrication process sequence for the vertical accelerometer reported in [25]. | 27 |
| Figure 1.25: The comparison of dynamic range of lateral and vertical accelerometers reported in the literature. Blue points indicate academic works. Commercial accelerometers are shown with green color. Red points indicate this work. The purple one indicates [53]. The grey one represents [49]. The orange one is [48]. | 32 |
| Figure 2.1: The illustration of the MEMS capacitive accelerometers | 34 |
| Figure 2.2: Accelerometer mechanical model: spring-proof mass-damper | 34 |
| Figure 2.3: (a) Unguided beam (b) Guided beam in their deflected forms | 37 |
| Figure 2.4: The series and parallel connected springs system (a) springs in parallel configuration (b) springs in series configuration. | 37 |
| Figure 2.5: Series connected half clamped beams forming a fixed-guided end beam. | 38 |
| Figure 2.6: The illustration of the crab legs structure used in the vertical accelerometer design. | 38 |
| Figure 2.7: Illustration of the (a) squeeze-film and (b) slide-film damping mechanisms [62]. | 39 |
| Figure 2.8: The illustration of the vertical accelerometer schematic structure of a thin hole-plate: (a) top view; (b) cross-sectional view [63]. | 41 |
| Figure 3.1: The illustration of the proposed the three axis accelerometer. | 46 |
| Figure 3.2: The layout of the lateral accelerometer design-1 | 52 |
| Figure 3.3: The FEM simulation model of the lateral accelerometer design-1. | 53 |

| | |
|--|----|
| Figure 3.4: (a) Mesher settings of the lateral accelerometer design-1 for the proof mass (b) for the spring region. | 53 |
| Figure 3.5: Mode analysis simulation results of the lateral accelerometer design (a) The first mode and (b) the second mode. | 54 |
| Figure 3.6: The layout of the vertical accelerometer design-1..... | 56 |
| Figure 3.7: The FEM simulation model of the vertical accelerometer design-1..... | 57 |
| Figure 3.8: (a) Mesher settings of the vertical accelerometer design-1 for the proof mass (b) for the spring region. | 57 |
| Figure 3.9: Mode analysis simulation result of the vertical accelerometer design-1 (a) The first mode and (b) the second mode. | 58 |
| Figure 3.10: The layout of the vertical accelerometer design-1 with perforation holes. | 60 |
| Figure 3.11: Mode analysis simulation result of the vertical accelerometer design-1 with perforation holes (a) The first mode and (b) the second mode. | 61 |
| Figure 3.12: The layout of the vertical accelerometer design-2..... | 63 |
| Figure 3.13: Mode analysis simulation result of the vertical accelerometer design-2 (a) The first mode and (b) the second mode..... | 64 |
| Figure 3.14: The layout of the vertical accelerometer design-2 with perforation holes. | 66 |
| Figure 3.15: Mode analysis simulation results of the vertical accelerometer design-2 with perforation holes (a) The first mode and (b) the second mode. | 67 |
| Figure 3.16: The layout of the vertical accelerometer design-3..... | 69 |
| Figure 3.17: Mode analysis simulation results of the vertical accelerometer design. (a) The first mode and (b) the second mode..... | 70 |
| Figure 3.18: The layout of the vertical accelerometer design-3 with perforation holes. | 72 |
| Figure 3.19: Mode analysis simulation result of the vertical accelerometer design 3 with perforation holes (a) the first mode and (b) the second mode..... | 73 |
| Figure 3.20: The layout of the lateral accelerometer design-1 for the second fabrication mask set..... | 75 |
| Figure 3.21: The first and the second mode of the lateral accelerometer design-1 for the second mask set..... | 77 |

| | |
|--|-----|
| Figure 3.22: The layout of the lateral accelerometer design-3 for the second fabrication mask set..... | 79 |
| Figure 3.23: The first and the second mode of the lateral accelerometer design-3 for the second fabrication mask set..... | 81 |
| Figure 3.24: The layout of the vertical accelerometer design -1 for the second fabrication mask set..... | 82 |
| Figure 3.25: The mode analysis result of the vertical accelerometer design-1 (a) the first mode (b) the second mode..... | 84 |
| Figure 3.26: The vertical accelerometer design-2 layout for the second fabrication mask set..... | 85 |
| Figure 3.27: The mode analysis result of the vertical accelerometer design-2 (a) the first mode (b) the second mode..... | 87 |
| Figure 3.28: The layout of the vertical accelerometer design-3 for the second fabrication mask set..... | 88 |
| Figure 3.29: The mode analysis results of the vertical accelerometer design-3 (a) the first mode (b) the second mode..... | 90 |
| Figure 3.30: The vertical accelerometer design-4 layout for the second fabrication mask set..... | 91 |
| Figure 3.31: The mode analysis results of the vertical accelerometer design-4 (a) the first mode (b) the second mode..... | 93 |
| Figure 3.32: The vertical accelerometer design-5 layout for the second mask set. | 94 |
| Figure 3.33: The mode analysis results of the vertical accelerometer design-5 (a) the first mode (b) the second mode..... | 96 |
| Figure 3.34: Various three axis accelerometer designs from the fabrication mask set-2. (a) The lateral accelerometer design-2 and the vertical accelerometer design-3 (b) The lateral accelerometer design-2 and the vertical accelerometer design-3 (c) The lateral accelerometer design-3 and the vertical accelerometer design-1..... | 100 |
| Figure 4.1: The sandwich structure formed by two-step anodic bonding in DGM-DWP..... | 102 |
| Figure 4.2: The sandwich structure formed by two-step anodic bonding as well as the Au-Si eutectic bonding in DGM-SOG..... | 102 |
| Figure 4.3: The comparison of two alternative fabrication processes for the fabrication MEMS three axis accelerometer..... | 103 |

| | |
|---|-----|
| Figure 4.4: The glass wafer is cleaned by using the piranha solution for 30 minutes. | 104 |
| Figure 4.5: Cr/Au layers are deposited in the range of 10/150nm, respectively..... | 106 |
| Figure 4.6: Cr/Au layers are patterned and etched..... | 107 |
| Figure 4.7: Glass wafers are etched in BHF solution for the formation of the vertical gap. | 107 |
| Figure 4.8: 10/150nm thick Cr/Au layers are completely etched after the formation of the vertical gap. | 107 |
| Figure 4.9: Cr/Au layers are deposited in the range of 10/150nm, respectively..... | 108 |
| Figure 4.10: Cr/Au layers are patterned and etched..... | 108 |
| Figure 4.11: The anchor formation is completed by using pure HF. | 108 |
| Figure 4.12: Cr/Au layers are deposited on the glass wafers in the range of 10/150 nm, respectively. | 109 |
| Figure 4.13: The bottom electrode pad metallization. | 109 |
| Figure 4.14: The top electrode pad metallization..... | 109 |
| Figure 4.15: The silicon wafer (SiGeB or SOI) is cleaned by using the piranha solution. (H ₂ SO ₄ : H ₂ O ₂). | 110 |
| Figure 4.16: An insulator is coated on the SiGeB or SOI wafer. | 110 |
| Figure 4.17: Patterning of the insulator layer is performed by using BHF. | 110 |
| Figure 4.18: Structures are transferred to the silicon wafer by using DRIE. | 111 |
| Figure 4.19: The anodic bonding process is performed. | 111 |
| Figure 4.20: The handle layer is removed by using different methods for the SiGeB and the SOI. Then, the devices are released..... | 111 |
| Figure 4.21: The glass-silicon-glass sandwich structure..... | 112 |
| Figure 4.22 The capacitive gap is nearly 1.1 μ m after 6 minutes RIE etching. | 113 |
| Figure 4.23: The capacitive gap is nearly 0.6 μ m after 10 minutes DRIE etching. However, the etch profile and the surface roughness are not suitable for the fabrication of the vertical accelerometer. | 114 |
| Figure 4.24: The measurement result of the surface profiler result after 72 minutes wet etching. | 114 |
| Figure 4.25: The capacitive gap patterned on the glass wafer. | 115 |
| Figure 4.26: The blue region is the patterned silicon oxide on the silicon wafer. ... | 115 |
| Figure 4.27: Cross-sectional view of the finger regions after DRIE etching..... | 116 |

| | |
|---|-----|
| Figure 4.28: The bottom glass and SiGeB wafers are anodically bonded. The wafer is observed from the bottom glass side. The silicon oxide layer, which is used to prevent short between highly doped silicon and pad metallization, causes weak anodic bonding in this region..... | 117 |
| Figure 4.29: An SEM image of the bonded wafer. The short between the pad metallization and the highly doped SiGeB wafer frame is prevented by using the silicon oxide layer..... | 118 |
| Figure 4.30: The illustration of the two-electrode anodic bonding..... | 119 |
| Figure 4.31: The triple stack observed after the first fabrication attempt..... | 119 |
| Figure 4.32: The fabricated three axis accelerometer sensor wafer..... | 120 |
| Figure 4.33: Suspended structures do not have any damage after the second anodic bonding..... | 121 |
| Figure 4.34: The illustration of the optimized two-step dicing process..... | 122 |
| Figure 4.35: The diced three axis accelerometer fabricated by using DGM-DWP. | 122 |
| Figure 4.36: (a) The diced glass-silicon glass multi-stack (b) The dicing lines of the bottom glass and top glass. | 123 |
| Figure 4.37: An SEM images of the glass-silicon-glass-structure fabricated by using the two-step anodic bonding | 124 |
| Figure 4.38: The vertical accelerometer test result. Rest capacitance values formed between the top electrode and the proof mass as well as the bottom electrode and the proof mass are 25.62 pF and 13.05 pF, respectively for DGM-DWP. | 126 |
| Figure 4.39: The lateral accelerometer test result. Rest capacitance values formed between the electrode#1 and the proof mass as well as the electrode #2 and the proof mass are 10.87 pF and 10.79 pF, respectively for DGM-DWP..... | 127 |
| Figure 4.40: (a) Three dimensional view of the vertical accelerometer design-2 with perforation holes is formed by using data taken from the optical profiler (b) The buckling measurement result of the accelerometer fabricated by using the SiGeB wafer. The measured buckling is nearly 0.7 μ m between the anchor region and the center of the proof mass..... | 128 |
| Figure 4.41: (a) Three dimensional view of the vertical accelerometer design-2 with perforation holes is formed by using data taken from the optical profiler (b) The buckling measurement result of the accelerometer fabricated by using the SOI wafer. | |

| | |
|---|-----|
| The measured buckling is nearly 17 nm between the anchor region and the center of the proof mass. | 129 |
| Figure 4.42: Glass wafers are cleaned in the piranha solution for 30 minutes. | 132 |
| Figure 4.43: 10/150nm thick Cr/Au layers are deposited on glass wafers by using the sputtering system. | 133 |
| Figure 4.44: The deposited Cr/Au layers are patterned by using lithography steps. | 133 |
| Figure 4.45: Glass wafers are etched in BHF solution for the formation of the vertical gap. | 133 |
| Figure 4.46: 10/150nm thick Cr/Au layers are completely etched. | 134 |
| Figure 4.47: 10/150nm thick Cr/Au layers are deposited on glass wafers by using the sputtering system for the formation of anchor regions. | 134 |
| Figure 4.48: Cr/Au layers are patterned by using lithography steps. | 134 |
| Figure 4.49: Glass wafers are etched by using pure HF for the formation of anchor region. There are recesses among the anchor region to transfer the pad metallization to outside. | 135 |
| Figure 4.50: 10/150nm thick Cr/Au layers are completely etched. | 135 |
| Figure 4.51: 10/150nm thick Cr/Au layers are deposited on glass wafers by using the sputtering system for pad metals. | 135 |
| Figure 4.52: (a-b) The pad metallization also includes the shield metallization for the two-step anodic bonding approach. The metallization for the Au-Si eutectic bonding (c) the bottom glass (d) the top glass pad metallization. | 136 |
| Figure 4.53: The structure pattern is transferred on the SOI wafer by using DRIE. | 137 |
| Figure 4.54: The anodic bonding process is performed between the bottom and SOI wafers. | 137 |
| Figure 4.55: The SOI wafer is thinned by using DRIE until the buried oxide layer. | 137 |
| Figure 4.56: The three-axis accelerometer is released on the hot plate. | 138 |
| Figure 4.57: The formation of the multi-layers is provided either the two-step anodic bonding or the Au-Si eutectic bonding. | 138 |
| Figure 4.58: The fabricated glass wafers (a) the vertical gap etch (b) the anchor formation. | 139 |
| Figure 4.59: The fabricated glass wafer for the two-step anodic bonding process (a) the bottom glass wafer (b) the top glass wafer. | 140 |

| | |
|---|-----|
| Figure 4.60: The fabricated glass wafers for the anodic bonding and then the Au-Si eutectic bonding..... | 141 |
| Figure 4.61: Structures are patterned on the SOI wafer by using DRIE..... | 142 |
| Figure 4.62: The first anodic bonding recipe optimized for the bonding of glass and SiGeB wafers is applied for glass and SOI wafers..... | 143 |
| Figure 4.63: The anchor region, which is anodically bonded to the bottom glass in the first bonding fabrication step, is damaged after etching of the buried oxide layer. | 144 |
| Figure 4.64: (a) The contact region and (b) anchor regions after the modified anodic bonding..... | 145 |
| Figure 4.65: The modified first anodic bonding recipe improves the bonding quality (a) the previous attempt (b) the modified recipe result..... | 145 |
| Figure 4.66: The handle layer removing process results (a) for the SOI wafer having 0.5 μ m thick buried oxide layer (b) for the SOI wafer having 2 μ m thick buried oxide layer..... | 146 |
| Figure 4.67: The optical images of (a) the bottom glass-the silicon stack (b) the vertical accelerometer design-4 (c) the lateral accelerometer design-3 after releasing process..... | 147 |
| Figure 4.68: The illustration of the second anodic bonding. | 148 |
| Figure 4.69: The triple stack is broken after the second anodic bonding. | 149 |
| Figure 4.70: The fabricated triple stack in the second attempt. There is small crack in the flag region. | 150 |
| Figure 4.71: (a) The spring region and (b) the proof mass of the lateral accelerometer are damaged during the second anodic bonding. | 151 |
| Figure 4.72: Modified metal masks for lateral accelerometer designs (a-b-c) modified bottom electrode masks (d-e-f) modified top electrode masks | 152 |
| Figure 4.73: The fabricated sensor wafer. (a) Wafer level image (b) close view image of the sensor region..... | 153 |
| Figure 4.74: There is slightly misalignment observed after the second anodic bonding. However, this is in the mask tolerance range..... | 154 |
| Figure 4.75: The comparison of previous (a-c) and last (b-d) fabrication runs. The damage given the suspended structure during the second anodic bonding is eliminated by modifying the shield metallization mask. | 155 |

| | |
|--|-----|
| Figure 4.76: The result of the first attempt for the anodic bonding and then the Au-Si eutectic bonding. The bonding temperature and force are 390°C, 3000 N, respectively..... | 156 |
| Figure 4.77: The fabricated glass-silicon-glass sandwich structure by using the Au-Si eutectic bonding. | 157 |
| Figure 4.78: The color of the gold frame around the sensor region is not uniform. 158 | |
| Figure 4.79: The result of the Au-Si eutectic bonding for 410°C and 2500 N. (a) The gold is melted and spreads around. (b) Contacts regions are damaged after the eutectic bonding. | 160 |
| Figure 4.80: The fabricated wafer during the optimization process of the Au-Si eutectic bonding. The temperature and the piston value (a) 390°C and 1500 N and 400°C and 1500 N (b) 410°C and 2500 N. | 161 |
| Figure 4.81: The fabricated wafer during the optimization process of the Au-Si eutectic bonding. The temperature and the piston value (a) 400°C and 2500 N (b) 390°C and 2500 N. | 162 |
| Figure 4.82: Close view of sensor region after the Au-Si eutectic bonding (390°C and 2500 N)..... | 163 |
| Figure 4.83: The comparison of the Au-Si eutectic bonding (a) 400°C and 2500 N (b) 390°C and 2500 N. | 163 |
| Figure 4.84: (a-d) Contacts regions of lateral accelerometers. (e) The bottom electrode contact region of the vertical accelerometer. (f) The top electrode contact region of the vertical accelerometer. | 164 |
| Figure 4.85: The photoresist is spilled into the glass-silicon-glass sandwich structure to eliminate the risk of leaking water during the dicing process..... | 165 |
| Figure 4.86: The top glass of some of sensors, which is fabricated by using the anodic bonding and then Au-Si eutectic bonding, detaches from the bottom glass-silicon stack | 166 |
| Figure 4.87: An SEM image of the glass-silicon-glass sandwich structure fabricated by using the anodic and then the Au-Si eutectic bonding. | 166 |
| Figure 4.88: Diced sensor for (a) fabricated with the two-step anodic bonding (b) fabricated with the anodic bonding and then the Au-Si eutectic bonding. | 167 |
| Figure 4.89: The summary of the fabrication optimization for the three-axis accelerometer implemented with the glass-silicon-glass multi-stack. | 168 |

| | |
|--|-----|
| Figure 4.90: Optimized process steps for the fabrication of the three-axis accelerometer..... | 169 |
| Figure 5.1: Agilent Precision Impedance Analyzer 4294A used during the C-V test. | 172 |
| Figure 5.2: The C-V measurement test setup for the three-axis accelerometer..... | 172 |
| Figure 5.3: The resonance frequency test is performed by using the automatic probe station. | 173 |
| Figure 5.4: The layout of the glass substrate designed for integration of the three axis accelerometer with readout circuit. | 174 |
| Figure 5.5: The fabricated glass substrate for integration of the three-axis accelerometer with the readout circuit. (a) The wafer level image (b) close view image of the glass substrate. | 175 |
| Figure 5.6: The 16 pin package used during the system level test..... | 176 |
| Figure 5.7: The prepared three-axis accelerometer package. The three-axis accelerometer die is integrated with three individual readout circuit, and the wire-bonding is performed. | 176 |
| Figure 5.8: $\sigma(t)$ Sample plot of Allan variance analysis results [73]. | 178 |
| Figure 5.9: The test setup used during the system level test of the three-axis accelerometer. | 180 |
| Figure 5.10: The lateral accelerometer test result designed for the fabrication mask set-1. (a) The C-V change for the left electrode. (b) The C-V change for the right electrode. | 182 |
| Figure 5.11: The vertical accelerometer test result designed for the fabrication mask set-1. (a) The C-V change for the bottom electrode. (b) The C-V for the top electrode. | 183 |
| Figure 5.12: The wafer map for sensors fabricated the three-electrode anodic bonding method..... | 185 |
| Figure 5.13: The rest capacitance of the lateral accelerometer design-3 for different pad diagram of the shield metallization. | 186 |
| Figure 5.14: The C-V characteristic of the vertical accelerometer design-4 (a) for the bottom electrode (b) for the bottom electrode..... | 187 |
| Figure 5.15: The wafer level map for sensors fabricated the anodic bonding and then the Au-Si eutectic bonding in fabrication run#5 shown in Figure 4.81 (b). | 189 |

| | |
|---|-----|
| Figure 5.16: Lateral accelerometer C-V test results (a) design-1 (b) design-2 (c) design-3..... | 191 |
| Figure 5.17: Vertical accelerometer C-V test results (a) design-1 (b) design-2. | 192 |
| Figure 5.18: Vertical accelerometer C-V test results (a) design-3 (b) design-4. | 193 |
| Figure 5.19: The resonance frequency measurement result for lateral accelerometer (a) design-1 (b) design-2 (c) design-3. | 195 |
| Figure 5.20: The resonance frequency measurement result for vertical accelerometer (a) design-2 (b) design-3 (c) design-4. | 196 |
| Figure 5.21: (a) The data is collected for 2 minutes at 23 MHz sampling frequency. (b) The Allan Variance graph of the lateral accelerometer design-2, D10-x..... | 198 |
| Figure 5.22: (a) The data is collected for 2 minutes at 23 MHz sampling frequency. (b) The Allan Variance graph of the lateral accelerometer design-2, D10-y axis. .. | 199 |
| Figure 5.23: (a) The data is collected for 2 minutes at 23 MHz sampling frequency. (b) The Allan Variance graph of the lateral accelerometer design-3, A01-x-axis.. | 200 |
| Figure 5.24: (a) The data is collected for 2 minutes at 23 MHz sampling frequency. (b) The Allan Variance graph of the lateral accelerometer design-3, A01-y-axis.. | 201 |
| Figure 5.25: (a) The data is collected for 2 minutes at 23 MHz sampling frequency. (b) The Allan Variance graph of the vertical accelerometer design-4, A01-z axis.. | 202 |
| Figure 5.26: (a) The data is collected for 2 minutes at 23 MHz sampling frequency. (b) The Allan Variance graphs for the vertical accelerometer design-2, B03..... | 203 |
| Figure 5.27: The comparison of Allan Variance graphs for D10-x and D10-y for the lateral accelerometer design-2 fabricated by using two-step anodic bonding. | 204 |
| Figure 5.28: The comparison of Allan Variance graphs for A10-x and A10-y for the lateral accelerometer design-3 fabricated by using two-step anodic bonding. | 204 |
| Figure 5.29: The comparison of Allan Variance graphs for B03 and C09 for the vertical accelerometer design-2 fabricated by using two-step anodic bonding. | 205 |
| Figure 5.30: (a) The data is collected for 2 minutes at 46 MHz sampling frequency. (b) The Allan Variance graph of the lateral accelerometer design-1, B09. | 207 |
| Figure 5.31 (a) The data is collected for 2 minutes at 46 MHz sampling frequency: (b) The Allan Variance graph of the lateral accelerometer design-2, D10. | 208 |
| Figure 5.32: (a) The data is collected for 2 minutes at 46 MHz sampling frequency. (b) The Allan Variance graph of the lateral accelerometer design-3, A06-x..... | 209 |

| | |
|---|-----|
| Figure 5.33: (a) The data is collected for 2 minutes at 46 MHz sampling frequency. (b) The Allan Variance graph of the lateral accelerometer design-3, A06-y..... | 210 |
| Figure 5.34: (a) The data is collected for 2 minutes at 46 MHz sampling frequency. (b) The Allan Variance of the vertical accelerometer design-2, B04. | 211 |
| Figure 5.35: (a) The data is collected for 2 minutes at 46 MHz sampling frequency. (b) The Allan Variance graph of the vertical accelerometer design-4, A06. | 212 |
| Figure 5.36: The comparison of Allan Variance graphs for B06 and B04 for the vertical accelerometer design-2 fabricated by using the anodic bonding and then Au-Si eutectic bonding..... | 213 |
| Figure 5.37: The comparison of Allan Variance graphs A06 and B01 for the vertical accelerometer design-4 fabricated by using the anodic bonding and then Au-Si eutectic bonding. | 213 |
| Figure 5.38: Allan Variance graphs of lateral accelerometers A01 versus A06 fabricated by using two-step anodic bonding and the Au-Si eutectic bonding, respectively. | 214 |
| Figure 5.39: The comparison Allan Variance graphs for the vertical accelerometer design-2 fabricated different methods. The red one corresponds to the anodic and then the Au-Si eutectic bonding. The purple one corresponds to the two-step anodic bonding..... | 214 |
| Figure 5.40: (a) The collected data and for 2 minutes at 23 MHz sampling frequency (b) the Allan Variance graph of the vertical accelerometer design-5. | 215 |
| Figure 5.41: Non-linearity result of lateral accelerometer A04 is 0.28 %. | 218 |
| Figure 5.42: Non-linearity result of lateral accelerometer B07 is 0.34 %. | 218 |
| Figure 5.43: Non-linearity result of vertical accelerometer C09 is 0.41 %. | 219 |
| Figure 6.1: The proposed fabrication method to hermetically seal the sensors region. | 225 |

CHAPTER 1

INTRODUCTION

Micro-Electro-Mechanical Systems (MEMS) introduces us with a technology enabling the integration of mechanical and electrical components. The first example of MEMS technology having certain stress-sensitive effects in silicon and germanium termed piezoresistance emerged in 1954. During the early 1960s, the first silicon diaphragm pressure sensor and strain gauges were introduced by Honeywell Research Center and Bell Lab. The silicon sensor technology attracted more attention in the late 1960s and the first commercialized pressure sensors took place in the market. These were primitive examples compared to today's standards; however, pressure sensors with non-planar diaphragm geometries exhibited superior performance in the early 1970s. These devices could arguably be regarded as the first real MEMS sensors [1]. There has been a major improvement in the field of MEMS during the half century. Especially, the progress in the micro fabrication and the batch fabrication techniques leads to miniaturization of the sensors. This has resulted small, rugged and low-cost devices such as accelerometers, strain gauges, microphones, air mass flow sensors, pressure sensor and more recently gyroscopes and yaw-rate sensors [2-3].

Today MEMS inertial sensors have been taking place many consumer electronics products, including smart phones, tablets, gaming systems, Tv remote control systems, and toys. [4]. Micromachined sensors obviously have huge commercial potential. The applications mentioned above have some common requirements such as small-size, low cost and low power consumption. Micromachined sensors satisfy these requirements as a result of advances in silicon MEMS technology. However,

MEMS inertial sensors have different performance requirements depending on the applications. Figure 1.1 shows performance requirements of accelerometers.

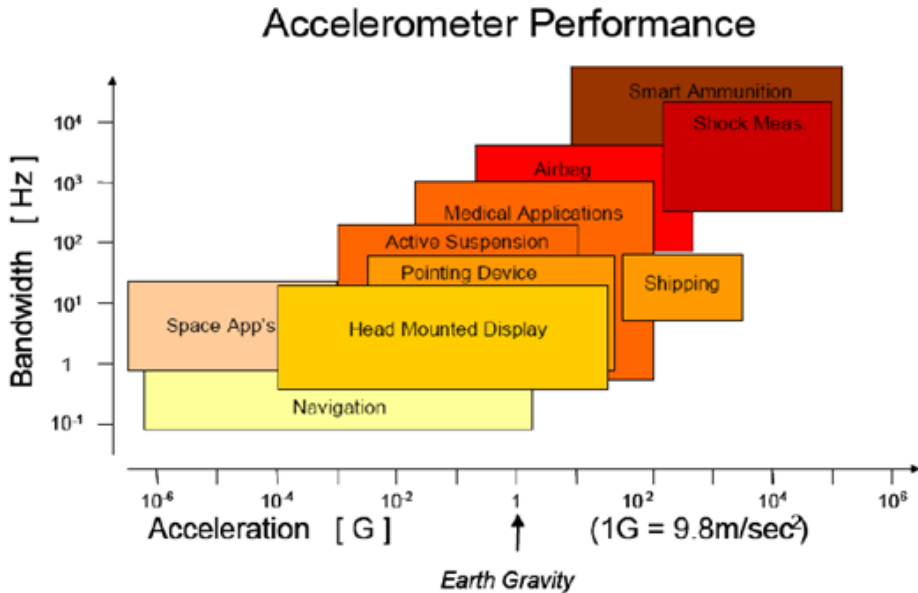


Figure 1.1: Different applications and performance requirements of the accelerometers [5].

Three-axial acceleration sensing is a must for most of these applications. Hence, single or dual axis accelerometers are assembled to provide three dimensional sensing. However, this leads to increase not only packaging size but also cost. Furthermore, the misalignment of individual accelerometers is a major problem causing cross-axis sensitivity. Therefore, there is a need for a fabrication process of a monolithic three-axis accelerometer. The aim of the study is to develop a process for the fabrication of a monolithic three-axis accelerometer implementing both the lateral and the vertical accelerometer in a same die.

In our previous works, the designing and fabrication of a MEMS capacitive differential lateral capacitive accelerometer was already successfully completed in METU-MEMS Research and Applications Center. In the scope of this study, a three-axis accelerometer is designed implementing both the MEMS capacitive differential lateral and the MEMS capacitive differential vertical accelerometers in the same die,

and a fabrication method is developed to form such a device. The MEMS capacitive lateral accelerometer can be easily fabricated as sense electrodes of the accelerometer can be implemented in the same plane. However, it is necessary to form a multi-stack to provide a top electrode for the MEMS capacitive differential vertical accelerometer to fabricate the three axis accelerometer in the same die. This is a main challenge of the fabrication of the three-axis accelerometer. Furthermore, another difficulty is to match performance parameters of the lateral and the vertical ones to each other. Therefore, a sandwich structure composed of glass-silicon- glass multi-stack is considered to fabricate the three-axis accelerometer providing not only a top electrode for the vertical accelerometer but also a cap for the entire structure.

Two alternatives fabrication processes are developed to form a glass-silicon-glass multi stack in the scope of this study. First attempt uses the anodic bonding in the last step of the formation of multi-stack while the second approach is implemented with the Au to Si eutectic bonding. Finally, the die level and the system level test of the three-axis accelerometer fabricated by using two alternatives bonding methods are performed. This study reports, for the first time in literature, the three-axis accelerometer fabricated by using the glass-silicon-glass sandwich structure implementing the lateral and the vertical accelerometers in the same die.

The organization of this chapter is as follow; Section 1.1 and Section 1.2 give brief information about MEMS accelerometers and classification. The state of the art studies in literature for three-axis accelerometer are given Section 1.3. The objective of the study and the outline of thesis are given in Section 1.4 and 1.5, respectively.

1.1. MEMS Accelerometers

Many producers of piezoelectric accelerometers emerged during the late 1940s and early 1950s. Brüel&Kjær (Denmark), Columbia Research Laboratories (Woodlyn, PA), Endevco (Pasadena, CA), Gulton Manufacturing (Metuchen, NJ), and Kistler Instruments (Buffalo, NY) were pioneers companies [6]. Microfabrication methods such as the anisotropic chemical etching of silicon, the ion implantation, and the anodic bonding developed during the late 1960s and early 1970s contributed to

improve the performance of microfabricated devices. A diffused, chemically micromachined, integrated silicon beam accelerometer was introduced by Gravel and Brosh in the late 1960s. In 1970s, the first piezoresistive micromachined accelerometer was reported by Roylance and Angell which was fully packed by help of a pair of pyrex glass wafers to protect the entire structure from environmental conditions. The first commercialized piezoresistive accelerometer was demonstrated by Barth et all., where the silicon fusion bonding method was used. Subsequent improvement emerged by monolithically integration of piezoresistive accelerometer with CMOS as well as temperature compensation circuitries. A novel piezoresistive accelerometer was introduced by Allen where in-plane and out-of-plane acceleration measured with the help of a specially designed vertical spring structure. A three axis piezoresistive accelerometer was reported by Kwon and Park where the bulk micromachining and the silicon direct bonding technology was utilized [7]. Figure 1.2 shows the historical genealogy of MEMS sensor and actuators [9].

Since 1987, MEMS has been transferred from the early stage of technology development to the mature stage of the mass production in the practical applications [8]. Accelerometer mentioned on the above are the first examples of piezoresistive accelerometers. Nowadays, the capacitive transduction is as popular as piezoresistive transduction for commercial accelerometers. The piezoresistive transduction is widespread among Japanese accelerometer companies (e.g., Matsushita, Fujitsu, Hitachi Metals and Hokuriku) while the companies from US and Europe (e.g., Bosch, Freescale, Kionix, STMicroelectronics and Analog Devices) mainly prefer to use the capacitive sensing. CMOS integrated circuits are used not only piezoresistive but also capacitive sensing methods for the amplification and the compensation implemented by either monolithic or hybrid approach. Automotive industry generally prefers capacitive transduction with integrated self-test by electrostatic actuation. Especially, three-axis sensing, size and cost in consumer electronics are the main concerns for the accelerometer [7]. Figure 1.3 shows decrease in the die size with respect to years. Today, the MEMS market reaches over 10 Billion's dollar per year, and it is estimated to grow over 20 Billion's dollar by 2018. Figure 1.4 shows the market forecast for MEMS sensors between 2012-2018 [11].

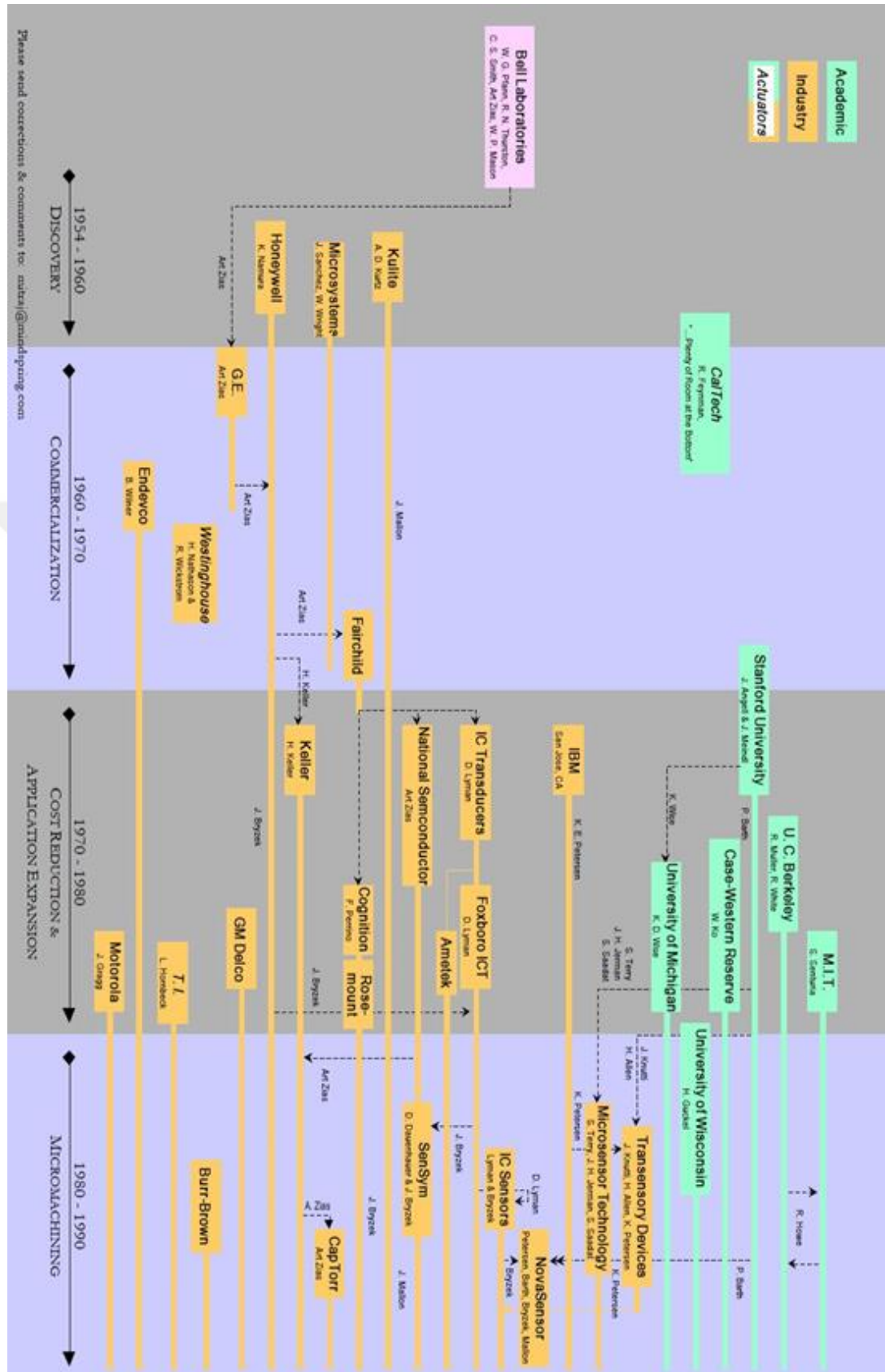


Figure 1.2: Historical genealogy of MEMS sensors and actuators in 1954-1990 [9].

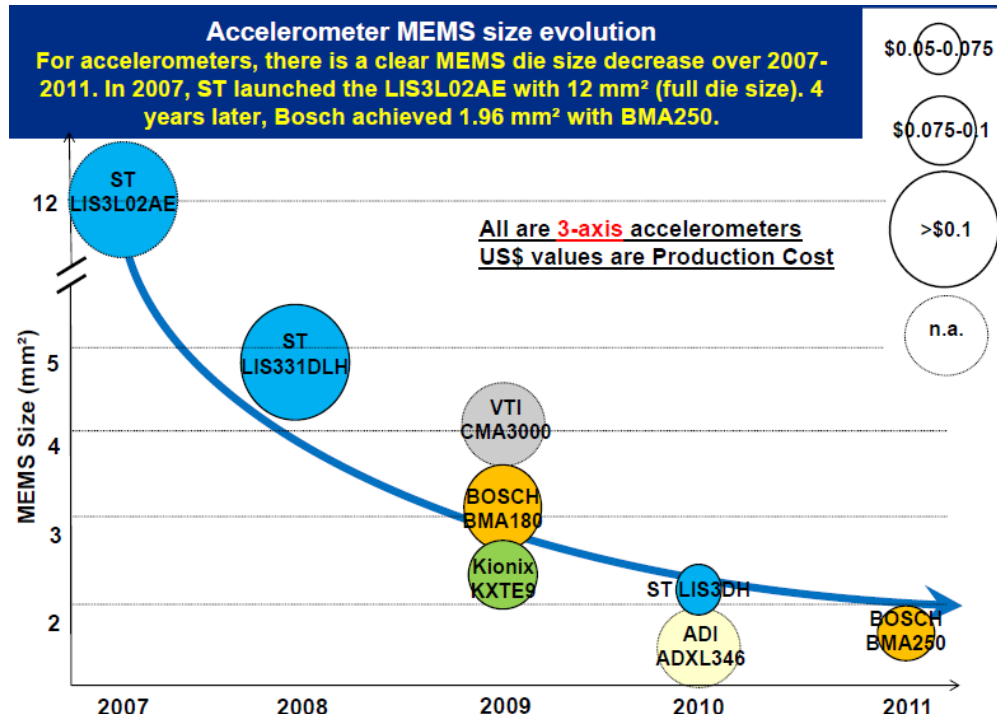


Figure 1.3: Die size versus year [10].

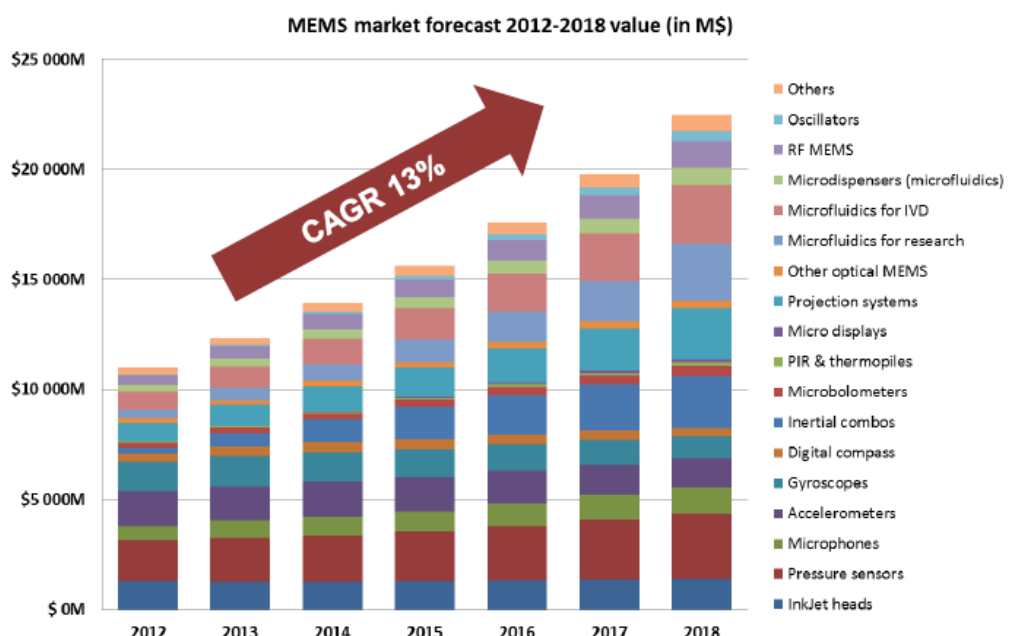


Figure 1.4: The estimation of the compounded annual growth rate (GAGR) for MEMS sensors [11].

1.2. Classification of MEMS Accelerometers

The classification of MEMS accelerometers are mainly based on transduction mechanisms. The main sensing mechanisms of MEMS accelerometer are capacitive, piezoresistive, tunneling, resonant and thermal [12].

Capacitive sensing: In the existence of acceleration, the proof mass moves from its rest position to opposite direction of acceleration and the capacitance formed among capacitive fingers changes. The capacitance change can be determined by using electronic circuitry. Capacitive sensing technique is a popular measurement method among MEMS sensors because of its robustness and compatibility with many fabrication processes. One of the main advantages of capacitive devices is to have simple structure. Moreover, the capacitive interfaces have widespread usage area for applications demanding low-cost, low power detection and as well as high precision inertial devices. Furthermore, they provide us with many advantages such as high sensitivity, good dc response, noise performance, low drift, and low temperature sensitivity. However, capacitive devices are vulnerable to electromagnetic interference (EMI) because of high impedance sense nodes. Therefore, it is necessary to development of proper packaging technology and to shield the accelerometer and its interface circuit [12].

Piezoresistive sensing: The piezoresistive sensing is one of the earliest methods and has been still utilized in the fabrication of many commercial sensors. In this method, the beam or the spring bend as a result of external acceleration, and the resistivity of the piezoresistive material placed into beams change. Thus, it is possible to determine external acceleration. The simple structure design and electronic circuit as well as easy fabrication process are main advantages of this transduction mechanism. However, this method has some disadvantages such as low output level, and high temperature dependency compared to the capacitive transduction [12].

Tunneling sensing: These devices use a constant tunneling current formed between the tunneling tip and its counter electrode to determine displacement. In this method, the tunneling current remains constant if the tip is as close as a few angstroms to its

counter electrode using electrostatic force generated by bottom deflection electrode. In the presence of the acceleration, the proof mass moves. The change of current is determined by the readout. The proof mass is moved to its rest position by readjusting the bottom deflection voltage. The measurement of acceleration can be performed by reading out the bottom deflection voltage with closed loop system. Tunneling accelerometers have not only small size but also high sensitivity. However, the main drawback is the requirement of stiff feedback loop which reduces the useful bandwidth [13].

Resonant devices: The resonant transduction working principles is based on monitoring the natural frequency of resonant devices. The natural frequency of the resonant devices changes in the presence of the acceleration. The acceleration can be determined by the shift in the resonance frequency [14].

Thermal devices: The thermal transduction is also used for acceleration sensing. The first thermal accelerometers depend on the temperature flux which is inversely proportional to separation between a heater and a heat-sink plate. The change of separation can be determined by measurement of the temperature with the help of thermopile. It is possible to fabricate devices with movable thermopile array and fixed heather or vice versa. Another type of the thermal accelerometer is based on free-convention heat transfer of a small hot air bubble in a sealed chamber. These kinds of accelerometers do not have any moving mechanical parts. A hot air bubble is formed by thermally isolated heather. The heat distribution of this bubble, which is asymmetric in terms of the heater, varies in existence of the acceleration. Acceleration is measured by two symmetrically placed temperature sensors sensing the heat profile [15].

It is also possible to encounter accelerometers fabricated by using different sensing mechanism such as optical, piezoelectric and electromagnetic [12].

1.3. Three Axis Accelerometers Reported in Literature

Applications mentioned above need three axis acceleration sensing. Therefore, there is an intensive investigation on the fabrication of three axis accelerometers in the literature. Generally, the most common methods for the fabrication of three axis accelerometers are the surface and the bulk micromachining. Furthermore, the design concept of the three axis accelerometer is also classified in terms of the proof mass. It is possible to encounter not only the single proof mass and but also individual proof mass structures for different axes. Furthermore, there are several vertical accelerometers are fabricated by using the glass-silicon-glass sandwich structure concept. In the following chapter, some of three axis accelerometers and vertical accelerometers fabricated by using sandwich structure concept reported in the literature will be discussed.

1.3.1. Post CMOS-MEMS Three Axis Accelerometers

A CMOS multi-channel readout integrated with tri-axis capacitive accelerometers on a single chip is reported in [16]. Figure 1.5 shows the proposed tri-axis CMOS-MEMS accelerometer design.

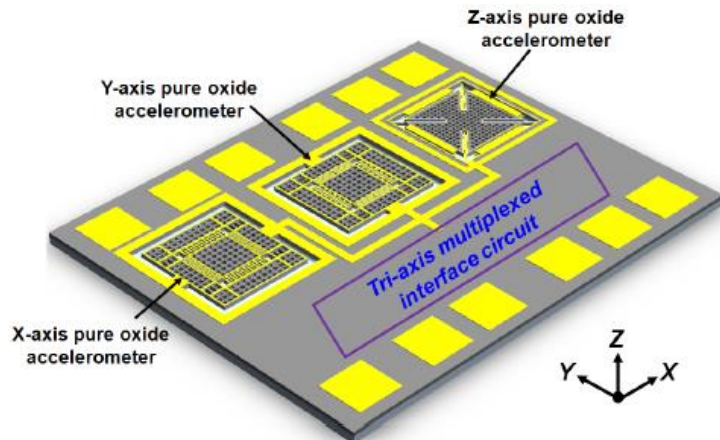


Figure 1.5: The illustration of the tri-axis CMOS-MEMS accelerometer design [16].

After the fabrication of the chip by the standard TSMC 0.35 μ m 2P4M CMOS process, the tri axis accelerometer is fabricated by using Post-CMOS fabrication

sequence. The post-CMOS fabrication process begins with metal etching process by using H_2SO_4 and H_2O_2 chemical solution (Figure 1.6 (a)). The planar dimensions of the MEMS structures and sensing gaps for the lateral and the vertical accelerometers are formed. Then, the passivation layer is etched by using reactive ion etching (RIE) to provide connections during the wire bonding. Finally, MEMS structures are suspended by isotropically etching of the Si substrate by XeF_2 (Figure 1.6 (c)). Figure 1.6 shows the fabrication process for the post-CMOS fabrication process.

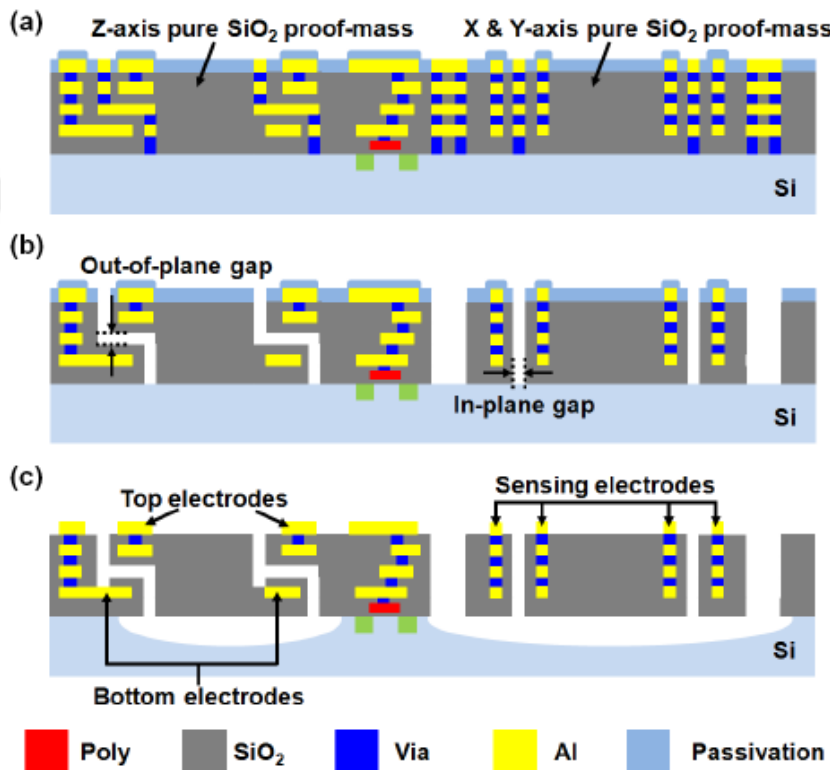


Figure 1.6: The post-CMOS fabrication process for tri-axis accelerometer reported in [16].

The fabricated tri-axis accelerometer has 2.72 mm^2 chip size. The sensitivity of the lateral and the vertical accelerometer are 105 mV/g , 127 mV/g and 58 mV/g , respectively. The non-linearity of the tri-axis accelerometer for x, y and z axis is 1 %, 0.5 % and 2.4 %, respectively. Cross-axis sensitivities are % 3, % 2.3 and % 8.8. The noise floor of the tri-axis accelerometer is $0.4\text{ mg}/\sqrt{Hz}$, $0.2\text{ mg}/\sqrt{Hz}$ and $0.9\text{ mg}/\sqrt{Hz}$. The full scale range of the lateral and the vertical accelerometer are 0.01 and 2 g, respectively [16].

A novel CMOS-MEMS three-axis accelerometer design is reported in [17]. The fabrication process depends on the TSMC 0.18- μm one poly-Si six metal/dielectric (1P6M) CMOS process. It is possible to form the in-plane and out-of-plane fully differential sensing electrodes as a result of the multilayer metal and dielectric used in CMOS technology. Thus, the sensing electrodes can be formed not only along the width/length but also along the thickness of the proof mass, which allows significantly increasing the number of sensing electrodes. Another advantage of the fabrication process is the formation of fully differential gap structure on the single proof mass. Figure 1.7 shows the design concept of the three axis accelerometer.

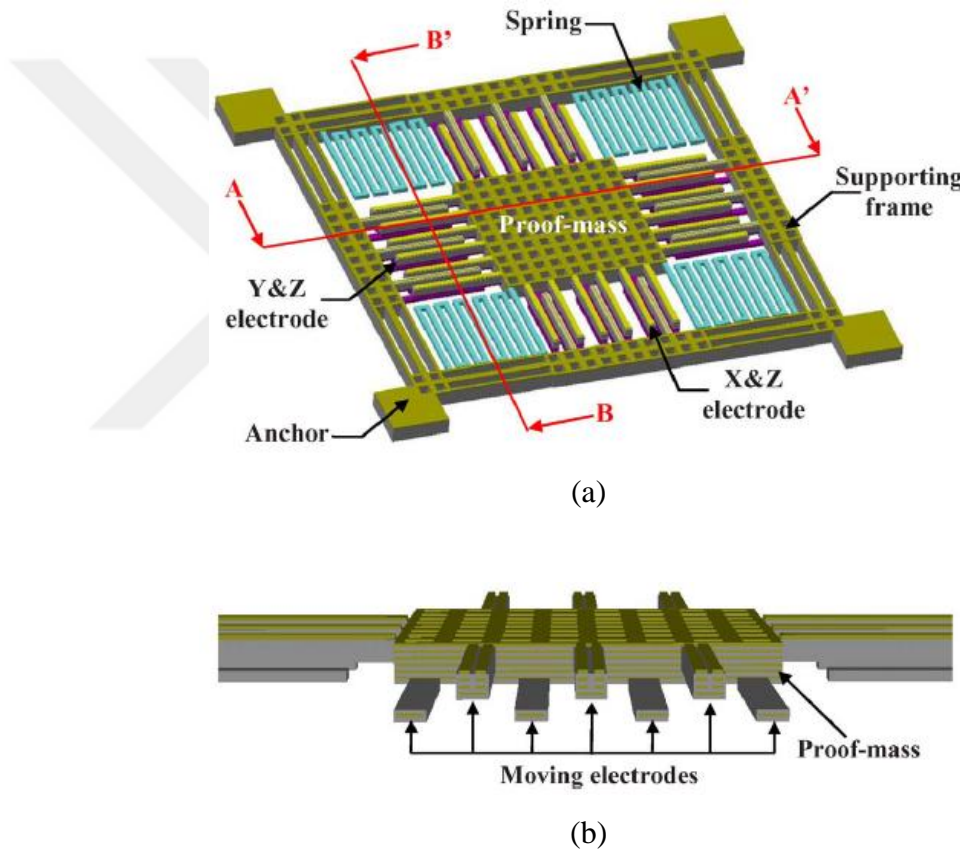


Figure 1.7: The illustration of the design concept for the three-axis accelerometer (a). The cross sectional view of the three axis accelerometer showing the sensing electrodes on the proof mass [17].

Figure 1.8 shows the fabrication process of the three-axis accelerometer. The fabrication process begins with patterning of the thin films (Figure 1.8-a). Next, the

aluminum and tungsten via are etched by using the metal wet etching H_2SO_4 and H_2O_2 solution. The dielectric is used as protection layer during etching of the exposed aluminum film. In this step, in-plane and out-of-plane sensing gaps and the micromechanical structures are patterned (Figure 1.8-b). Then, the process continues with the reactive ion etching process (RIE) to remove the passivation layer (Figure 1.8-c). The process is completed by using XeF_2 silicon isotropic etching to release the structures (Figure 1.8-d).

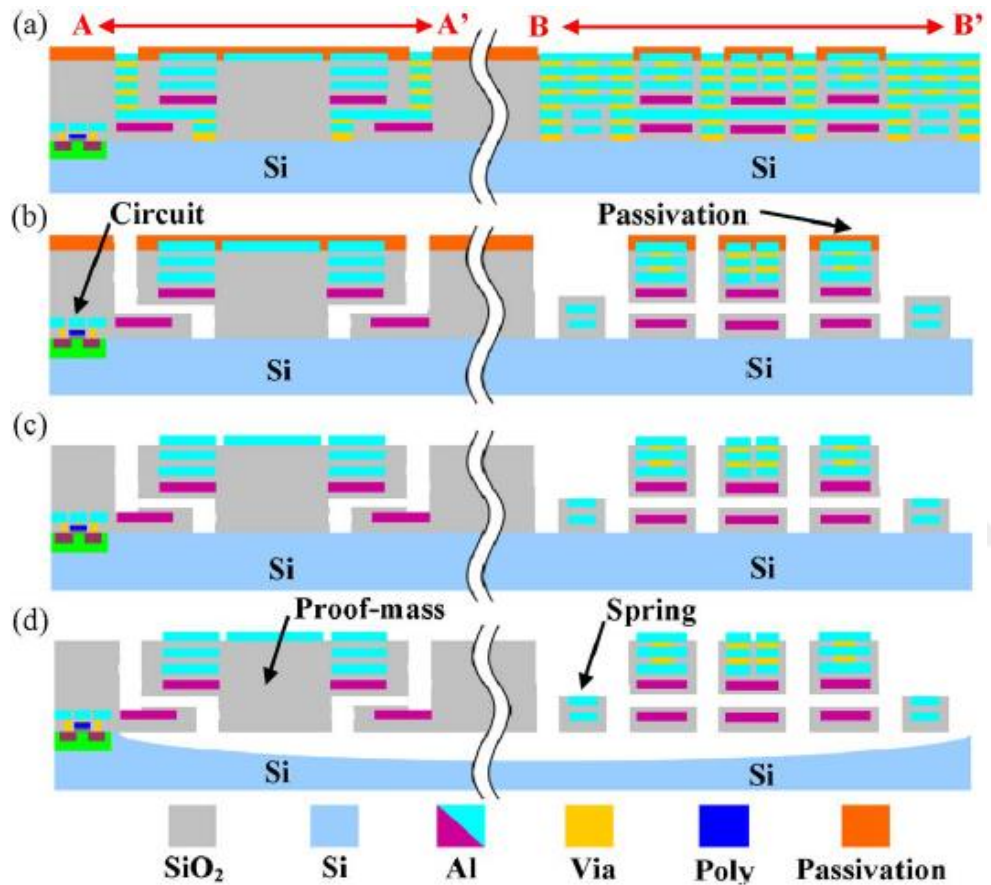


Figure 1.8: The post-CMOS process for the three axis accelerometer reported in [17].

The fabricated three-axis accelerometer has $400 \times 400 \mu\text{m}^2$ die size. The nonlinearities of for three sensing axes are 3.2 %, 1.4 % and 2.8 % for x, y and z axis. The full scale range is nearly 0.01~1g for all axes. The noise level is 2.1 mg/ $\sqrt{\text{Hz}}$, 2.0 mg/ $\sqrt{\text{Hz}}$ and 2.1 mg/ $\sqrt{\text{Hz}}$, respectively. While the acceleration is applied in the x axis direction, the cross axis sensitivities of y and z axis are 6.6 %

and %5, respectively. When the acceleration is applied in y axis, the cross-axis sensitivities of x-axis and y-axis are % 5.4 and 2.3 %, respectively. The-cross axis sensitivities of x and y axes in terms of the acceleration applied in the z axis direction are 5.2 % and 5.2 %, respectively [17].

A novel single proof-mass tri-axis capacitive type complementary metal oxide semiconductor MEMS accelerometer is demonstrated in [18]. The z-axis of the tri-axis accelerometer is specially designed to reduce the cross-axis sensitivity. The tri-axis accelerometer is fabricated by using the TSMC 2P4M fabrication process.

Figure 1.9 shows the illustration of design of the tri-axis accelerometer. The fabrication process continues on the substrate fabricated by using TSMC 0.35 μm CMOS 2P4M processing. The fabrication process provides one passivation layer, four aluminum metal layers (M1 to M4), four silicon dioxide dielectric films, and several tungsten vias stacked and patterned on top of the silicon substrate. The multi-stack mentioned above have nearly 7 μm structural thicknesses. The fabrication process includes several steps such as wet etching of the metal layers, dry etching of dielectric layers, and isotropic bulk silicon etching from the front side substrate shown in Figure 1.10 (b-e). The die size of tri axis accelerometer chip is 1.78 x 1.38 mm^2 .

The full scale measurement range is 0.8~6g. Nonlinearities of x, y and z axes are 2.64 %, 3.15 %, 3.36 %, respectively. The cross-axis sensitivities of different axes are in the range of 1 % and 8.3 %. The noise levels of each axis are 120 mg/ $\sqrt{\text{Hz}}$, 271 mg/ $\sqrt{\text{Hz}}$, 357 mg/ $\sqrt{\text{Hz}}$, respectively [18].

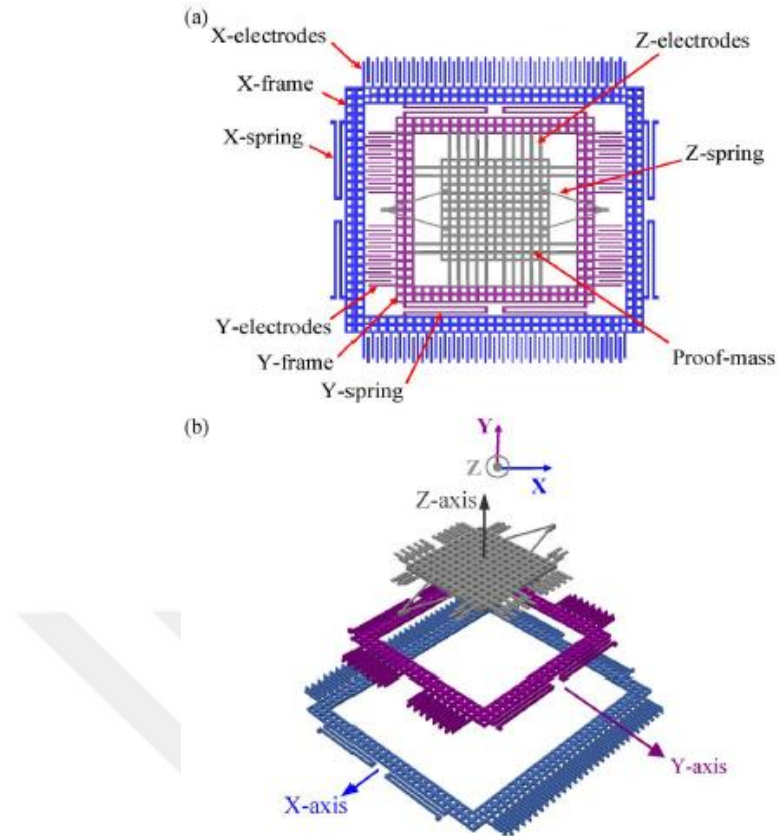


Figure 1.9: The illustration of the design of the tri-axis accelerometer reported in [18].

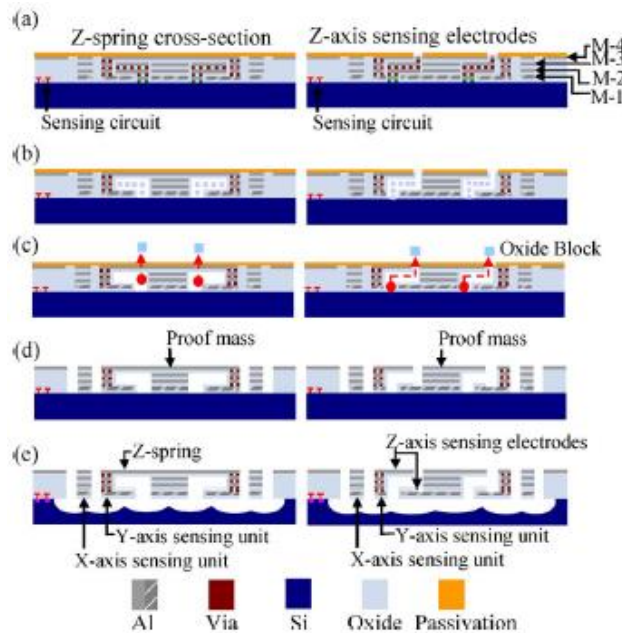


Figure 1.10: The fabrication process for the tri-axis accelerometer reported in [18].

1.3.2. Bulk Micromachined Three-Axis Accelerometers

The tri-axis accelerometer operating in a low-pressure environment is reported in [19]. The sensors are fabricated by using HARPSSTM process on a 40 μm -thick SOI substrate, where in-plane and out-of-plane nanoscale capacitive airgaps are implemented.

Figure 1.11 shows the design concept of the tri-axis accelerometer. Not only in-plane but also the out-of-plane accelerometers are implemented on 40 μm -thick silicon-on-insulator (SOI) substrate, where the latest version of the HARPSSTM fabrication process is used. During the fabrication process, the structure pattern is defined by etching of the lateral trenches, where the thermal oxide is used as a mask. Lateral gaps are patterned by using a thin layer (grown 300 nm) of sacrificial oxide. Side electrodes and bridging electrodes are formed by filling the trenches with polysilicon and TEOS oxide. It is need for growing an additional 300 nm thermal oxide layer to define out-of-plane gaps. Then, the fabrication process continues with deposition and patterning of the poly silicon for top electrodes and out-of-plane accelerometer flexures. Finally, the sensor is released by using hydrofluoric acid (HF). After the fabrication is completed, the substrate wafer is bonded to another wafer to provide a cap and hermetic sealing. Therefore, the fabrication of the capping wafer is independently completed. Firstly, trenches are formed and filled with an insulator. Through-silicon vias (TSV) formation are completed with this fabrication process step. Next, a recess is formed on the capping wafer. Next, a gold layer is deposited, and patterned to provide eutectic bonding with MEMS sensor. Finally, after the bonding of the sensor wafer and the capping wafer, gold traces and pads are patterned on the bonded cap.

Figure 1.12 shows the cross sectional view of the tri axis accelerometer. The size of the fabricated sensor is 1mm x 1mm x 40 μm . The sensitivities of the sensors are 2.76 fF/g for x/y axes and 3.2 fF/g for z axis. Nonlinearities are 0.31% for x/y axes and 0.91 % for z axis at 2g. The output noise floor is -90 dBVRms/ $\sqrt{\text{Hz}}$ at 1 Hz.

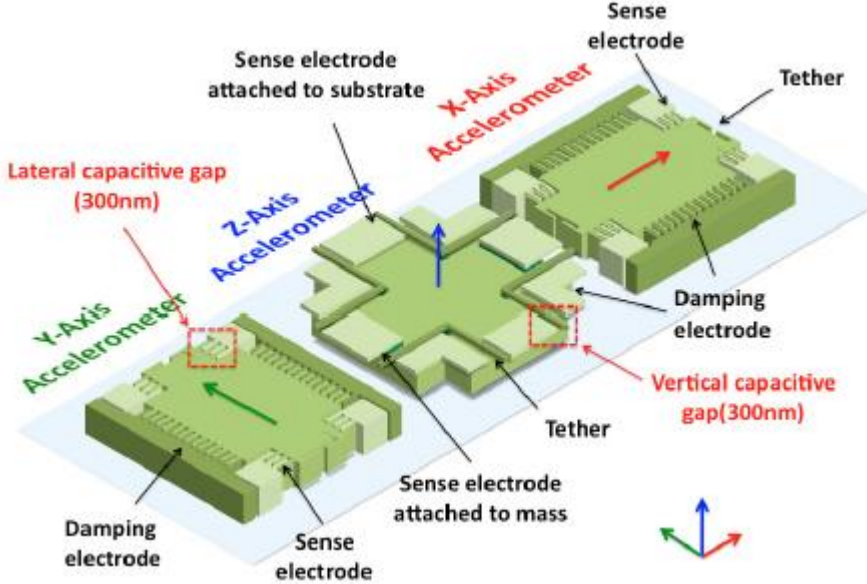


Figure 1.11: The illustration of the proposed tri-axis accelerometer reported in [19].

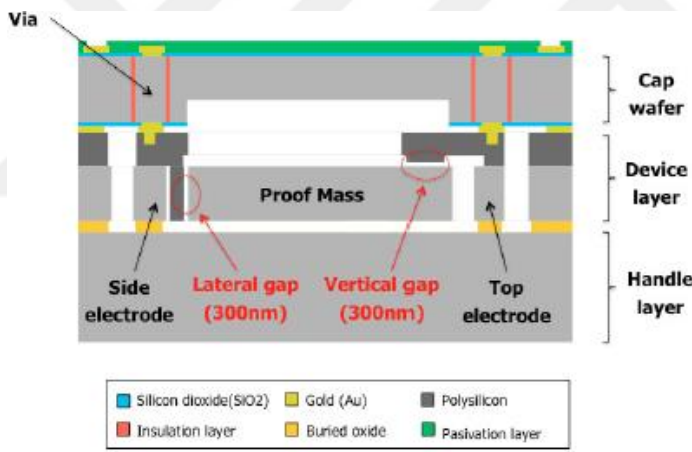


Figure 1.12: Cross-sectional view of the tri-axis accelerometer reported in [19].

A new three axis accelerometer design is presented in [20]. The three axis accelerometer is implemented with individual lateral and vertical accelerometers in a concentric structure. Figure 1.13 shows the conceptual design of the sensor. The tri-axial accelerometer is fabricated by using a fabrication process depending on modified SOG bulk micromachining and DRIE etching. The fabrication process begins with the formation of pedestals on the device layer of a SOI wafer, where the structural layer is selected as 55 μm . The vertical capacitive gap is defined through

the height of the pedestal. Next, the electrical contacts are formed on the top of the pedestals with deposition of a multi-layer metallization. Then, the fabrication process continues with the glass wafer. Interconnect/capacitors places and the bond paths are formed through two metallization step on the glass wafer. Afterwards, the anodic bonding process is performed between the SOI wafer and the glass wafer. Next step is removing of the handle layer of SOI. Finally, the devices are patterned by using DRIE in the range of a depth of 50 μm and minimum width 3 μm . Figure 1.14 shows explanatory fabrication process for the reported devices. Table 1.1 summarizes the device performance of the reported tri-axial accelerometer.

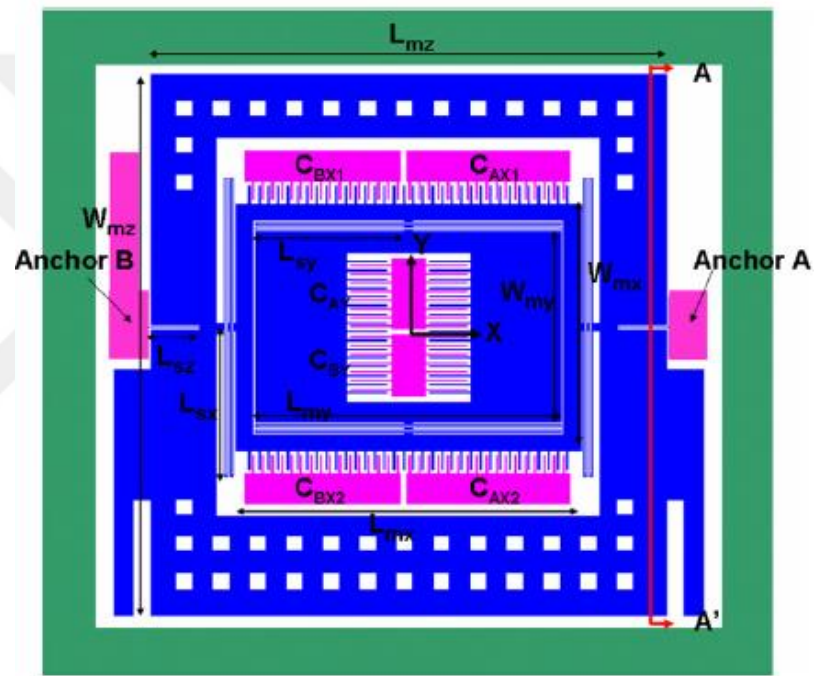


Figure 1.13: The illustration of the three axis accelerometer design reported in [20].

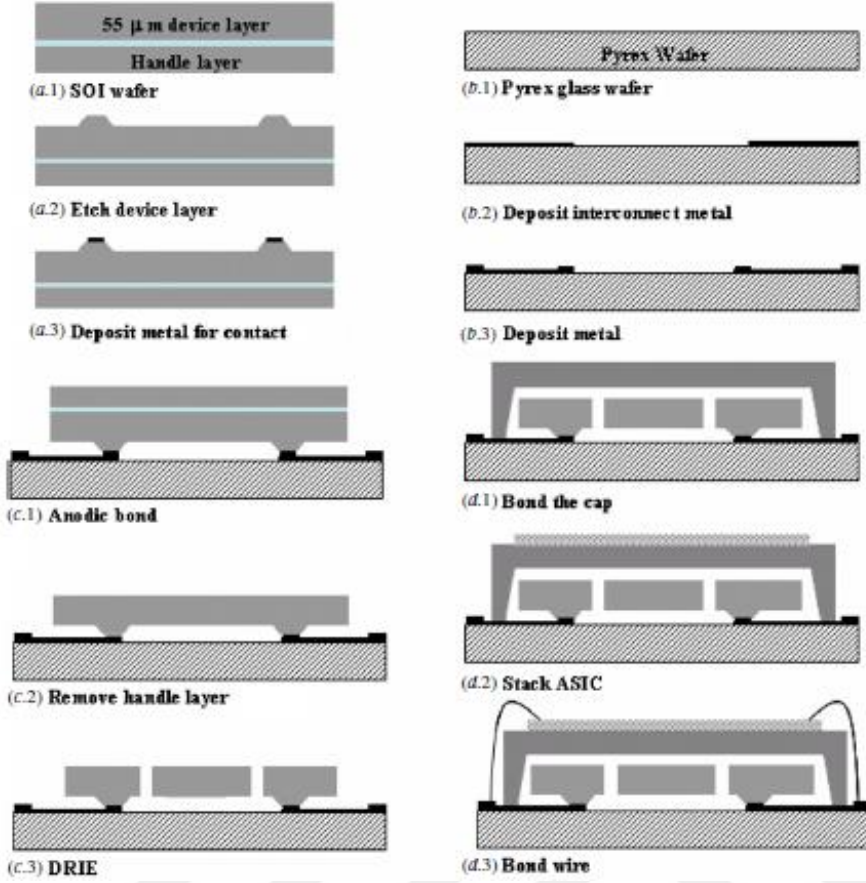


Figure 1.14: The fabrication steps of the tri-axial accelerometer reported in [20].

Table 1.1: The performance parameters of the reported accelerometer [20].

| | x-axis | y-axis | z-axis |
|--|--------|--------|--------|
| Measured sensitivity (V g⁻¹) | 1.422 | 1.241 | 1.434 |
| Measured linearity (% of FS) | 0.52 | 0.56 | 0.24 |
| Measured S/N ratio @ 0.5 g f = 37 Hz (dB) | 70.0 | 68.2 | 76.6 |
| Designed noise floor (μg Hz^{-1/2}) | 35.4 | 60.3 | 26.3 |
| Measured noise floor (μg Hz^{-1/2}) | 138 | 159 | 49 |
| Designed mechanical damping ratio | 1.31 | 1.60 | 0.69 |
| Designed pull-in voltage of CA (V) | 10.58 | 10.70 | 8.45 |
| Measured pull-in voltage of CA (V) | 12.2 | 14.0 | 6.0 |

A monolithic capacitive three-axis accelerometer having micro-g resolution is demonstrated in [21]. The three-axis accelerometer is formed by implementing three individual single-axis accelerometers, which mitigates the size of the entire system. Figure 1.15 shows the design concept of the three axis accelerometer.

The three-axis accelerometer is fabricated by implementing the surface and the bulk micromachining methods. The first step in the fabrication process is a shallow 3.5- μm -deep p++ boron diffusion on both sides of a $<100>$ double-side polished p-type silicon wafer, where the thickness of suspension beams and the area of the proof-mass and supporting rim is defined. Next, Deep Reactive Ion Etching (DRIE) is used to form 70 μm -deep trenches. After that, trenches are completely filled with a combination of LPCVD silicon oxide (sacrificial layer), silicon nitride and doped polysilicon. The polysilicon in the refilled trenches is utilized to forms not only vertical sense/drive electrodes and high aspect ratio spring for in plane devices but also vertical stiffeners for the out-of-plane device. After the polysilicon deposition, it is necessary to perform an annealing step to reduce any compressive stress in polysilicon layer. Afterwards, Reactive Ion Etching (RIE) is used to etch the polysilicon and nitride films. The process continues with deposition of another LPCVD silicon oxide. The contact opening is defined in this step by patterning oxide and etching in Ethylene-Diamine-Pyrocatechol (EDP) solution. Next, the contact metal is electroplated. Some of the single-crystal silicon is etched by using DRIE to not only minimize the etch period in the anisotropic wet etching but also help undercut the electrodes for in-plane devices by the etchant. Following step is the anisotropic wet etching both to release the proof-mass and the supporting rim as well as remove the unnecessary silicon region around the sense/drive electrodes for in-plane devices. This step is critical to obtain high sensitivity in-plane devices. Finally, the sacrificial oxide layer is etched by using hydrofluoric acid (HF).

The fabricated three axis accelerometer sensors have 475- μm -thick structural layer, large area polysilicon sense/drive electrodes, and small sensing gap ($<1.5\ \mu\text{m}$). The size of the accelerometer is $7 \times 9\ \text{mm}^2$. The designed full scale range of the three axis accelerometer is $\pm 1\text{g}$. The total measurement noise floor of the hybrid accelerometer

integrated with a CMOS readout circuit is $1.60 \mu\text{g}/\sqrt{\text{Hz}}$ and $1.08 \mu\text{g}/\sqrt{\text{Hz}}$ for in-plane and out-of plane sensors, respectively.

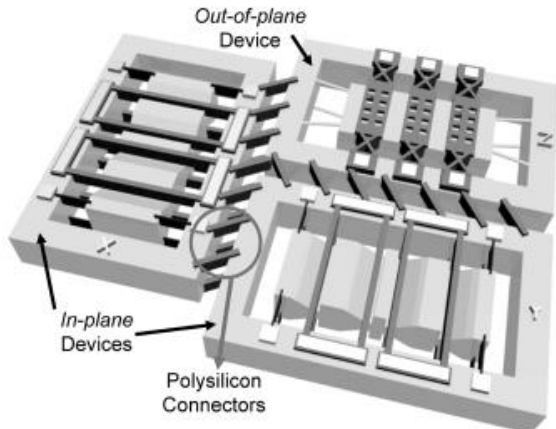


Figure 1.15: The illustration of the three axis accelerometer structure reported in [21].

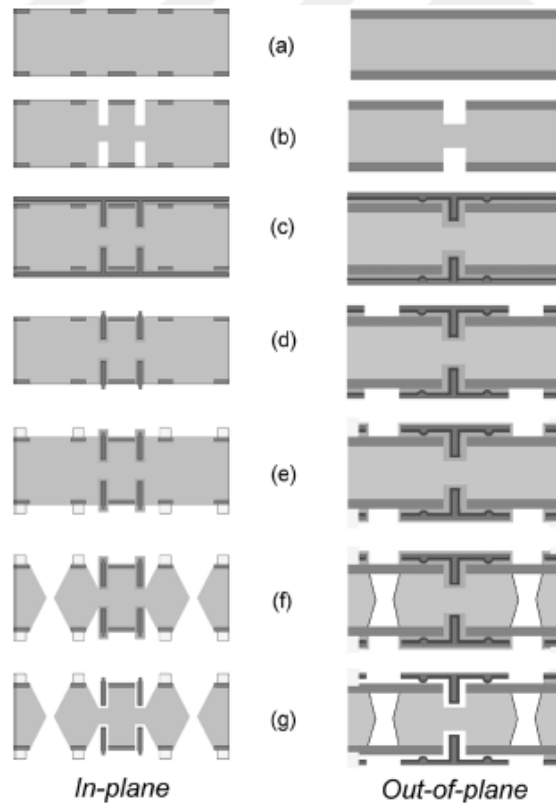


Figure 1.16: The fabrication process flows for the three axis accelerometer reported in [21].

A monolithic three-axis accelerometer is presented in [22]. The device is fabricated by using bulk micromachining method. Furthermore, the sensor has another glass wafer to provide encapsulation. Figure 1.17 shows the illustration of the device structure. The device is fabricated by using a SOI wafer, where the structural layer is 6 μm . Figure 1.18 shows the fabrication process flows of the three axis accelerometer. The process starts with formation of the proof masses by two successive vertical plasma etching of the handle wafer according to the Bosch process. In the first etching, the formation of 3- μm -deep recess is completed. Then, the second etching process is self-stooping process, and it continues until reaching oxide layer. Next, a glass wafer is bonded to SOI wafer by using the anodic bonding to protect the device. Afterwards, beams structures are formed by TMAH etch of the structural layer. In the next step, another glass wafer having a recess and aluminum pattern is anodically bonded to the previously formed glass-SOI stack. The metal on the glass provides not only electrodes and bonding pads but also contacts to silicon. The acceleration sensitivity of the fabricated three axis accelerometer is 1.51 fF/g.

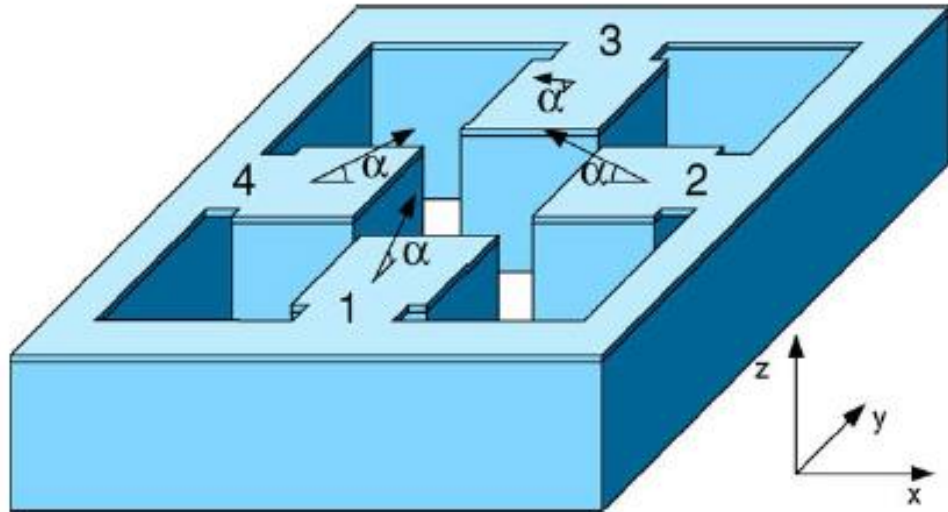


Figure 1.17. The schematic representation of the three axis accelerometer reported in [22].

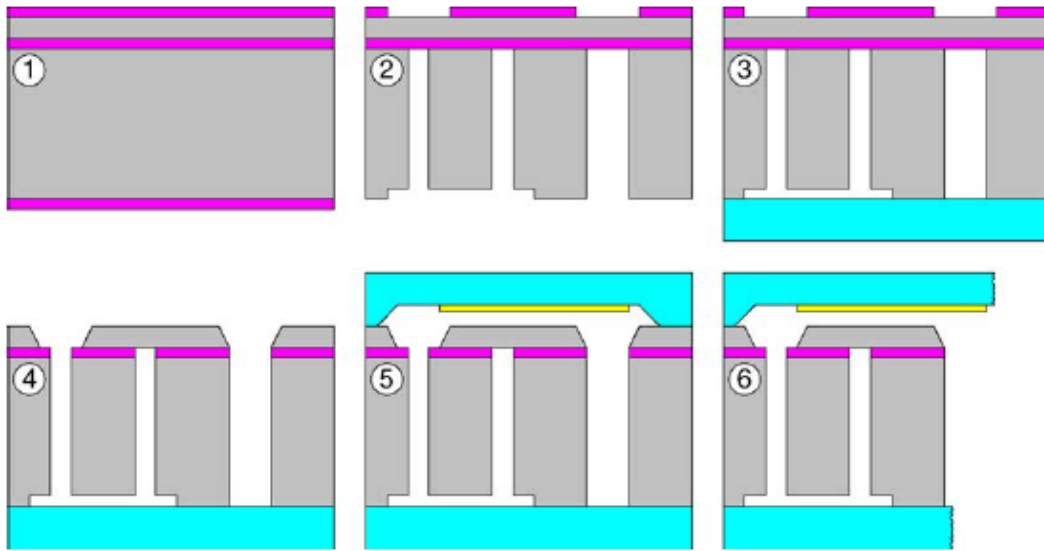


Figure 1.18: The fabrication process steps for the three axis accelerometer reported in [22].

1.3.3. Vertical Accelerometers Reported in the Literature

As the proposed three-axis accelerometer in the scope of this study is implemented not only lateral but also vertical accelerometers, in this part, some of vertical accelerometers presented in the literature will be discussed.

A differential capacitive accelerometer is reported in [23]. The vertical accelerometer is fabricated by using the glass-silicon-glass sandwich structure concept with a SOI wafer. Figure 1.19 shows the schematic representation of the vertical accelerometer. The vertical accelerometer is formed by three main parts. The upper electrode and the lower electrode plate with a thin conductive metal layer are formed on a top and bottom glass substrates, respectively. The third layer of the accelerometer is a single crystal silicon structure with beams and a proof mass placed between the upper and lower electrode plates. The process starts with definition of a capacitive gap on the silicon structure by using TMAH eth. The lift-off process is used to form chrome-gold electrode pad for wire bonding. The bottom and top electrodes are also defined. Next, the device structure is patterned on the SOI wafer, and the anodic bonding method is utilized to bond the glass wafer and SOI wafers. Afterwards, the handle layer of the SOI wafer is removed, and the buried oxide layer can be used as mask

layer in the next step. Another capacitive gap is defined on the back side of the structural layer. Then, the beam and mass block are formed together with a single DRIE step, which is the most critical step. Finally, the top glass wafer is anodically bonded to the previously bonded the glass-silicon stack. After the dicing process, the wire bonding pads are exposed. Figure 1.20 shows the illustration the fabrication process for the reported vertical accelerometer.

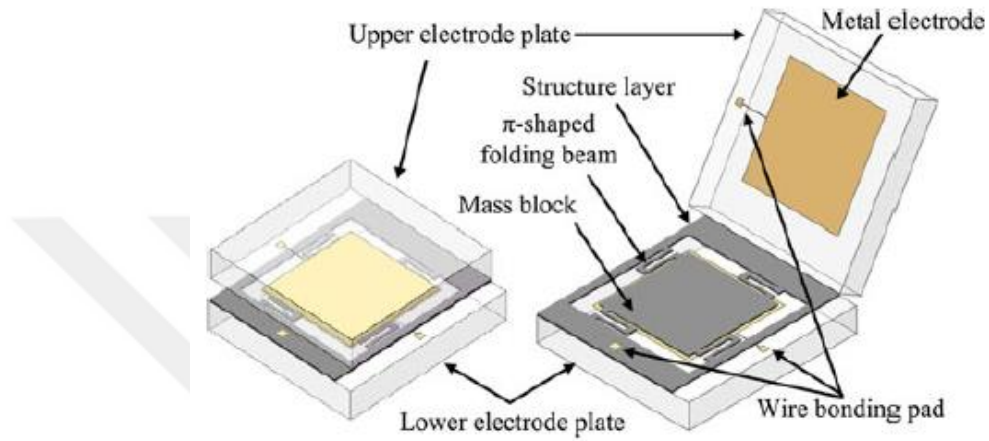


Figure 1.19: The schematic of the vertical accelerometer reported [23].

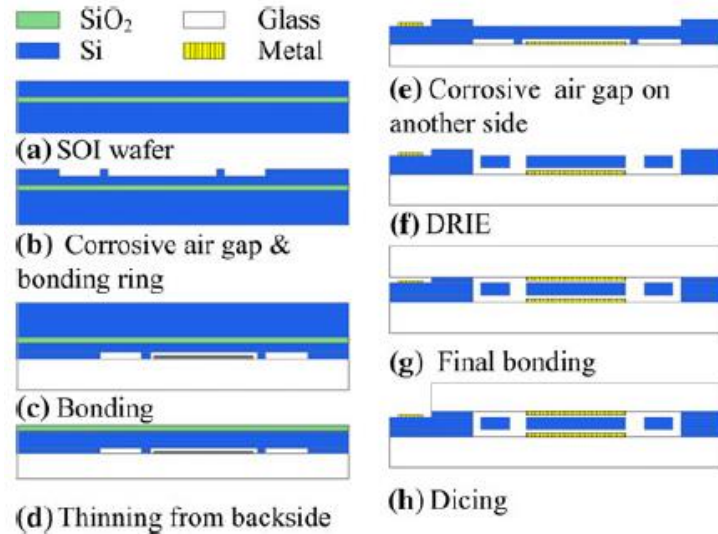


Figure 1.20: The fabrication process steps for the reported vertical accelerometer [23].

The fabricated vertical accelerometer has the size of the $6.1 \times 5.4 \times 1.7 \text{ mm}^3$. The rest capacitance of the vertical accelerometer is 37.13 pF. The non-linearity of the sensor is 0.022 %. The dynamic range of the vertical accelerometer is 103.4 dB.

A capacitive MEMS accelerometer with highly symmetrical sandwich structure (glass-silicon-glass) is presented in [24]. A double-device-layer SOI (D-SOI) wafer having identical the buried oxide and the structural layer on both sides is used to obtain the highly symmetrical beam-mass structure. Figure 1.21 shows the design concept of the sandwich accelerometer. The thermal oxidation of both sides of the wafer is the first step of the fabrication process, and the fabrication process continues patterning of the oxide layer. Then, the shallows grooves ($1.5 \mu\text{m}$) on both sides of the wafer are formed, where the initial capacitive gap is defined. Afterwards, the buried oxide is etched by using HF, and the previous step is again repeated for the formation of the beam structure. However, this time, TMAH solution is prepared in different ways to reduce the undercut rate of the convex corner. By using modified TMAH solution, beams structure is successfully formed. The phosphorous diffusion for Cr/Au electrodes ohmic contact is the next step in the fabrication process flow. Then, Cr/Au metal layers are sputtered and patterned for the formation of electrodes on the proof mass. DRIE is used to release the beam-mass structure followed by TMAH anisotropic etching. The device layers are protected during long time TMAH etch. The formation of the beam structure is completed after HF etching of SiO_2 and the BOX under the beams. Finally, the fabrication process is finalized after anodically bonding of two identical glass wafers to the silicon wafer. Figure 1.22 shows the fabrication process of the vertical accelerometer.

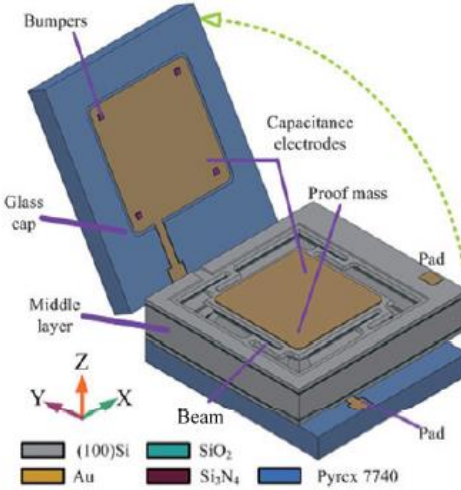


Figure 1.21: The schematic view of the reported device in [24].

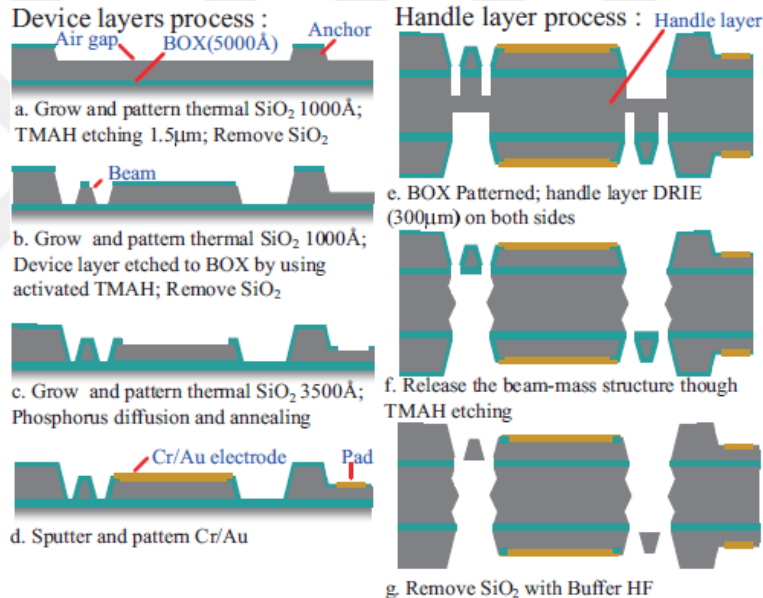


Figure 1.22: The fabrication process flow for the fabricated devices [24].

A novel capacitive-type z-axis accelerometer is demonstrated in [25]. The vertical accelerometer is composed of special designed gap-closing differential sensing electrodes. Figure 1.23 shows illustration of the reported accelerometer. The fabrication process starts with growth of 1 μm -thick thermal oxide on the SOI wafer, and continues with patterning the in-plane shape of the accelerometer on the structural layer. Next, LPCVD Si_xN_y film is deposited, which is followed by

patterning of the second mask. The anisotropic silicon etching is performed by using the KOH solution, which acts as via hole between the structural layer and the handle silicon layer. The surface of the bulk micromachined cavity is protected by growing 1 μm -thick oxide layer. Then, the LPCVD Si_xN_y films are etched by using RIE both the front-side and the backside of the SOI wafer. Next, the surface of the backside of the SOI wafer is deposited with the thermal oxide layer. After patterning of the thermal oxide, the patterning of the proof mass and sensing electrodes on the handle silicon layer are performed by using DRIE etching. Afterwards, the silicon oxide layer is removed by using buffer oxide etch solution. The second DRIE is employed to define the in-plane shape of the accelerometer, forming the proof mass, upper sensing electrode and springs on the structural layer. The etching mask and protective layers are etched by using the HF solution. The final step is to provide the electrical interconnection between the device and the handle silicon layer by using the silver paste in the bulk micromachined cavity (Figure 1.24). The fabricated chip size is 5 mm x 5 mm. The vertical accelerometer sensitivity is 196.3 mV/g (42.5 fF/g). The nonlinearity is 2 % over the range of 0.1-1 g. The cross-axis sensitivity of the accelerometer is approximately 1.94 % for x axis and 1.32 % for y axis over same measurement range.

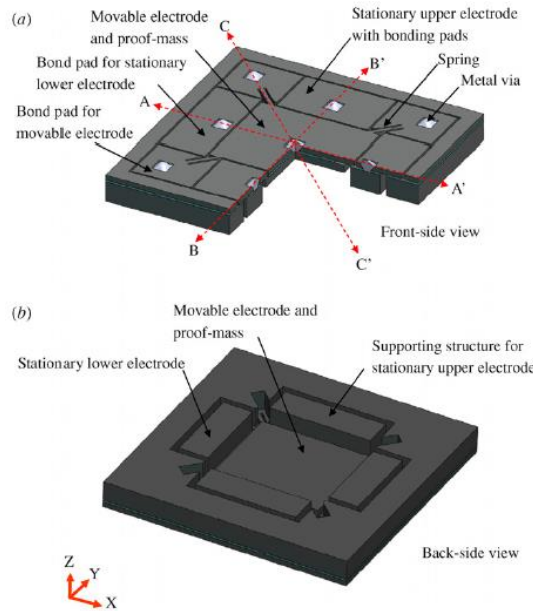


Figure 1.23: The schematic demonstration of the vertical accelerometer reported in [25].

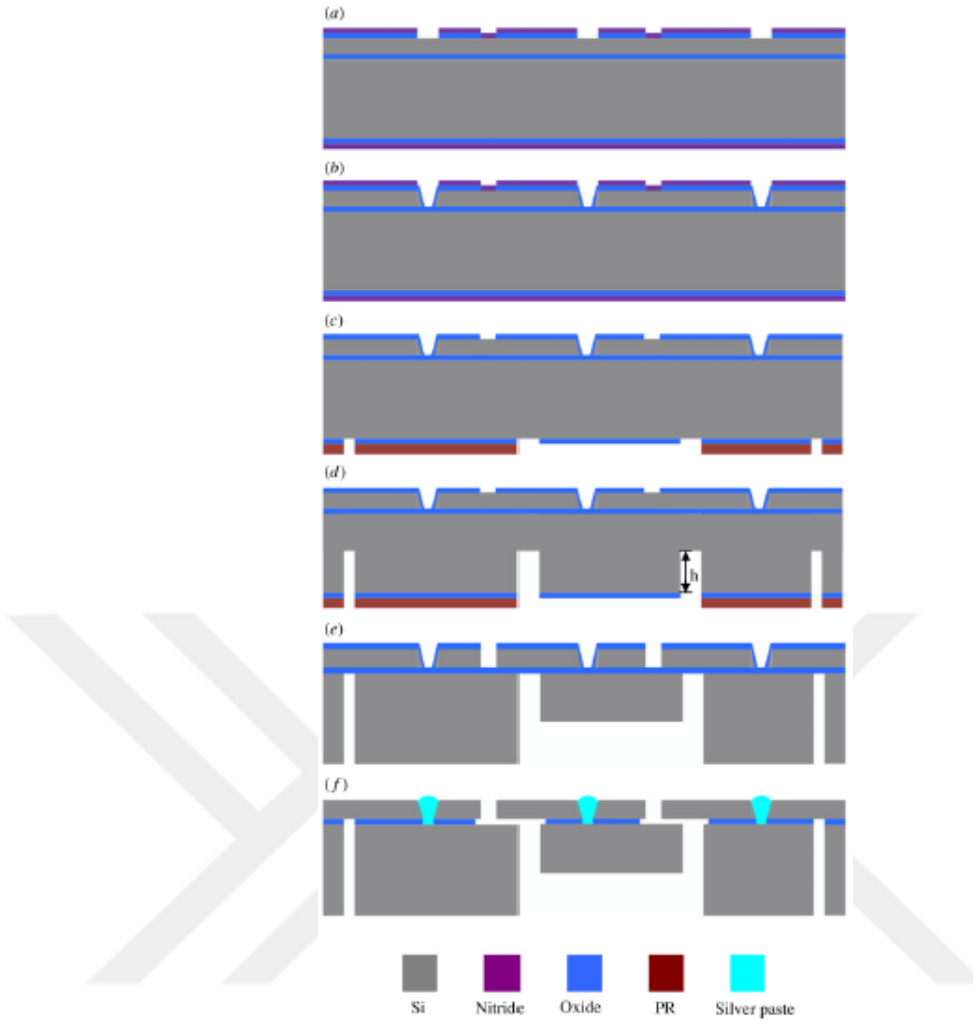


Figure 1.24: The fabrication process sequence for the vertical accelerometer reported in [25].

1.4. Objectives of This Study

Literature on three-axis capacitive MEMS accelerometers is extensively investigated. It is observed that there is lack of tactical grade three-axis MEMS capacitive accelerometer implementations. The reported three-axis accelerometers in the literature are generally fabricated by using the post-CMOS fabrication process, where the structural thickness and performance parameters of sensors are limited. Although high performance lateral accelerometers are already reported in the literature, the three-axis accelerometer formed by using the individual high

performance accelerometers is vulnerable the alignment problem. Therefore, there is need for the three-axis accelerometer fabricated in the same die.

The main objective of this thesis is to develop a fabrication process for the formation of the three-axis accelerometer by implementing the lateral and the vertical accelerometer in the same die. Furthermore, it is also aimed to match performance parameters of the lateral and the vertical accelerometers each other, which is another challenge for the three-axis accelerometer fabrication. In the scope of this thesis, following achievements are gained:

- Two alternative fabrication processes are optimized for the three-axis accelerometer.
- Differential vertical accelerometer is fabricated by using a glass-silicon-glass sandwich structure.
- The glass-silicon-glass sandwich structure fabricated with optimized recipe is also used as a cap for different applications, which are not required vacuum.
- The two-step dicing process is optimized, which can be also used for the similar applications.
- Performance parameters of lateral and the vertical accelerometer are very similar to each other for the fabricated three axis accelerometer.

The fabricated three-axis accelerometer in the scope of this thesis is unique one in the literature. Although there are many vertical accelerometer is reported by using the glass-silicon-glass sandwich structure concept, for the first time, a three axis accelerometer is fabricated by using the glass-silicon-glass sandwich structure concept, where the second glass wafer provides not only a top electrode for the vertical accelerometer but also a cap for the entire structure. Table 1.2 summarizes performance parameters of some of the accelerometer reported in the literature. Figure 1.25 shows the comparison of performance parameters of the reported accelerometer with respect to this work.

Table 1.2: The comparison of the performance parameter of the three axis accelerometer with respect to the reported accelerometer in the literature.

| Year | Ref. | Fabrication Methods | | Single Mass Three Axis Accelerometers | | | Lateral Accelerometers | | | Vertical Accelerometers | | |
|------|------|----------------------|------|---------------------------------------|---|----------------------------|------------------------|--|--------------------|-------------------------|--|--------------------|
| | | Post-CMOS or Surface | Bulk | Range (x/y/z) (g) | Noise (x/y/z) ($\mu\text{g}/\text{Hz}$) | Dynamic Range (dB) (x/y/z) | Range (g) | Noise ($\mu\text{g}/\sqrt{\text{Hz}}$) | Dynamic Range (dB) | Range (g) | Noise ($\mu\text{g}/\sqrt{\text{Hz}}$) | Dynamic Range (dB) |
| 1990 | [26] | - | × | - | - | - | - | - | - | ± 5 | 1000 | 70 |
| 1992 | [27] | - | × | - | - | - | - | - | - | - | - | 80 |
| 1995 | [28] | × | - | - | - | - | ± 150 | - | - | - | - | - |
| 1996 | [29] | × | - | - | - | - | ± 5 | 600 | 78 | - | - | - |
| 1996 | [30] | × | - | - | - | - | ± 3.5 | 500 | 76 | - | - | - |
| 1997 | [31] | × | - | - | - | - | - | 110-160 | 84-81 | - | 990 | 70 |
| 1997 | [32] | - | - | - | - | | 5 | - | 44 | - | - | - |
| 1998 | [33] | - | × | $\pm 8/\pm 10$ | - | - | - | - | - | - | - | - |
| 1998 | [34] | - | - | - | - | - | - | - | - | 35 | - | - |
| 1998 | [35] | × | - | - | - | - | ± 5 | 3000 | 64 | - | - | - |
| 2000 | [36] | × | × | - | - | - | - | - | - | ± 1.2 | 20 | 95 |
| 2000 | [37] | × | - | - | - | - | ± 13 | 1000 | 79 | - | - | - |
| 2000 | [38] | × | - | - | - | - | - | - | - | ± 27 | 6000 | 73 |
| 2002 | [39] | - | - | ± 1 | 40 | 87 | - | - | - | - | - | - |

Table 1.2 (continued)

| | | | | | | | | | | | | | |
|----|-------------|---------------|---|---|------------------------|----------------|-----------|------------|-------------------|-------|---------|--------|-------|
| 05 | 2004 | [40] | - | × | $\pm 15/\pm 15/\pm 10$ | 750/750/100 | - | - | - | - | - | - | - |
| | 2005 | [21] | | × | | | | ± 1 | 1.6 | 112 | ± 1 | 1.08 | 116 |
| | 2009 | [43] | × | - | - | - | - | - | - | - | 1 | 760 | 59 |
| | 2009 | [44] | × | - | - | - | - | ± 3 | 700 | 69 | ± 3 | 900 | 67 |
| | 2008 | [41] | × | - | - | - | - | - | - | - | 1 | 110 | 73.4 |
| | 2008 | [42] | × | | | 12/14/110 | 88.4/73.4 | - | - | - | - | - | - |
| | 2010 | [23] | - | - | - | - | - | - | - | - | - | 89.97 | 103.4 |
| | 2010 | [45] | - | × | - | - | - | - | - | - | ± 1 | - | - |
| | 2010 | [18] | × | - | - | - | - | 0.8~6 | 120000/ 271000 | | 0.8~6 | 357000 | |
| | 2010 | [47] | - | × | - | - | - | ± 1 | 138/159 | 74/72 | ± 1 | 49 | 83 |
| | 2010 | [48] | - | - | - | - | - | ± 11.7 | 1.7 | 136 | | | |
| | 2011 | [49] | - | - | - | - | - | ± 40 | 6 | 131.9 | | | |
| | 2012 | [17] | × | - | 0.01~1 | 2100/2000/2100 | - | - | - | - | - | - | - |
| | 2012 | [50] | × | - | ± 1 | 220 | 70 | - | - | - | - | - | - |
| | 2013 | [16] | × | - | - | - | - | 0.01~2 | 400/200 | - | 0.01~2 | 900 | - |
| | 2013 | [51] | - | × | 0.0616/0.317/ 3.68 | 9.24/8.54/331 | - | - | - | - | - | - | - |
| | 2013 | [52] | - | × | 0. 1~3 | - | - | - | - | - | - | - | - |
| | 2013 | [53] | - | × | - | - | - | - | 13.2 | 122 | - | 17.8 | 131 |
| | 2013 | This Study | - | × | - | - | - | 25.8 | 5 | 125 | 38.5 | 10.5 | 122 |

Table 1.2 (continued)

| Commercial Accelerometers | | | | | | | | | |
|---------------------------|-------------------------|-----------------------------------|----------------------------------|------------------------|-----------------------------------|--------------------------|-------------------------|-----------------------------------|--------------------------|
| | | | | Lateral Accelerometers | | | Vertical Accelerometers | | |
| | Range (x/y/z) (g) | Noise (x/y/z) (μ g/Hz) | Dynamic Range (dB) (x/y/z) | Range (g) | Noise (μ g/ \sqrt{Hz}) | Dynamic Range (dB) | Range (g) | Noise (μ g/ \sqrt{Hz}) | Dynamic Range (dB) |
| ADXL377 [54] | | | | 200 | 2700 | 97 | 200 | 4300 | 93 |
| BMA355 [55] | 16 | 150 | 100 | | | | | | |
| H3LIS331DL [56] | 400 | 15000 | 88 | | | | | | |
| MMA8452Q [57] | 4 | 99 | 92 | | | | | | |

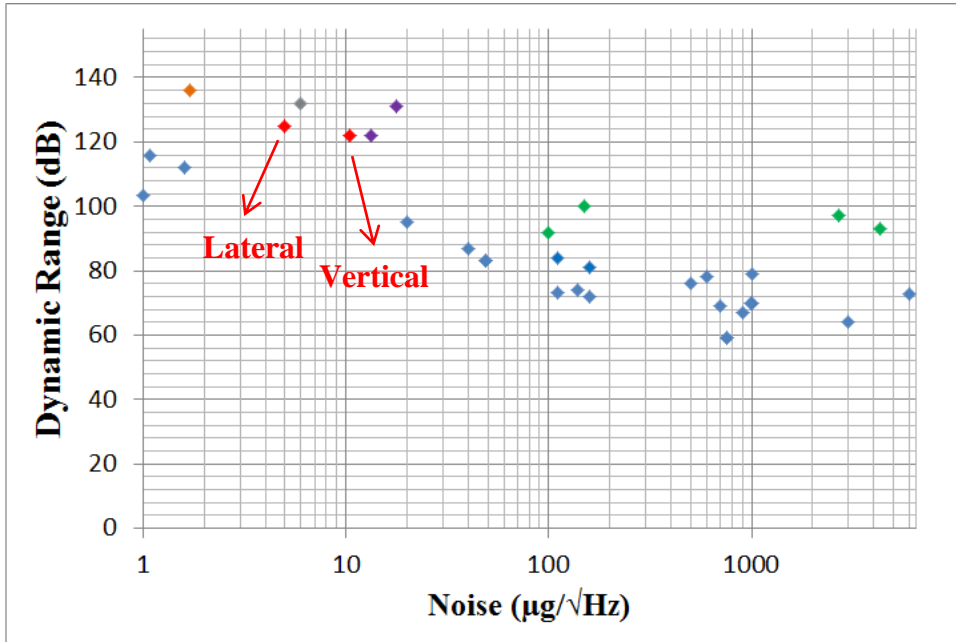


Figure 1.25: The comparison of dynamic range of lateral and vertical accelerometers reported in the literature. Blue points indicate academic works. Commercial accelerometers are shown with green color. Red points indicate this work. The purple one indicates [53]. The grey one represents [49]. The orange one is [48].

1.5. Outline of the Thesis

There are six chapters in the scope of the thesis. Chapter 1 is the introduction part in which the history of the MEMS accelerometer, the classification of accelerometers and comprehensive literature search about the three-axis accelerometer as well as the vertical accelerometer are discussed. Finally, the chapter is concluded by the objectives of this study. Chapter 2 gives the basic theory about the lateral and vertical accelerometer as well as the design parameters. Chapter 3 starts with illustration of the three-axis accelerometer design and continues with detailed explanations of performance and design parameters of lateral and vertical accelerometers. Furthermore, mechanical simulation results are also given in this section. Chapter 4 explains two alternatives processes for the fabrication of the three-axis accelerometer. Chapter 5 starts with the functionality test procedure and presents system level results for three-axis accelerometer. Chapter 6 gives the conclusion about this work and suggestions about the future work on the fabrication process.

CHAPTER 2

THEORETICAL BACKGROUND

This chapter gives the information about the theoretical background of the capacitive accelerometers. The basic operation principles and the equations used during the design of the accelerometer are comprehensively explained in this section.

2.1. Basic Operation Principles of the Accelerometer

The micromechanical capacitive accelerometer is composed of three main mechanical structures: the spring region, the proof mass and capacitive fingers. The movable part of the accelerometer is the proof mass region, and it is attached to the anchor region with the help of the spring structures. There are capacitive fingers on both sides of the accelerometer and the capacitance of both sides equal to each other in the rest position of the proof mass. Figure 2.1 shows the illustration of the capacitive accelerometer. The design of the lateral accelerometer permits the motion of the proof mass in-plane directions. In existence of the acceleration, the proof mass deflects to the opposite side of the acceleration and the capacitance formed between fingers of the proof mass and fixed electrodes on both sides alters. Thus, the acceleration can be measured by differentially reading the capacitance changes of both sides.

Mechanical model of the accelerometer is simply composed of a spring-mass-damper system. The physical model of the accelerometer is shown in Figure 2.2. When the accelerometer is exposed to the acceleration, the movement of the proof mass is opposed to the acceleration direction in terms of the Newton's law of motion. It is

important to analyze the physical model as it gives general understanding of the accelerometer. The dynamic behavior of the system can be expressed with following equation:

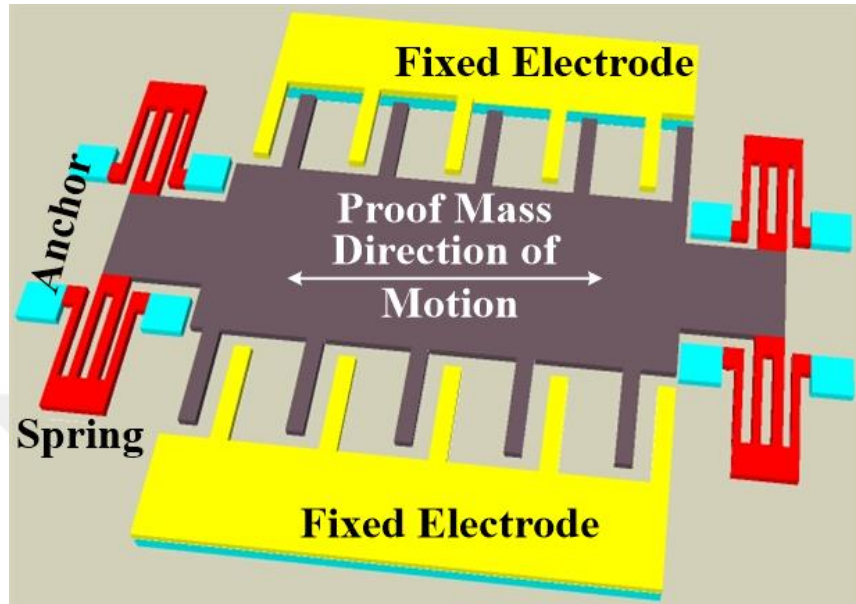


Figure 2.1: The illustration of the MEMS capacitive accelerometers

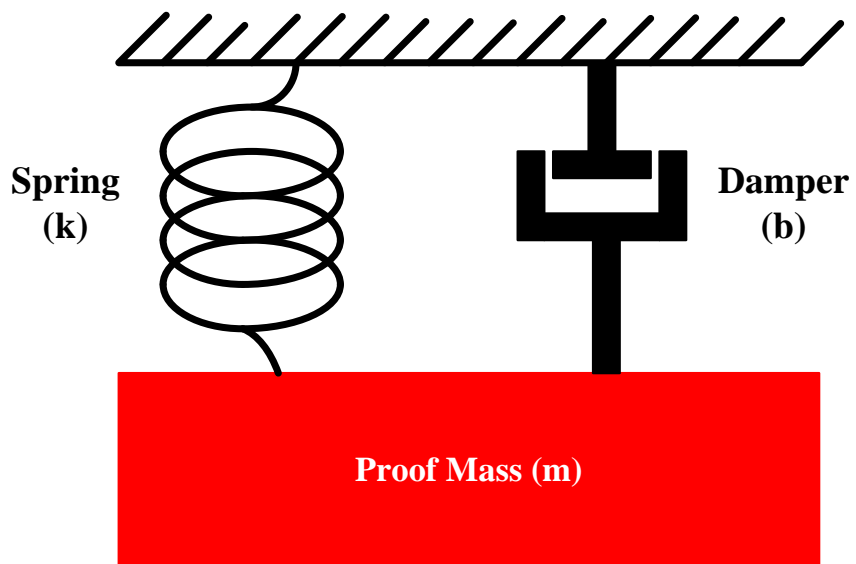


Figure 2.2: Accelerometer mechanical model: spring-proof mass-damper

$$F = -ma = m\ddot{x} + b\dot{x} + kx \quad (2.1)$$

where a is defined as the external acceleration and x is the movement of proof mass. Laplace transform of equation is defined with the following equation:

$$ma(s) = ms^2X(s) + bsX(s) + kX(s) \quad (2.2)$$

$$\frac{X(s)}{a(s)} = \frac{1}{s^2 + \frac{b}{m}s + \frac{k}{m}} \quad (2.3)$$

and the resonance frequency (w_0) and the quality factor (Q) can be expressed with following equations:

$$w_0 = \sqrt{\frac{k}{m}} \quad \text{and} \quad Q = \frac{w_0 m}{b} \quad (2.4)$$

2.2. Spring Constant Estimation

The spring constant is one of the important factors affecting the characteristic of the sensor. It is possible to increase or decrease to the movement of the proof mass by spring constant. During the operation of the capacitive sensors, the proof mass of the sensor is easily able to move in the sensitive axes. However, the spring constant of the other axes must be as high as possible to prevent cross-axis sensitivities. Therefore, spring constant selection is one of the major steps among designs parameters. The spring constant can be calculated in terms of bending of the beam. If the parallelism is not preserved between the fixed end and the free end during the bending of the beam, it is described as “Deflection of a Cantilever Beam (unguided).” When the parallelism between the fixed end and the free end is preserved, this situation is called “Deflection of a Fixed-Guided End Beam” [58]. Figure 2.3 shows the bending of beam structures. The main condition of spring constant for MEMS accelerometer is the deflection of an unguided cantilever beam conditions. The spring constants for this condition are given with the following equation:

$$k_x = \frac{Ehw^3}{l^3} \quad k_y = \frac{Ehw^3}{4l^3} \quad k_z = \frac{Ewh^3}{4l^3} \quad (2.5)$$

where k_x , k_y , k_z is the spring constants of the applied force direction. E is the Young's Modulus, h is the thickness, w is the width and l is the length of the beam. The spring constant of complex systems can be calculated by parallel and series configuration of springs. The connection of series and parallel spring is shown in Figure 2.4. The equivalent spring constant for the parallel and series connected springs are calculated by using equation (2.6) and (2.7), respectively.

$$k_{eq} = k_1 + k_2 \quad (2.6)$$

$$k_{eq} = \frac{k_1 k_2}{k_1 + k_2} \quad (2.7)$$

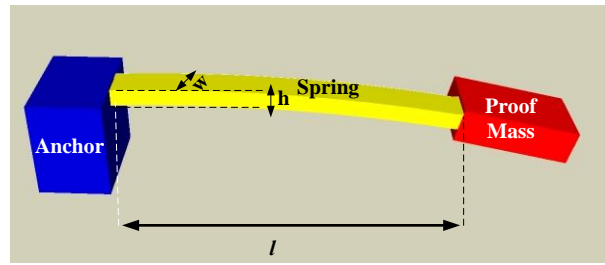
The model including two half-length unguided beams connected serial each other can be used to calculate the spring constant of the fixed-guided end beam. Figure 2.5 shows a guided beam divided in two unguided beam parts. Two segments are assumed to be two separate unguided springs connected in series configuration, and the spring constant is calculated as given in equation:

$$k_1 = k_2 = k = \frac{Ehw^3}{4l^3}; l = \frac{l}{2} \quad (2.8)$$

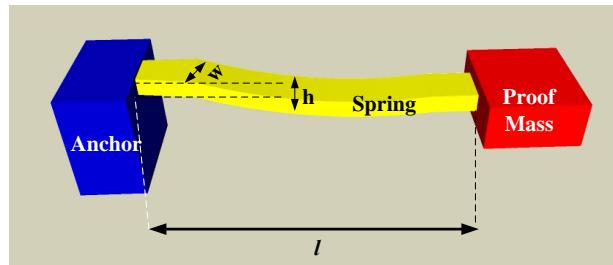
$$k_{eq} = \frac{k_1 k_2}{k_1 + k_2} = \frac{k}{2} \quad (2.9)$$

$$k_{eq} = \frac{Ehw^3}{l^3} \quad (2.10)$$

where k_1 and k_2 are the spring constants of each unguided segments of the guided spring, E is the Young's Modulus, h is the thickness, w is the width and l is the length of the spring.

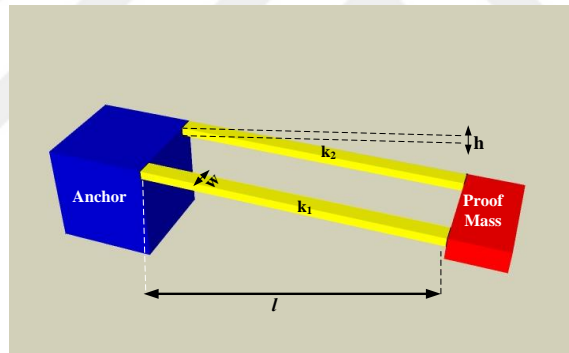


(a)

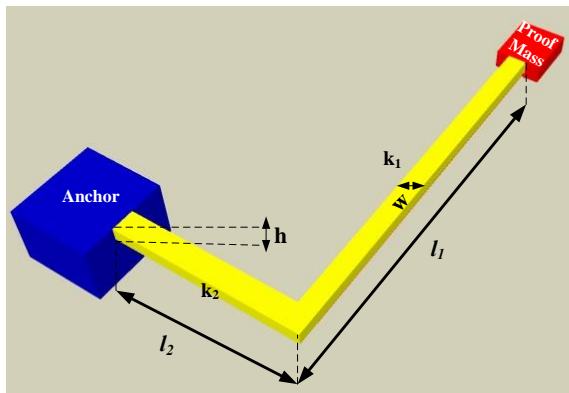


(b)

Figure 2.3: (a) Unguided beam (b) Guided beam in their deflected forms



(a)



(b)

Figure 2.4: The series and parallel connected springs system (a) springs in parallel configuration (b) springs in series configuration.

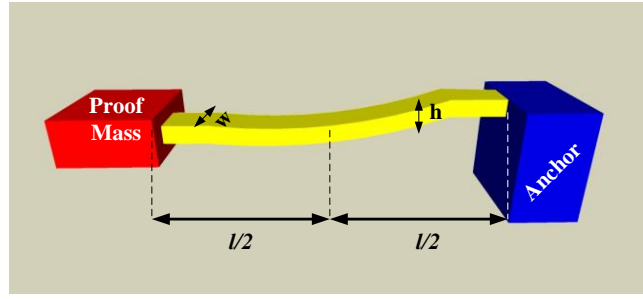


Figure 2.5: Series connected half clamped beams forming a fixed-guided end beam.

The motion of the proof mass can also be provided in the z-direction by using suitable structure. One of the common types of structures is crab legs structure, which is used to provide the vertical motion to the proof mass. Figure 2.6 shows the crab legs structure. The spring constant equation of crab legs structure is given in [60].

$$k = \frac{4Ew \left(\frac{h}{l_c}\right)^3}{1 + \frac{l_s}{l_c} \left[\left(\frac{l_s}{l_c}\right)^2 + 12 \frac{1+v}{1+\left(\frac{w}{h}\right)^2} \right]} \quad (2.11)$$

where E is the young modulus, h structural thickness, v is the passion ratio.

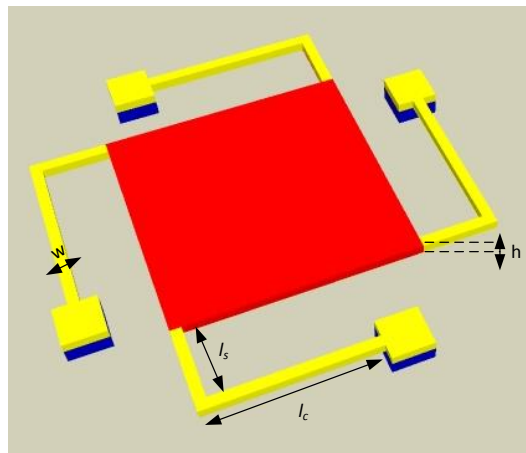


Figure 2.6: The illustration of the crab legs structure used in the vertical accelerometer design.

2.3. Damping Coefficient Estimation

Although the effect of the surface forces is generally ignored for macro systems, the movement of the miromachined devices is highly effected by the damping force of the surrounding air. Therefore, the effect of the surface forces plays an important role as the structure decreases in size. The squeeze film air damping becomes more important if only the thickness of the gas film is smaller than the one third of width of the plate. Therefore, the squeeze film air damping is major damping mechanism for the dynamic behavior of many MEMS devices using technologies such as the capacitive sensing and the electrical driving [61].

The proof mass of the general lateral accelerometer moves parallel to the substrate surfaces. In squeeze film air damping, the motion of the proof mass causes to squeeze air molecules between the mass and substrate, and squeezed air molecules try to escape from decreasing volume under the mass. Therefore, the squeeze film air damping between capacitive fingers becomes major damping mechanism under the atmospheric pressure for lateral accelerometer. Figure 2.7 represents squeeze film air damping [62]. Moreover, the slide film damping has minor effect on the damping coefficient of the lateral accelerometer. In the slide film damping effect, there is a friction between upper and lower surfaces of the mass and air molecules during lateral motion of the proof mass. The illustration of the slide film air damping is shown in Figure 2.7.

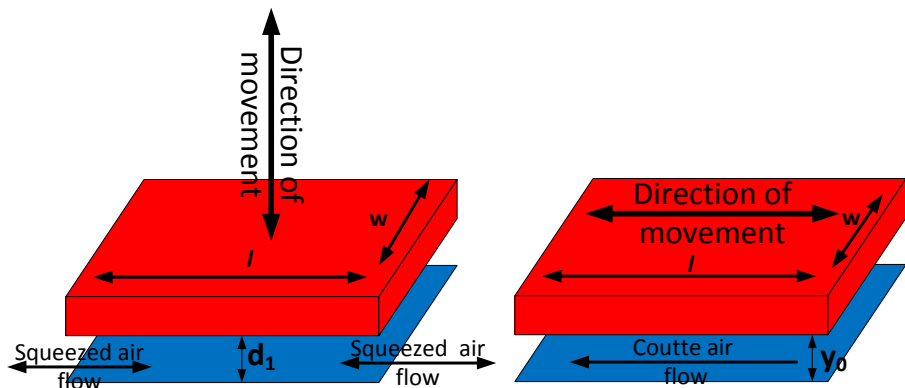


Figure 2.7: Illustration of the (a) squeeze-film and (b) slide-film damping mechanisms [62].

The damping coefficient of a lateral accelerometer can be obtained by the solution to the Reynolds equation for incompressible gas usually given in complicated series. There are many forms of solution in literatures. The common conclusion is that the damping coefficient can be written as [61]

$$b = \frac{\mu l w^3}{d_1^3} \beta(\eta) \quad (2.12)$$

where μ is the coefficient of viscosity of the fluid d_1 is the capacitive gap, $\eta = w/l$ and $\beta(\eta)$ is a correction factor. For a strip plate $\beta(0) = 1$, and for a square plate (i.e., $w=l$), $\beta(1) = 0.42$. The damping coefficient of the vertical accelerometer without perforation holes can also be expressed with the following equation:

$$b = 2 \left(\frac{0.42 \mu l w^3}{d_1^3} \right) \quad (2.13)$$

If the proof mass of the vertical accelerometer uniformly perforated with holes (Figure 2.8), the derivation of squeeze film air damping is presented in [63]. The damping coefficient is given with the following equation:

$$b = 2 \left(8 \mu \sqrt{l^4 h^2} \frac{1}{\beta^4 \sqrt{1 - \beta^2}} \left[\frac{1}{r_c^2} + \frac{r_c^2}{\lambda^4} \right] \right) \quad (2.14)$$

where l length of proof mass area, h is the structural thickness and β is ratio between r_0/r_c . λ and $K(\beta)$ can be expressed with following equation:

$$\lambda = \frac{2}{\beta} \sqrt[4]{\frac{h d_1^3}{3 K(\beta)}} \quad (2.15)$$

$$K(\beta) = 4\beta^2 - \beta^4 - 4 \ln \beta - 3 \quad (2.16)$$

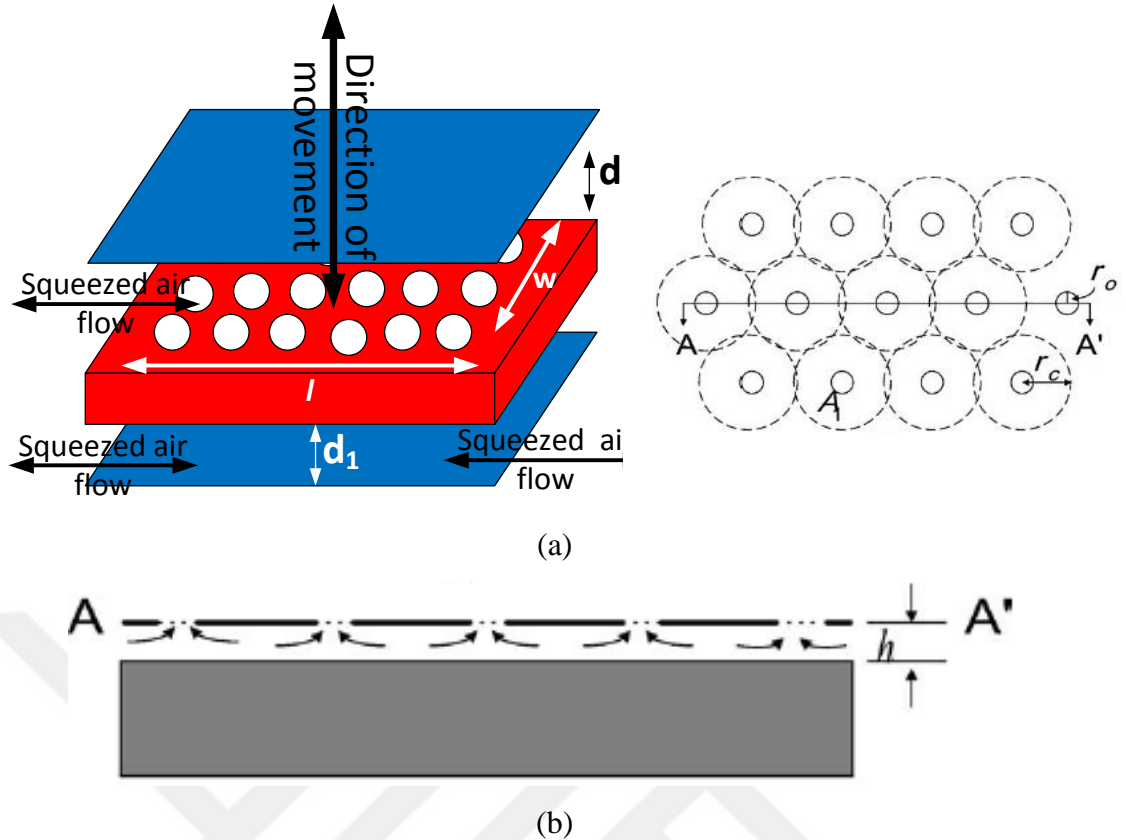


Figure 2.8: The illustration of the vertical accelerometer schematic structure of a thin hole-plate: (a) top view; (b) cross-sectional view [63].

2.4. Sensitivity

In existence of the acceleration, the proof mass moves to opposite direction of the acceleration and the capacitance changes among capacitive fingers. While the capacitance value of one side of the accelerometer increases, the capacitance value of the other side of the accelerometer decreases. Sensitivity of the accelerometer can be described as the capacitance change of the accelerometer with respect to deflection of the proof mass. The sensitivity of accelerometer has close relation with the type of the readout circuit. If open-loop circuitry is used in order to calculate sensitivity of the accelerometer, we can use following equation for the sensitivity:

$$\frac{\partial C}{\partial x} = \frac{N \cdot \varepsilon_0 \cdot A}{(d_1 - x)^2} - \frac{N \cdot \varepsilon_0 \cdot A}{(d_2 + x)^2} \quad (2.17)$$

where N is the number of capacitive fingers, ϵ_0 is the permittivity of the air and is equal to 8.85×10^{-12} F/m, A is the capacitive area of each finger, d_1 is the small spacing between capacitive fingers, d_2 is the large spacing between capacitive fingers and x is the amount of proof mass deflection.

When closed-loop readout is used, the sensitivity of the accelerometer can be obtained with the following equation:

$$\frac{\partial C}{\partial x} = \frac{N \cdot \epsilon_0 \cdot A}{d_1^2} - \frac{N \cdot \epsilon_0 \cdot A}{d_2^2} \quad (2.18)$$

However, the sensitivity of the vertical accelerometer can be calculated in closed loop readout with the following Equation:

$$\frac{\partial C}{\partial x} = \frac{\epsilon_0 A}{d_1^2} \quad (2.19)$$

2.5. Operation Range of the Accelerometer

The operation range of the accelerometer can be defined as the magnitude of the maximum and the minimum acceleration successfully detected by accelerometer on the sensitive axis. The type of readout circuitry is important factor to calculate the operation range of the accelerometer. While the finger spacing plays important role for determining operation range in open-loop readout circuit, the feedback force applied by circuit is taken into account in closed-loop readout circuit to calculate the operation range of the accelerometer.

In open-loop readout circuit, the amount of motion of the proof mass is limited to the finger spacing of the accelerometer. Therefore, the maximum deflection of the proof mass can equal to the finger spacing. The operation range of the accelerometer in open-loop readout circuit can be expressed with the following equation:

$$F = ma_{range} = kd_1 \quad (2.20)$$

$$a_{range} = \frac{kd_1}{m} = d_1 w^2 \quad (2.21)$$

where k is the spring constant of the accelerometer, d_1 is the small spacing between capacitive fingers and m is the total mass of the accelerometer. In closed loop mode, the measurement range of the accelerometer is the amount of acceleration that can be suppressed by the feedback force. The feedback force is based on circuit properties and the size of the accelerometer. The electrostatic drive force is:

$$F = \frac{1}{2} \frac{\partial C}{\partial x} V^2 \quad (2.22)$$

The operation range of the accelerometer can be expressed with the following equation:

$$F = ma_{range} \rightarrow a_{range} = \frac{\frac{1}{2} \frac{\partial C}{\partial x} V^2}{m} c \quad (2.23)$$

where $\partial C / \partial x$ is the sensitivity of the accelerometer, V is the voltage applied by the readout circuit as the feedback pulse, c is the pulse width percentage of the applied feedback voltage and m is the mass of the accelerometer.

It is possible to further investigate range of the lateral and vertical accelerometer in terms of the structural parameters. The range of the lateral accelerometer can be summarized in terms of the following equations:

$$a_{range} = \frac{1}{2} \frac{\partial C}{\partial x} \frac{V^2}{m} = \frac{\frac{1}{2} \varepsilon_0 x h x \text{Finger}_{length} x \left(\frac{1}{d_1^2} - \frac{1}{d_2^2} \right) x V^2}{width x length x h} \quad (2.24)$$

$$= \frac{\frac{1}{2} \varepsilon_0 x \text{Finger}_{length} x \left(\frac{1}{d_1^2} - \frac{1}{d^2} \right) x V^2}{width x length}$$

The range of the lateral accelerometer is proportional to the finger length and inversely proportional to the finger gap of the accelerometer. However, it is independent of the structural thickness of the wafer used during the fabrication.

The range of the vertical accelerometer can be also summarized in terms of the following equations:

$$a_{range} = \frac{1}{2} \frac{\partial C}{\partial x} \frac{V^2}{m} = \frac{\frac{1}{2} \varepsilon_0 x \text{ width} \times \text{length} \times \left(\frac{1}{d_1^2}\right) x V^2}{\text{width} \times \text{length} \times h} \quad (2.25)$$

$$= \frac{\frac{1}{2} \varepsilon_0 x \left(\frac{1}{d_1^2}\right) x V^2}{h}$$

The range of the vertical accelerometer is proportional to V^2 and inversely proportional to the structural thickness and the capacitive gap of the accelerometer. Therefore, there is a trade-off between range of the vertical and lateral accelerometer.

2.6. Brownian Noise

Molecular collisions from a surrounding gas or liquid environment lead to the agitation of an observable object and the agitation is directly related to the fluid's viscosity. The temperature dependent random motion of the microstructure due to the molecular agitation of the gas molecules can be defined as Brownian noise [64].

$$Brownian\ Noise = \sqrt{\frac{4k_B T b}{m^2}} \quad (2.26)$$

where k_B is Boltzmann constant, T is the operation temperature, b is the total damping of the system and m is the mass of the proof mass. There are two important parameters to fabricate low-mechanical noise accelerometer. Large mass of the proof mass and low damping should be taken into consideration to fabricate low-mechanical noise accelerometer.

2.7. Summary of the Chapter

This chapter explains the operation principles of the lateral and the vertical accelerometer and gives equations used during the design of the accelerometer.

CHAPTER 3

DESIGN CONCEPT OF THE THREE AXIS ACCELEROMETER

In the scope of this study, the designed three axis accelerometer is formed by implementing lateral and vertical accelerometers in a same die. Therefore, lateral and vertical accelerometers are separately designed, and the three axis accelerometer is formed by implementing the lateral and the vertical accelerometer in the same die. Design and performance parameters of lateral and the vertical accelerometers are given in this chapter. Furthermore, design parameters of the lateral and the vertical accelerometer are confirmed by using the finite element model (FEM) simulation tool.

3.1. Design of Three Axis Accelerometer

In the scope of this study, the capacitive three-axis accelerometer is designed and fabricated. The proposed design concept of the three-axis accelerometer is to fabricate the differential lateral and the differential vertical accelerometer in a same substrate. Figure 3.1 shows the conceptual design of the three-axis accelerometer. The glass-silicon-glass sandwich structure is considered to fabricate three-axis accelerometer. The differential lateral accelerometer can easily fabricate by using a glass wafer and a silicon wafer. However, the fabrication of the differential vertical accelerometer is a challenging one, and it needs three wafers. By using a glass wafer and a silicon wafer, the capacitance is only formed between the proof mass and the electrode of the bottom glass wafer for the vertical accelerometer. To fabricate the differential vertical accelerometer, there is a need for the formation of the top electrode. The formation of the top electrode can be provided by using a second glass

wafer, which also provided a cap for the entire structures. The three axis accelerometer mask set-1 is designed for only the two-step anodic bonding fabrication method. As the glass-silicon-glass structure is formed by using two-step anodic bonding, the spring constant of both lateral and vertical accelerometers are quite high for this mask set. Furthermore, the proof mass of the vertical accelerometer is fabricated with and without perforation. In the second mask set, there are three different lateral accelerometer designs used in the current study. Two of them are designed by METU-MEMS VLSI group members. One of them is designed in [58]. The other lateral accelerometer is designed by our IMU group member. The last lateral accelerometer and all vertical accelerometer are designed to match same performance parameters. Device parameters of lateral and the vertical accelerometers will be comprehensively given in the following sections. Table 3.1, Table 3.2, Table 3.3 and Table 3.4 show constants and design parameters used during the designing of lateral and vertical accelerometers. Table 3.5 and Table 3.6 show equations used during the calculation of important parameters of the lateral and vertical accelerometer, respectively.

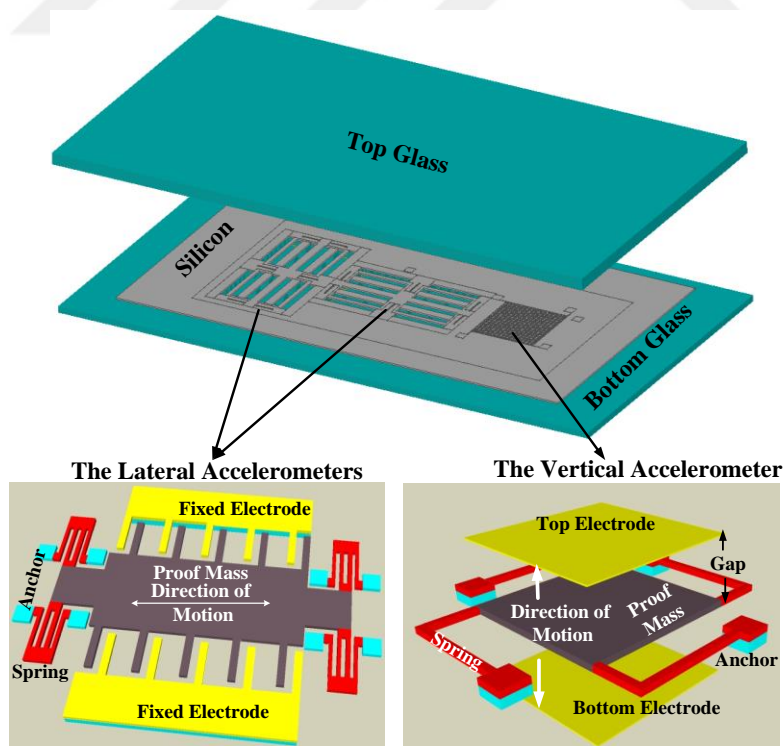


Figure 3.1: The illustration of the proposed the three axis accelerometer.

Table 3.1: Constants used during the calculation of the design parameter of the three axis accelerometer.

| Constants | Abbreviations | Values |
|---------------------------------------|---------------|-------------------------------------|
| Young modulus <100> [59] | E | 130 GPa |
| Young modulus <111> [59] | E | 168.9 GPa |
| Dielectric constant | ϵ_0 | $8.85 \times 10^{-12} \text{ F/m}$ |
| Boltzmann constant | k_B | $1.38 \times 10^{-23} \text{ J/K}$ |
| Viscosity of air | μ | $1.85 \times 10^{-5} \text{ kg/ms}$ |
| Density | ρ | 2330 kg/m^3 |
| Structural thickness | h | $35 \mu\text{m}$ |
| Poisson ratio | ν | 0.22 |

Table 3.2: Abbreviations of electrical design parameters of the three axis accelerometer.

| Electrical Parameters | Abbreviations |
|--|---------------------------------|
| Capacitive finger length | l_{finger} |
| Capacitive finger width | w_{finger} |
| Capacitive length | C_{length} |
| Spacing between the substrate and suspended structure | d_0 |
| Capacitive gap | d_1 |
| Capacitive anti-gap | d_2 |
| Rest capacitance | C |
| Rest capacitance (for capacitive gap) | C_{gap} |
| Rest capacitance (for capacitive anti gap) | $C_{anti-gap}$ |
| Sensitivity | $\frac{\partial C}{\partial x}$ |

Table 3.3: Abbreviations of mechanical design parameters of the three axis accelerometer.

| Mechanical Parameters | Abbreviations |
|--------------------------------------|---------------|
| Spring length | l_{spring} |
| Spring width | w_{spring} |
| Number of spring | N_{spring} |
| Spring constant | k |
| Crab-legs spring length ratio | l_s/l_c |

Table 3.4: Abbreviations of physical design parameters of the three axis accelerometer.

| Physical Parameters | Abbreviations |
|---|-------------------|
| Area | A |
| Mass of proof mass | M |
| Number of fingers per side | $N_{fingers}$ |
| Number of perforation holes | N_{holes} |
| Radius of the perforation holes | r_{holes} |
| Resonance frequency | f |
| Range | a_{range} |
| Pulse width ratio of the readout circuit | c |
| Clock frequency of the readout | f_{clock} |
| mu_effective | $\mu_{effective}$ |
| Damping coefficient | b |
| Temperature | T |
| Beta | β |
| K(Beta) | $K(\beta)$ |
| Lambda | λ |
| Brownian Noise | a_{mech} |
| Quality Factor | Q |
| Voltage | V |

Table 3.5: Design parameters of the lateral accelerometer.

| Identity | Lateral accelerometer equations |
|---------------------------------|---|
| A | $A_{ProofMass} + N_{Fingers} \times (l_{Fingers} \times w_{Fingers})$ |
| M | $A \times h \times \rho$ |
| C | $C = \frac{N \cdot \varepsilon_0 \cdot A}{d_1} + \frac{N \cdot \varepsilon_0 \cdot A}{d_2}$ |
| C_{gap} | $C_{gap} = \frac{N \cdot \varepsilon_0 \cdot A}{d_1}$ |
| $C_{anti-gap}$ | $C_{anti-gap} = \frac{N \cdot \varepsilon_0 \cdot A}{d_2}$ |
| $\frac{\partial C}{\partial x}$ | $\frac{\partial C}{\partial x} = \frac{N \cdot \varepsilon_0 \cdot A}{d_1^2} - \frac{N \cdot \varepsilon_0 \cdot A}{d_2^2}$ |
| k | $k_{lateral} = \frac{Ehw^3}{l^3}$ |
| f | $f = \frac{1}{2\pi} \sqrt{\frac{k}{m}}$ |
| a_{range} | $a_{range} = \frac{\frac{1}{2} \frac{\partial C}{\partial x} V^2}{m \times 9.81} c$ |
| c | $1 - (f_{clock} \times 8 \times 10^{-7})$ |
| b [61] | $b = 2N \left(\frac{\mu l w^3}{d_1^3} \beta(\eta) \right) + 2(N-1) \left(\frac{\mu l w^3}{d_2^3} \beta(\eta) \right)$ |
| a_{mech} [64] | $a_{mech} = \sqrt{\frac{4k_B Tb}{M^2}}$ |

Table 3.6: Design parameters of the vertical accelerometer.

| Identity | Vertical accelerometer equations |
|------------------------------------|---|
| A | $A_{ProofMass} - N_{holes} \times (\pi \times r_{holes}^2)$ |
| M | $A \times h \times \rho$ |
| C | $C = \frac{N \cdot \varepsilon_0 \cdot A}{d_1}$ |
| C_{gap} | $C_{gap} = \frac{N \cdot \varepsilon_0 \cdot A}{d_1}$ |
| $C_{anti-gap}$ | - |
| $\frac{\partial C}{\partial x}$ | $\frac{\partial C}{\partial x} = \frac{\varepsilon_0 A}{d_1^2}$ |
| k [60] | $k_{vertical} = \frac{4Ew \left(\frac{h}{l_c}\right)^3}{1 + \frac{l_s}{l_c} \left[\left(\frac{l_s}{l_c}\right)^2 + 12 \frac{1 + \nu}{1 + \left(\frac{w}{h}\right)^2} \right]}$ |
| f | $f = \frac{1}{2\pi} \sqrt{\frac{k}{m}}$ |
| a_{range} | $a_{range} = \frac{\frac{1}{2} \frac{\partial C}{\partial x} V^2}{m \times 9.81} c$ |
| c | $1 - (f_{clock} \times 8 \times 10^{-7})$ |
| b without perforation holes [61] | $b = 2 \left(\frac{0.42 \mu l^4}{d_1^3} \right)$ |
| b with perforation holes [63] | $b = 2 \left(8 \mu \sqrt{l_{finger}^4 h^2} \frac{1}{\beta^4 \sqrt{1 - \beta^2}} \left[\frac{1}{r_c^2} + \frac{r_c^2}{\lambda^4} \right] \right)$ |
| λ [63] | $\lambda = \frac{2}{\beta} \sqrt[4]{\frac{h g_1^3}{3K(\beta)}}$ |
| $K(\beta)$ [63] | $K(\beta) = 4\beta^2 - \beta^4 - 4 \ln \beta - 3$ |
| a_{mech} [64] | $a_{mech} = \sqrt{\frac{4k_B T b}{M^2}}$ |

3.2. Three Axis Accelerometer Designs

Design and performance parameters of the three axis accelerometer will be comprehensively given in the following section. Two different mask sets are used to fabricate the three axis accelerometer. The spring constant of the three axis accelerometer is intentionally designed high for the first mask set. In the second mask, the lateral and vertical accelerometer design parameters are tried to set each other. Furthermore, there are three lateral accelerometer designs in the second mask set of the three axis accelerometer. Two of them are previously designed by METU MEMS inertial sensors group members. Furthermore, the last lateral accelerometer and all vertical accelerometer are designed to match same performance parameters. The spring length and the proof mass of vertical accelerometer designs are different from each other. However, design and performance parameters are close to that of lateral accelerometers.

3.2.1. Three-Axis Accelerometer Design Mask Set-1

The first fabrication mask set is drawn to see feasibility of the two-step anodic bonding fabrication method. As the main concern is to show the feasibility of the fabrication process, the performance of the three axis accelerometer is not a concern in the first fabrication mask set. During the two-step anodic bonding, as the suspended structure is exposed to potential difference, the stiffness of accelerometers in z-axis is designed high as much as possible for both lateral and vertical accelerometers. The detailed information about different designs is comprehensively given in the following section. The fabrication result of this mask set is used for the designing of the second fabrication mask set.

3.2.1.1. Lateral Accelerometer Design-1

Six double folded spring structures are used for the designing of the lateral accelerometer design-1. Double-folded springs are placed to ends and middle of accelerometer to prevent undesired movement of accelerometer as much as possible. Moreover, the lateral accelerometer has perforation holes to decrease the mass of the

proof mass. The length of springs of the accelerometer is intentionally drawn as small as possible to increase stiffness in z-axis. Figure 3.2 shows the layout of the lateral accelerometer design. Table 3.7 show design and performance parameters of accelerometers.

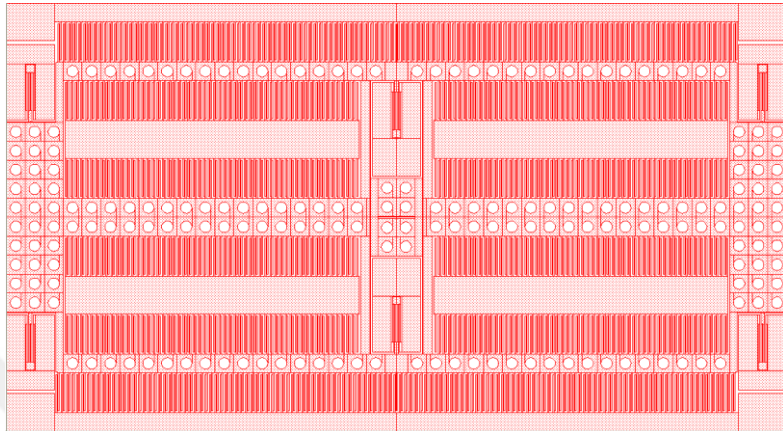


Figure 3.2: The layout of the lateral accelerometer design-1.

Table 3.7: Design and performance parameters of the lateral accelerometer design-1.

| Design Parameters | | | |
|------------------------------|-----------------------|----------------------------------|-----------------------|
| Cell Width (μm) | 4100 | Spring Length (μm) | 200 |
| Cell Length (μm) | 2200 | Spring Width (μm) | 7 |
| Number of Fingers | 360 | Number of Springs | 6 |
| Finger Length (μm) | 200 | Cap. Gap (μm) | 3 |
| Finger Width (μm) | 7 | Cap. Anti-gap (μm) | 10 |
| Proof Mass (kg) | 224×10^{-9} | Structural Thickness (μm) | 35 |
| Performance Parameters | | | |
| Spring Constant (N/m) | 1170 | Rest Cap. (pF) | 9.56 |
| Damping (kg/s) | 3.84×10^{-3} | Sensitivity (F/m) | 2.23×10^{-6} |
| Res. Freq. (Hz) | 11502 | Range @ 5V (g) | 6.34 g |
| Quality Factor | 4.21 | Brownian Noise (μg/√Hz) | 3.62 |

The lateral accelerometer design-1 is verified by using Coventorware. The mechanical model of the lateral accelerometer designed-1 is formed except capacitive fingers. The mass of capacitive fingers are uniformly distributed to the mass of the proof mass of the lateral accelerometer during the simulation for the simplicity Springs and the proof mass of the accelerometer are separately modeled than connected with linkage boundary conditions. Figure 3.3 shows the Coventorware simulation model of the lateral accelerometer design-1. Then, the model is divided into its finite element by using mesher setting shown Figure 3.4. Table 3.8 shows the comparison of the hand calculation with simulation results. Table 3.9 shows simulation mode analysis results for the lateral accelerometer design-1. Figure 3.5 shows finite element mod analysis results of the lateral accelerometer design.

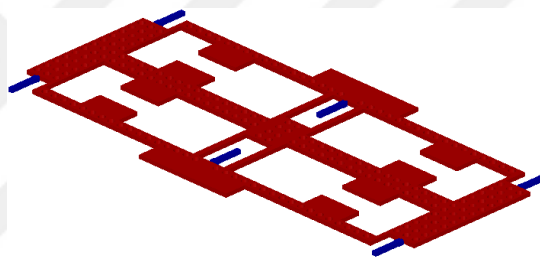


Figure 3.3: The FEM simulation model of the lateral accelerometer design-1.

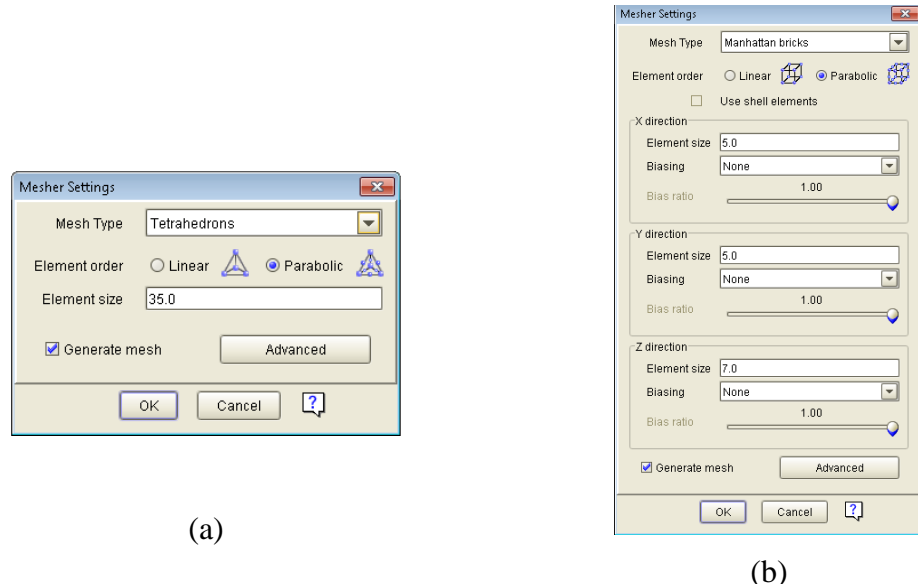
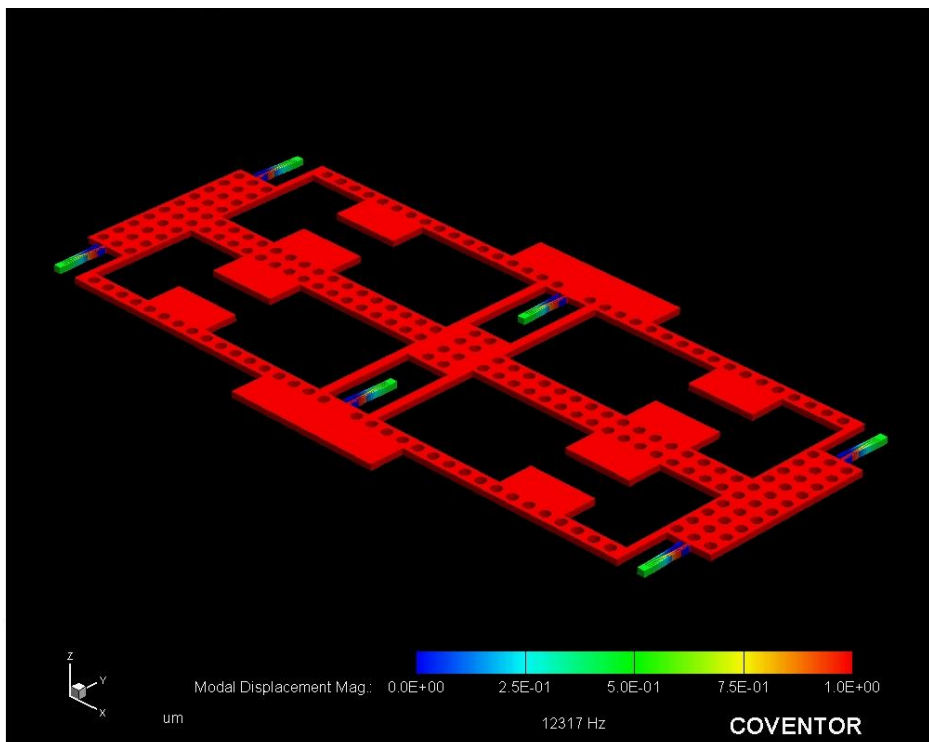
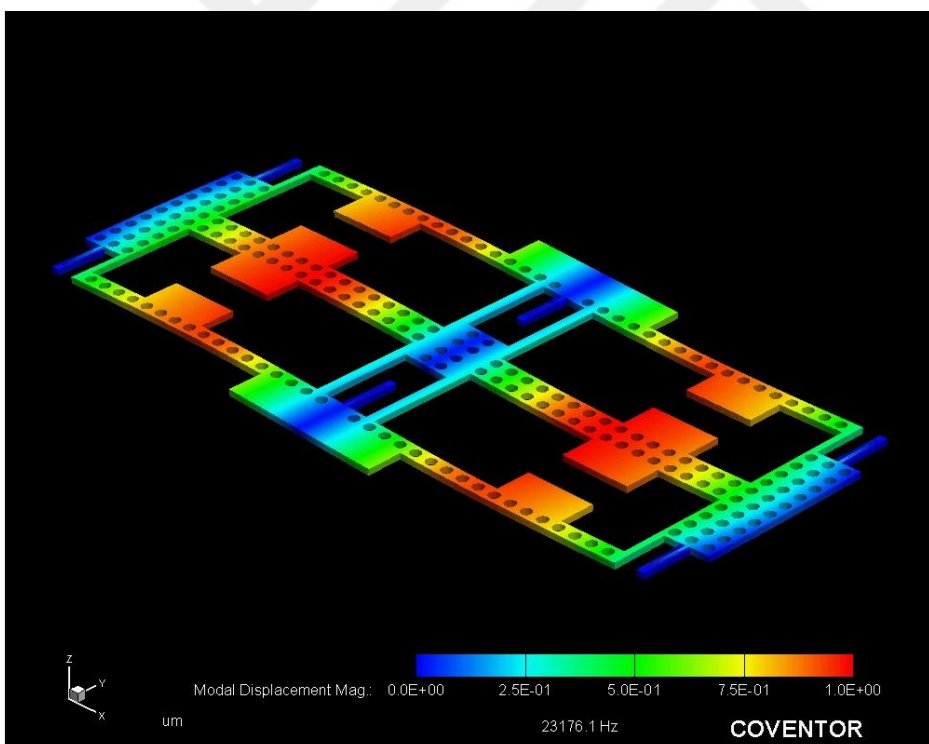


Figure 3.4: (a) Mesher settings of the lateral accelerometer design-1 for the proof mass (b) for the spring region.



(a)



(b)

Figure 3.5: Mode analysis simulation results of the lateral accelerometer design (a) The first mode and (b) the second mode.

Table 3.8: The comparison of the hand calculation and the simulation result for the lateral accelerometer design-1.

| Lateral design-1 | Hand calculations | Simulation results |
|--------------------------|-----------------------|-----------------------|
| Proof mass (kg) | 2.24×10^{-7} | 2.20×10^{-7} |
| Resonance frequency (Hz) | 11502 | 12317 |

Table 3.9: Simulation mod analysis results of the lateral accelerometer design-1.

| Mode domain | FEM Simulation results | |
|-------------|------------------------|-----------------------|
| | Frequency (Hz) | Generalized mass (kg) |
| 1 | 12317 | 2.20×10^{-7} |
| 2 | 23176 | 9.60×10^{-8} |
| 3 | 27215 | 1.17×10^{-7} |
| 4 | 28284 | 4.10×10^{-7} |
| 5 | 32417 | 4.82×10^{-8} |

3.2.1.2. Vertical Accelerometer Design-1

The crab-legs structure is selected to provide motion to the proof mass in the z axis direction. Instead of capacitive fingers, capacitive electrodes are placed not only the bottom but also the top side of the vertical accelerometer, where the capacitive gap is determined as $2 \mu\text{m}$. The proof mass is intentionally drawn without perforation holes to observe the Brownian noise of the sensor. Figure 3.6 shows the vertical accelerometer design-1. Table 3.10 show design and performance parameters of the accelerometer. The vertical accelerometer design is verified by using Coventorware. The mechanical model of the vertical accelerometer is formed. Springs and the proof mass of the accelerometer are separately modeled than connected with linkage boundary conditions. Figure 3.7 shows Coventorware simulation model of the vertical accelerometer design. Then, the model is divided into its finite element by using mesher setting shown Figure 3.8. It is noted that the Manhattan bricks mesh type is suitable for the structure which does not have any perforation holes. If the structure includes the perforation holes, the mesh type should be selected as

tetrahedrons. Table 3.11 shows the comparison of the hand calculation with simulation results. Figure 3.9 shows simulation mode analysis results for the vertical accelerometer design-1. Table 3.12 shows the simulation result of the vertical accelerometer for five different mod domains.

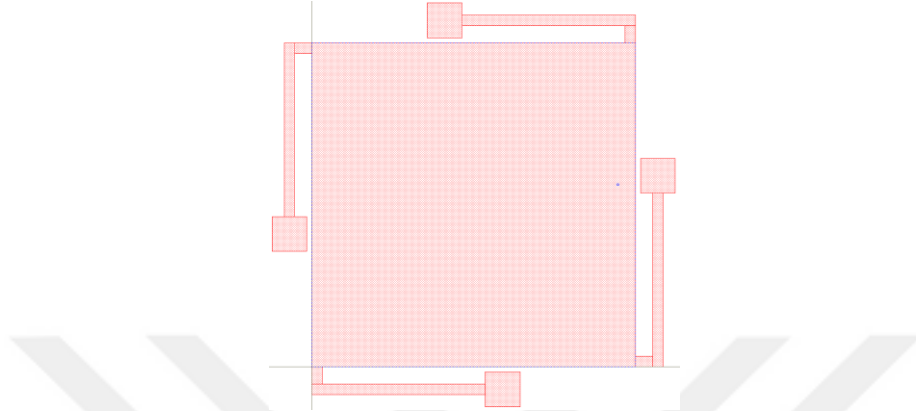


Figure 3.6: The layout of the vertical accelerometer design-1.

Table 3.10: Design and performance parameters of vertical accelerometer design-1.

| Design Parameters | | | |
|---|-----------------------|----------------------------------|-----------------------|
| Cell Width (μm) | 2200 | Spring Length (μm) | 1000 |
| Cell Length (μm) | 2200 | Spring Width (μm) | 60 |
| Number of Holes | - | Number of Springs | 4 |
| Radius of Holes (μm) | - | l_s/l_c | 0.1 |
| Electrodes Area (μm)² | 1865 x 1865 | Cap. Gap (μm) | 2 |
| Proof Mass (kg) | 284×10^{-9} | Structural Thickness (μm) | 35 |
| Performance Parameters | | | |
| Spring Constant (N/m) | 1266 | Rest Cap. (pF) | 15.4 |
| Damping (kg/s) | 2.35×10^1 | Sensitivity (F/m) | 7.70×10^{-6} |
| Res. Freq. (Hz) | 10636 | Range @ 5V (g) | 17.3 |
| Quality Factor | 8.24×10^{-4} | Brownian Noise (μg/√Hz) | 224 |

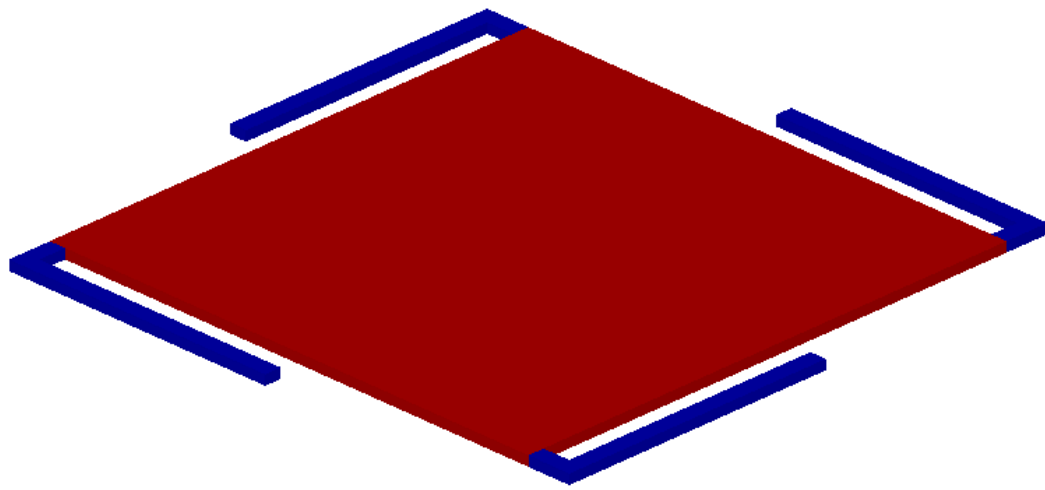


Figure 3.7: The FEM simulation model of the vertical accelerometer design-1.

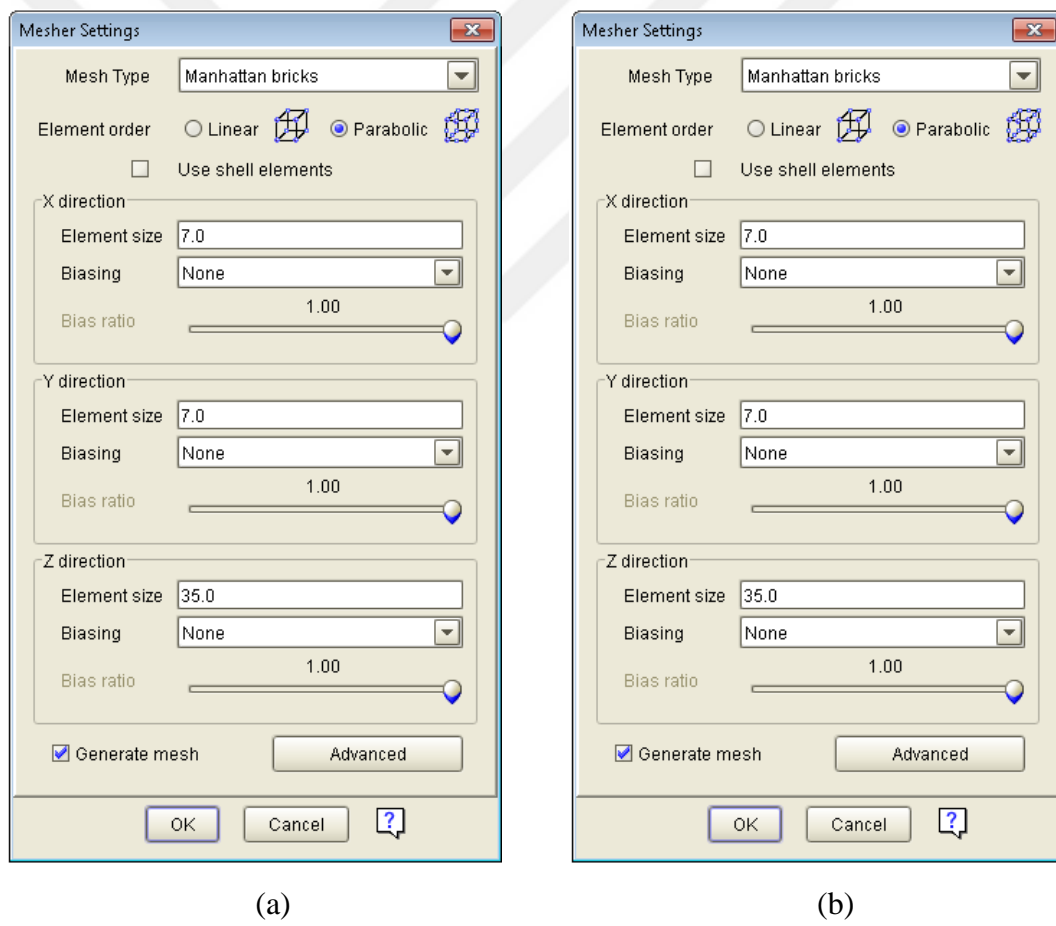
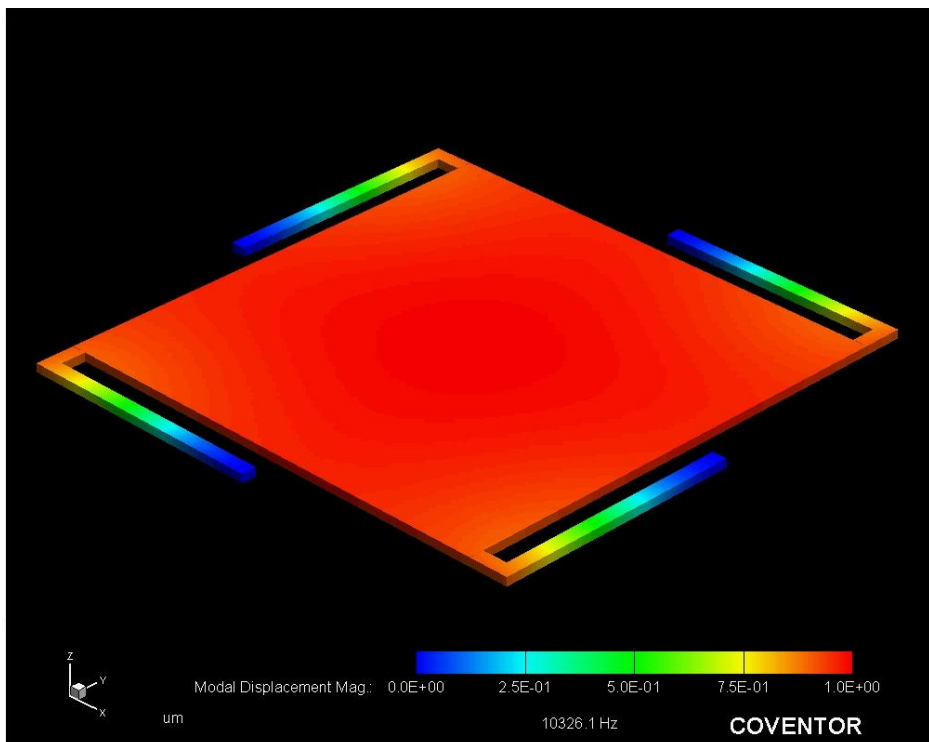
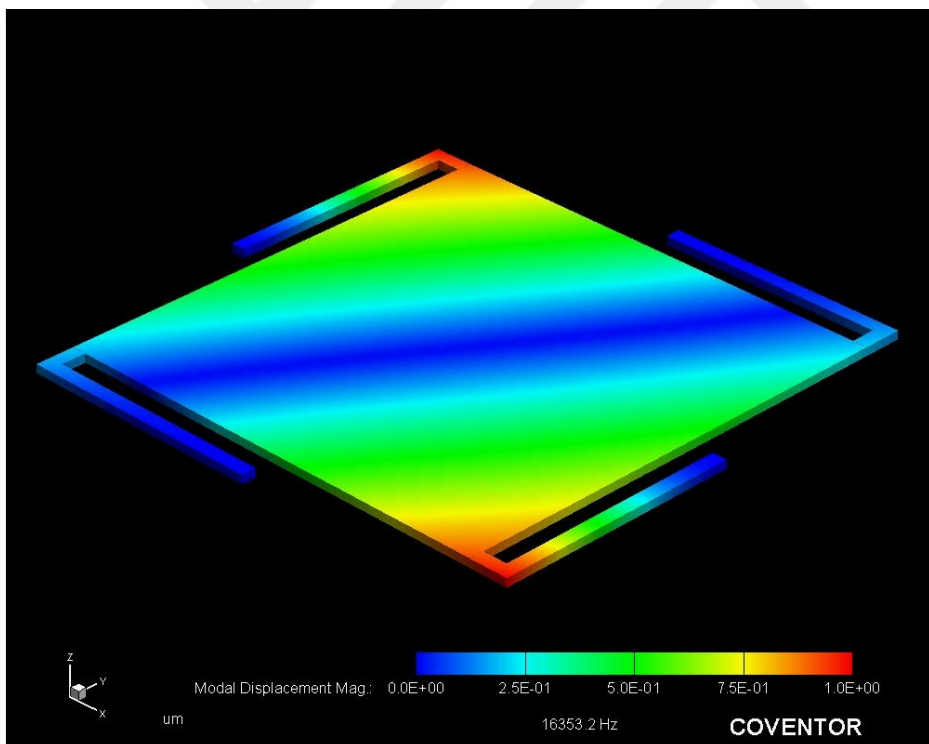


Figure 3.8: (a) Mesher settings of the vertical accelerometer design-1 for the proof mass (b) for the spring region.



(a)



(b)

Figure 3.9: Mode analysis simulation result of the vertical accelerometer design-1 (a) The first mode and (b) the second mode.

Table 3.11: The comparison of the hand calculation and the simulation result for the vertical accelerometer design-1.

| Vertical design-1 | Hand calculations | Simulation results |
|---------------------------------|----------------------|----------------------|
| Proof mass (kg) | 284×10^{-9} | 283×10^{-7} |
| Resonance frequency (Hz) | 10636 | 10326 |

Table 3.12: Simulation mode analysis results of the vertical accelerometer design-1.

| Mode domain | FEM Simulation results | |
|-------------|------------------------|-----------------------|
| | Frequency (Hz) | Generalized mass (kg) |
| 1 | 10326 | 2.73×10^{-7} |
| 2 | 16353 | 4.89×10^{-8} |
| 3 | 16353 | 4.89×10^{-8} |
| 4 | 49076 | 3.78×10^{-8} |
| 5 | 83108 | 2.95×10^{-8} |

3.2.1.3. Vertical Accelerometer Design-1 with Perforation Holes

The accelerometer is same with the previous accelerometer design except perforation holes. The proof mass of the vertical accelerometer is perforated with holes to decrease both the mass of the proof mass and the damping coefficient. The other design parameter is same with previous design, however; the resonance frequency of the vertical accelerometer changes as a result of decrease in the mass of the proof mass. There are 324 perforation holes of which radius is $30 \mu\text{m}$. Figure 3.10 shows the layout of the vertical accelerometer. Table 3.13 show design and performance parameters of the vertical accelerometer. The vertical accelerometer design is simulated by using the Coventorware and five different mode domains are determined. As the design includes the perforation holes, the mesh type for the proof mass is selected as tetrahedrons. However, the meshed type of spring structures is determined by using the Manhattan bricks. Table 3.14 shows the comparison of the hand calculation with simulation results. Figure 3.11 shows simulation mode analysis results for the vertical accelerometer design-1 with perforation holes. Table 3.15

shows the simulation result of the vertical accelerometer for five different mode domains.

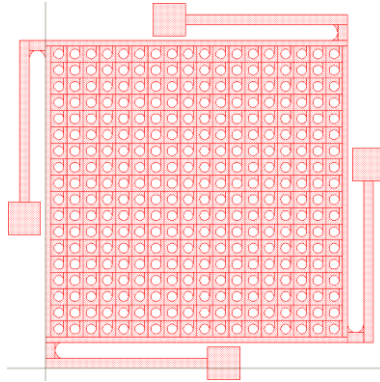
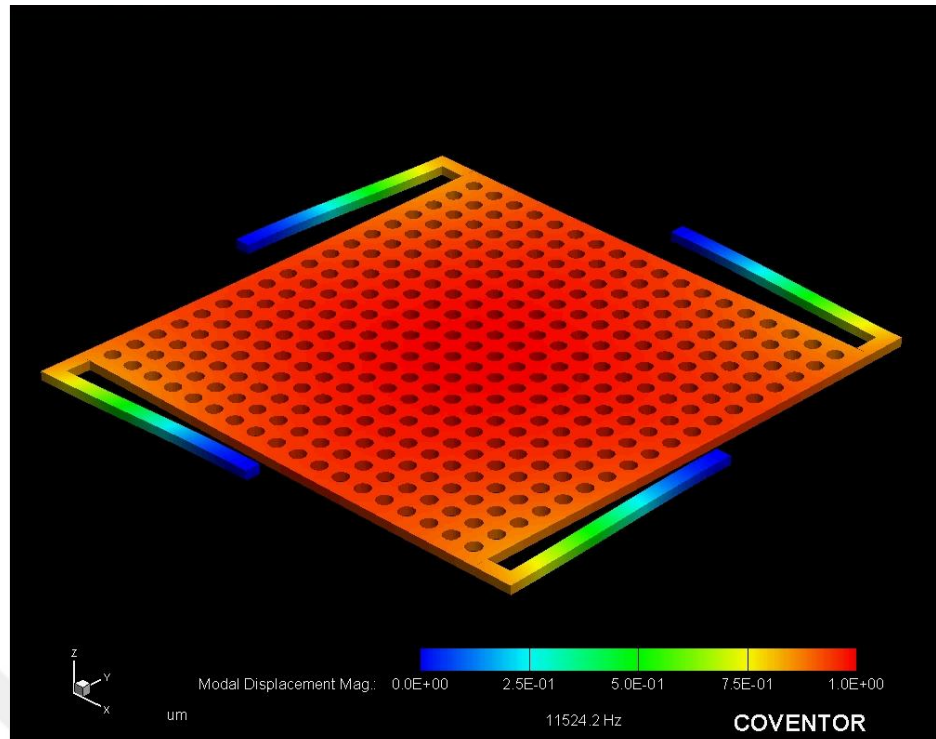


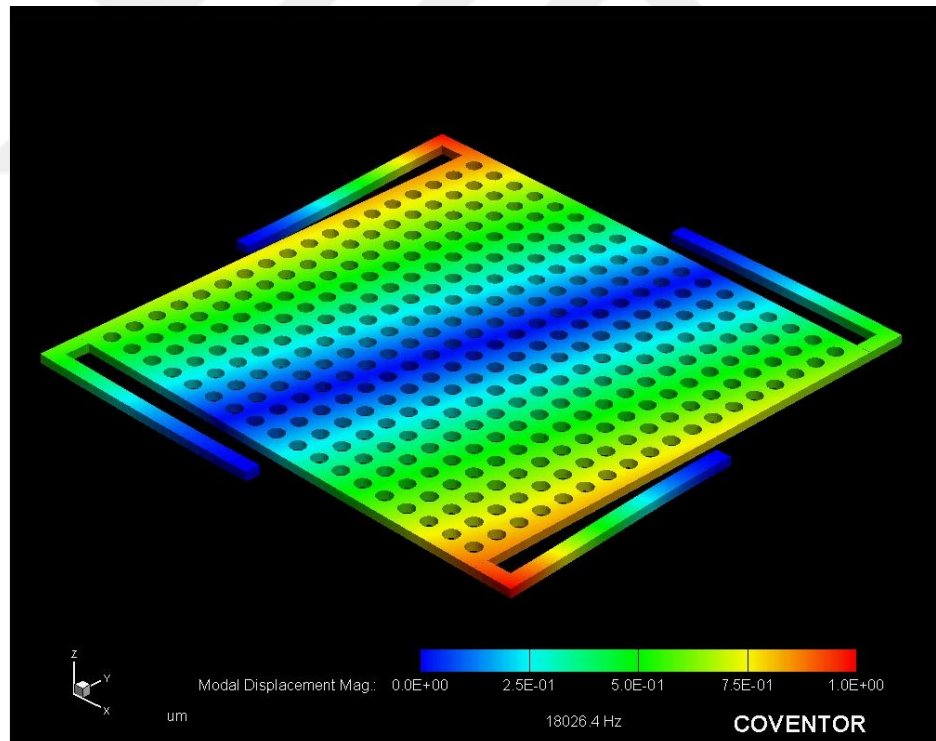
Figure 3.10: The layout of the vertical accelerometer design-1 with perforation holes.

Table 3.13: Design and performance parameters of the vertical accelerometer design-1 with perforation holes.

| Design Parameters | | | |
|---|-----------------------|--------------------------------|-----------------------|
| Cell Width (μm) | 2200 | Spring Length (μm) | 1000 |
| Cell Length (μm) | 2200 | Spring Width (μm) | 60 |
| Number of Holes (μm) | 324 | Number of Springs | 4 |
| Radius of Holes (μm) | 30 | l_s/l_c | 0.1 |
| Electrodes Area (μm)² | 1865 x 1865 | Cap. Gap (μm) | 2 |
| Proof Mass (kg) | 209×10^{-9} | Struc. Thickness (μm) | 35 |
| Performance Parameters | | | |
| Spring Constant (N/m) | 1266 | Rest Cap. (pF) | 11.3 |
| Damping (kg/s) | 1.96×10^{-2} | Sensitivity (F/m) | 5.67×10^{-6} |
| Res. Freq. (Hz) | 12392 | Range @ 5V | 17.3 |
| Quality Factor | 8.28×10^{-1} | Brownian Noise (μg/√Hz) | 8.8 |



(a)



(b)

Figure 3.11: Mode analysis simulation result of the vertical accelerometer design-1 with perforation holes (a) The first mode and (b) the second mode.

Table 3.14: The comparison of the hand calculation and the simulation result for the vertical accelerometer design-1 with perforation holes.

| Vertical design-1 with holes | Hand calculations | Simulation results |
|------------------------------|----------------------|----------------------|
| Proof mass (kg) | 209×10^{-9} | 194×10^{-9} |
| Resonance frequency (Hz) | 12392 | 11524 |

Table 3.15: Simulation mode analysis results of the vertical accelerometer design-1 with perforation holes.

| Mode domain | FEM Simulation results | |
|-------------|------------------------|-----------------------|
| | Frequency (Hz) | Generalized mass (kg) |
| 1 | 11524 | 1.94×10^{-7} |
| 2 | 18026 | 5.07×10^{-8} |
| 3 | 18030 | 5.06×10^{-8} |
| 4 | 45694 | 3.14×10^{-8} |
| 5 | 71844 | 2.51×10^{-8} |

3.2.1.4. Vertical Accelerometer Design-2

Although the same proof mass area is used for the design of the vertical accelerometer, the main difference is width of springs. The width of springs is decreased to $20 \mu\text{m}$ in the current design. Figure 3.12 shows the layout of the vertical accelerometer. Table 3.16 show design and performance parameters of the vertical accelerometer. The vertical accelerometer design is simulated by using the Coventorware and five different mode domains are determined. The mesh type of the proof mass and spring regions are selected as Manhattan bricks. Table 3.17 shows the comparison of the hand calculation with simulation results. Figure 3.13 shows simulation mode analysis results for the vertical accelerometer design-2. Table 3.18 shows the simulation result of the vertical accelerometer for five different mode domains.

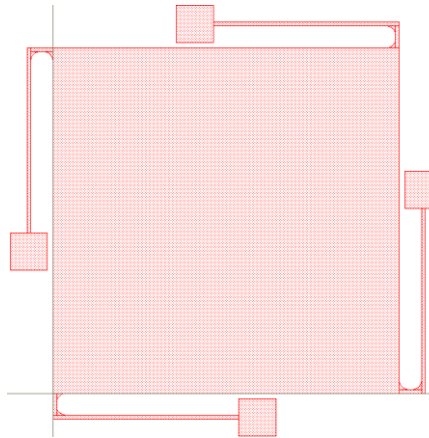
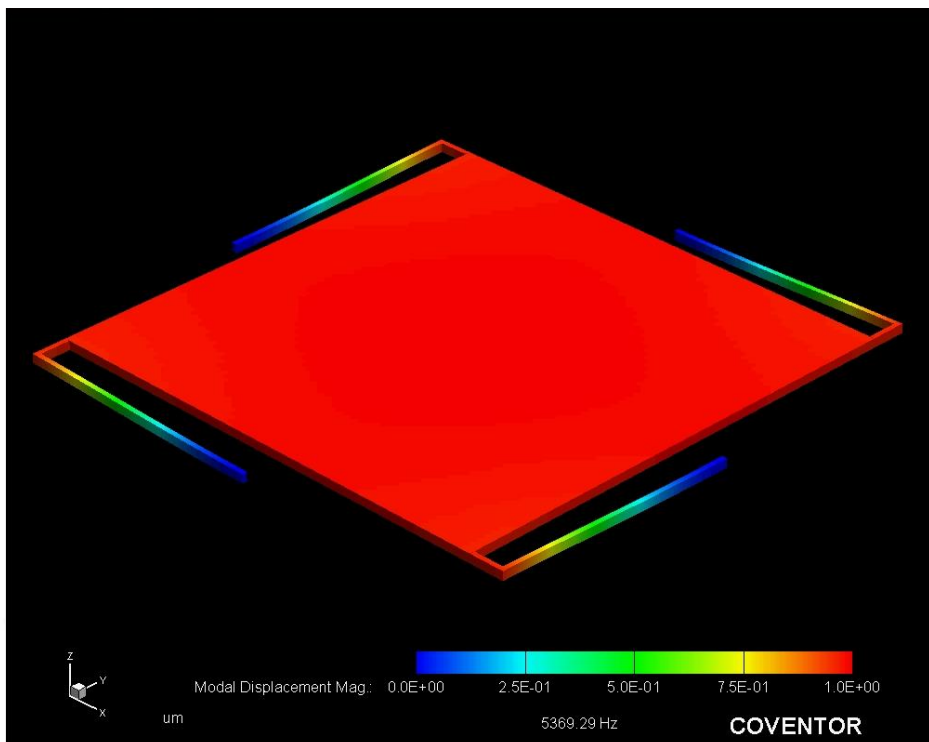


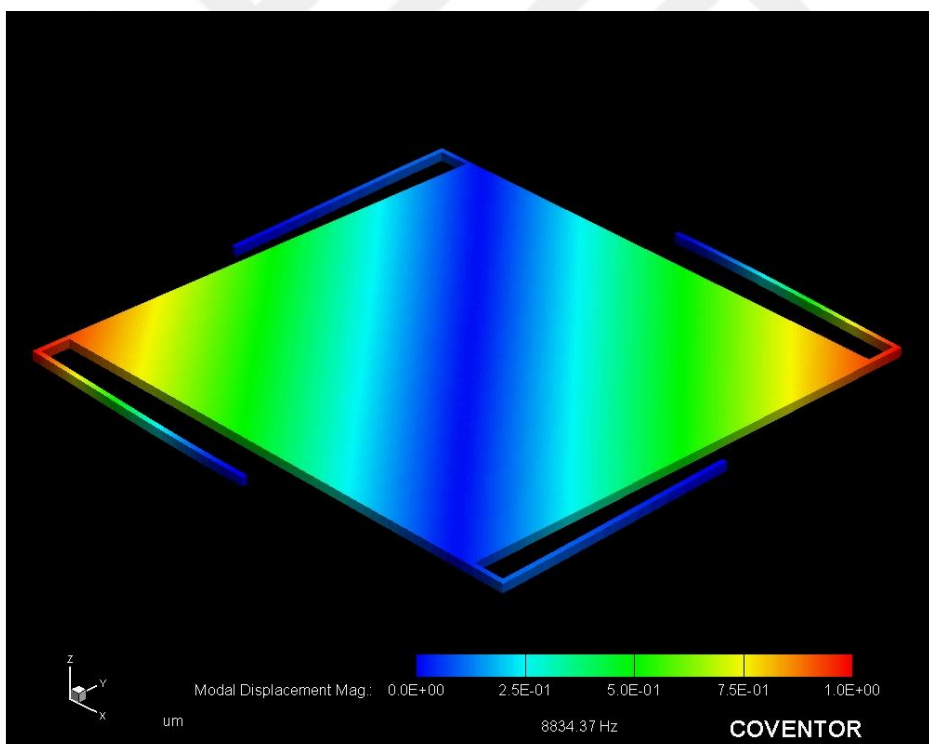
Figure 3.12: The layout of the vertical accelerometer design-2.

Table 3.16: Design and performance parameters of the vertical accelerometer design-2.

| Design Parameters | | | |
|------------------------------|-----------------------|----------------------------------|-----------------------|
| Cell Width (μm) | 2200 | Spring Length (μm) | 1000 |
| Cell Length (μm) | 2200 | Spring Width (μm) | 20 |
| Number of Holes | - | Number of Springs | 4 |
| Radius of Holes (μm) | - | l_s/l_c | 0.12 |
| Electrodes Area (μm) | 1865 x 1865 | Cap. Gap (μm) | 2 |
| Proof Mass (kg) | 284×10^{-9} | Structural Thickness (μm) | 35 |
| Performance Parameters | | | |
| Spring Constant (N/m) | 249 | Rest Cap. (pF) | 15.4 |
| Damping (kg/s) | 23.5 | Sensitivity (F/m) | 7.70×10^{-6} |
| Res. Freq. (Hz) | 4717 | Range @ 5V | 17.3 |
| Quality Factor | 3.57×10^{-4} | Brownian Noise (μg/√Hz) | 224 |



(a)



(b)

Figure 3.13: Mode analysis simulation result of the vertical accelerometer design-2
(a) The first mode and (b) the second mode.

Table 3.17: The comparison of the hand calculation and the simulation result for the vertical accelerometer design-2.

| Vertical design-2 | Hand calculations | Simulation results |
|---------------------------------|----------------------|----------------------|
| Proof mass (kg) | 284×10^{-9} | 280×10^{-9} |
| Resonance frequency (Hz) | 4717 | 5369 |

Table 3.18: Simulation mode analysis results of the vertical accelerometer design-2.

| Mode domain | FEM Simulation results | |
|-------------|------------------------|-----------------------|
| | Frequency (Hz) | Generalized mass (kg) |
| 1 | 5369 | 2.80×10^{-7} |
| 2 | 8834 | 4.40×10^{-8} |
| 3 | 8834 | 4.40×10^{-8} |
| 4 | 32674 | 1.18×10^{-8} |
| 5 | 32674 | 1.18×10^{-8} |

3.2.1.5. Vertical Accelerometer Design-2 with Perforation Holes

The proof mass region is perforated with holes to decrease the damping coefficient and the mass of the proof mass in the current design. The width of springs is $20 \mu\text{m}$. Figure 3.14 shows the layout of the vertical accelerometer. Table 3.19 show design and performance parameters of the vertical accelerometer. The vertical accelerometer design is simulated by using the Coventorware and five different mode domains are determined. The mesh type of the proof mass and spring regions are selected as tetrahedrons and Manhattan bricks, respectively. Table 3.20 shows the comparison of the hand calculation with simulation results. Figure 3.15 shows simulation mode analysis results for the vertical accelerometer design-1. Table 3.21 shows the simulation result of the vertical accelerometer for five different mode domains.

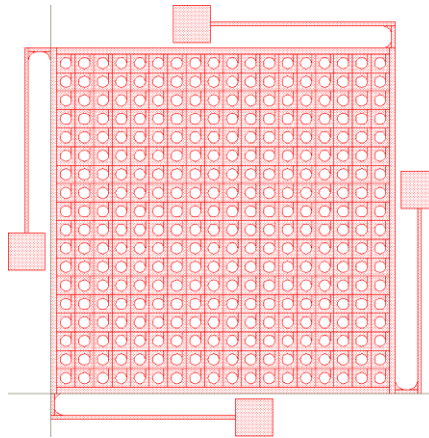


Figure 3.14: The layout of the vertical accelerometer design-2 with perforation holes.

Table 3.19: Design and performance parameters of the vertical accelerometer design 2 with perforation holes.

| Design Parameters | | | |
|---|-----------------------|--------------------------------|-----------------------|
| Cell Width (μm) | 2200 | Spring Length (μm) | 1000 |
| Cell Length (μm) | 2200 | Spring Width (μm) | 20 |
| Number of Holes | 324 | Number of Springs | 4 |
| Radius of Holes (μm) | 30 | l_s/l_c | 0.12 |
| Electrodes Area (μm)² | 1865 x 1865 | Cap. Gap (pF) | 2 |
| Proof Mass (kg) | 209×10^{-9} | Struc. Thickness (μm) | 35 |
| Performance Parameters | | | |
| Spring Constant (N/m) | 249 | Rest Cap. (pF) | 11.3 |
| Damping (kg/s) | 1.96×10^{-2} | Sensitivity (F/m) | 5.67×10^{-6} |
| Res. Freq. (Hz) | 5496 | Range @ 5V (g) | 17.3 |
| Quality Factor | 3.67×10^{-1} | Brownian Noise (μg/√Hz) | 8.8 |

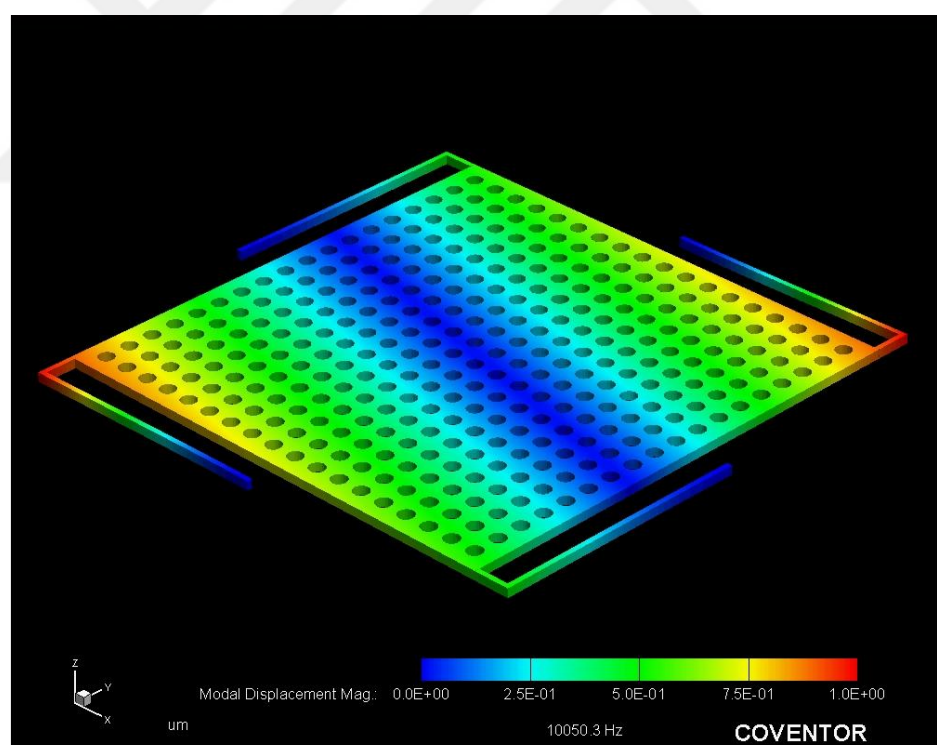
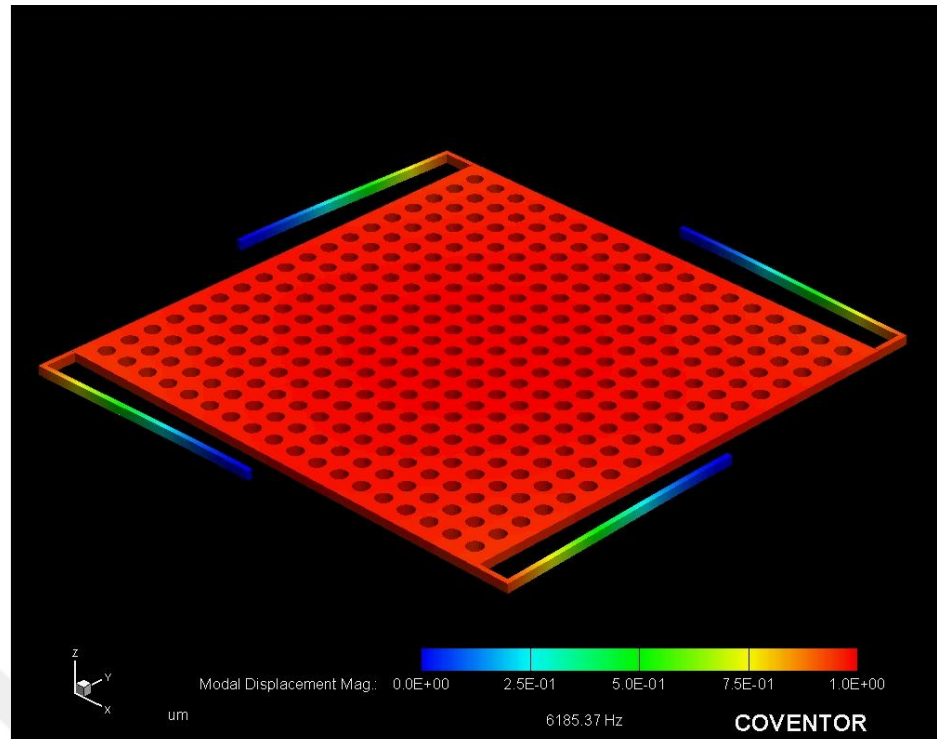


Figure 3.15: Mode analysis simulation results of the vertical accelerometer design-2 with perforation holes (a) The first mode and (b) the second mode.

Table 3.20: The comparison of the hand calculation and the simulation result for the vertical accelerometer design-2 with perforation holes.

| Vertical design-2 with holes | Hand calculations | Simulation results |
|------------------------------|----------------------|----------------------|
| Proof mass (kg) | 209×10^{-9} | 280×10^{-9} |
| Resonance frequency (Hz) | 5496 | 6185 |

Table 3.21: Simulation mode analysis results of the vertical accelerometer design-2 with perforation holes.

| Mode domain | FEM Simulation results | |
|-------------|------------------------|-----------------------|
| | Frequency (Hz) | Generalized mass (kg) |
| 1 | 6185 | 2.04×10^{-7} |
| 2 | 10050 | 4.25×10^{-8} |
| 3 | 1053 | 4.25×10^{-8} |
| 4 | 37046 | 1.14×10^{-7} |
| 5 | 37155 | 1.14×10^{-7} |

3.2.1.6. Vertical Accelerometer Design-3

The folded spring structure is attached to the proof mass in the current design. The proof mass region is drawn without perforation holes. The width and the length of springs are $7 \mu\text{m}$ and $833 \mu\text{m}$, respectively. There are eight springs attached to the proof mass. Figure 3.16 shows the layout of the vertical accelerometer. Table 3.22 show design and performance parameters of the vertical accelerometer. The vertical accelerometer design is simulated by using the Coventorware and five different mode domains are determined. The mesh type of the proof mass and spring regions are selected as the Manhattan bricks. Table 3.23 shows the comparison of the hand calculation with simulation results. Figure 3.17 shows simulation mode analysis results for the vertical accelerometer design-3. Table 3.24 shows the simulation result of the vertical accelerometer for five different mode domains.

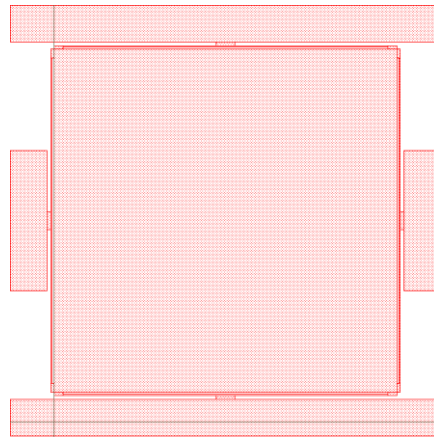
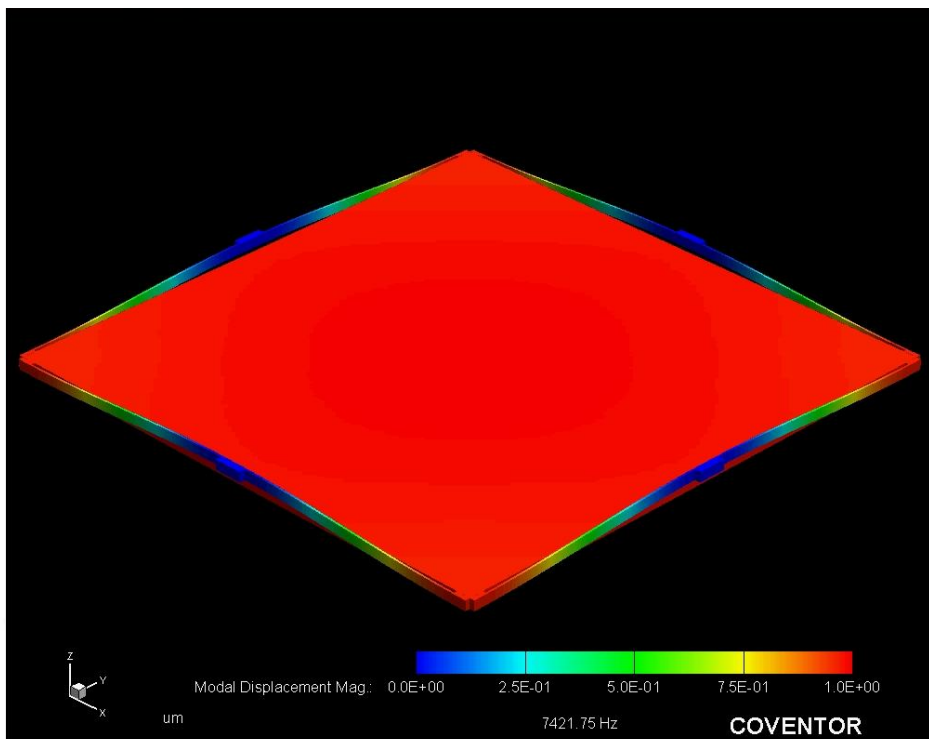


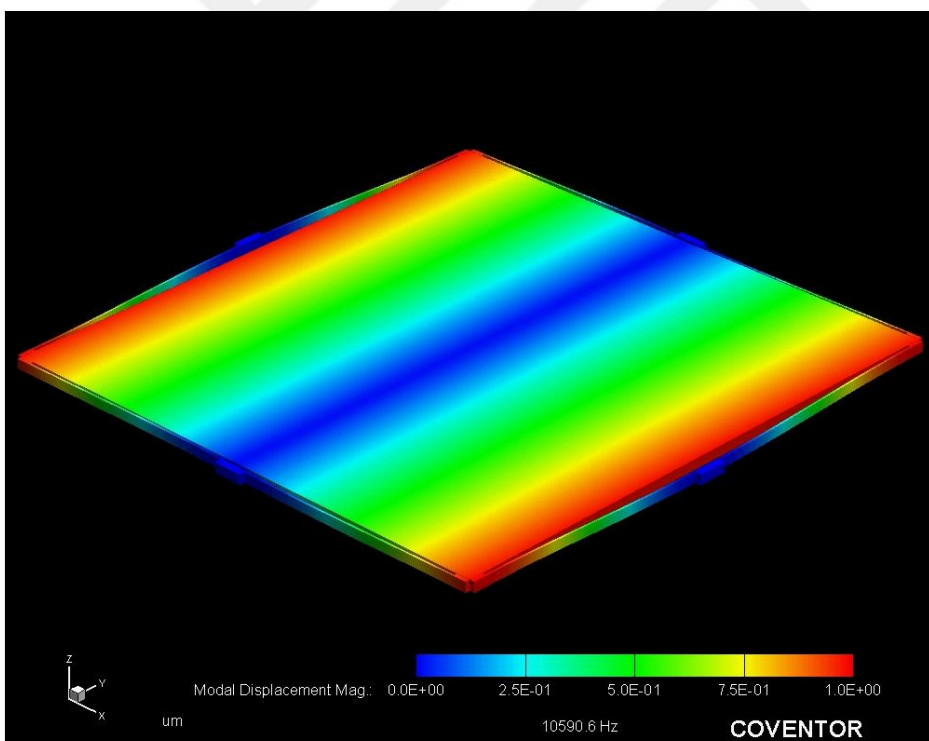
Figure 3.16: The layout of the vertical accelerometer design-3.

Table 3.22: Design and performance parameters of the vertical accelerometer design-3.

| Design Parameters | | | |
|-------------------------------------|-----------------------|---|-----------------------|
| Cell Width (μm) | 2200 | Spring Length (μm) | 833 |
| Cell Length (μm) | 2200 | Spring Width (μm) | 7 |
| Number of Holes | - | Number of Springs | 8 |
| Radius of Holes (μm) | - | l_s/l_c | - |
| Electrodes Area (μm^2) | 1865 x 1865 | Cap. Gap (pF) | 2 |
| Proof Mass (kg) | 284×10^{-9} | Structural Thickness (μm) | 35 |
| Performance Parameters | | | |
| Spring Constant (N/m) | 702 | Rest Cap. (pF) | 15.4 |
| Damping (kg/s) | 23.5 | Sensitivity (F/m) | 7.70×10^{-6} |
| Res. Freq. (Hz) | 7917 | Range @ 5V (g) | 17.3 |
| Quality Factor | 6.00×10^{-4} | Brownian Noise ($\mu\text{g}/\sqrt{\text{Hz}}$) | 224 |



(a)



(b)

Figure 3.17: Mode analysis simulation results of the vertical accelerometer design.
(a) The first mode and (b) the second mode.

Table 3.23: The comparison of the hand calculation and the simulation result for the vertical accelerometer design-3.

| Vertical design-3 | Hand Calculations | Simulation Results |
|---------------------------------|----------------------|----------------------|
| Proof mass (kg) | 209×10^{-9} | 278×10^{-9} |
| Resonance frequency (Hz) | 7917 | 7421 |

Table 3.24: Simulation mode analysis results of the vertical accelerometer design-3.

| Mode domain | FEM simulation results | |
|-------------|------------------------|-----------------------|
| | Frequency (Hz) | Generalized mass (kg) |
| 1 | 7421 | 2.78×10^{-7} |
| 2 | 10590 | 9.31×10^{-8} |
| 3 | 10590 | 9.31×10^{-8} |
| 4 | 49805 | 3.85×10^{-8} |
| 5 | 87325 | 5.44×10^{-8} |

3.2.1.7. Vertical Accelerometer Design-3 with Perforation Holes

The proof mass region is perforated with holes in the current design. The width and length of springs are $7 \mu\text{m}$ and $833 \mu\text{m}$, respectively. There are eight spring is attached to the proof mass. Figure 3.18 shows the layout of the vertical accelerometer. Table 3.25 show design and performance parameters of the vertical accelerometer. The vertical accelerometer design is simulated by using the Coventorware and five different mode domains are determined. The mesh type of the proof mass and spring regions are selected as tetrahedrons and Manhattan bricks, respectively. Table 3.26 shows the comparison of the hand calculation with simulation results. Figure 3.19 shows simulation mode analysis results for the vertical accelerometer design-3 with perforation holes. Table 3.27 shows the simulation result of the vertical accelerometer for five different mode domains.

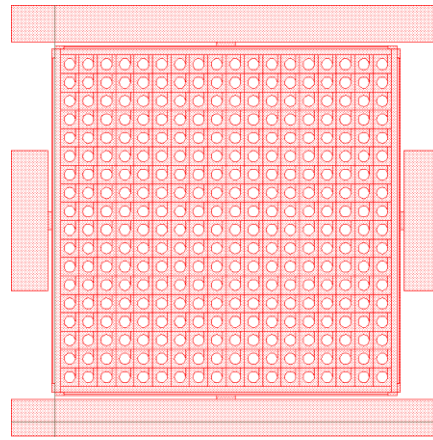
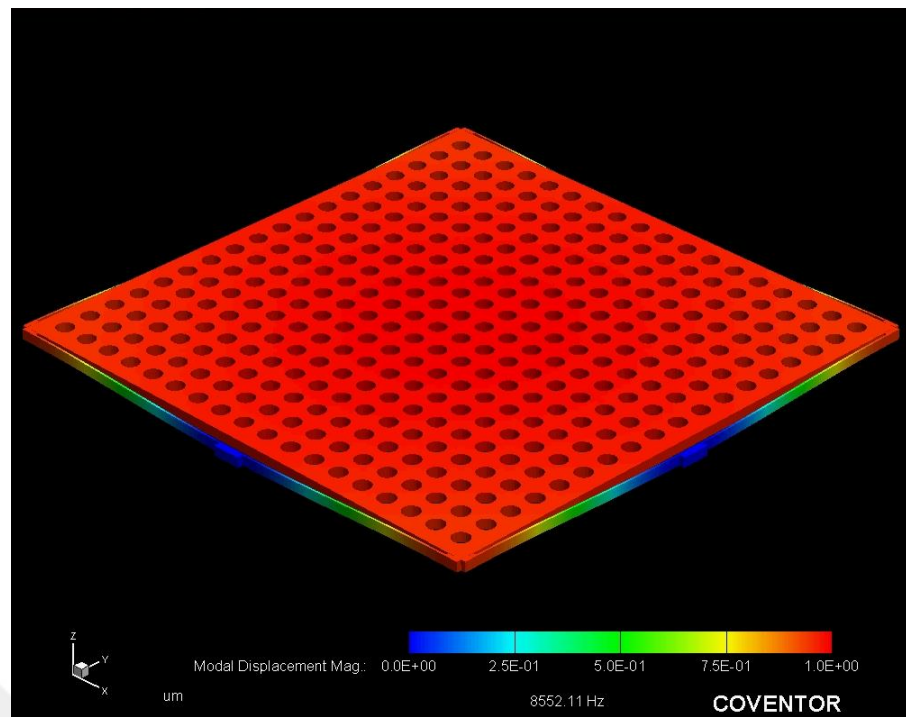


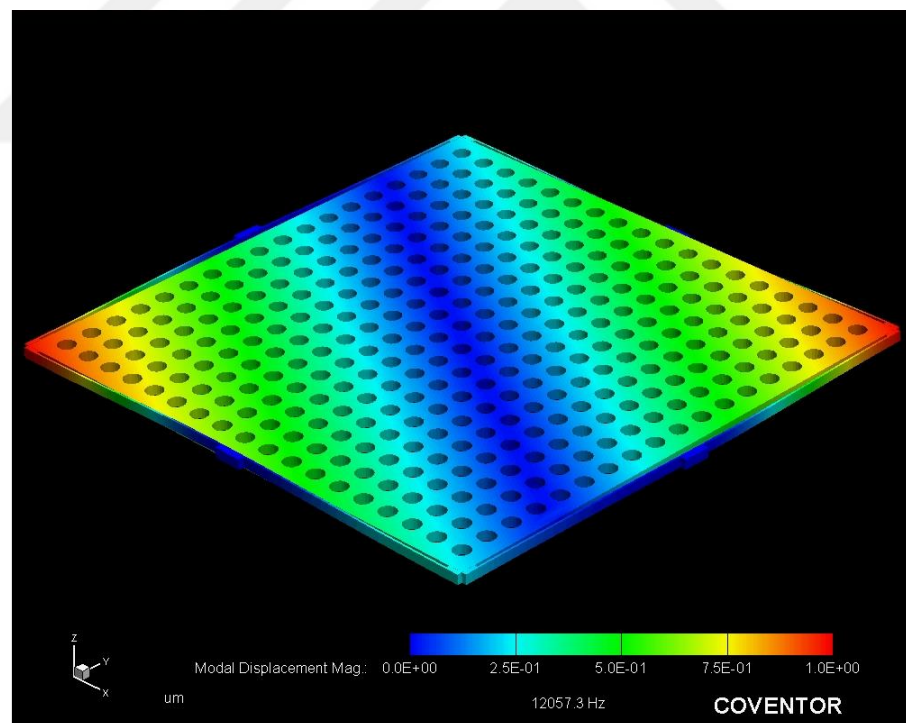
Figure 3.18: The layout of the vertical accelerometer design-3 with perforation holes.

Table 3.25: Design and performance parameters of the vertical accelerometer design-3 with perforation holes.

| Design Parameters | | | |
|---|-----------------------|--------------------------------|-----------------------|
| Cell Width (μm) | 2200 | Spring Length (μm) | 833 |
| Cell Length (μm) | 2200 | Spring Width (μm) | 7 |
| Number of Holes | - | Number of Springs | 8 |
| Radius of Holes (μm) | 30 | l_s/l_c | - |
| Electrodes Area (μm)² | 1865 x 1865 | Cap. Gap (pF) | 2 |
| Proof Mass (kg) | 209×10^{-9} | Struc.l Thickness (μm) | 35 |
| Performance Parameters | | | |
| Spring Constant (N/m) | 702 | Rest Cap. (pF) | 11.3 |
| Damping (kg/s) | 1.96×10^{-2} | Sensitivity (F/m) | 5.67×10^{-6} |
| Res. Freq. (Hz) | 9225 | Range @ 5V (g) | 17.3 |
| Quality Factor | 6.16×10^{-1} | Brownian Noise (μg/√Hz) | 8.8 |



(a)



(b)

Figure 3.19: Mode analysis simulation result of the vertical accelerometer design 3 with perforation holes (a) the first mode and (b) the second mode.

Table 3.26: The comparison of the hand calculation and the simulation result for the vertical accelerometer design 3 with perforation holes.

| Vertical design-3 with holes | Hand calculations | Simulation results |
|------------------------------|----------------------|----------------------|
| Proof mass (kg) | 209×10^{-9} | 201×10^{-9} |
| Resonance frequency (Hz) | 9225 | 8552 |

Table 3.27: Simulation mode analysis results of the vertical accelerometer design 3 with perforation holes.

| Mode domain | FEM Simulation results | |
|-------------|------------------------|-----------------------|
| | Frequency (Hz) | Generalized mass (kg) |
| 1 | 8552 | 2.01×10^{-7} |
| 2 | 12057 | 3.81×10^{-8} |
| 3 | 12057 | 3.81×10^{-8} |
| 4 | 46378 | 3.01×10^{-8} |
| 5 | 77676 | 2.92×10^{-8} |

3.2.2. Three Axis Accelerometer Design Mask set-2

In the first fabrication mask set, performance parameters of lateral and vertical accelerometer are not taken into consideration. The aim of the first mask set is to show the feasibility of the proposed fabrication process. Therefore, in the second mask set, three axis accelerometers are designed to obtain high performance. Therefore, design parameters of the lateral and the vertical accelerometer are tried to set each other. Furthermore, there are three lateral accelerometer designs in the second fabrication mask set of the three axis accelerometer. Two of them are previously designed by METU-MEMS VLSI inertial sensors group members, and these accelerometers are high performance accelerometers. Furthermore, the last lateral accelerometer and all vertical accelerometer are designed to match same performance parameters. The spring length and the proof mass of vertical accelerometer designs are different from each other. However, design and

performance parameters are close to that of lateral accelerometers. Although the second anodic bonding is only taken into account for the formation of the glass-silicon-glass multi- stack in the first mask set, the second mask is drawn such a way which is suitable not only the two-step anodic bonding but also the anodic bonding and then the Au-Si eutectic bonding fabrication methods.

3.2.2.1. Lateral Accelerometer Design-1

The lateral accelerometer designed in [58] is modified. The structure is same reported in [58] except the spring length and spring width. However, the spring constant is almost same that of the demonstrated accelerometer. Figure 3.20 shows the structure of the accelerometer. Table 3.28 shows the design parameters of the lateral accelerometer design-1. Table 3.29 shows the comparison of the hand calculation with simulation results. Table 3.30 shows the simulation result of the lateral accelerometer design-1 for five different mode domains. Figure 3.21 shows simulation mode analysis results for the lateral accelerometer design-1.

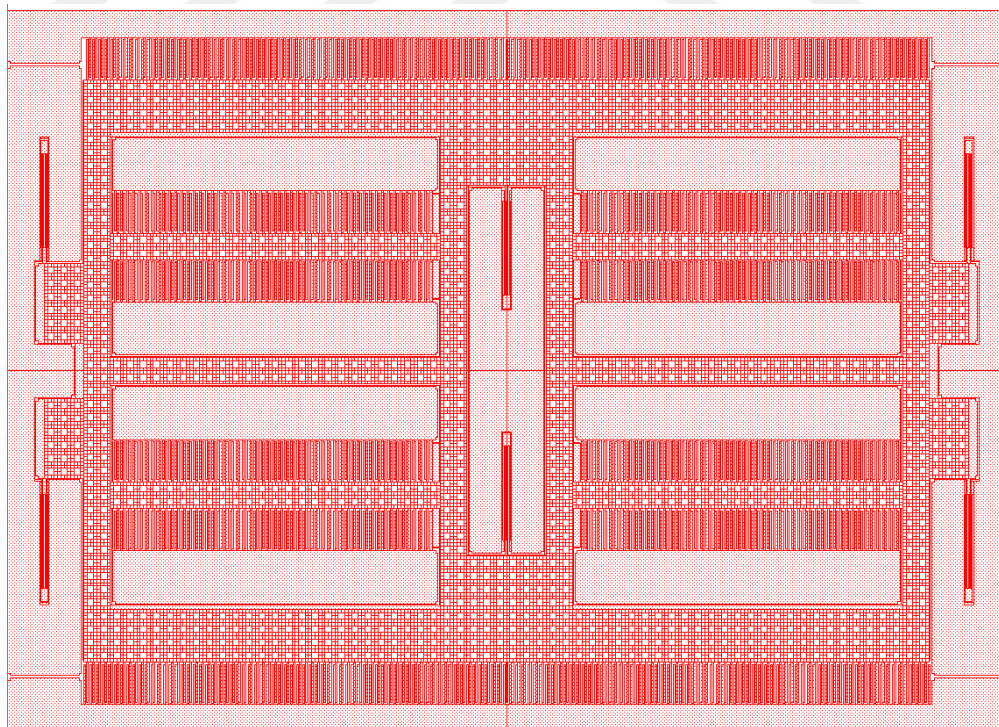


Figure 3.20: The layout of the lateral accelerometer design-1 for the second fabrication mask set.

Table 3.28: Performance parameters of the lateral accelerometer design-1.

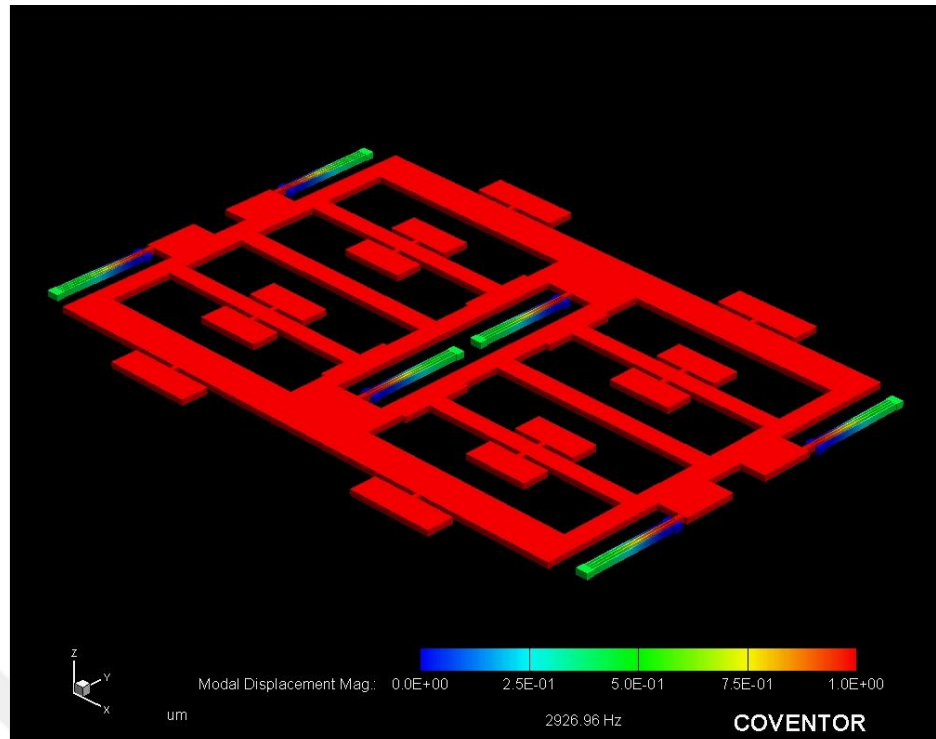
| Performance Parameters | |
|----------------------------|-------------------------------|
| Proof mass | 219×10^{-9} kg |
| Finger spacing | 2 μ m |
| Spring constant | 56 N/m |
| Damping | 8×10^{-3} kg/s |
| Resonance frequency | 2549 Hz |
| Rest capacitance | 9.75 pF |
| Sensitivity | 3.75×10^{-6} |
| Range | 10.8 g @ 5 V |
| Brownian noise | 5 μ g/ $\sqrt{\text{Hz}}$ |

Table 3.29: The comparison of the hand calculation and the simulation result for the lateral accelerometer design-1.

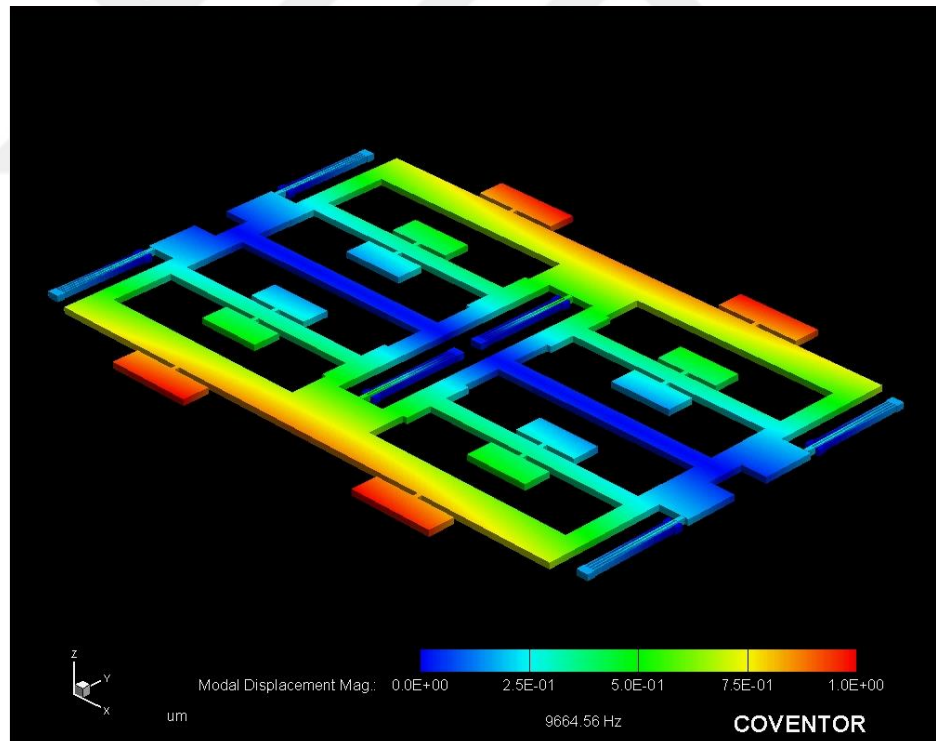
| Lateral design-1 | Hand calculations | Simulation results |
|---------------------------------|-----------------------|-----------------------|
| Proof mass (kg) | 2.19×10^{-7} | 2.31×10^{-7} |
| Resonance frequency (Hz) | 2549 | 2926 |

Table 3.30: Simulation mode analysis results of the lateral accelerometer design-1.

| Mode domain | FEM Simulation results | |
|-------------|------------------------|-----------------------|
| | Frequency (Hz) | Generalized mass (kg) |
| 1 | 2926 | 2.37×10^{-7} |
| 2 | 9664 | 7.19×10^{-8} |
| 3 | 11086 | 1.35×10^{-7} |
| 4 | 16755 | 1.00×10^{-7} |
| 5 | 25195 | 5.13×10^{-8} |



(a)



(b)

Figure 3.21: The first and the second mode of the lateral accelerometer design-1 for the second mask set.

3.2.2.2. Lateral Accelerometer Design-2

The second lateral accelerometer is designed by one of the METU-MEMS VLSI inertial sensor group members. Capacitive fingers are placed not only sides of the lateral accelerometer but also center of the lateral accelerometer to increase the sensitivity. Four double folded spring structures are used for the lateral accelerometer design-2. Table 3.31 shows design parameters of the lateral accelerometer design-2. Table 3.32 and Table 3.33 show the comparison and simulation results.

Table 3.31: Performance Parameters of the lateral accelerometer design-2.

| Performance Parameters | |
|----------------------------|------------------------------------|
| Proof mass | 8×10^{-8} |
| Resonance frequency | 2500 Hz |
| Rest capacitance | 6 pF |
| Sensitivity | 1.4×10^{-6} |
| Range | 30 g @ 8 V |
| Brownian noise | $8.5 \mu\text{g}/\sqrt{\text{Hz}}$ |

Table 3.32: The comparison of the hand calculation and the simulation result for the lateral accelerometer design-2.

| Lateral design-2 | Hand calculations | Simulation results |
|---------------------------------|--------------------|-----------------------|
| Proof mass (kg) | 8×10^{-8} | 6.85×10^{-8} |
| Resonance frequency (Hz) | 2500 | 2595 |

Table 3.33: Simulation mode analysis results of the lateral accelerometer design-2.

| Mode Domain | FEM Simulation results | |
|-------------|------------------------|-----------------------|
| | Frequency (Hz) | Generalized mass (kg) |
| 1 | 2595 | 6.85×10^{-8} |
| 2 | 14908 | 4.02×10^{-8} |
| 3 | 19390 | 2.06×10^{-8} |

3.2.2.3. Lateral Accelerometer Design-3

Capacitive fingers are placed not only sides of the lateral accelerometer but also the center of the lateral accelerometer to increase the sensitivity. Six double folded spring structures are attached to the proof mass of the lateral accelerometer. Double-folded springs are replaced to both ends and middle of the accelerometer to prevent undesired movement of the accelerometer as much as possible. Figure 3.22 shows the structure of the accelerometer. Table 3.34 shows the design and performance parameters of the lateral accelerometers. Table 3.35 shows the comparison of the hand calculation with simulation results. Figure 3.23 shows finite element mode analysis results of the lateral accelerometer design-3. Table 3.36 shows simulation mode analysis results for the lateral accelerometer design-3.

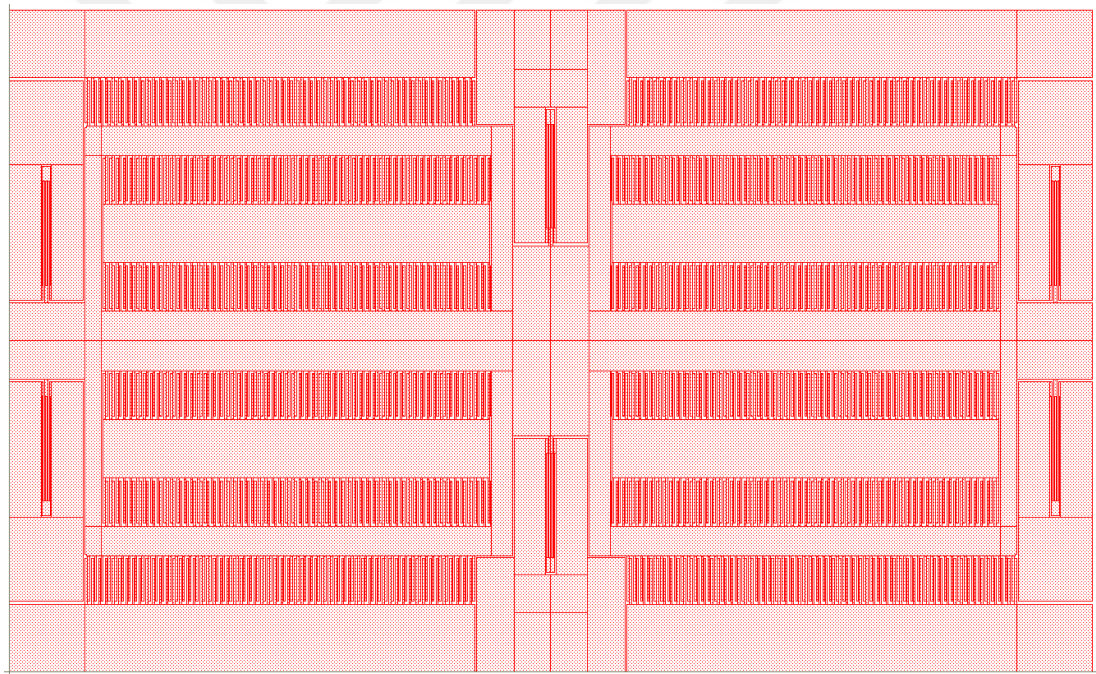


Figure 3.22: The layout of the lateral accelerometer design-3 for the second fabrication mask set.

Table 3.34: Design and performance parameters of lateral accelerometer design-3.

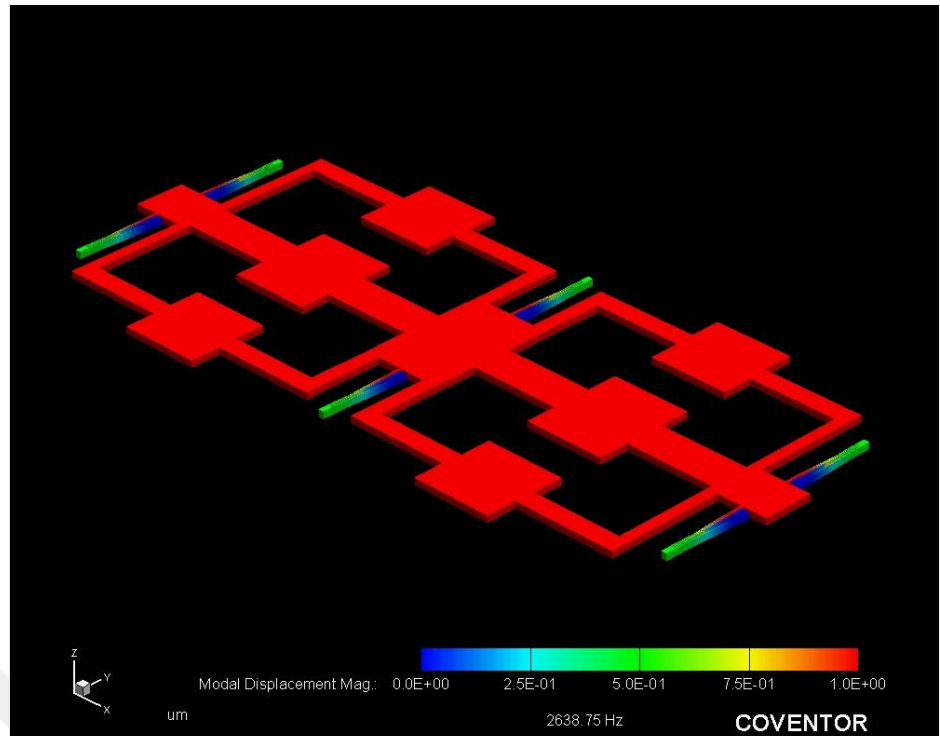
| Design Parameters | | | |
|------------------------------|----------------------|--------------------------------|-----------------------|
| Cell Width (μm) | 3690 | Spring Length (μm) | 355 |
| Cell Length (μm) | 2250 | Spring Width (μm) | 4 |
| Number of Fingers | 348 | Number of Springs | 6 |
| Finger Length (μm) | 155×10^{-6} | Cap.Gap (μm) | 2 |
| Finger Width (μm) | 7 | Cap. anti-gap (μm) | 7 |
| Proof Mass (kg) | 206×10^{-9} | Struc. Thickness (μm) | 35 |
| Performance Parameters | | | |
| Spring Constant (N/m) | 50.8 | Rest Cap. (pF) | 10.4 |
| Damping (kg/s) | 9.1×10^{-3} | Sensitivity (F/m) | 3.71×10^{-6} |
| Res. Freq (Hz). | 2495 | Range @ 5V (g) | 11.4 |
| Quality Factor | 0.35 | Brownian Noise (μg/√Hz) | 5.73 |

Table 3.35: The comparison of the hand calculation and the simulation result for the lateral accelerometer design-3.

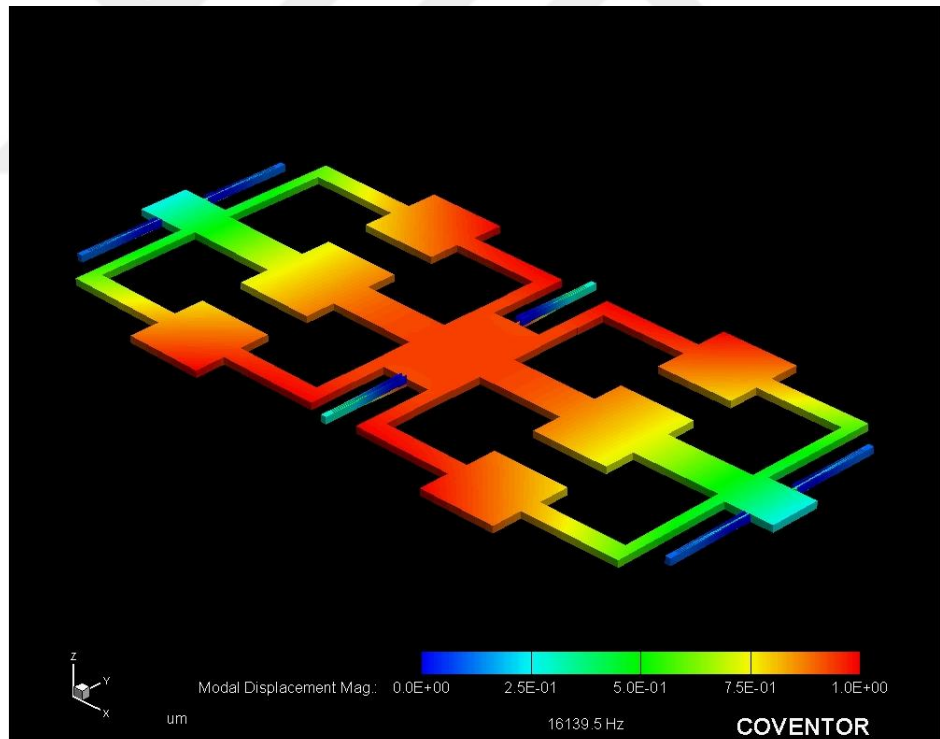
| Lateral design-3 | Hand calculations | Simulation results |
|---------------------------------|-----------------------|-----------------------|
| Proof mass (kg) | 2.06×10^{-7} | 2.05×10^{-7} |
| Resonance frequency (Hz) | 2495 | 2639 |

Table 3.36: Simulation mode analysis results of the lateral accelerometer design-3.

| Mode domain | FEM Simulation results | |
|-------------|------------------------|-----------------------|
| | Frequency (Hz) | Generalized mass (kg) |
| 1 | 2639 | 2.06×10^{-7} |
| 2 | 16140 | 1.38×10^{-7} |
| 3 | 16436 | 5.47×10^{-8} |
| 4 | 22246 | 8.51×10^{-8} |
| 5 | 27865 | 4.30×10^{-8} |



(a)



(b)

Figure 3.23: The first and the second mode of the lateral accelerometer design-3 for the second fabrication mask set.

3.2.2.4. Vertical Accelerometer Design-1

The crab-legs structure is selected to provide the motion to the proof mass in the z axis direction. Instead of capacitive fingers, capacitive electrodes are placed not only the bottom but also the top side of the vertical accelerometer, where the capacitive gap is determined as 2μ . The effect of the fringing field is not taken into consideration during the conceptual design of the vertical accelerometer. Therefore, it is expected that the rest capacitance value of the vertical accelerometer design-1 is slightly higher than its calculated value. Furthermore, there are perforation holes on the proof mass of the accelerometer. The main aim of using perforation holes is to decrease not only the damping coefficient but also the mass of the proof mass. It is expected that the Brownian noise is also low as a result of damping coefficient. Figure 3.24 shows the vertical accelerometer design-1. Table 3.37 shows the design and performance parameters of the vertical accelerometer design-1. Figure 3.25 shows finite element mode analysis results of the vertical accelerometer design-1 for the second fabrication mask set. Table 3.38 shows the comparison of the hand calculation with simulation results. Table 3.39 shows simulation mode analysis results for the vertical accelerometer design-1

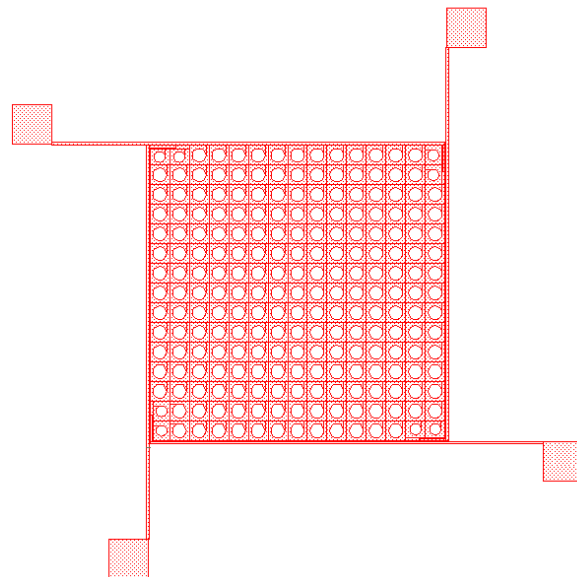


Figure 3.24: The layout of the vertical accelerometer design -1 for the second fabrication mask set.

Table 3.37: Design and performance parameters of vertical accelerometer design-1.

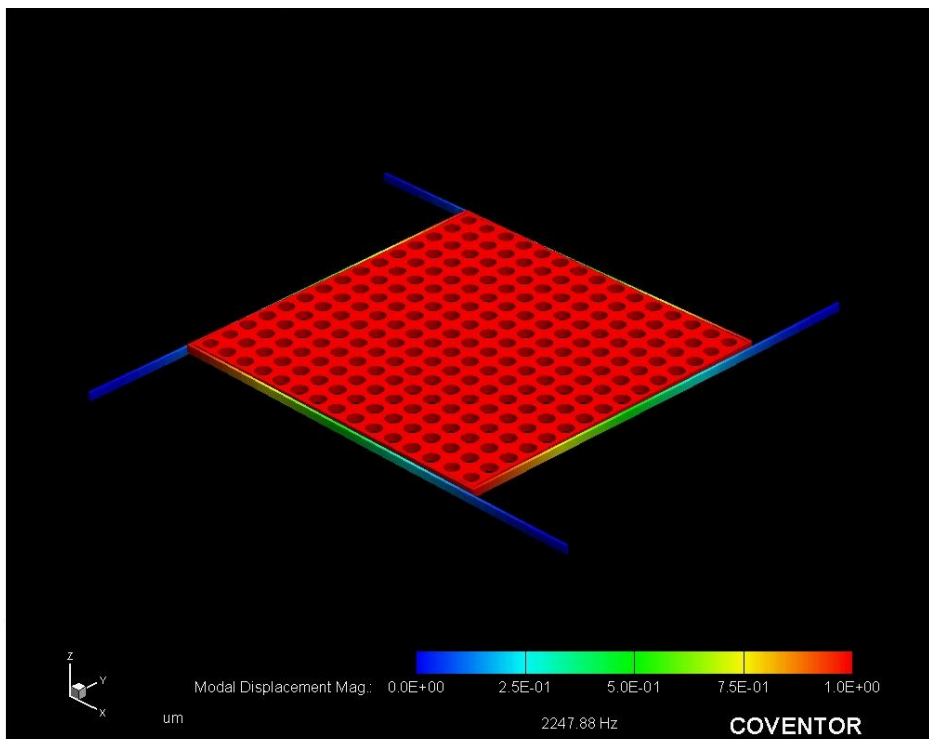
| Design Parameters | | | |
|---|-----------------------|--------------------------------|-----------------------|
| Cell Width (μm) | 2900 | Spring Length(μm) | 2000 |
| Cell Length (μm) | 2900 | Spring Width (μm) | 12 |
| Number of Holes | 225 | Number of Springs | 4 |
| Radius of Holes (μm) | 35 | l_s/l_c | 6.75×10^{-2} |
| Electrodes Area (μm)² | 1500 x 1500 | Capacitive Gap (μm) | 2 |
| Proof Mass (kg) | 113×10^{-9} | Struc. Thick. (μm) | 35 |
| Performance Parameters | | | |
| Spring Constant (N/m) | 43.5 | Rest Cap. (pF) | 6.12 |
| Damping (kg/s) | 10.6×10^{-3} | Sensitivity (F/m) | 3.06×10^{-6} |
| Res.Freq. (Hz) | 2275 | Range @ 5V (g) | 17.3 |
| Quality Factor | 0.15 | Brownian Noise (μg/√Hz) | 11.97 |

Table 3.38: The comparison of the hand calculation and the simulation result for the vertical accelerometer design-1.

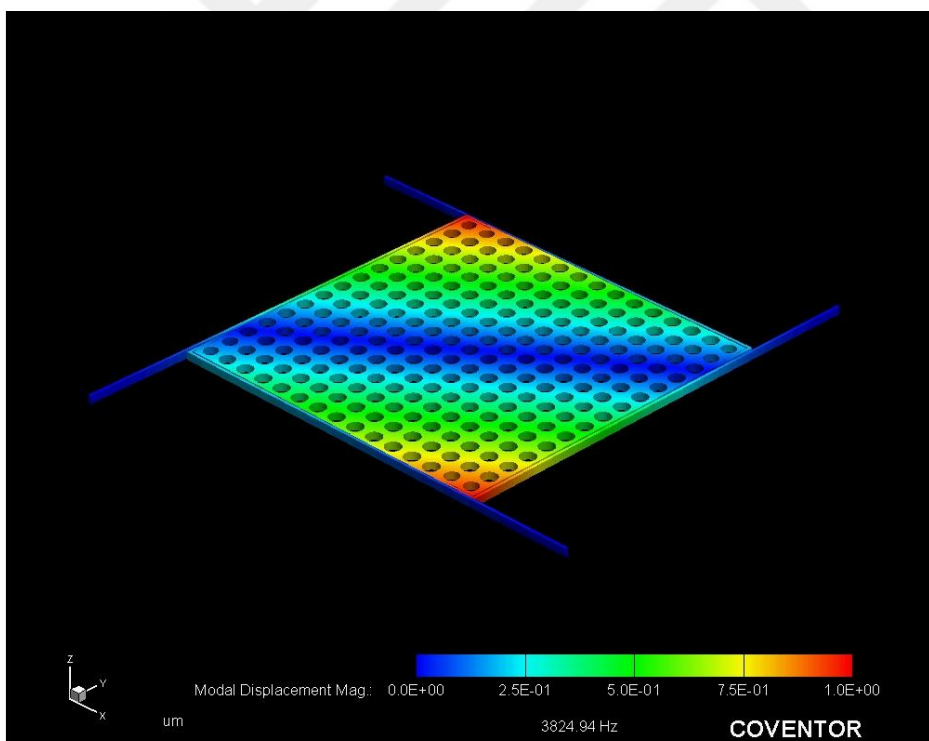
| Vertical design-1 | Hand calculations | Simulation results |
|---------------------------------|-----------------------|-----------------------|
| Proof mass (kg) | 1.13×10^{-7} | 1.16×10^{-7} |
| Resonance frequency (Hz) | 2275 | 2247 |

Table 3.39: Simulation mode analysis results of the vertical accelerometer design-1.

| Mode domain | FEM Simulation results | |
|-------------|------------------------|-----------------------|
| | Frequency (Hz) | Generalized mass (kg) |
| 1 | 2247 | 1.16×10^{-7} |
| 2 | 3824 | 2.04×10^{-8} |
| 3 | 3825 | 2.04×10^{-8} |
| 4 | 18477 | 5.79×10^{-9} |
| 5 | 18478 | 5.79×10^{-9} |



(a)



(b)

Figure 3.25: The mode analysis result of the vertical accelerometer design-1 (a) the first mode (b) the second mode.

3.2.2.5. Vertical Accelerometer Design-2

The vertical accelerometer design-2 has crab-legs structure to provide motion of the vertical accelerometer in the z direction. The capacitance will be formed by using electrodes placed the top and the bottom side of the proof mass, where the capacitive gap is selected as 2μ . The effect of the fringing field is not taken into consideration during the conceptual design of the vertical accelerometer design-2. Therefore, it is expected that the rest capacitance value of the vertical accelerometer design-2 is slightly higher than its calculated value. The spring length is $1500 \mu\text{m}$ for the vertical accelerometer design-2. Therefore, the proof mass of the vertical accelerometer is increased to obtain the same resonance frequency with lateral accelerometers. Furthermore, there are perforation holes on the proof mass of the accelerometer. The main aim of using perforation holes is to decrease not only the damping coefficient but also the mass of the proof mass. It is expected that the Brownian noise is also low as a result of damping coefficient. Figure 3.26 shows the vertical accelerometer design-2. Table 3.40 shows performance and design parameters of the vertical accelerometer design-2. Table 3.41 shows the comparison of the hand calculation with simulation results. Table 3.42 shows simulation mode analysis results for the vertical accelerometer design-2. Figure 3.27 shows finite element mode analysis results of the vertical accelerometer design-2.

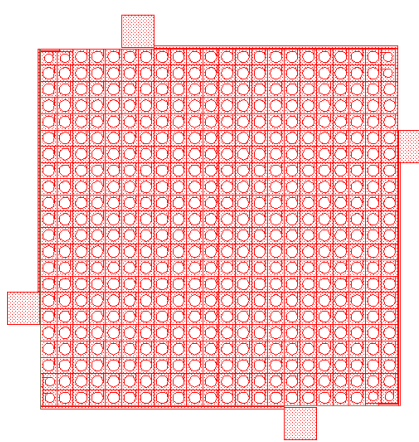


Figure 3.26: The vertical accelerometer design-2 layout for the second fabrication mask set.

Table 3.40: Design and performance parameters of the vertical accelerometer design-2.

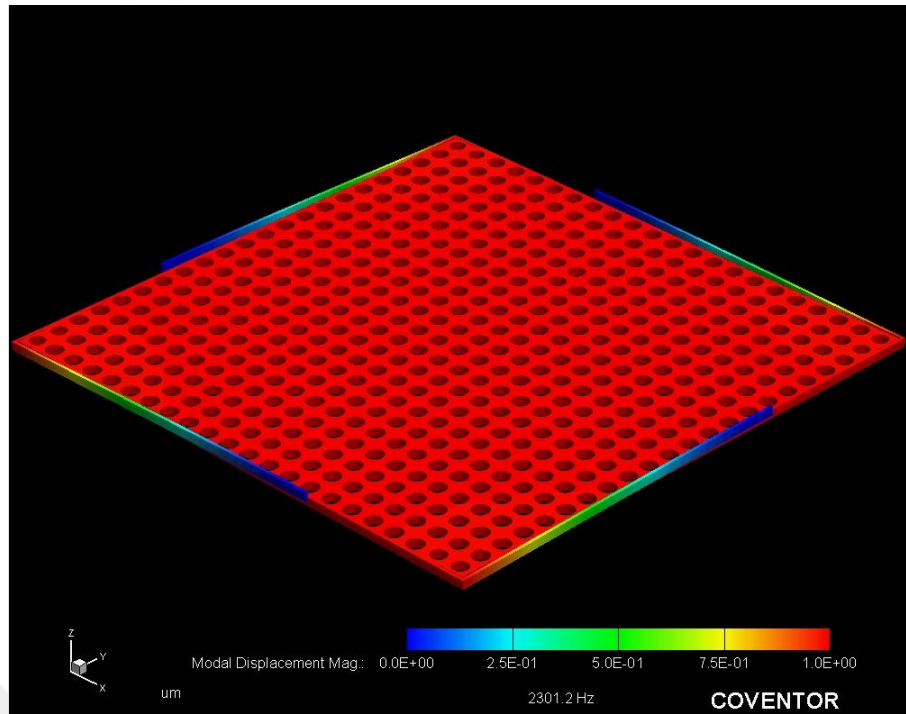
| Design Parameters | | | |
|---|-----------------------|--------------------------------|-----------------------|
| Cell Width (μm) | 2610 | Spring Length(μm) | 1500 |
| Cell Length (μm) | 2670 | Spring Width (μm) | 12 |
| Number of Holes | 484 | Number of Springs | 4 |
| Radius of Holes (μm) | 35 | l_s/l_c | 8.17×10^{-2} |
| Electrodes Area (μm)² | 2200 x 2200 | Capacitive Gap (μm) | 2 |
| Proof Mass (kg) | 243×10^{-9} | Struc. Thick. (μm) | 35 |
| Performance Parameters | | | |
| Spring Constant (N/m) | 49.7 | Rest Cap. (pF) | 13.2 |
| Damping (kg/s) | 1.06×10^{-2} | Sensitivity (F/m) | 6.59×10^{-6} |
| Res.Freq. (Hz) | 2278 | Range @ 5V (g) | 17.3 |
| Quality Factor | 0.32 | Brownian Noise (μg/√Hz) | 5.56 |

Table 3.41: The comparison of the hand calculation and the simulation result for the vertical accelerometer design-2.

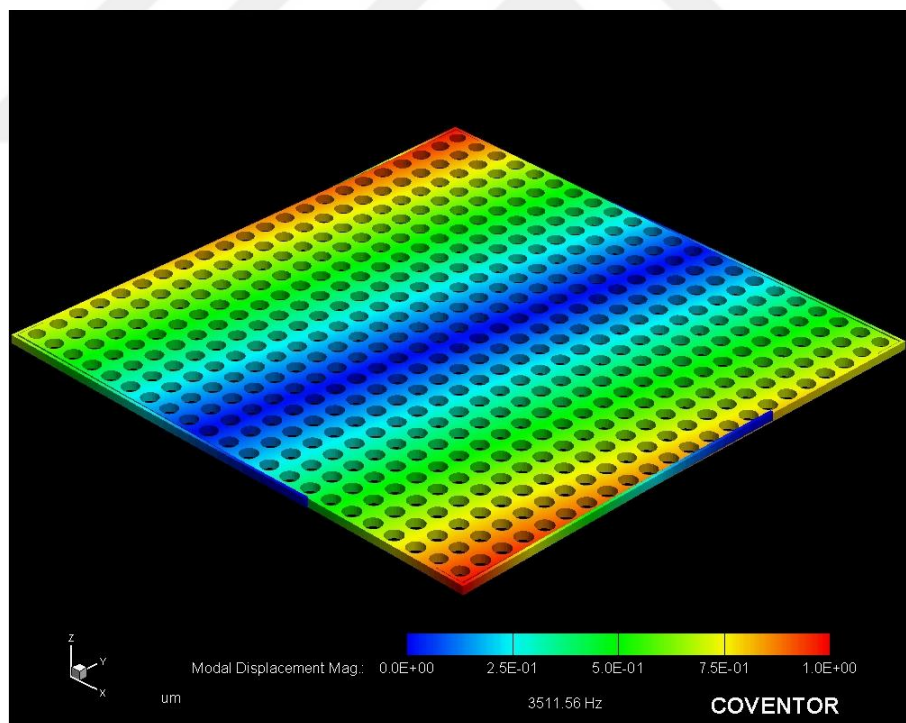
| Vertical design-2 | Hand calculations | Simulation results |
|---------------------------------|-----------------------|-----------------------|
| Proof mass (kg) | 2.43×10^{-7} | 2.45×10^{-7} |
| Resonance Frequency (Hz) | 2278 | 2301 |

Table 3.42: Simulation mode analysis results of the vertical accelerometer design-2.

| Mode Domain | FEM Simulation Results | |
|-------------|------------------------|-----------------------|
| | Frequency (Hz) | Generalized Mass (kg) |
| 1 | 2301 | 2.45×10^{-7} |
| 2 | 3511 | 6.27×10^{-8} |
| 3 | 3511 | 6.27×10^{-8} |
| 4 | 16068 | 4.08×10^{-8} |
| 5 | 16068 | 4.08×10^{-8} |



(a)



(b)

Figure 3.27: The mode analysis result of the vertical accelerometer design-2 (a) the first mode (b) the second mode.

3.2.2.6. Vertical Accelerometer Design-3

The structure of the vertical accelerometer design-3 is based on crab-legs to move the vertical accelerometer in the z direction. The capacitance will be formed by using electrodes placed the top and the bottom side of the proof mass, where the capacitive gap is selected as 2μ . The effect of the fringing field is not taken into consideration during the conceptual design of the vertical accelerometer design-3. Therefore, it is expected that the rest capacitance value of the vertical accelerometer design-3 is slightly higher than its calculated value. The design is similar to the vertical accelerometer design-1. The spring length is $1800 \mu\text{m}$ for the vertical accelerometer design-3. Therefore, the proof mass of the vertical accelerometer is low compared with the vertical accelerometer design-2. The resonance frequency of the vertical accelerometer design-3 is close to that of lateral accelerometers. Perforation holes are used on the proof mass to decrease not only the damping coefficient but also the mass of the proof mass. It is expected that the Brownian noise is also low as a result of damping coefficient. Figure 3.28 shows the layout of the vertical accelerometer design-3. Table 3.43 shows design and performance parameters of the vertical accelerometer design-3. Table 3.44 shows the comparison of the hand calculation with simulation results. Table 3.45 shows simulation mode analysis results for the vertical accelerometer design-3. Figure 3.29 shows finite element mode analysis results of the vertical accelerometer design-3.

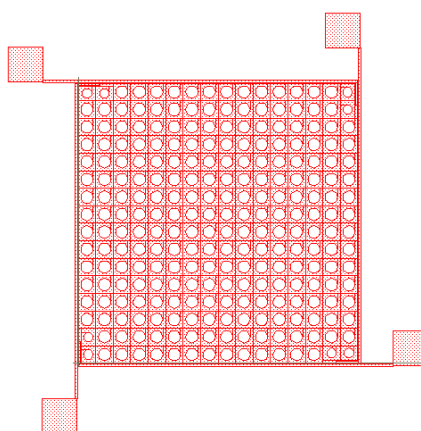


Figure 3.28: The layout of the vertical accelerometer design-3 for the second fabrication mask set.

Table 3.43: Design and performance parameters of vertical accelerometer design-3.

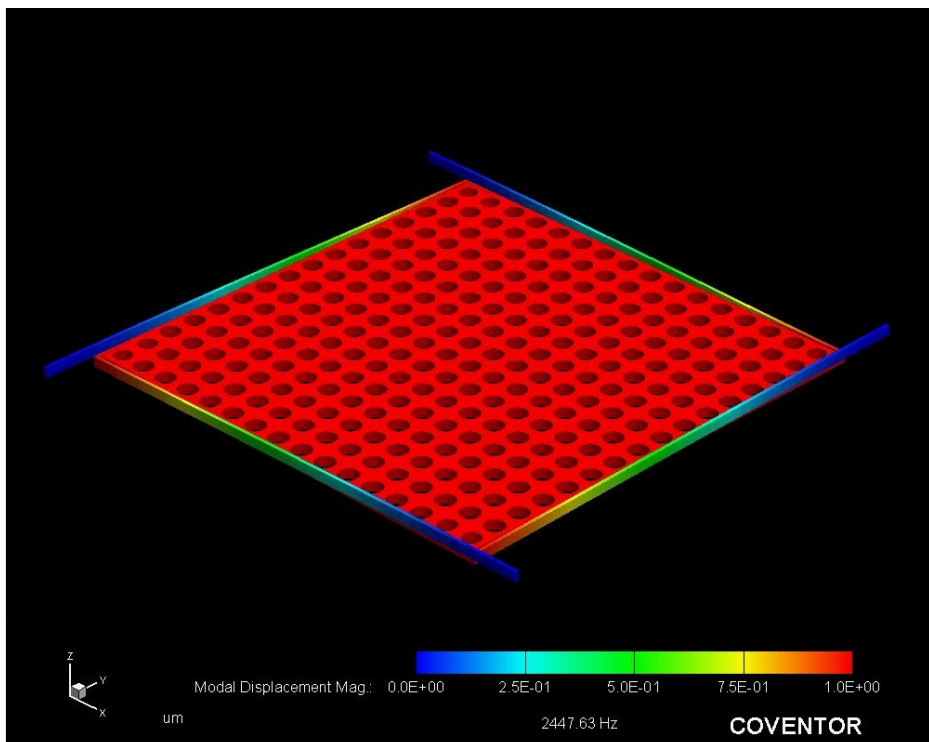
| Design Parameters | | | |
|---|-----------------------|--------------------------------|-----------------------|
| Cell Width (μm) | 2400 | Spring Length(μm) | 1800 |
| Cell Length (μm) | 2400 | Spring Width (μm) | 12 |
| Number of Holes | 256 | Number of Springs | 4 |
| Radius of Holes (μm) | 35 | l_s/l_c | 6.67×10^{-2} |
| Electrodes Area (μm)² | 1600x 1600 | Capacitive Gap (μm) | 2 |
| Proof Mass (kg) | 128×10^{-9} | Struc. Thick. (μm) | 35 |
| Performance Parameters | | | |
| Spring Constant (N/m) | 31.8 | Rest Cap. (pF) | 6.97 |
| Damping (kg/s) | 5.61×10^{-3} | Sensitivity (F/m) | 3.48×10^{-6} |
| Res.Freq. (Hz) | 2505 | Range @ 5V (g) | 17.3 |
| Quality Factor | 0.36 | Brownian Noise (μg/√Hz) | 7.64 |

Table 3.44: The comparison of the hand calculation and the simulation result for the vertical accelerometer design-3.

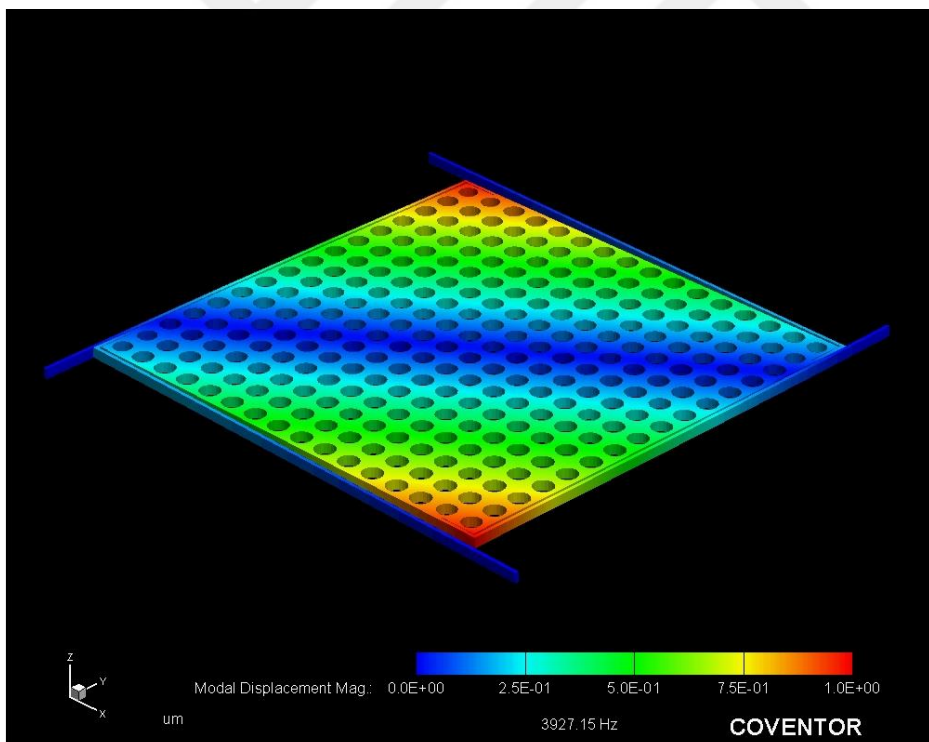
| Vertical design-3 | Hand calculations | Simulation results |
|---------------------------------|-----------------------|-----------------------|
| Proof mass (kg) | 1.28×10^{-7} | 1.31×10^{-7} |
| Resonance frequency (Hz) | 2505 | 2447 |

Table 3.45: Simulation mode analysis results of the vertical accelerometer design-3.

| Mode domain | FEM Simulation results | |
|-------------|------------------------|-----------------------|
| | Frequency (Hz) | Generalized mass (kg) |
| 1 | 2447 | 1.31×10^{-7} |
| 2 | 3927 | 2.29×10^{-8} |
| 3 | 3927 | 2.29×10^{-8} |
| 4 | 19218 | 1.05×10^{-8} |
| 5 | 19221 | 1.05×10^{-8} |



(a)



(b)

Figure 3.29: The mode analysis results of the vertical accelerometer design-3 (a) the first mode (b) the second mode.

3.2.2.7. Vertical Accelerometer Design-4

The vertical accelerometer design-4 is based on crab-legs structure to move the proof mass of the vertical accelerometer in the z direction in the presence of the acceleration. The capacitance will be formed by using electrodes placed the top and the bottom side of the proof mass, where the capacitive gap is selected as 2μ . The effect of the fringing field is not taken into consideration during the conceptual design of the vertical accelerometer design-4. Therefore, it is expected that the rest capacitance value of the vertical accelerometer design-4 is slightly higher than its calculated value. The main difference from previous design is spring width and length. The spring length is decreased to $1000 \mu\text{m}$, and the spring width is set to $4 \mu\text{m}$ to obtain same resonance frequency with lateral accelerometers. Perforation holes are used on the proof mass to decrease not only the damping coefficient but also the mass of the proof mass. It is expected that the Brownian noise is also low as a result of damping coefficient. Figure 3.30 shows the layout of the vertical accelerometer design-4. Table 3.46 show design and performance parameters of the vertical accelerometer design-3. Table 3.47 shows the comparison of the hand calculation with simulation results. Table 3.48 shows simulation mode analysis results for the vertical accelerometer design-3. Figure 3.31 shows finite element mode analysis results of the vertical accelerometer design-3.

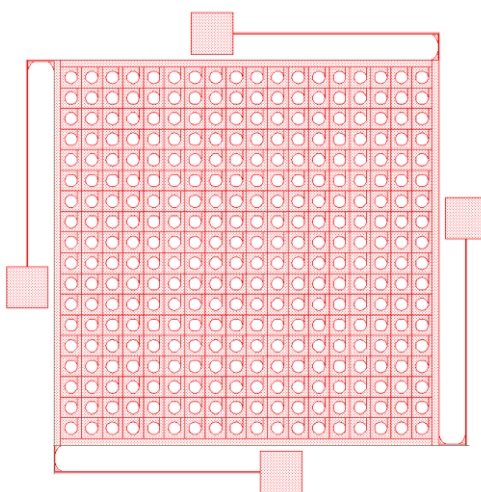


Figure 3.30: The vertical accelerometer design-4 layout for the second fabrication mask set.

Table 3.46: Design and performance parameters of vertical accelerometer design-4.

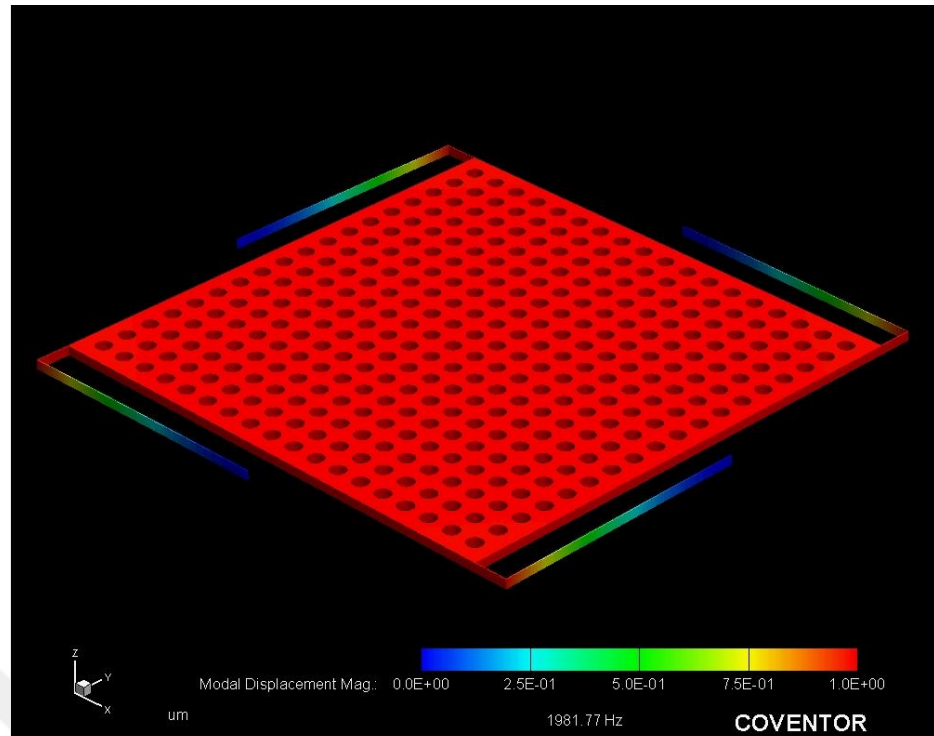
| Design Parameters | | | |
|---|-----------------------|--------------------------------|-----------------------|
| Cell Width (μm) | 2320 | Spring Length(μm) | 1000 |
| Cell Length (μm) | 2270 | Spring Width (μm) | 4 |
| Number of Holes | 324 | Number of Springs | 4 |
| Radius of Holes (μm) | 30 | l_s/l_c | 1.28×10^{-1} |
| Electrodes Area (μm)² | 1865x 1865 | Capacitive Gap (μm) | 2 |
| Proof Mass (kg) | 209×10^{-9} | Struc. Thick. (μm) | 35 |
| Performance Parameters | | | |
| Spring Constant (N/m) | 40.6 | Rest Cap. (pF) | 11.3 |
| Damping (kg/s) | 1.96×10^{-2} | Sensitivity (F/m) | 5.66×10^{-6} |
| Res.Freq. (Hz) | 2221 | Range @ 5V (g) | 17.3 |
| Quality Factor | 0.14 | Brownian Noise (μg/√Hz) | 8.8 |

Table 3.47: The comparison of the hand calculation and the simulation result for the vertical accelerometer design-4.

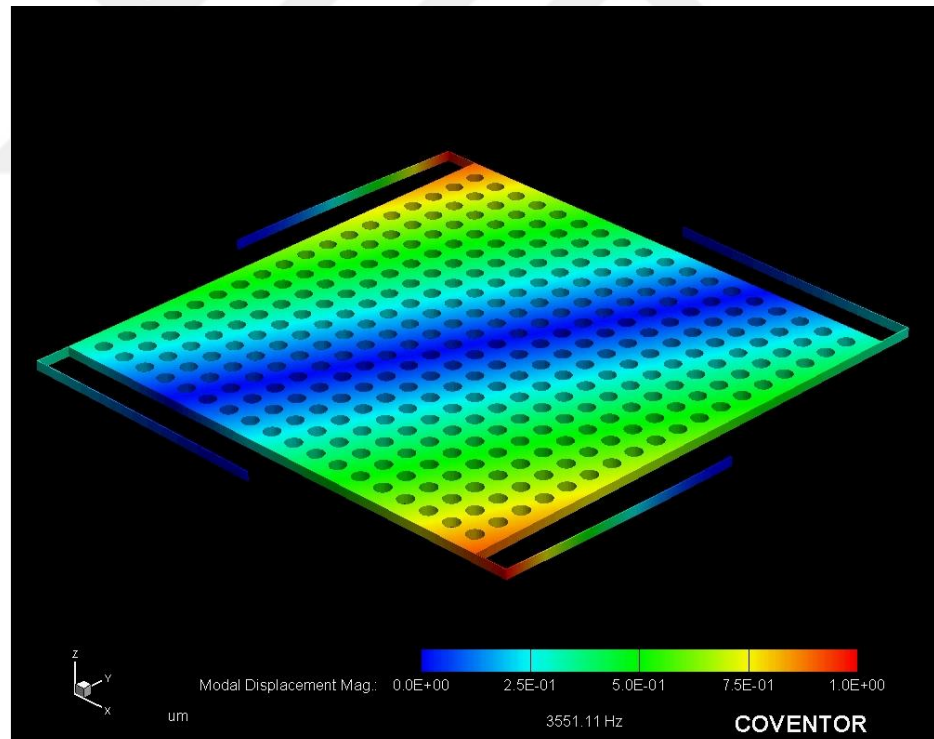
| Vertical design-4 | Hand calculations | Simulation results |
|---------------------------------|-----------------------|-----------------------|
| Proof mass (kg) | 2.09×10^{-7} | 2.08×10^{-7} |
| Resonance frequency (Hz) | 2221 | 1981 |

Table 3.48: Simulation mode analysis results of the vertical accelerometer design-4.

| Mode domain | FEM Simulation results | |
|-------------|------------------------|-----------------------|
| | Frequency (Hz) | Generalized mass (kg) |
| 1 | 1981 | 2.08×10^{-7} |
| 2 | 3551 | 3.42×10^{-8} |
| 3 | 3551 | 3.42×10^{-8} |
| 4 | 3783 | 8.66×10^{-8} |
| 5 | 3783 | 8.66×10^{-8} |



(a)



(b)

Figure 3.31: The mode analysis results of the vertical accelerometer design-4 (a) the first mode (b) the second mode.

3.2.2.8. Vertical Accelerometer Design-5

The vertical accelerometer design-5 has same proof mass with the vertical accelerometer design-4. The main difference is the spring width which is equal to 20 μm . The vertical accelerometer resonance frequency is high compared with other vertical accelerometer designs. Figure 3.32 shows the layout of the vertical accelerometer design-5. Table 3.49 show design and performance parameters of the vertical accelerometer design-5. Table 3.50 shows the comparison of the hand calculation and the simulation result. Table 3.51 shows simulation mode analysis results for the vertical accelerometer design-5. Figure 3.33 shows finite element mode analysis results of the vertical accelerometer design-5.

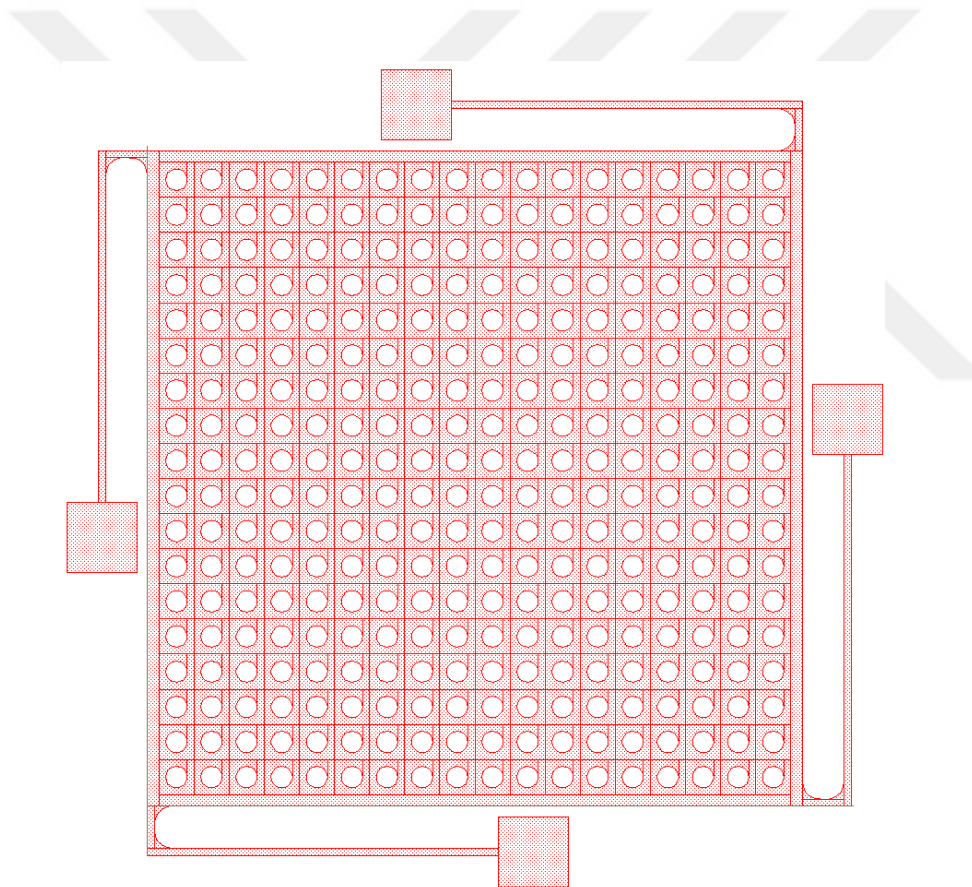


Figure 3.32: The vertical accelerometer design-5 layout for the second mask set.

Table 3.49: Design and performance parameters of vertical accelerometer design-5.

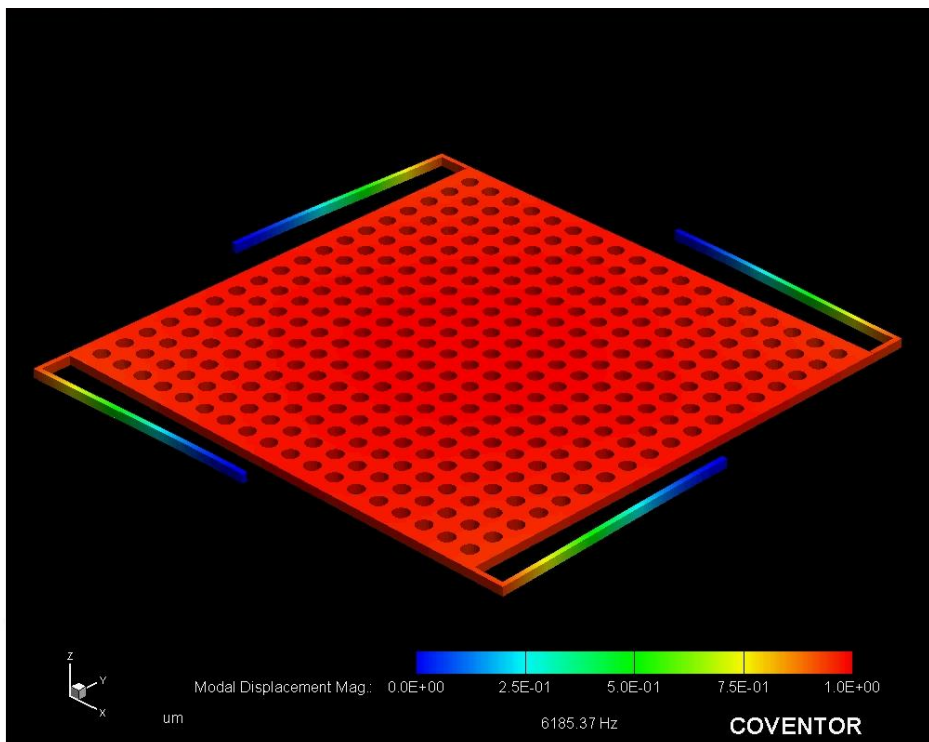
| Design Parameters | | | |
|---|-----------------------|--------------------------------|-----------------------|
| Cell Width (μm) | 2320 | Spring Length(μm) | 1000 |
| Cell Length (μm) | 2270 | Spring Width (μm) | 20 |
| Number of Holes | 324 | Number of Springs | 4 |
| Radius of Holes (μm) | 30 | l_s/l_c | 1.2×10^{-1} |
| Electrodes Area (μm)² | 1865x 1865 | Capacitive Gap (μm) | 2 |
| Proof Mass (kg) | 209×10^{-9} | Struc. Thick. (μm) | 35 |
| Performance Parameters | | | |
| Spring Constant (N/m) | 249 | Rest Cap. (pF) | 11.3 |
| Damping (kg/s) | 1.96×10^{-2} | Sensitivity (F/m) | 5.66×10^{-6} |
| Res.Freq. (Hz) | 5496 | Range @ 5V (g) | 17.3 |
| Quality Factor | 0.36 | Brownian Noise (μg/√Hz) | 8.8 |

Table 3.50: The comparison of the hand calculation and the simulation result for the vertical accelerometer design-5

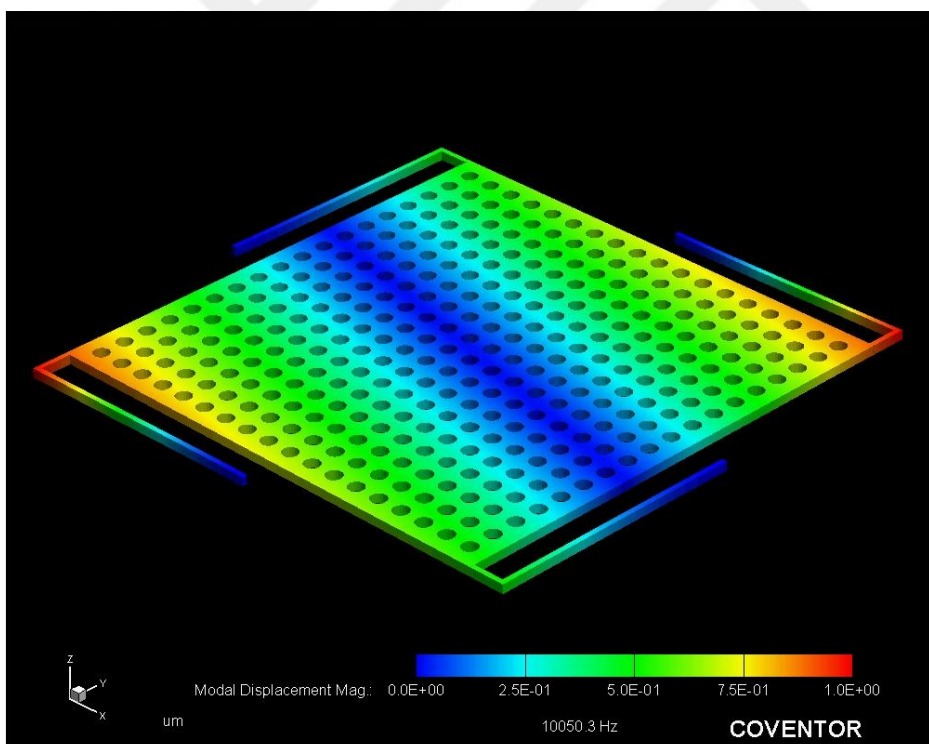
| Vertical design-5 | Hand Calculations | Simulation Results |
|---------------------------------|-----------------------|-----------------------|
| Proof mass (kg) | 2.09×10^{-7} | 2.04×10^{-7} |
| Resonance Frequency (Hz) | 5496 | 6185 |

Table 3.51: Simulation mode analysis results of the vertical accelerometer design-5.

| Mode Domain | FEM Simulation results | |
|-------------|------------------------|-----------------------|
| | Frequency (Hz) | Generalized mass (kg) |
| 1 | 6185 | 2.04×10^{-7} |
| 2 | 10050 | 4.26×10^{-8} |
| 3 | 10053 | 4.26×10^{-8} |
| 4 | 37047 | 1.15×10^{-7} |
| 5 | 37156 | 1.14×10^{-7} |



(a)



(b)

Figure 3.33: The mode analysis results of the vertical accelerometer design-5 (a) the first mode (b) the second mode.

3.3. Three Axis Accelerometer Design

The three-axis accelerometer is formed by implementing the lateral and the vertical accelerometer in a same die. Each lateral accelerometer is combined with different design of the vertical accelerometer. Table 3.52 and Table 3.53 show the summarization of design and performance parameters of three-axis accelerometers. There are different three-axis accelerometer dies are formed by integrating the lateral and the vertical accelerometer in a same die. Figure 3.34 shows the layout of some of them.

3.4. Summary of the Chapter

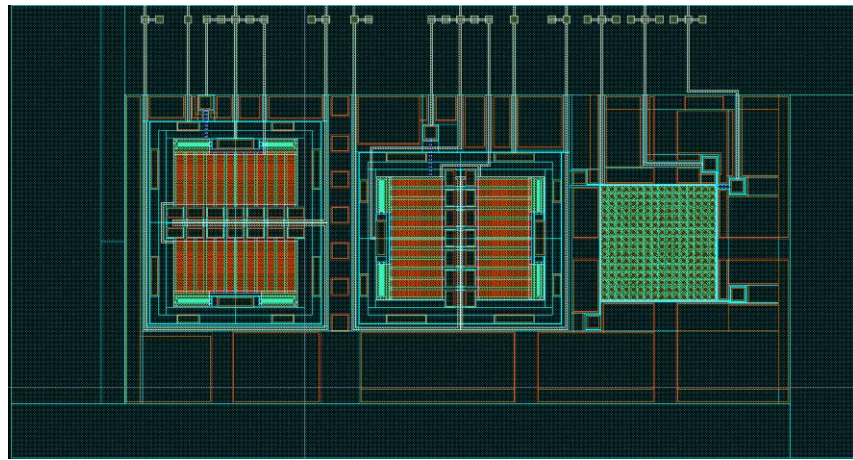
Design and performance parameters of lateral and vertical axis accelerometer designs are comprehensively given in this chapter. The design verification of the lateral and vertical axis accelerometer is performed by using Coventorware simulation tool. Totally four different lateral axis accelerometers and ten different vertical axis accelerometer designs are combined for designing of the three-axis accelerometer.

Table 3.52: Summarization of design and performance parameters of the lateral accelerometer and the vertical accelerometer for mask set1.

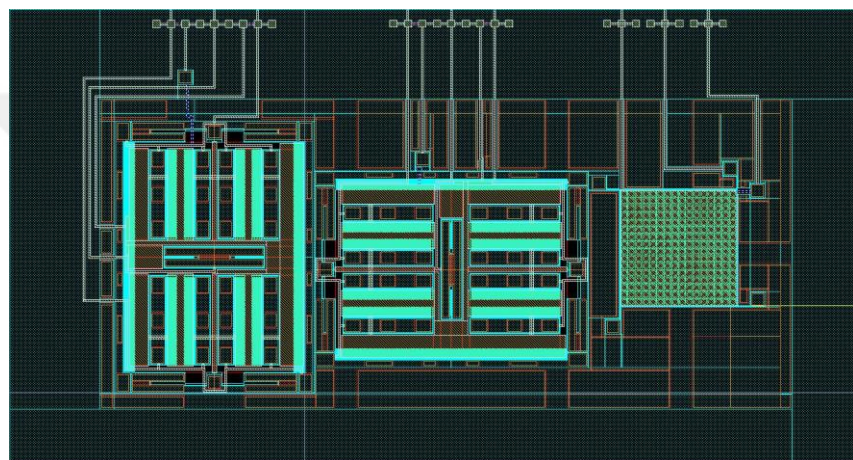
| Parameters | Lateral Accelerometers | | Vertical Accelerometers | | | | | |
|---|------------------------|------------------------|-------------------------|------------------------|------------------------|------------------------|------------------------|--|
| | Design-1 | Design-1 | Design-2 | Design-3 | Design-4 | Design-5 | Design-6 | |
| Finger Length (μm) | 205 | - | - | - | - | - | - | |
| Finger Width (μm) | 7 | - | - | - | - | - | - | |
| Capacitive Length (μm) | 200 | 1865 | 1865 | 1865 | 1865 | 1865 | 1865 | |
| Capacitive Gap (μm) | 3 | 2 | 2 | 2 | 2 | 2 | 2 | |
| Anti-Gap (μm) | 10 | - | - | - | - | - | - | |
| Spring Length (μm) | 200 | 1000 | 1000 | 1000 | 1000 | 833 | 833 | |
| Spring width (μm) | 7 | 60 | 60 | 20 | 20 | 7 | 7 | |
| Number of Springs | 6 | 4 | 4 | 4 | 4 | 4 | 4 | |
| Spring Constant (N/m) | 1680 | 1266 | 1266 | 249 | 249 | 702 | 702 | |
| Proof Mass Area (μm)² | 2.75 x10 ⁻⁶ | 3.48 x10 ⁻⁶ | 2.56 x10 ⁻⁶ | 3.48 x10 ⁻⁶ | 2.56 x10 ⁻⁶ | 3.48 x10 ⁻⁶ | 2.56 x10 ⁻⁶ | |
| Proof Mass (kg) | 2.24 x10 ⁻⁷ | 2.84 x10 ⁻⁷ | 2.09 x10 ⁻⁷ | 2.84 x10 ⁻⁷ | 2.09 x10 ⁻⁷ | 2.84 x10 ⁻⁷ | 2.09 x10 ⁻⁷ | |
| Number of finger per side | 360 | 1 | 1 | 1 | 1 | 1 | 1 | |
| Resonance Frequency (Hz) | 13776 | 10636 | 12392 | 4717 | 5496 | 7917 | 9225 | |
| Rest capacitance (pF) | 10.5 | 15.4 | 11.3 | 15.4 | 11.3 | 15.4 | 11.3 | |
| Sensitivity (F/m) | 3.76 x10 ⁻⁶ | 7.70 x10 ⁻⁶ | 5.67 x10 ⁻⁶ | 7.70 x10 ⁻⁶ | 5.67 x10 ⁻⁶ | 7.70 x10 ⁻⁶ | 5.67 x10 ⁻⁶ | |
| Range (g) @5V | 6.3 | 17.3 | 17.3 | 17.3 | 17.3 | 17.3 | 17.3 | |
| Quality Factor | 5 | 0.15 | 0.39 | 0.39 | 0.58 | 0.58 | 0.61 | |
| Brownian Noise (μg/√Hz) | 3.62 | 224 | 8.8 | 224 | 8.8 | 224 | 8.8 | |

Table 3.53: Summarization of design and performance parameters of the lateral accelerometer and the vertical accelerometer for mask set 2.

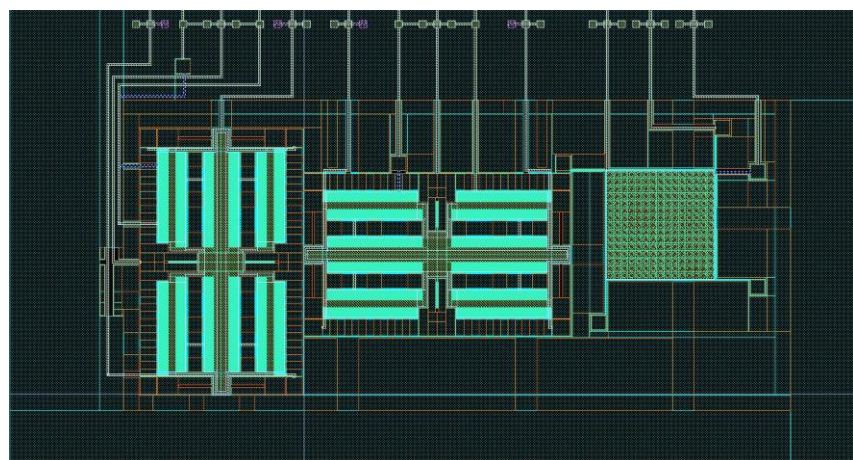
| Parameters | Lateral Accelerometers | | | Vertical Accelerometers | | | | |
|---|------------------------|-----------------------|-----------------------|-------------------------|-----------------------|-----------------------|-----------------------|-----------------------|
| | Design-1 | Design-2 | Design-3 | Design-1 | Design-2 | Design-3 | Design-4 | Design-5 |
| Finger Length (μm) | 155 | 100 | 159 | - | - | - | - | - |
| Finger Width (μm) | 7 | 4 | 7 | - | - | - | - | - |
| Capacitive Length (μm) | 150 | 95 | 152 | 1500 | 1600 | 1600 | 1875 | 1875 |
| Capacitive Gap (μm) | 2 | 3 | 2 | 2 | 2 | 2 | 2 | 2 |
| Anti-Gap (μm) | 7 | 9 | 7 | - | - | - | - | - |
| Spring Length (μm) | 3550 | 435 | 355 | 2000 | 1500 | 1800 | 1000 | 1000 |
| Spring width (μm) | 4 | 4 | 4 | 7 | 7 | 7 | 4 | 20 |
| Number of Springs | 6 | 4 | 6 | 4 | 4 | 4 | 4 | 4 |
| Spring Constant (N/m) | 56.3 | 20.7 | 56.0 | 28 | 38.4 | 38.4 | 40.6 | 249 |
| Proof Mass Area (μm)² | 2.69×10^{-6} | - | 2.53×10^{-6} | 1.61×10^{-6} | 1.57×10^{-6} | 1.57×10^{-6} | 2.56×10^{-6} | 2.56×10^{-6} |
| Proof Mass (kg) | 2.19×10^{-7} | 4.6×10^{-8} | 2.06×10^{-7} | 1.32×10^{-7} | 1.28×10^{-7} | 1.28×10^{-7} | 2.09×10^{-7} | 2.09×10^{-7} |
| Number of finger per side | 352 | 456 | 348 | 1 | 1 | 1 | 1 | 1 |
| Resonance Frequency (Hz) | 2549 | 2630 | 2621 | 2275 | 2278 | 2505 | 2221 | 5496 |
| Rest capacitance (pF) | 10.5 | 5.9 | 10.5 | 7.14 | 6.97 | 6.97 | 11.3 | 11.3 |
| Sensitivity (F/m) | 3.76×10^{-6} | 1.33×10^{-6} | 3.76×10^{-6} | 3.57×10^{-6} | 3.48×10^{-6} | 3.48×10^{-6} | 5.66×10^{-6} | 5.66×10^{-6} |
| Range (g) @5V | 11.1 | 10.9 | 11.4 | 17.3 | 17.3 | 17.3 | 17.3 | 17.3 |
| Quality Factor | 0.57 | 0.38 | 0.35 | 0.15 | 0.32 | 0.36 | 0.14 | 0.36 |
| Brownian Noise (μg/√Hz) | 5.73 | 7.85 | 6.06 | 11.9 | 5.65 | 7.64 | 8.8 | 8.8 |



(a)



(b)



(c)

Figure 3.34: Various three axis accelerometer designs from the fabrication mask set-2. (a) The lateral accelerometer design-2 and the vertical accelerometer design-3
(b) The lateral accelerometer design-2 and the vertical accelerometer design-3
(c) The lateral accelerometer design-3 and the vertical accelerometer design-1.

CHAPTER 4

FABRICATION PROCESS

This chapter presents fabrication processes for the formation of the three axis accelerometer. The proposed fabrication processes are based on the glass-silicon-glass sandwich structure concept. In our facility, the anodic bonding and the Au-Si eutectic bonding technologies are available. Therefore, two methods are proposed for the formation of the glass-silicon-glass sandwich structure: two-step anodic bonding as well as the anodic bonding and the Au-Si eutectic bonding. Figure 4.1 and Figure 4.2 summarize the considered fabrication approaches for the formation of the glass-silicon-glass structure. Two different silicon wafers are used for the formation of glass-silicon-glass structure: a highly doped $<100>$ silicon-germanium (SiGeB) and a $<111>$ single crystal SOI wafers. In the first fabrication approach called double glass modified dissolved wafer process (DGM-DWP), a highly doped silicon-germanium (SiGeB) wafer is used, where the structural layer is 35 μm $<100>$ highly doped region. Two-step anodic is considered for the formation of the glass-silicon-glass fabrication process. Figure 4.3 shows the cross sectional view of the proposed fabrication process. In the second fabrication method called double glass modified silicon on glass (DGM-SOG), a SOI wafer is used, where the structural layer is 35 μm $<111>$ single crystal silicon. Two-step anodic bonding as well as the anodic bonding and then the Au-Si eutectic bonding methods are applied in DGM-SOG.

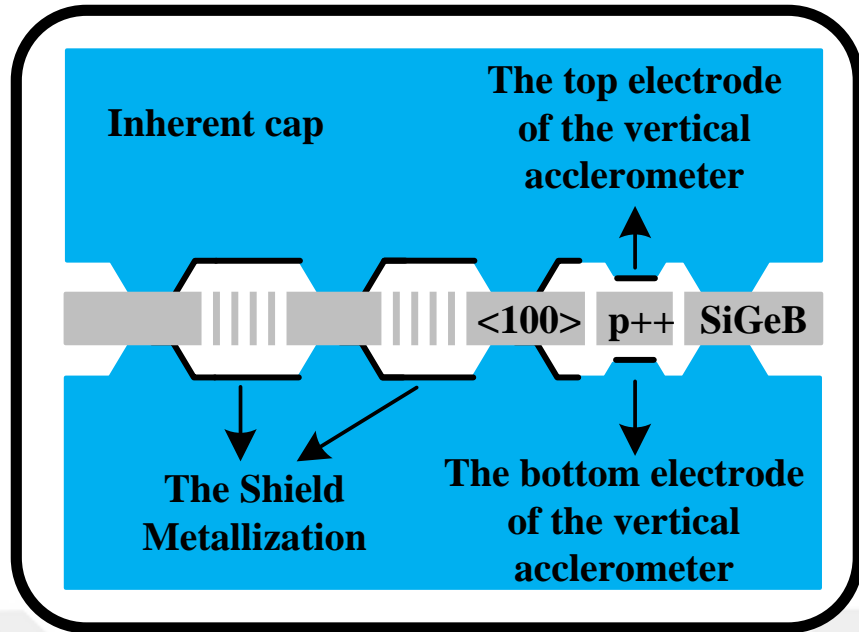


Figure 4.1: The sandwich structure formed by two-step anodic bonding in DGM-DWP.

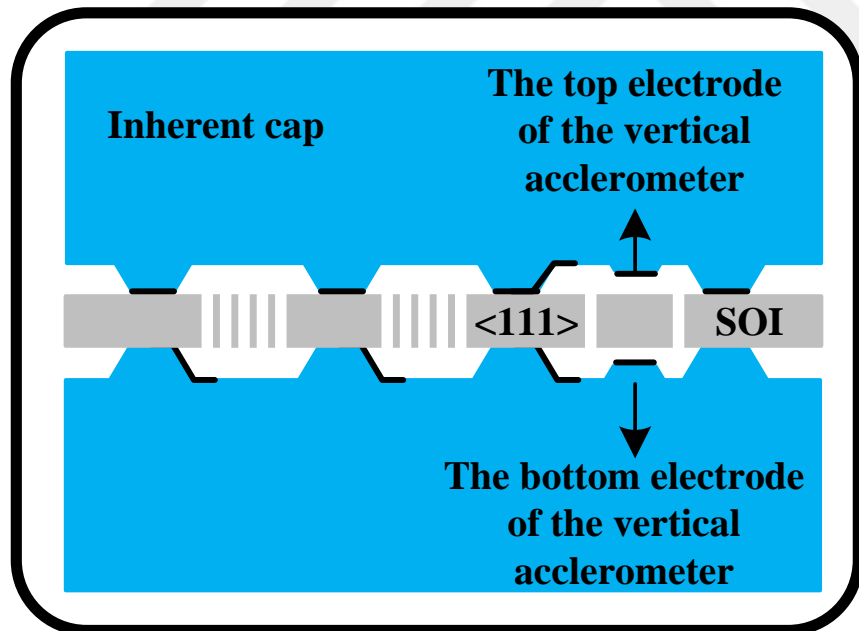


Figure 4.2: The sandwich structure formed by two-step anodic bonding as well as the Au-Si eutectic bonding in DGM-SOG.

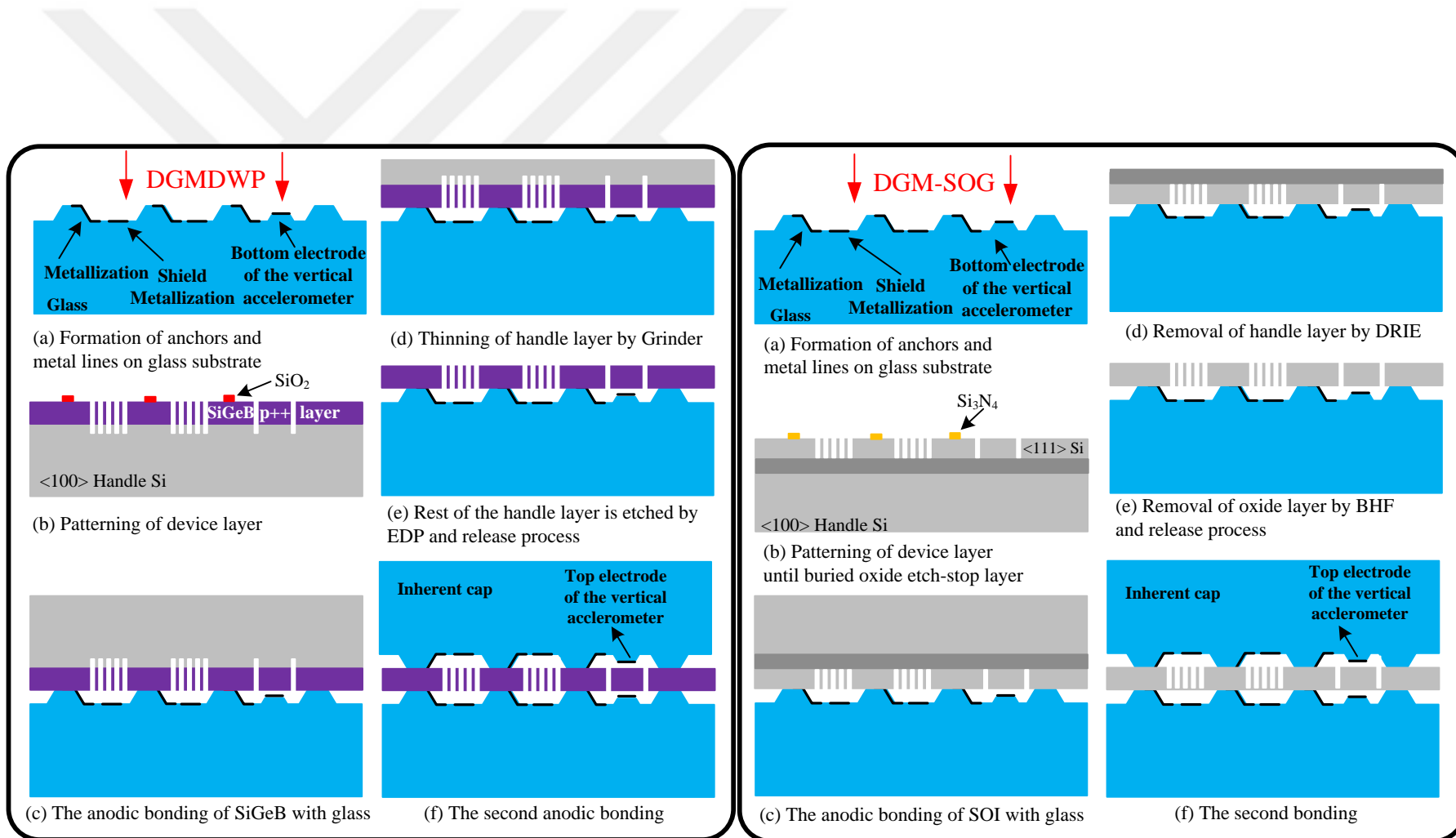


Figure 4.3: The comparison of two alternative fabrication processes for the fabrication MEMS three axis accelerometer.

4.1. Double Glass Modified Dissolved Wafer (DGM-DWP) Fabrication Process and Optimization

4.1.1. Definition of Process Steps

The fabrication process begins with cleaning of glass wafers in the piranha solution for 30 minutes (Figure 4.4).

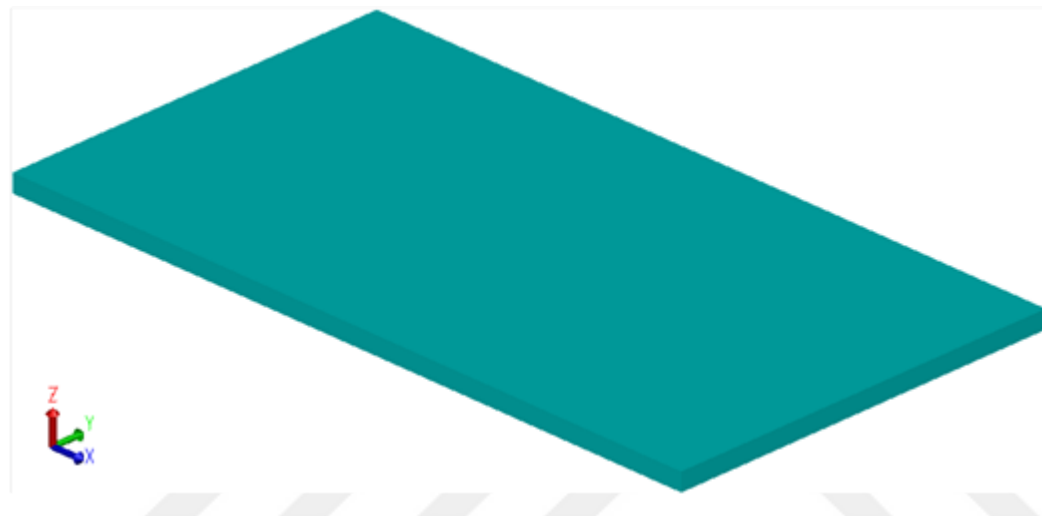


Figure 4.4: The glass wafer is cleaned by using the piranha solution for 30 minutes.

The capacitive gap formation for the vertical accelerometer is the next step. Cleaned glass wafers are etched in the buffered hydrofluoric acid (BHF) solution for 10 minutes. This step is necessary to improve adhesion of Cr/Au layers to the glass wafer by providing a rough surface on the glass wafer. Then, 10/150nm thick Cr/Au layers are deposited by using the sputtering system (Figure 4.5). This layer is also used as a masking layer during the formation of the capacitive gap. Then, the deposited Cr/Au layer is patterned by using lithography steps. Next, wet etchants are used to etch Cr/Au layer (Figure 4.6). Then, glass wafers are etched by using BHF in the desired level (Figure 4.7). This step is also critical as the performance parameters of the vertical accelerometer are mainly based on the vertical capacitive gap. After the formation of the capacitive gap, the photoresist is removed by using wet chemical. Then, 10/150nm thick Cr/Au layers are completely etched in wet etchant

(Figure 4.8). Then, the fabrication process continues with anchor region formation. Glass wafers are again put into BHF solution for 10 minutes to improve adhesion of 10/150nm thick Cr/Au deposition during the sputtering (Figure 4.9). This layer is also used as a masking layer during the formation of the anchor region. Then, Cr/Au layers are patterned with help of lithography steps. Next, Cr/Au layers are etched by using wet etchants (Figure 4.10). Then, glass wafers are etched by using pure hydrofluoric acid (HF) for 85 seconds in the range of 8-12 μm (Figure 4.11). After the formation of the anchor region, the photoresist is removed by using wet chemical. Then, 10/150nm thick Cr/Au layers are etched in wet commercial etchants.

The last step in glass wafers fabrication is the formation of the pad metallization. The pad metallization process starts with putting the glass wafer into BHF for 10 minutes. 10/150nm thick Cr/Au layers are deposited on glass wafers by using the sputtering system (Figure 4.12). Then, 10/150nm thick Cr/Au layers are etched by using wet commercial etchant to form the pad metallization for the desired fabrication method of the glass-silicon-glass multi stack (Figure 4.13 and Figure 4.14). It is noted the shield metallization is also formed in this step to prevent the bonding of the suspended structures to the top glass as the second anodic bonding is considered for the formation of the glass-silicon-glass sandwich structures.

Glass wafers fabrication is completed after the formation of the pad metallization. Now, the fabrication process is continued with the silicon wafer. The silicon wafer is cleaned by using the piranha solution (H_2SO_4 : H_2O_2) (Figure 4.15). Then, the first step is deposition of an insulator layer in the range of 0.2 μm on the silicon (Figure 4.16). Then, the insulator layer is patterned (Figure 4.17), and structures are transferred on the silicon wafer by using Deep Reactive Ion Etching (DRIE) (Figure 4.18). This step is one of the most important part of the fabrication process as many performance parameters of the lateral accelerometer depend on the capacitive finger gap.

The next step is to anodically bond the bottom glass and the silicon wafer. Therefore, the glass and silicon wafer are cleaned by using the piranha solution. Before the anodic bonding, the native oxide layer on the silicon wafer is etched by short BHF

etching. Then, the silicon and the bottom glass wafers are anodically bonded each other (Figure 4.19).

Afterwards, the handle layer of the silicon wafer is etched. During the fabrication process, the highly doped SiGeB and SOI wafers are used. Therefore, this step is different for each wafer. If the highly doped SiGeB wafer is used, the handle layer is thinned by using either mixture of hydrofluoric acid /nitric acid /acetic acid (HNA) wet etchant or the grinder. Then, the rest of the handle layer is etched by using ethylenediamine pyrocatechol (EDP) solution. If the SOI wafer is used during the fabrication process, the handle layer is completely removed until the buried oxide layer by using DRIE (Figure 4.20). For the SOI wafer, the buried oxide layer is etched by using BHF for 24 minutes. Then, the suspended structure is released by putting the bottom glass-silicon stack into the Acetone, the IPA and the Methanol solution for 5 minutes, respectively, and then, the bottom glass-the silicon stack is dried on the hot plate for 5 minutes. Sensors are released after EDP etching with same way mentioned above as there is no buried oxide layer for the SiGeB wafer.

The final step is to form the glass-silicon-glass multi stack by using the two-step anodic bonding (Figure 4.21).

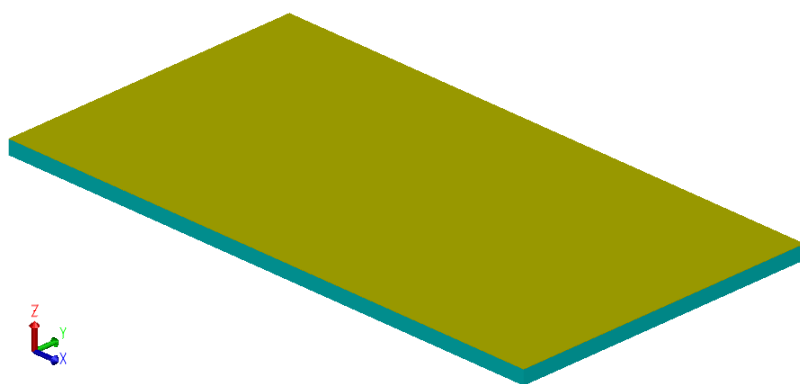


Figure 4.5: Cr/Au layers are deposited in the range of 10/150nm, respectively.

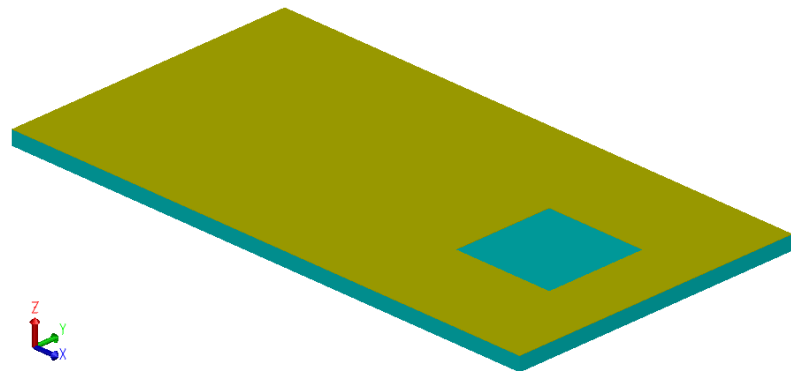


Figure 4.6: Cr/Au layers are patterned and etched.

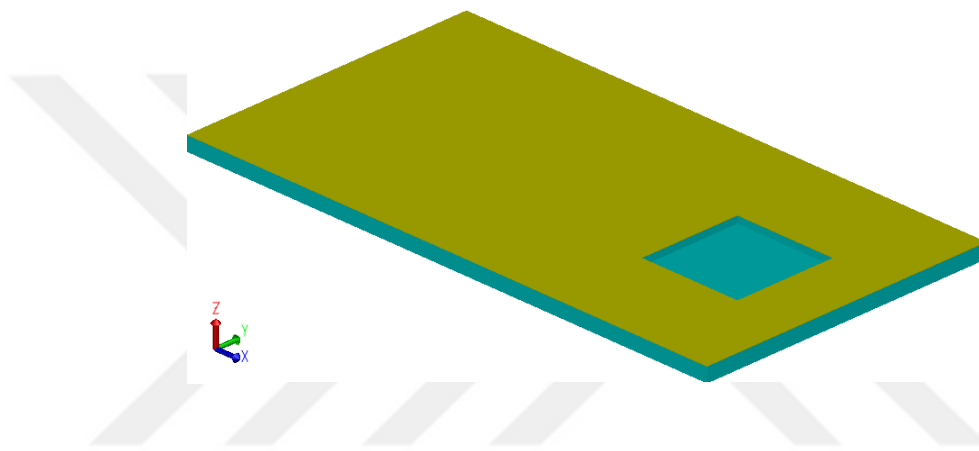


Figure 4.7: Glass wafers are etched in BHF solution for the formation of the vertical gap.

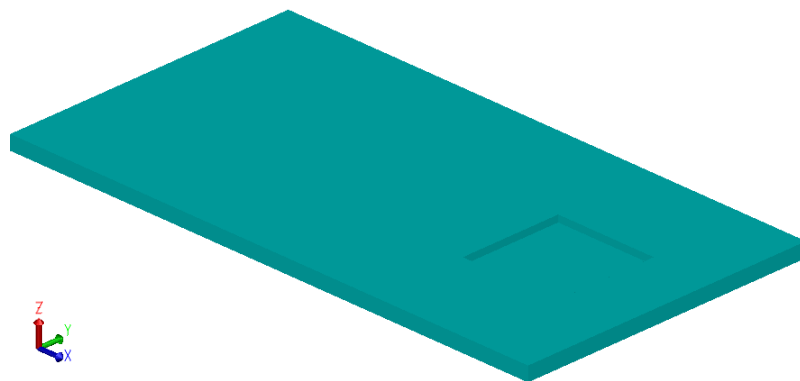


Figure 4.8: 10/150nm thick Cr/Au layers are completely etched after the formation of the vertical gap.

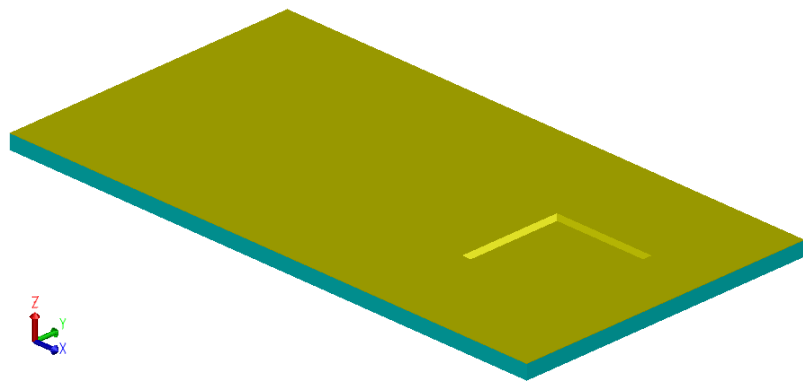


Figure 4.9: Cr/Au layers are deposited in the range of 10/150nm, respectively.

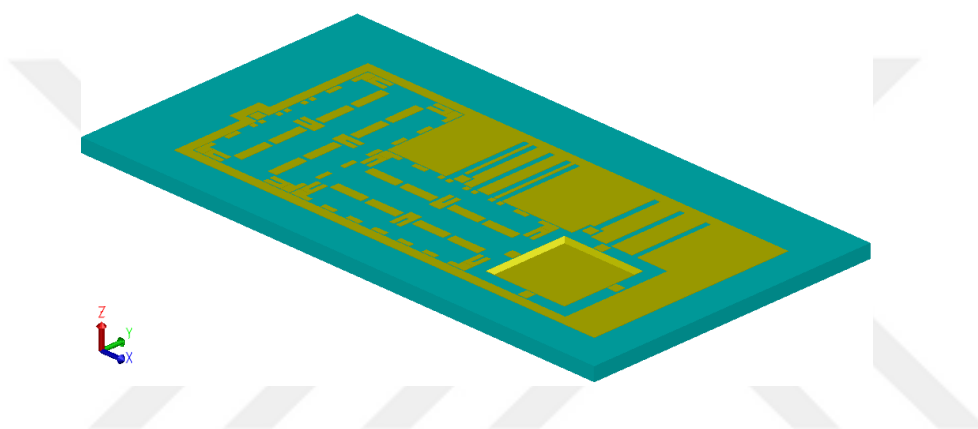


Figure 4.10: Cr/Au layers are patterned and etched.

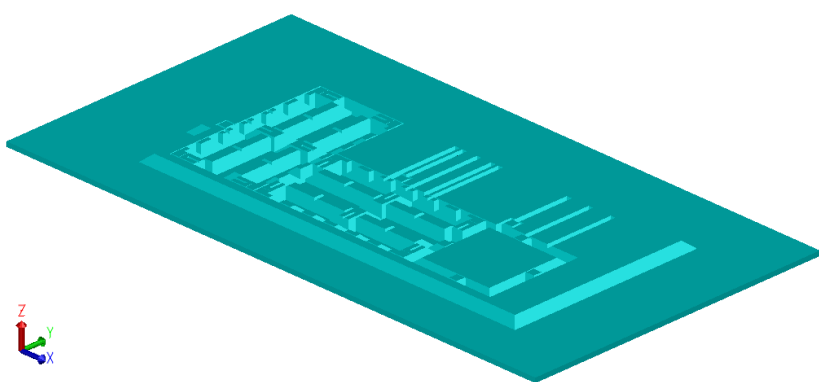


Figure 4.11: The anchor formation is completed by using pure HF.

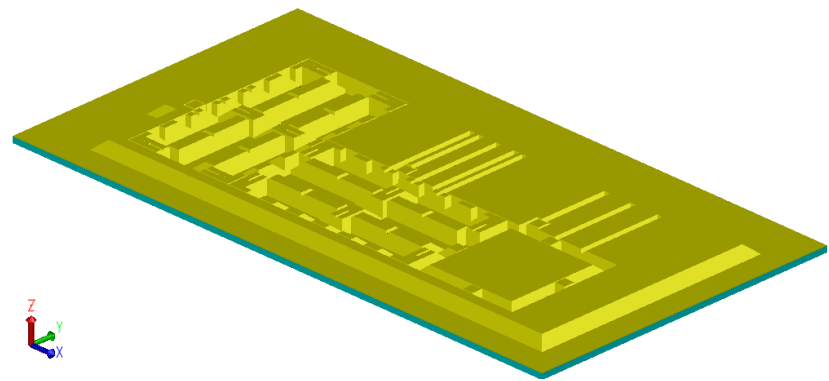


Figure 4.12: Cr/Au layers are deposited on the glass wafers in the range of 10/150 nm, respectively.

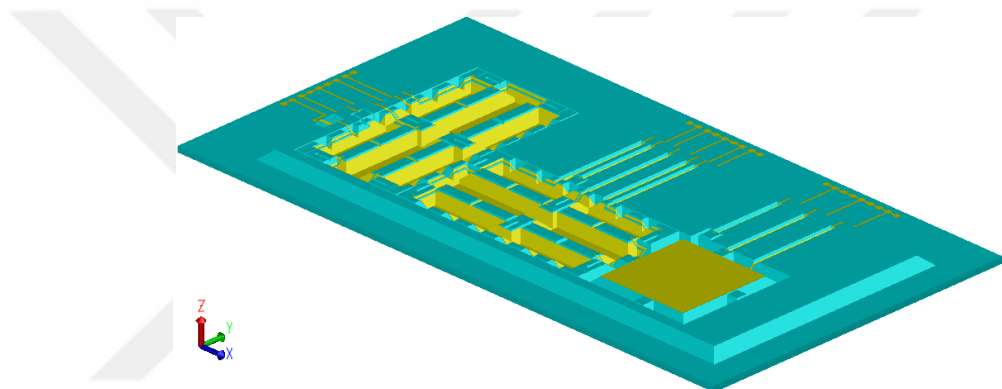


Figure 4.13: The bottom electrode pad metallization.

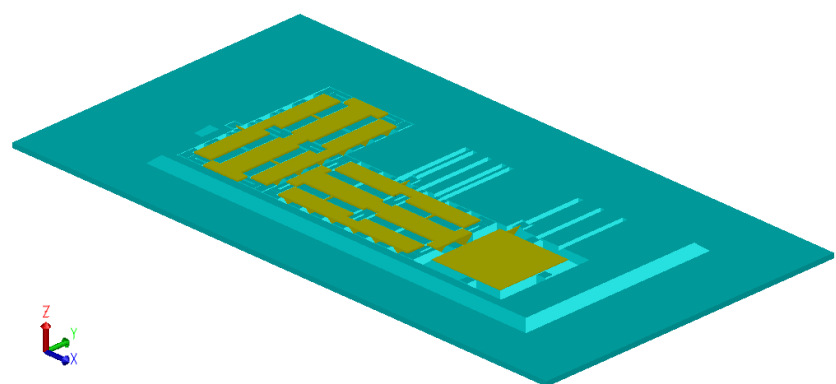


Figure 4.14: The top electrode pad metallization.

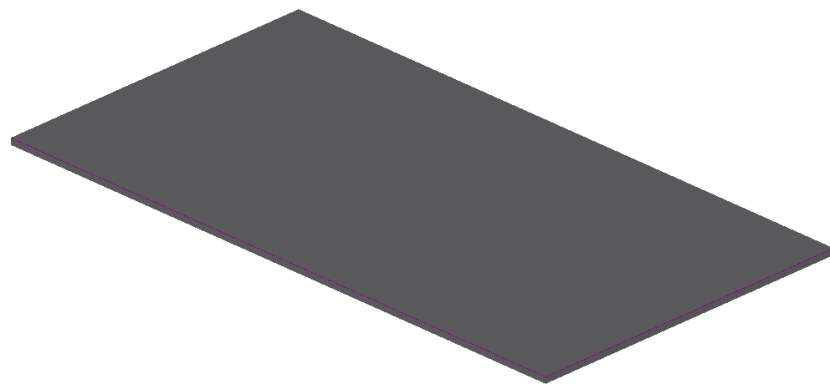


Figure 4.15: The silicon wafer (SiGeB or SOI) is cleaned by using the piranha solution. (H_2SO_4 : H_2O_2).

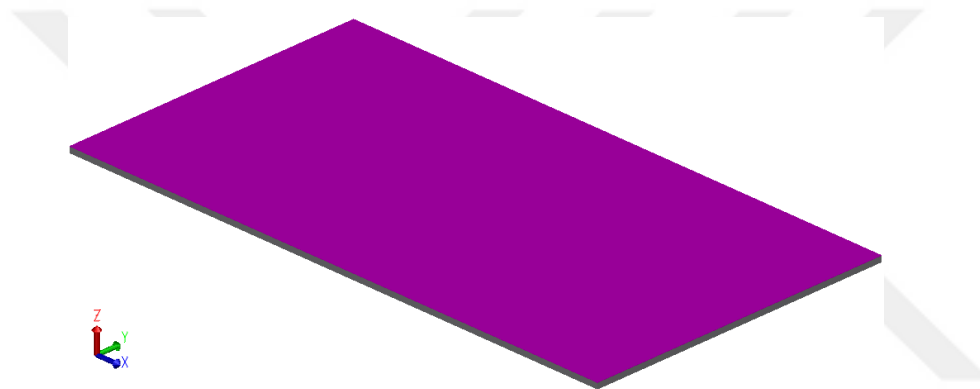


Figure 4.16: An insulator is coated on the SiGeB or SOI wafer.

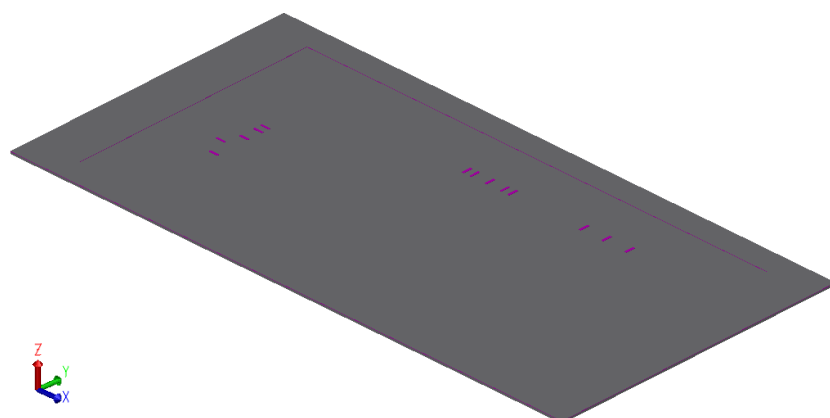


Figure 4.17: Patterning of the insulator layer is performed by using BHF.

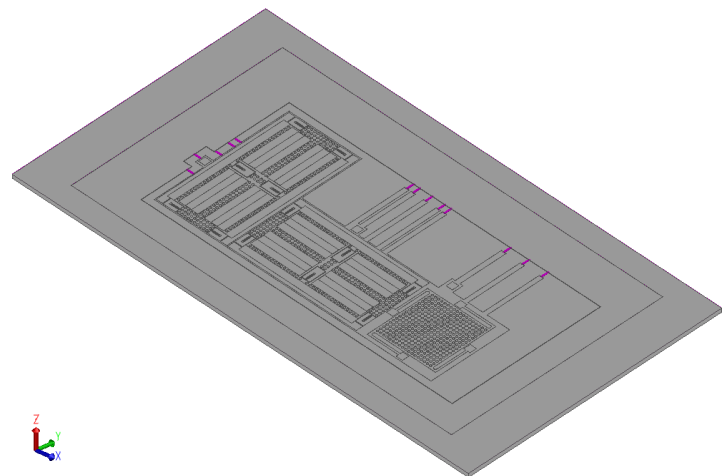


Figure 4.18: Structures are transferred to the silicon wafer by using DRIE.

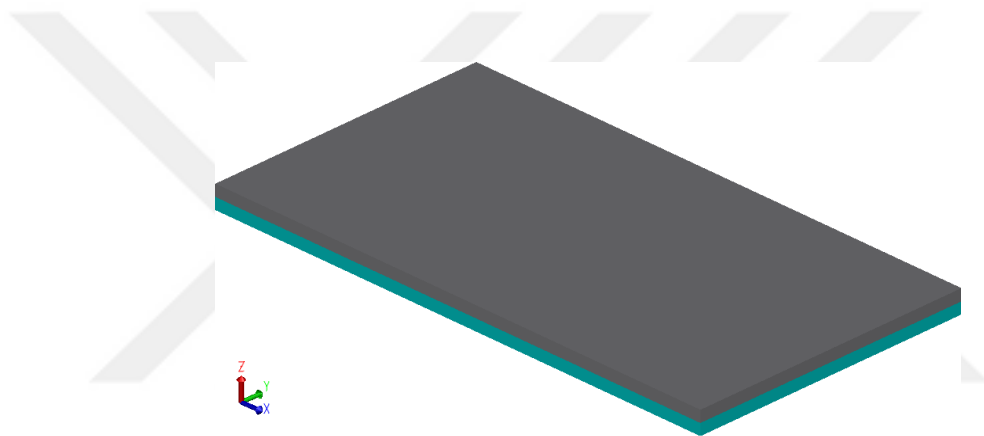


Figure 4.19: The anodic bonding process is performed.

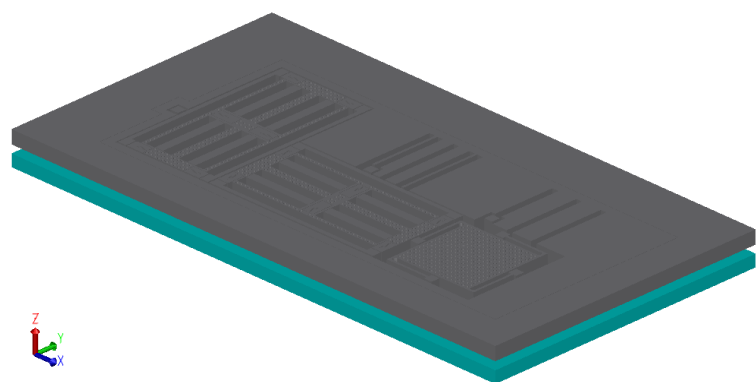


Figure 4.20: The handle layer is removed by using different methods for the SiGeB and the SOI. Then, the devices are released.

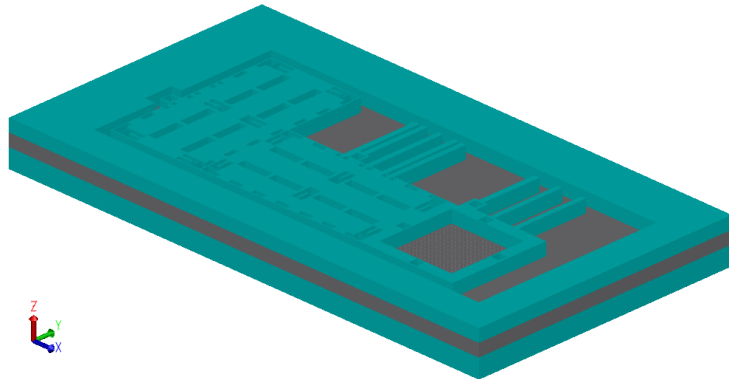


Figure 4.21: The glass-silicon-glass sandwich structure

4.1.2. Vertical Capacitive Gap Optimization

The precise control of the vertical capacitive gap depth is crucial to fabricate the desired vertical accelerometer. The vertical gap optimization process is performed by using dry and wet etch techniques. Firstly, Reactive Ion Etching (RIE) and DRIE are used to reach the desired capacitive gap depth for the vertical accelerometer. The glass wafer is coated by using the photoresist. After patterning of the photoresist, the glass wafer is etched by using RIE. Although the etching of glass is achieved by using RIE, it is observed that the surface roughness is high (Figure 4.22). After the RIE result, the capacitive gap is tried to form by using the DRIE. The glass wafer is prepared in a same way. However, the etch result is similar to that of the RIE result. After 10 minutes the DRIE etch, the capacitive gap is nearly 0.6 μm . However, the etch profile and the surface roughness are not suitable for the formation of the vertical capacitive gap (Figure 4.23).

The uniform surface roughness for the capacitive gap optimization is not provided by using the RIE and DRIE. Therefore, the wet etchant is considered to form the desired capacitive gap depth. There are two possible solutions for the etching of the glass. One of them is to use the pure HF, and the other one is the BHF (HF: NH₄F:1:5) solution. The desired capacitive gap for the vertical accelerometer is 2 μm . The pure HF can be a fast solution to form the capacitive gap, however; it is difficult to precise etching of the vertical capacitive gap in the range of 2 μm . Therefore, the BHF solution is preferred as an etchant for the vertical capacitive gap formation. During

the formation of the vertical gap, the glass wafer is deposited with Cr/Au layers in the range of the 10/150nm. After photolithographic processes, the metal and the photoresist thickness are measured by using the surface profiler. The metal and photoresist thickness is approximately determined as 1.6 μm before starting the glass etching. Then, the glass wafer is etched in the BHF (HF:NH₄F:1:5) solution for 30 minutes. Next, the wafer is removed from the BHF solution, and the vertical capacitive gap and the thickness of metallization as well as the photoresist thickness are measured as 2.5 μm . By subtracting two results with each other and dividing it to etch period, the etch rate can be easily calculated as nearly 30 nm. The vertical capacitive gap is intentionally etched in the range of 2.16 μm after 72 minutes etching period. After the deposition of 10/150nm thick Cr/Au layers for the formation of capacitive electrodes, the gap will approximately be in the range of 2 μm . It is observed in the different fabrication runs that the minimum and maximum etch rate of the BHF (1:5) solution for the pyrex glass wafer is nearly 28 and 33 nm/minute, respectively. Figure 4.24 shows the measurement result of the surface profiler after 72 minutes wet etching. Figure 4.25 shows the capacitive gap pattern on the glass wafer. It is observed that the undercut is nearly 9 μm for 1 μm -depth capacitive gap. After the optimization of the capacitive gap for the vertical accelerometer, the fabrication process continued with the formation of anchor points and the pad metallization steps.

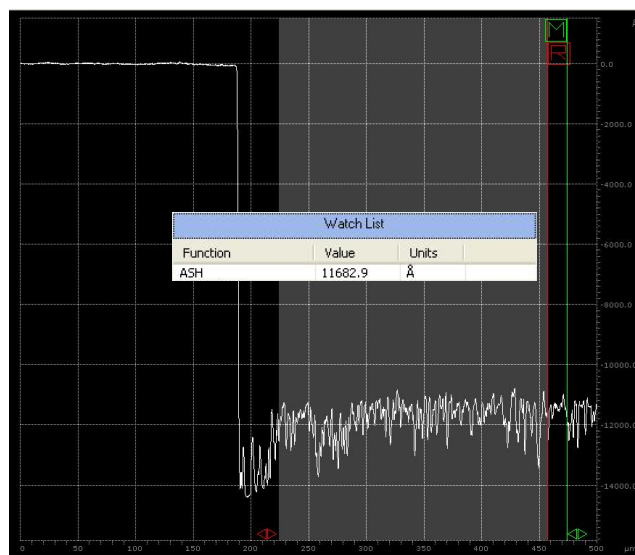


Figure 4.22 The capacitive gap is nearly 1.1 μm after 6 minutes RIE etching.

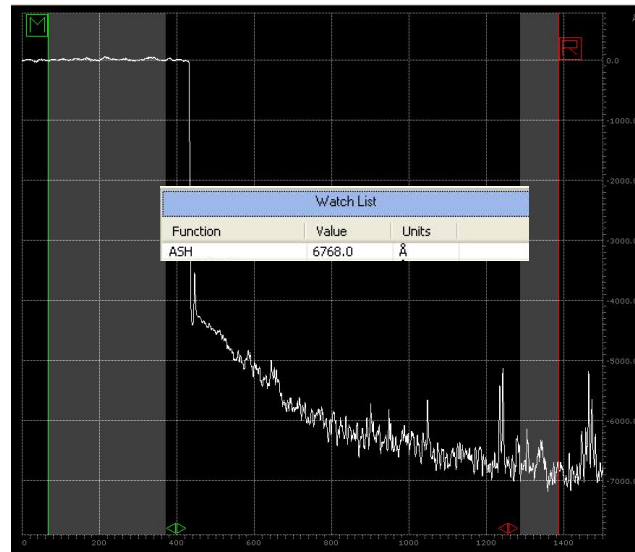


Figure 4.23: The capacitive gap is nearly $0.6 \mu\text{m}$ after 10 minutes DRIE etching. However, the etch profile and the surface roughness are not suitable for the fabrication of the vertical accelerometer.

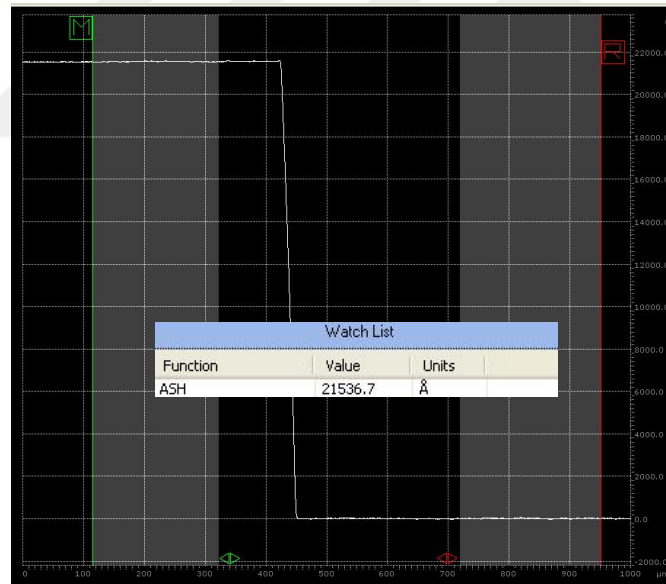


Figure 4.24: The measurement result of the surface profiler result after 72 minutes wet etching.

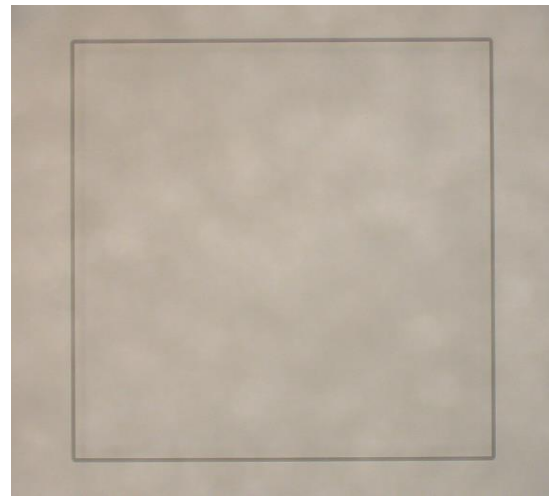


Figure 4.25: The capacitive gap patterned on the glass wafer.

4.1.3. Silicon Wafer Fabrication

4.1.3.1. Deposition of an Insulator Layer on Silicon Wafer

The fabrication of the SiGeB wafer starts with deposition of an insulator layer. This layer prevents the short between the pad metallization and the highly doped silicon region. During the fabrication of the SiGeB wafer, the silicon oxide is used as an insulator layer which is growth on SiGeB wafer by using PECVD in the range of the 0.2 μm . After photolithographic processes, the silicon oxide is patterned by using BHF (HF: NH₄F:1:7) for 2 minutes (Figure 4.26).

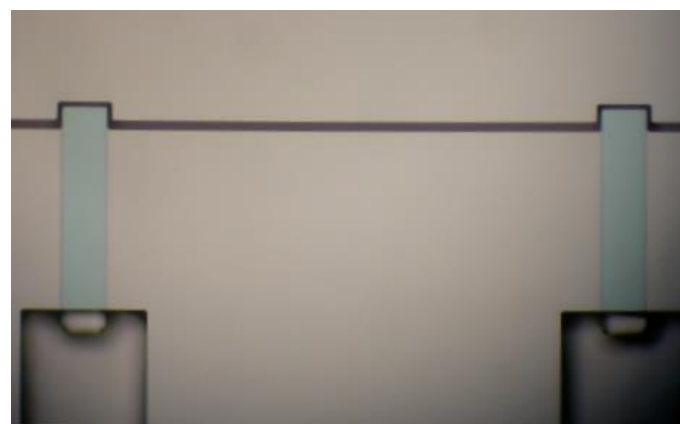


Figure 4.26: The blue region is the patterned silicon oxide on the silicon wafer.

4.1.3.2. DRIE Optimization

After the deposition and the patterning of the insulator layer, the next step is to pattern devices on the SiGeB wafer by using DRIE. As many performance parameters of the lateral accelerometer are based on the capacitive gap among fingers, this step is important. Table 4.1 shows the DRIE recipe used during the fabrication process. Figure 4.27 shows cross-sectional view of the wafer.

Table 4.1: The DRIE recipe used during the fabrication of three axis accelerometer.

| | Etch Step | Passivation step |
|--------------|---|--|
| Step Time | 2.5 s | 1.5 s |
| Gas Flows | SF ₆ : 375 sccm, O ₂ : 35sccm, C ₄ F ₈ : 50 to 0 sccm | C ₄ F ₈ : 250 sccm |
| Pressure | 15 mTorr (1.5s), 30 to 25 mTorr for the rest | 25 mTorr |
| Coil Power | 2200 W | 2200 W |
| Platen Power | 45 to 35 W | 0 |
| Temperature | +10°C | |

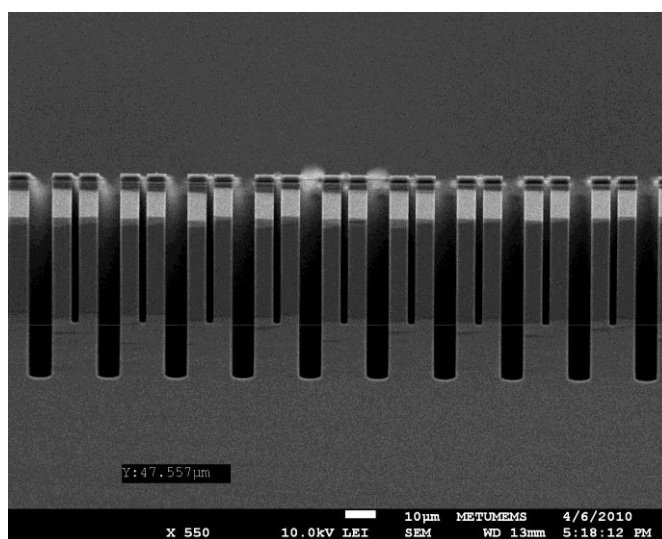


Figure 4.27: Cross-sectional view of the finger regions after DRIE etching.

4.1.4. The First Anodic Bonding Recipe Optimization

The glass wafer and the SiGeB wafer are cleaned in the piranha solution for 10 and 30 minutes, respectively. Then, the SiGeB wafer is put into the BHF solution for 5 seconds to remove the native oxide. The etch time is limited to 5 seconds as the SiGeB is already have the insulator layer. After 5 seconds etching, it is observed that the SiGeB is hydrophobic. Then, the first anodic bonding is performed under the conditions of 1000V and 350°C. Figure 4.28 shows optical images of the bottom glass-SiGeB stack after the first anodic bonding.

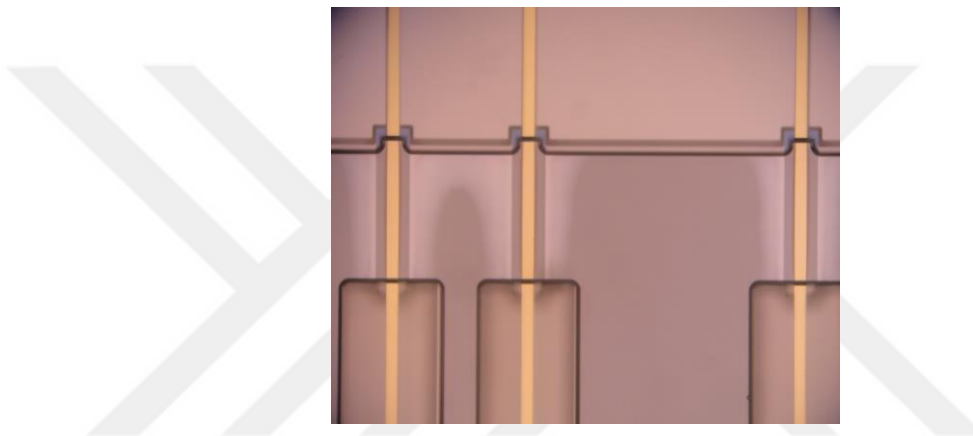


Figure 4.28: The bottom glass and SiGeB wafers are anodically bonded. The wafer is observed from the bottom glass side. The silicon oxide layer, which is used to prevent short between highly doped silicon and pad metallization, causes weak anodic bonding in this region.

4.1.5. Thinning of the Bottom Glass-SiGeB Stack

The next step is to remove the handle layer. The thinning process from 500 μm to 150 μm is performed by using either a mixture of hydrofluoric acid, nitric acid and acidic acid (HNA) solution or the grinder. The rest of the handle layer is removed by using the ethylene diamine pyrocatechol (EDP) solution for three hours. Figure 4.29 shows the bottom glass-the SiGeB wafer after removing of the handle layer.

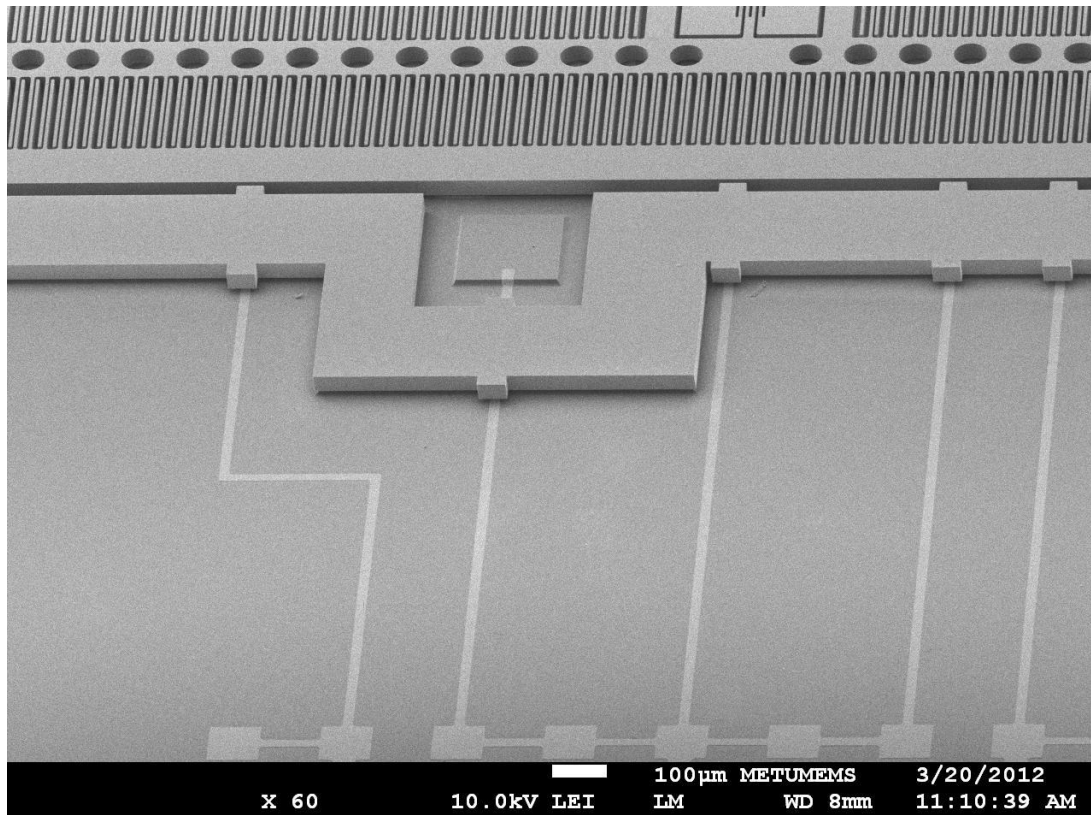


Figure 4.29: An SEM image of the bonded wafer. The short between the pad metallization and the highly doped SiGeB wafer frame is prevented by using the silicon oxide layer.

4.1.6. Two-Electrode Anodic Bonding Optimization

The most important part of the fabrication process is to form the glass-silicon-glass structure without any problem. Although it is possible to fabricate the lateral accelerometers only the bottom glass-silicon stack, it is necessary to form a multi-stack for the fabrication of the vertical capacitive accelerometers. Multi-stack structures can be formed with two-electrode and three-electrode anodic bonding methods, as presented in [65], demonstrating how to bond more than two substrates. The two-electrode method [65] is considered for the fabrication. The detailed investigation about the two-electrode anodic bonding is given in [66]. There are several problem is observed in the fabrication by using the two electrode method. In this section, the problem observed during the fabrication and the solutions is

summarized. Figure 4.30 shows the illustration of the second anodic bonding for the glass-silicon-glass multi-stack. Figure 4.31 shows the results of the first attempt.

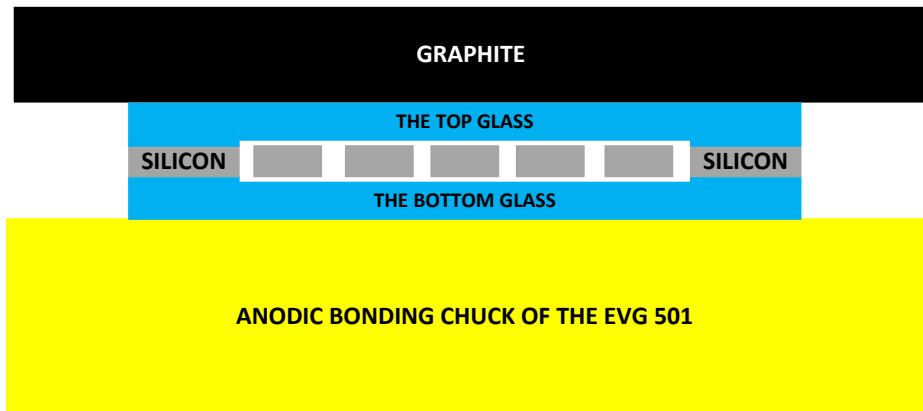


Figure 4.30: The illustration of the two-electrode anodic bonding.

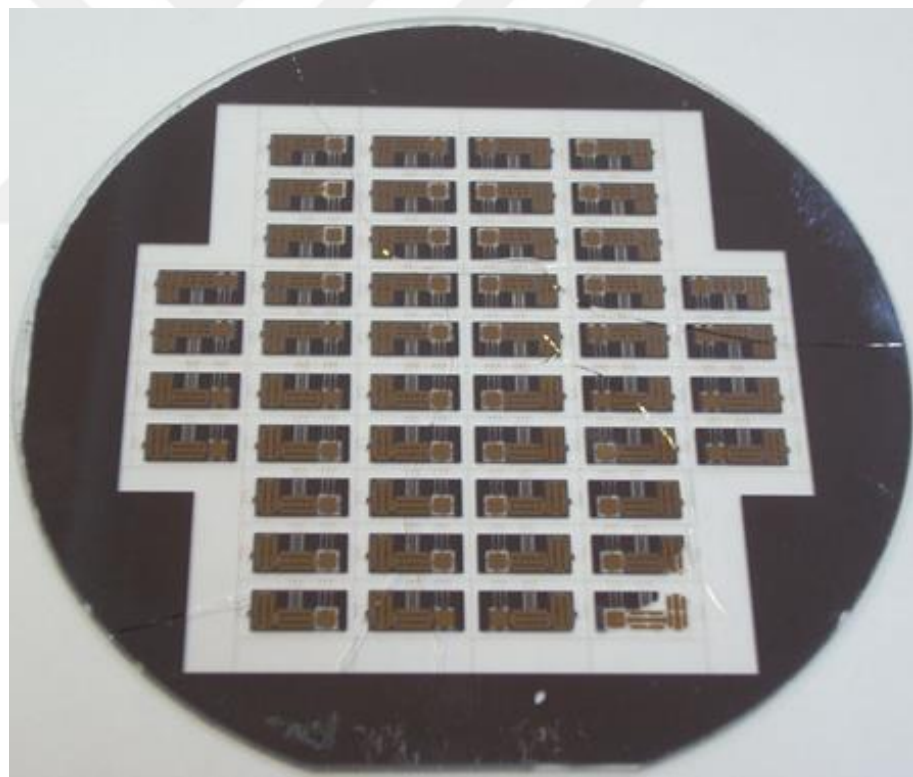


Figure 4.31: The triple stack observed after the first fabrication attempt.

The main problem observed during the formation of the glass-silicon-glass is cracks. Therefore, in the following fabrication run, the second anodic bonding process steps

are separately implemented without applying voltage to find which step causes to the problem. When the recipe is applied without voltage, there are not any cracks on wafers. Therefore, there are two possible reasons for the cracking problem which is related with either the high voltage or the cooling step in terms of results. Then, the second anodic bonding recipe is modified. There are two main changes in the recipe. The first one is related with the piston. The piston moves up position after applying voltage. The second one is related with the duration of the applied voltage. The applied potential difference is set 900V. Furthermore, the applied voltage is manually cut off when the bonding current equals to zero. By using the modified recipe, the formation of glass-silicon-glass sandwich structure is successfully completed. However, it is observed that there is a strong interaction between the chuck and the triple stack. It may be explained with charging as it is not possible to ground the silicon between glass wafers during the second anodic bonding method. Figure 4.32 shows the fabricated three-axis accelerometer sensor wafer. Figure 4.33 shows suspended structures after the second anodic bonding.

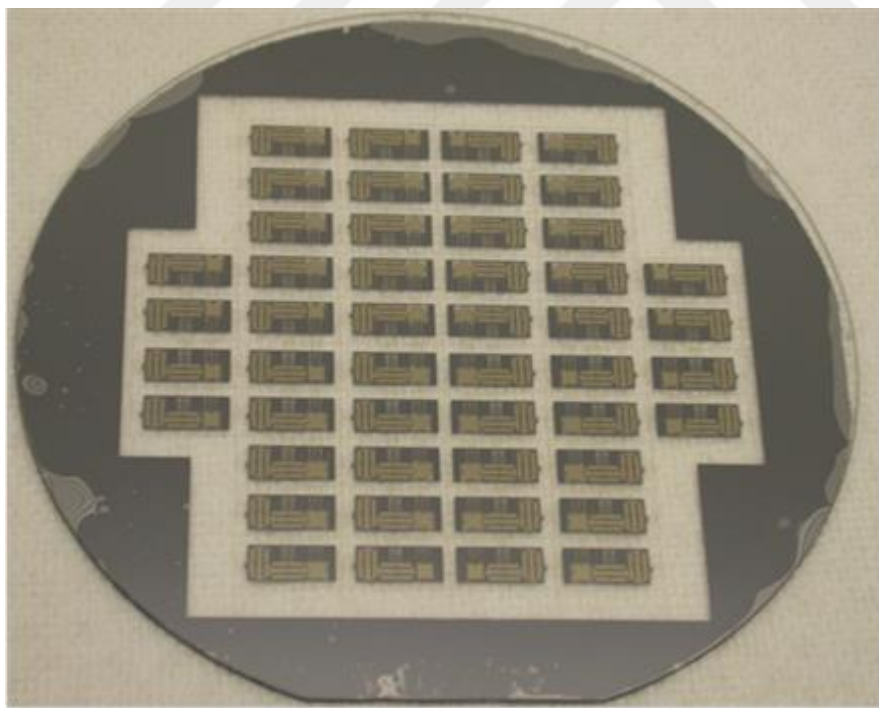


Figure 4.32: The fabricated three axis accelerometer sensor wafer



Figure 4.33: Suspended structures do not have any damage after the second anodic bonding.

4.1.7. Two-Step Dicing Process

It is necessary to uncover pad metals after the second anodic bonding process. Therefore, a dicing process is optimized to uncover pad metals. The optimized dicing process involves in two-step, where the top glass and bottom glass are half-cut, respectively. Then, sensors are manually separated from each other. It is noted that the dicing process requires the water. Therefore, the important parameter is the blade height. The blade height is set such a value that not only sensors are easily separated each other but also the water does not leak inside to the sandwich structure. The thickness of the triple stack together with the dicing tape is approximately measured as 1.070 mm by using microscope of the dicer. The blade height is set to 0.72 mm for both top and bottom glass wafers Figure 4.34 shows a representative image of the optimized dicing process. After the dicing process, it is observed that there is no the water flow inside sensors. Figure 4.35 shows the diced three-axis accelerometer. Figure 4.36 shows the two-step dicing process. Figure 4.37 shows an SEM image of the glass-silicon-glass sandwich structure.

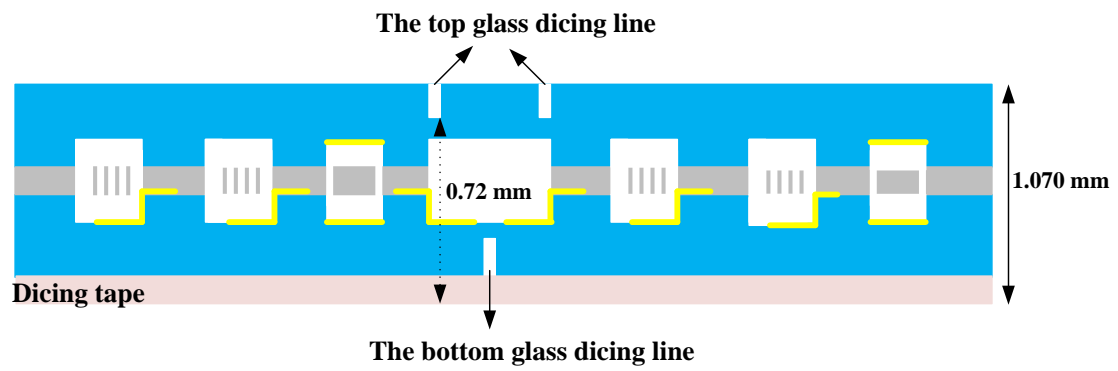


Figure 4.34: The illustration of the optimized two-step dicing process.

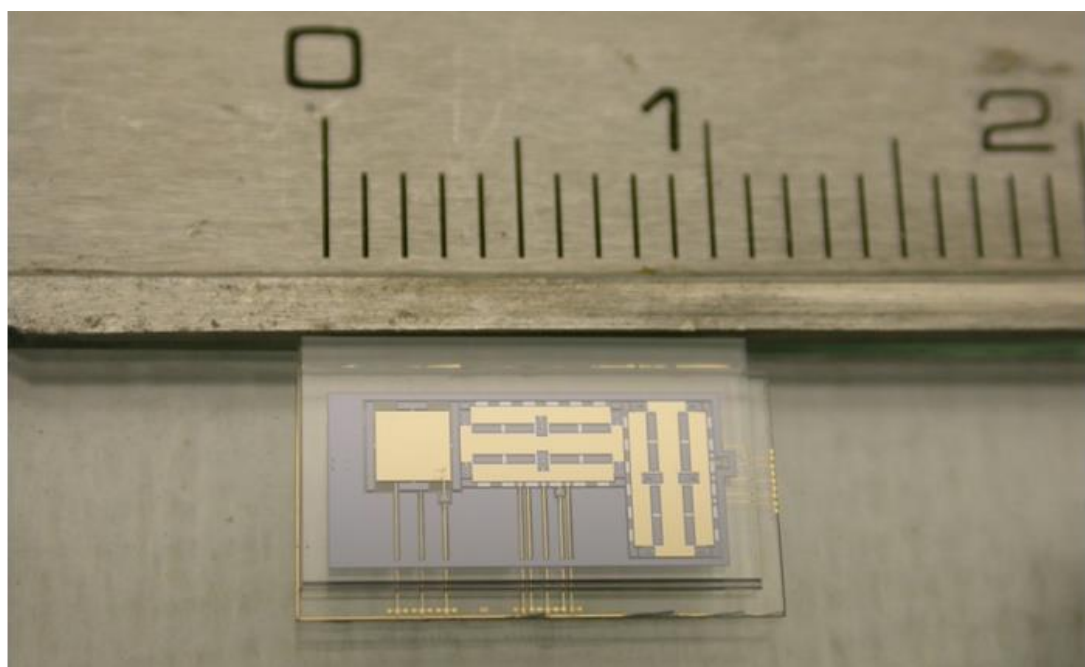
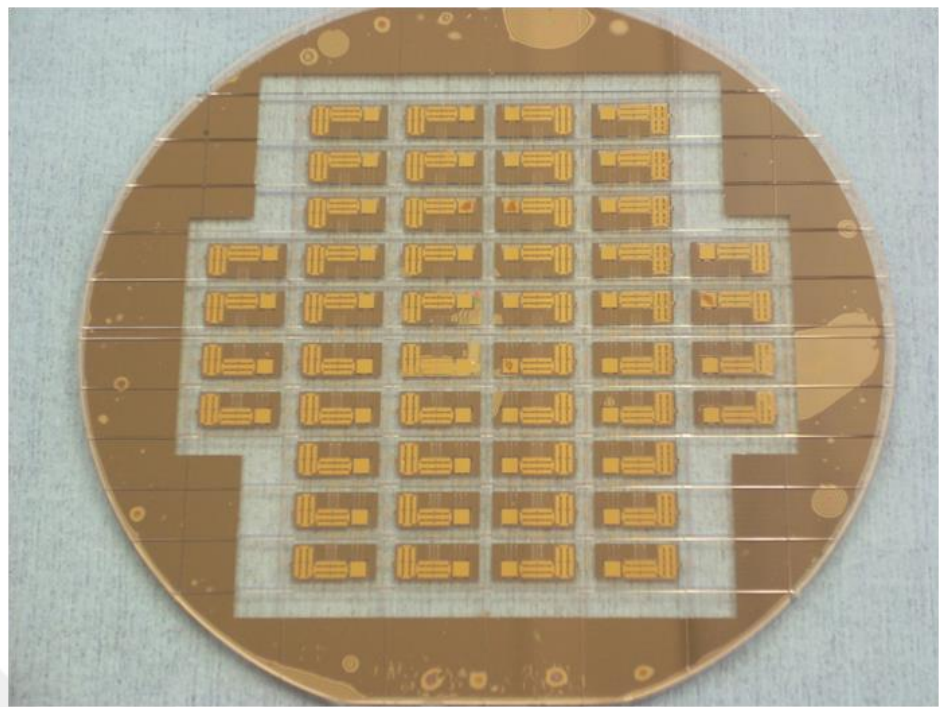
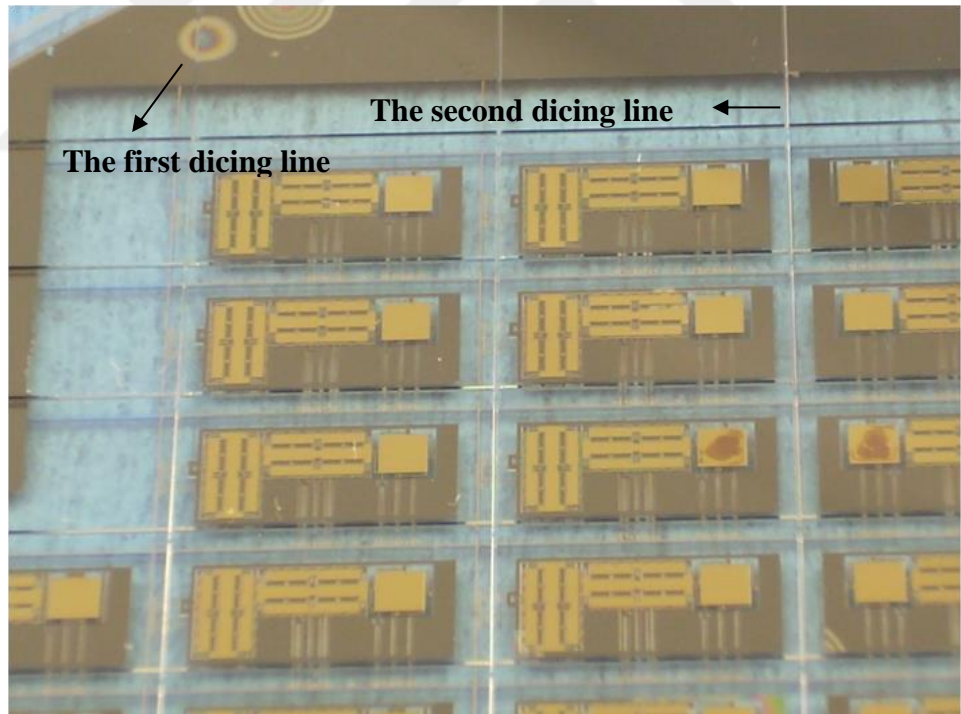


Figure 4.35: The diced three axis accelerometer fabricated by using DGM-DWP.



(a)



(b)

Figure 4.36: (a) The diced glass-silicon glass multi-stack (b) The dicing lines of the bottom glass and top glass.

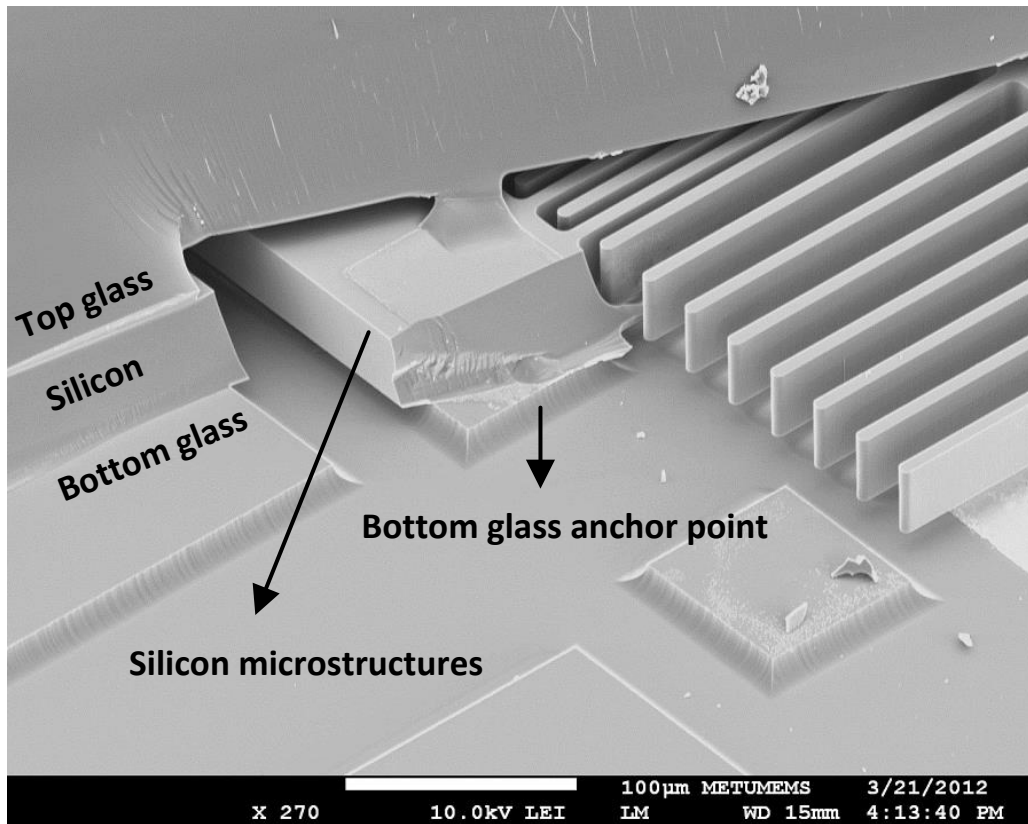


Figure 4.37: An SEM images of the glass-silicon-glass-structure fabricated by using the two-step anodic bonding.

4.1.8. Die Level Test Result and Further Observation

The fabricated sensors are tested under the probe station to verify their functionality. The test procedure includes the measurement of the rest capacitance and the capacitance change with respect to the applied voltage. The detailed information of about the die level test will be given in the die level and the system level test chapter. The rest capacitance and the capacitance change are determined by using Agilent 4294A Precision Impedance Analyzer. Each of the lateral and the vertical accelerometers located in the same die are measured separately by applying DC bias voltages applied between their proof masses and one of their electrodes while their other electrodes are connected to ground for eliminating the parasitic capacitance during the die level tests. Figure 4.38 and Figure 4.39 show the rest capacitance and the capacitance-voltage change (C-V) characteristics of the fabricated devices for the lateral and the vertical accelerometer, respectively. Table 4.2 shows comparison of

theoretical and measured values for the rest capacitance and the capacitance change of the lateral and vertical accelerometers. The test result and the theoretical calculation are in good agreement with for the lateral accelerometer. The calculated capacitance is slightly higher than the designed value as a result of fringing field. However, there is high mismatch for the capacitance of the vertical accelerometer formed between the bottom electrode and the proof mass as well as the top electrode and the proof mass.

Table 4.2: The rest capacitance and the C-V characteristics of lateral and vertical accelerometers.

| Designed | Rest Capacitance (pF) | |
|-----------------|-----------------------|----------|
| | Elect.#1 | Elect.#2 |
| Lateral | 9.56 | 9.56 |
| Vertical | 11.32 | 11.32 |
| Measured | Rest Capacitance (pF) | |
| | Elect.#1 | Elect.#2 |
| Lateral | 10.87 | 10.79 |
| Vertical | 25.62 | 13.05 |

The possible reason of the capacitance mismatch is comprehensively investigated for the vertical accelerometer. The kind of the silicon wafer is firstly taken into account. As the SiGeB wafer used during the fabrication process is highly doped, the structural layer may have the stress as a result of high doping level. Even though this stress can be considerably reduced in highly doped epitaxially-grown SiGeB wafers by introducing Ge into the lattice, still it can cause the buckling and prevent the operation of vertical accelerometers. Even a small amount of height difference between the anchor region and the proof mass causes the capacitance mismatch in the vertical accelerometer; however, this is not a major problem for the lateral accelerometer. Therefore, the buckling of the proof mass of the vertical accelerometer is measured by using an optical profiler for the first mask set. Figure 4.40 shows the buckling measurement result for the vertical accelerometer fabricated by using the SiGeB wafer.

The bucking measurement is repeated for the vertical accelerometer having same design concept; however, this time a SOI wafer is used instead of the SiGeB wafer to

compare the buckling result. Figure 4.41 shows the buckling measurement result for the same design of the vertical accelerometer fabricated by using the SOI wafer. The buckling is highly low compared with that of SiGeB wafer. Therefore, it is decided that the fabrication process continues with the SOI wafer.

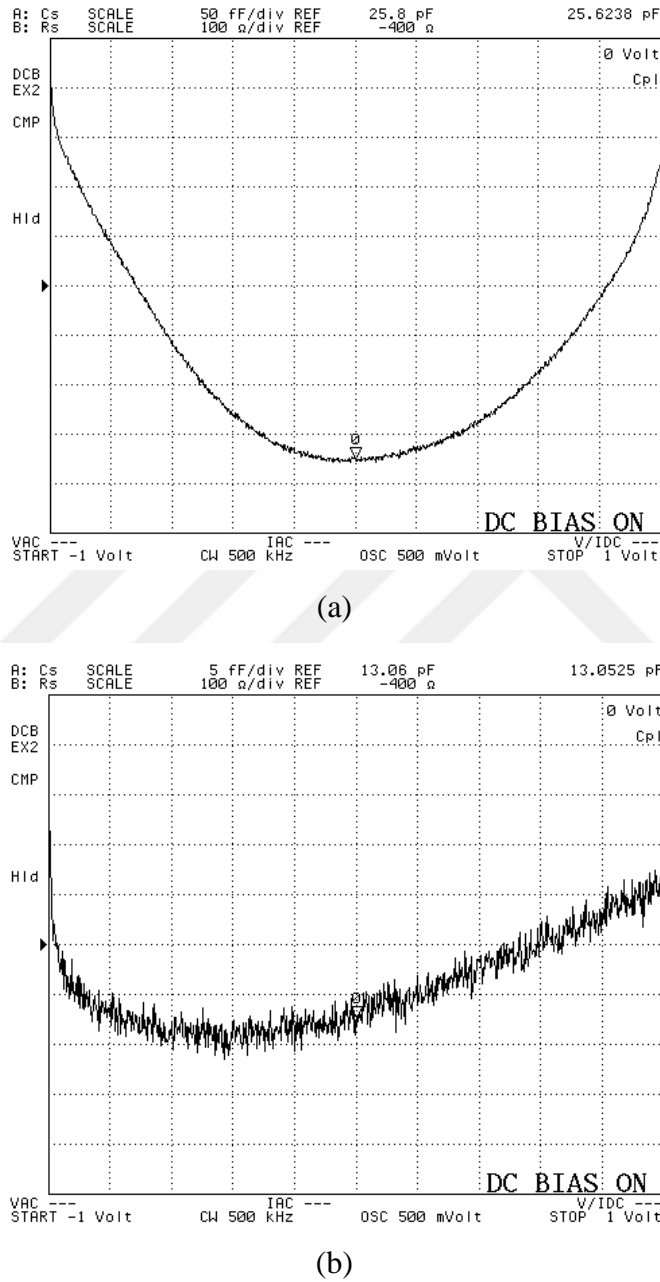
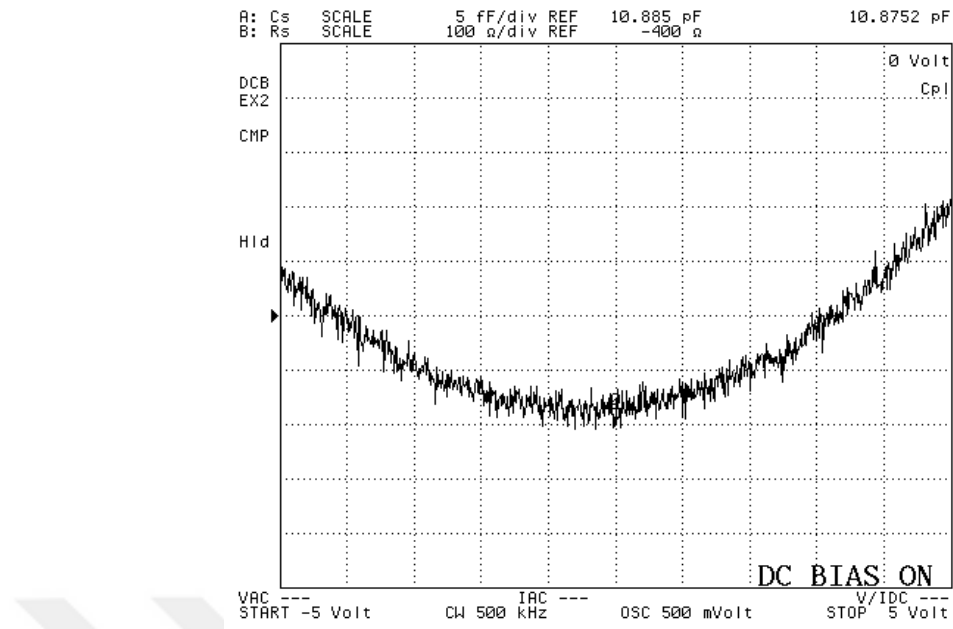
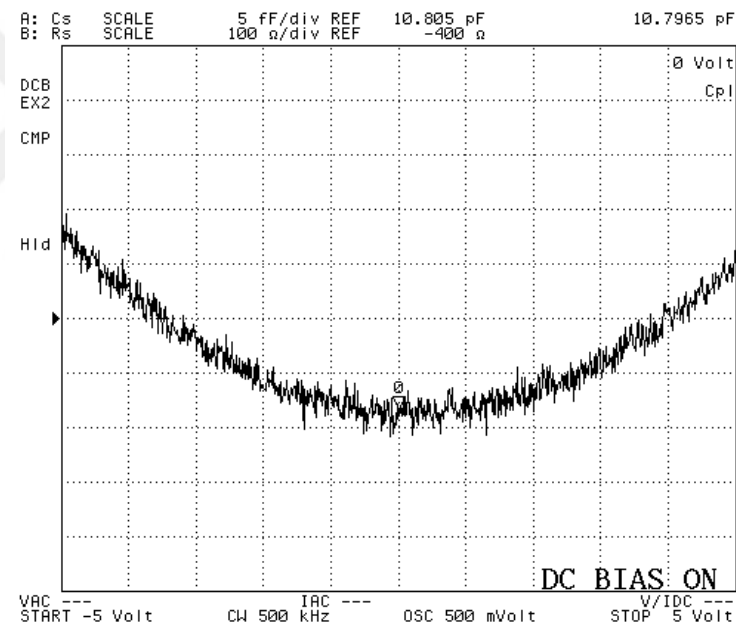


Figure 4.38: The vertical accelerometer test result. Rest capacitance values formed between the top electrode and the proof mass as well as the bottom electrode and the proof mass are 25.62 pF and 13.05 pF, respectively for DGM-DWP.

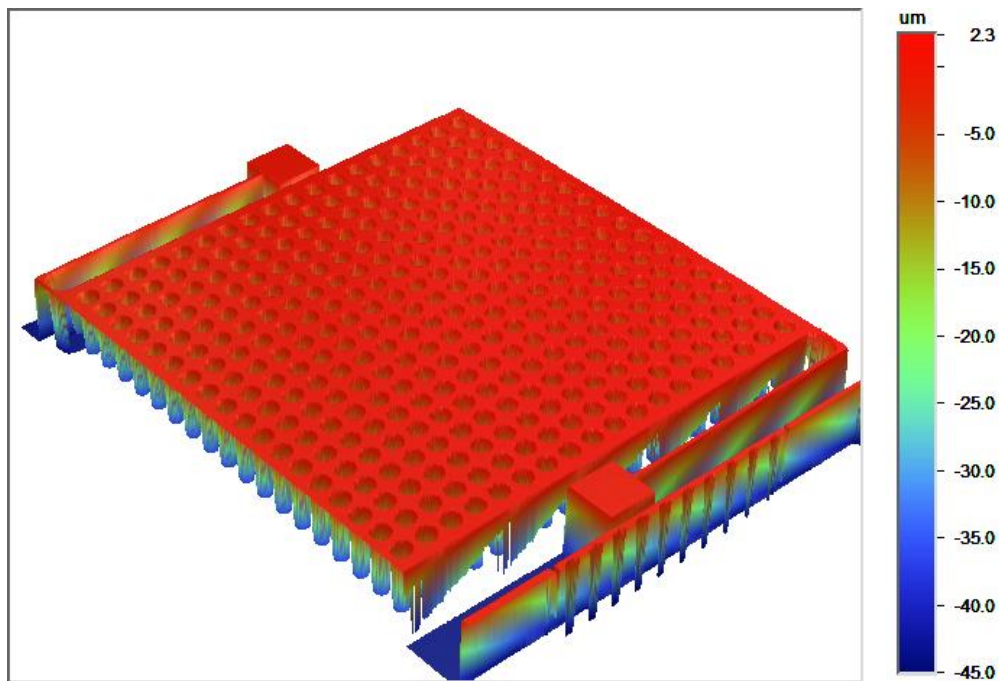


(a)

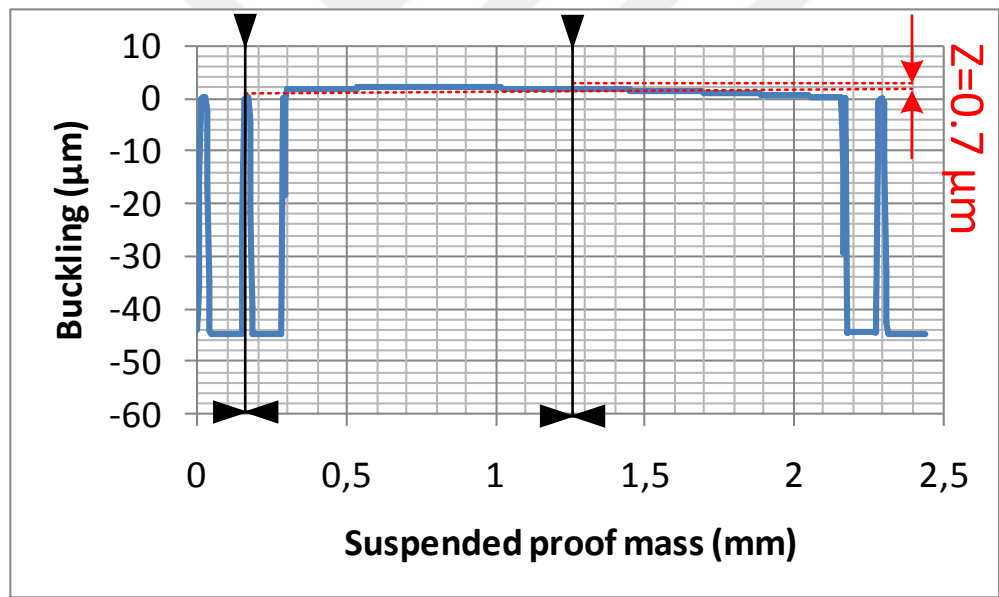


(b)

Figure 4.39: The lateral accelerometer test result. Rest capacitance values formed between the electrode#1 and the proof mass as well as the electrode #2 and the proof mass are 10.87 pF and 10.79 pF, respectively for DGM-DWP.

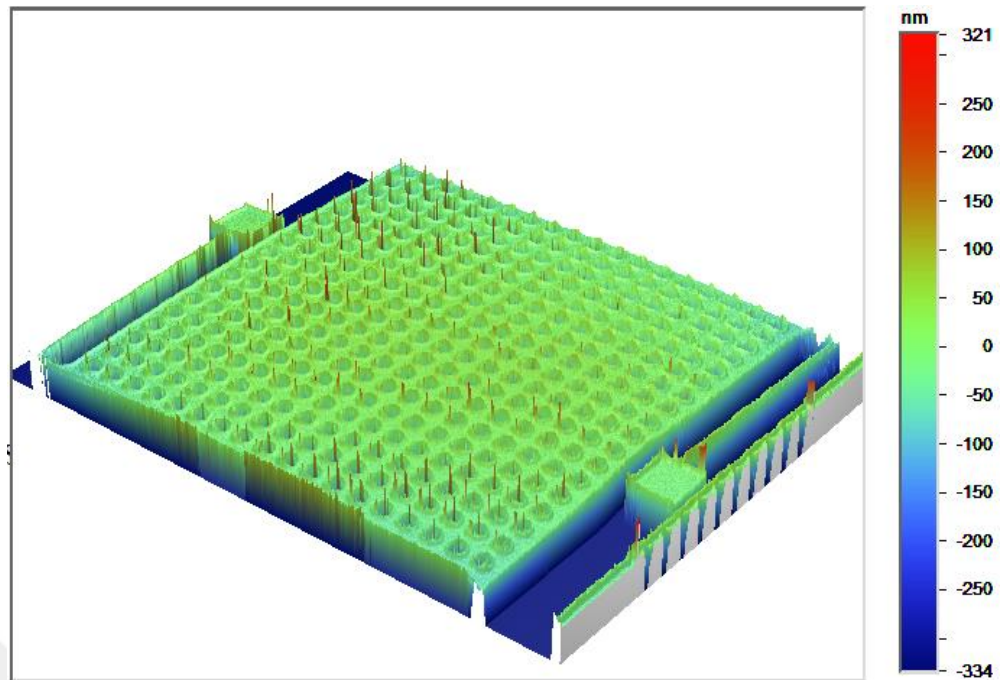


(a)

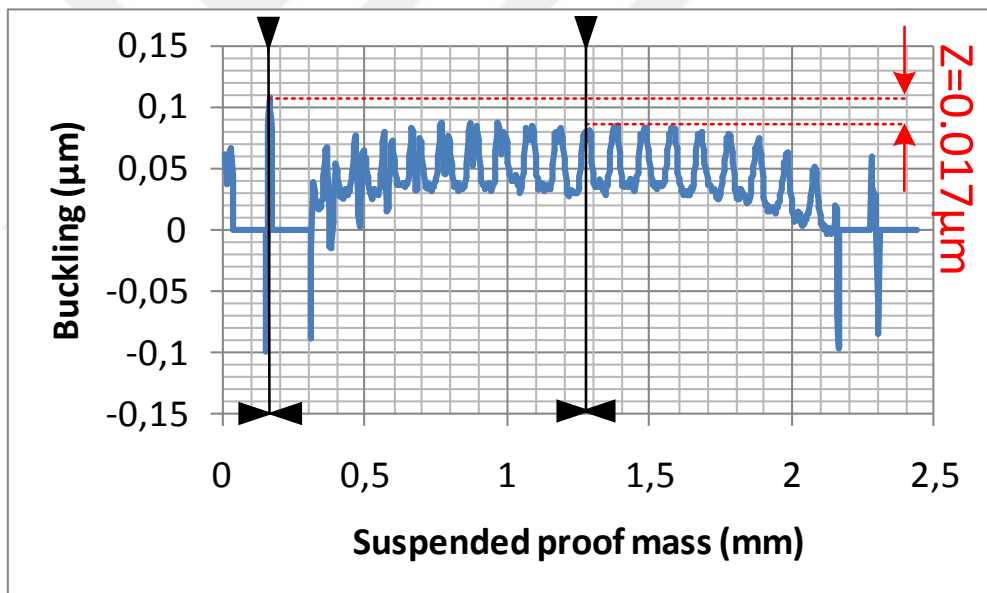


(b)

Figure 4.40: (a) Three dimensional view of the vertical accelerometer design-2 with perforation holes is formed by using data taken from the optical profiler (b) The buckling measurement result of the accelerometer fabricated by using the SiGeB wafer. The measured buckling is nearly 0.7 μm between the anchor region and the center of the proof mass.



(a)



(b)

Figure 4.41: (a) Three dimensional view of the vertical accelerometer design-2 with perforation holes is formed by using data taken from the optical profiler (b) The buckling measurement result of the accelerometer fabricated by using the SOI wafer. The measured buckling is nearly 17 nm between the anchor region and the center of the proof mass.

4.2. Double Glass Modified Silicon on Glass (DGM-SOG) Fabrication Process and Optimization

After results of the first mask set, the new fabrication of the mask set is prepared for the double glass modified silicon on glass (DGM-SOG) fabrication process. The fabrication mask set is almost same with the previous one. However, the insulator mask is removed from the fabrication process as the pad metallization is transferred external world from recesses formed among anchor regions. Moreover, there are fabrication masks not only the two-step anodic bonding but also the anodic bonding and then the Au-Si eutectic bonding methods for the formation of the glass-silicon-glass sandwich structure. The DGM-SOG fabrication process almost uses same steps with DGM-DWP fabrication process, which are previously optimized such as: the vertical gap etching, the two-step dicing process. In the following part, the process details will be given.

4.2.1. Definition of Process Steps

The fabrication process begins with cleaning of glass wafers in the piranha solution for 30 minutes. The fabrication process continues with the capacitive gap formation for the vertical accelerometer. Cleaned glass wafers are put into the buffered hydrofluoric acid (BHF) solution for 10 minutes. This step improves adhesion of Cr/Au layer to the glass wafer by providing a rough surface on the glass wafer. Then, 10/150nm thick Cr/Au layers are deposited by using the sputtering system (Figure 4.43). This layer is also used as a masking layer during the formation of the capacitive gap. Then, the deposited Cr/Au layer is patterned with help of lithography steps. Next, Cr/Au layer is etched by using wet etchants (Figure 4.44). Then, glass wafers is etched by using BHF in the desired level (Figure 4.45). This step is also critical as the performance parameters of the vertical accelerometer are mainly based on the vertical capacitive gap. After the formation of the capacitive gap (Figure 4.46), the photoresist is removed by using SVC wet chemical. Then, 10/150nm thick Cr/Au layers are etched in wet etchants.

Then, the fabrication process continues with the anchor region formation. Glass wafers are again put into BHF solution for 10 minutes to improve adhesion of 10/150nm thick Cr/Au deposition during the sputtering (Figure 4.47). This layer is also used as a masking layer during the formation of the anchor region. Then, the deposited Cr/Au layer is patterned with help of lithography steps. Next, Cr/Au layers are etched by using wet etchants (Figure 4.48). Then, glass wafers are etched by using pure hydrofluoric acid (HF) for 85 seconds in the range of 8-12 μm (Figure 4.49). In this step, recesses are formed among the anchor region to transfer the pad metallization to external world. After the formation of anchor region, the photoresist is removed by using wet chemical. Then, 10/150nm thick Cr/Au layers are etched in wet commercial etchants (Figure 4.50).

The last step in the glass wafer fabrication is the formation of pad metallization. As the formation of the glass-silicon-glass multi-stack is provided by two different methods, there are two different the pad metallization mask for the bottom and the top glass wafers. If the glass-silicon-glass multi-stack is formed by using two-step anodic bonding, the pad metallization mask must also include the shied metallization to prevent the bonding of the suspended structure to the top glass during the second anodic bonding. Therefore, the parasitic capacitance is introduced as a result of the shield metallization. However, the bonding is more durable and reliable. When the glass-silicon-glass multi stack is formed by using the anodic bonding and then the Au-Si eutectic bonding, there is no need for the shield metallization. Therefore, the Au-Si eutectic bonding enables voltage free bonding of the bottom glass-silicon stack to the top glass. The other advantage of the fabrication process is to eliminate the shield metallization, which causes undesired parasitic capacitances. Furthermore, the metallization deposited for the formation of the top electrode is also used to provide the Au-Si eutectic bonding for the entire structure.

The pad metallization process starts with putting glass wafer into BHF for 10 minutes. 10/150nm thick Cr/Au layers are deposited on glass wafers by using the sputtering system (Figure 4.51). Then, 10/150nm thick Cr/Au layers are etched by using wet commercial etchant to form the pad metallization for the desired formation

method of the glass-silicon-glass multi stack, where pad metals are oriented in the same direction (Figure 4.52 (a-b-c-d)).

Glass wafers fabrication is completed after the formation of the pad metallization. The fabrication process is continued with the silicon wafer. The silicon fabrication process is the one of the most important part of the fabrication process as many performance parameters of lateral accelerometer depend on the capacitive finger gap. The silicon wafer is coated with photoresist, and the structure is patterned on the wafer. Then, the structure pattern is transferred on the wafer by using DRIE (Figure 4.53).

The next step is to anodically bond the bottom glass and the silicon wafer. Therefore, the glass and the silicon wafer are cleaned by using the piranha solution. Before the anodic bonding, the native oxide layer on the silicon wafer is etched by short BHF etching. Then, the silicon and the bottom glass wafers are anodically bonded each other (Figure 4.54). Afterwards, the handle layer of the SOI wafer is completely removed until the buried oxide layer by using DRIE (Figure 4.55). The buried oxide layer is etched by using BHF for 24 minutes. Then, the suspended structure is released by putting the bottom glass-the silicon stack into the Acetone, the IPA and the Methanol solution for 5 minutes, respectively, and then, the bottom glass-the silicon stack is dried on the hot plate for 5 minutes (Figure 4.56). The final step is to form the glass-silicon-glass multi stack by using either the two-step anodic bonding or the anodic bonding and then the Au-Si eutectic bonding (Figure 4.57).

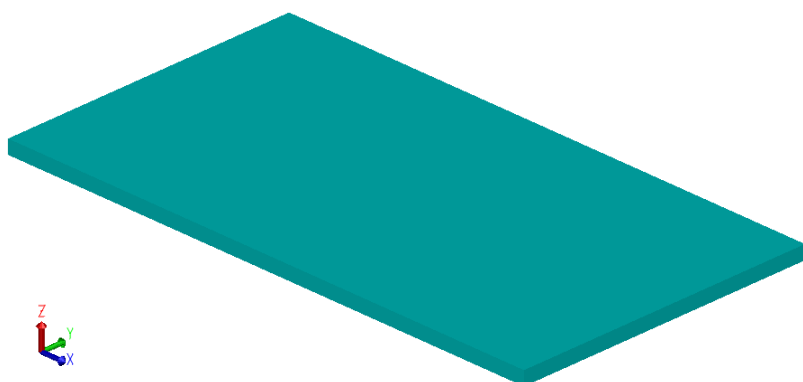


Figure 4.42: Glass wafers are cleaned in the piranha solution for 30 minutes.

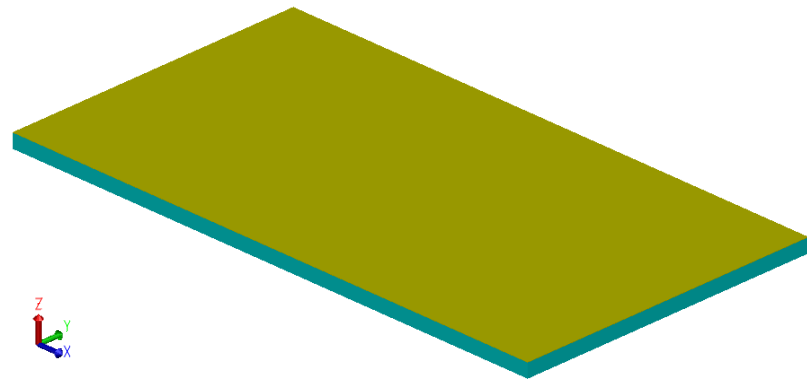


Figure 4.43: 10/150nm thick Cr/Au layers are deposited on glass wafers by using the sputtering system.

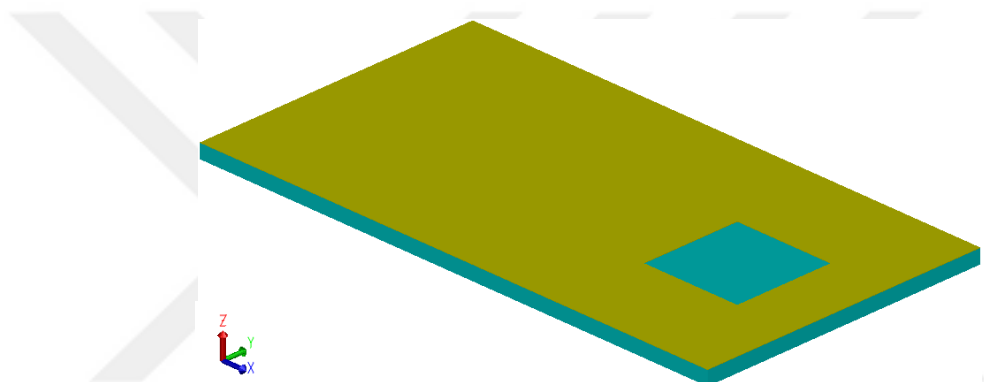


Figure 4.44: The deposited Cr/Au layers are patterned by using lithography steps.

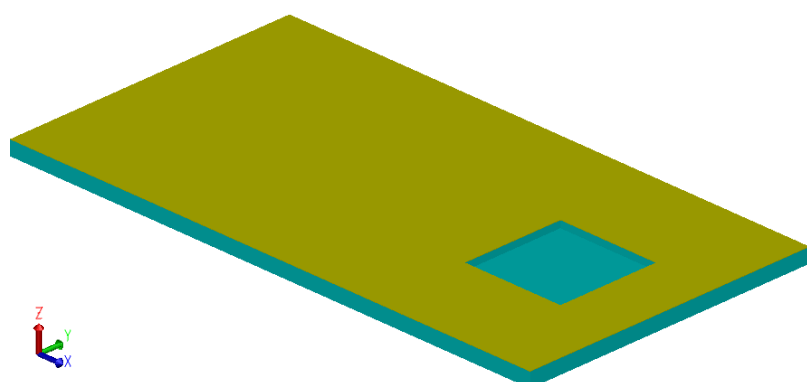


Figure 4.45: Glass wafers are etched in BHF solution for the formation of the vertical gap.

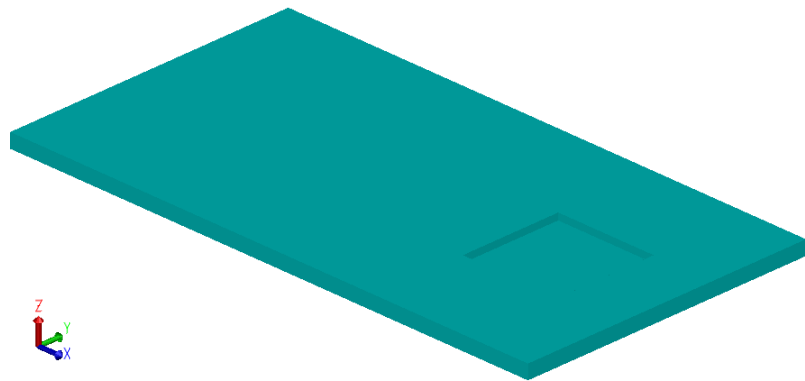


Figure 4.46: 10/150nm thick Cr/Au layers are completely etched.

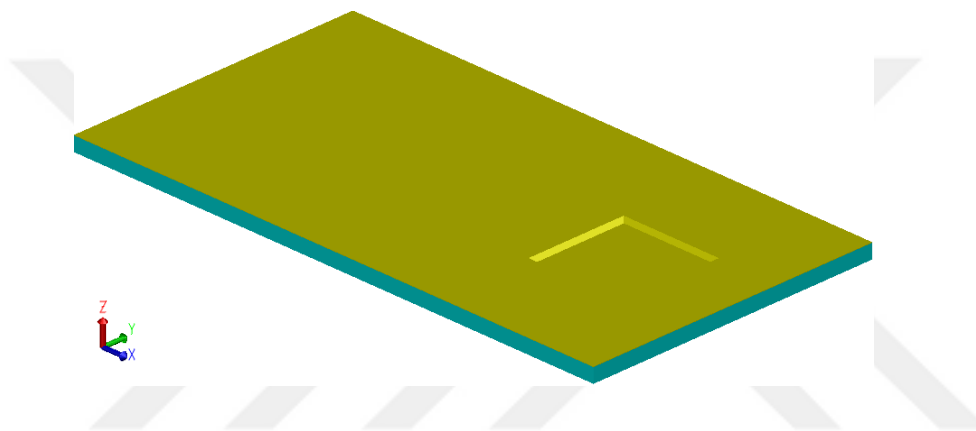


Figure 4.47: 10/150nm thick Cr/Au layers are deposited on glass wafers by using the sputtering system for the formation of anchor regions.

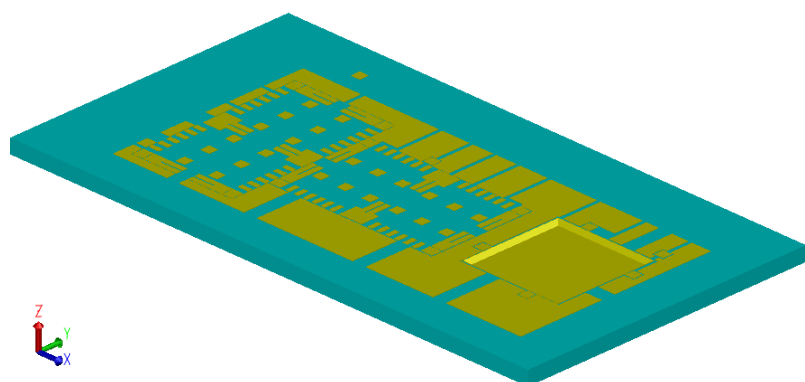


Figure 4.48: Cr/Au layers are patterned by using lithography steps.

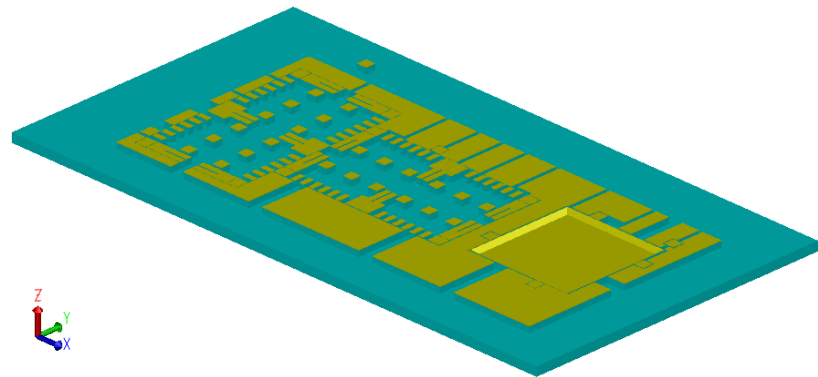


Figure 4.49: Glass wafers are etched by using pure HF for the formation of anchor region. There are recesses among the anchor region to transfer the pad metallization to outside.

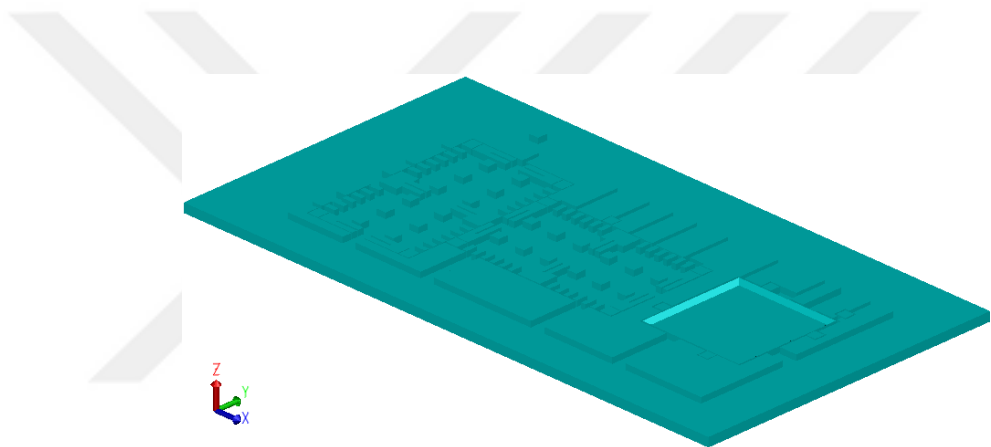


Figure 4.50: 10/150nm thick Cr/Au layers are completely etched.

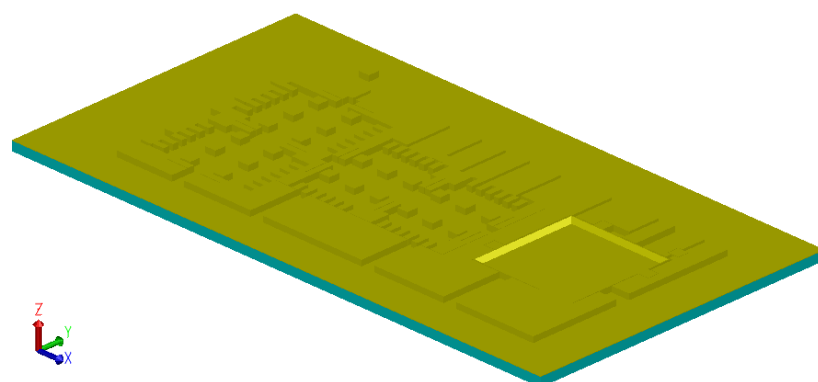


Figure 4.51: 10/150nm thick Cr/Au layers are deposited on glass wafers by using the sputtering system for pad metals.

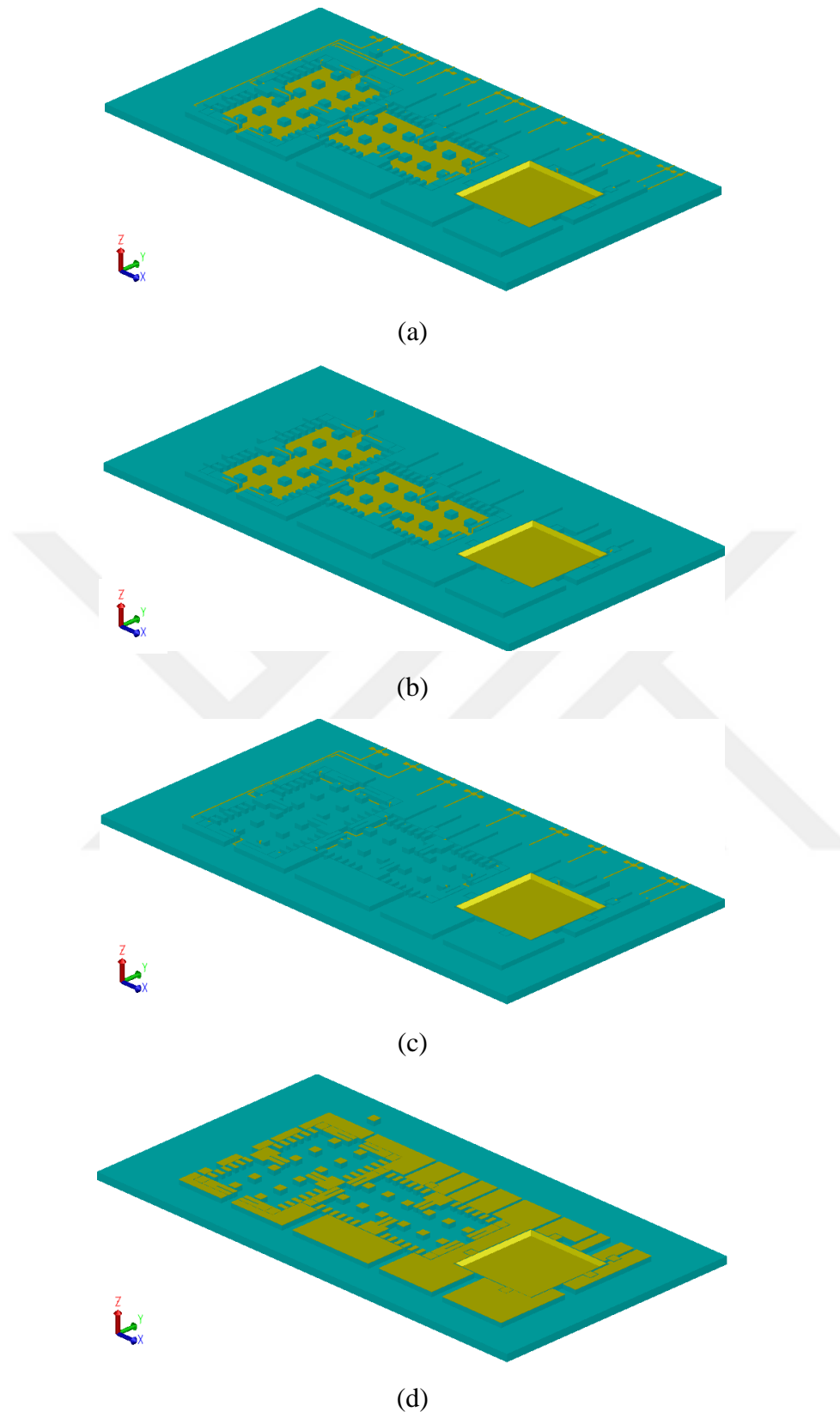


Figure 4.52: (a-b) The pad metallization also includes the shield metallization for the two-step anodic bonding approach. The metallization for the Au-Si eutectic bonding (c) the bottom glass (d) the top glass pad metallization.

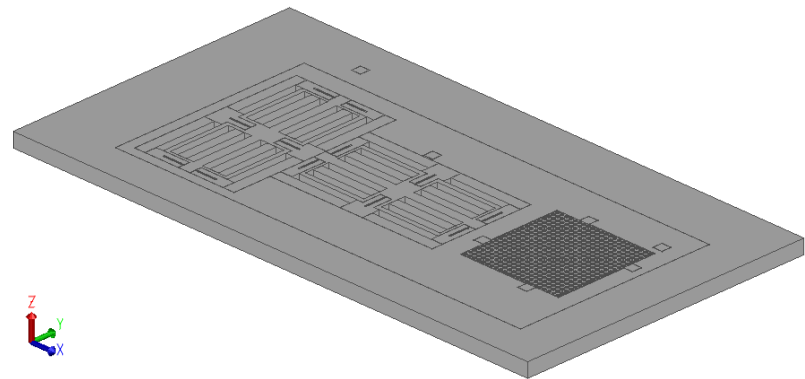


Figure 4.53: The structure pattern is transferred on the SOI wafer by using DRIE.

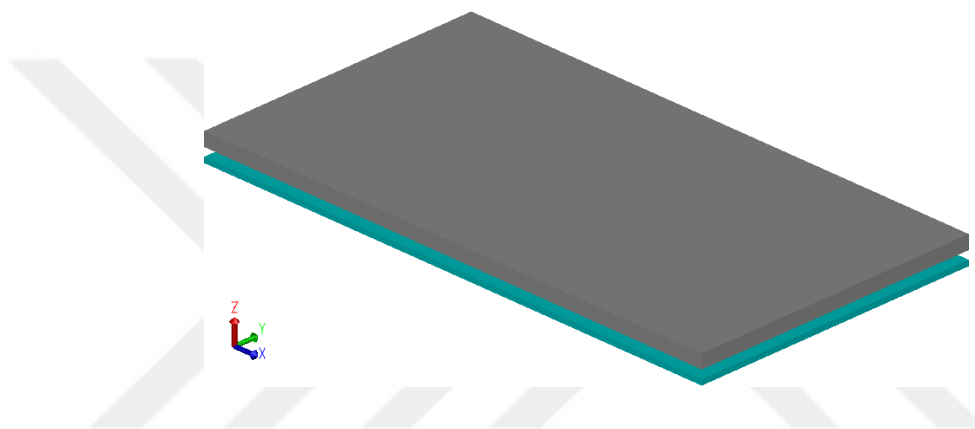


Figure 4.54: The anodic bonding process is performed between the bottom and SOI wafers.

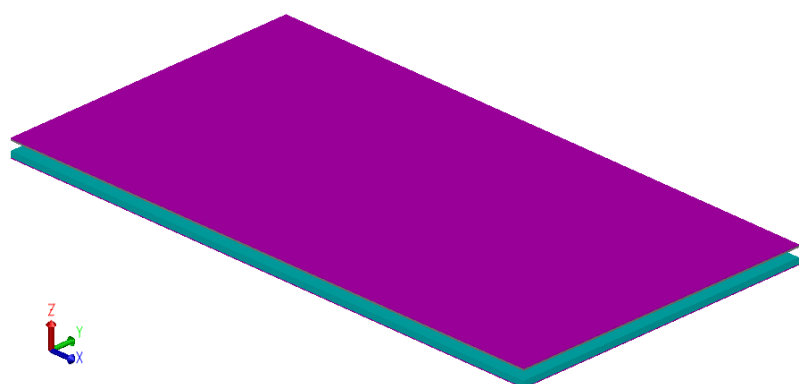


Figure 4.55: The SOI wafer is thinned by using DRIE until the buried oxide layer.

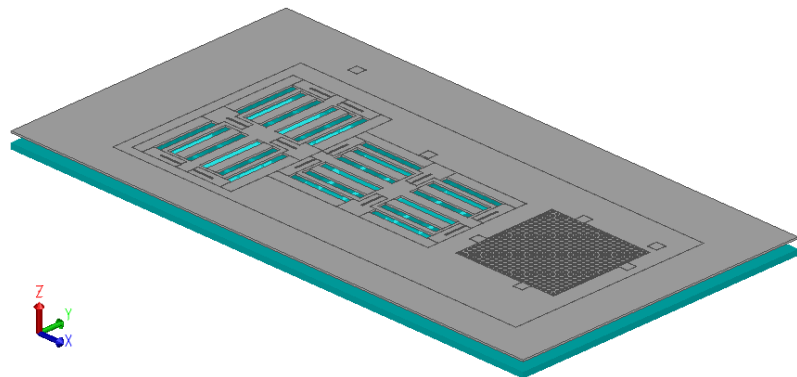


Figure 4.56: The three-axis accelerometer is released on the hot plate.

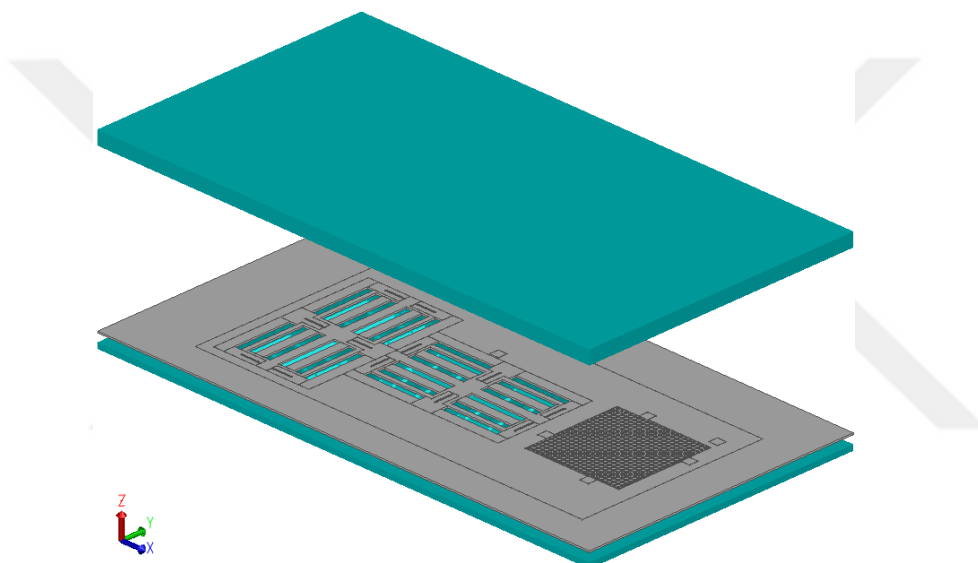


Figure 4.57: The formation of the multi-layers is provided either the two-step anodic bonding or the Au-Si eutectic bonding.

4.2.2. Fabrication of Glass Wafers

The vertical gap etch optimization is explained in the previous part. The glass fabrication process is completed by using the optimized data explained in the previous section. Figure 4.58 shows the glass wafer of which the vertical gap and anchor formation is completed. Figure 4.59 and Figure 4.60 show fabricated glass wafers for the two-step anodic bonding and the anodic and then the Au-Si eutectic bonding fabrication processes, respectively.

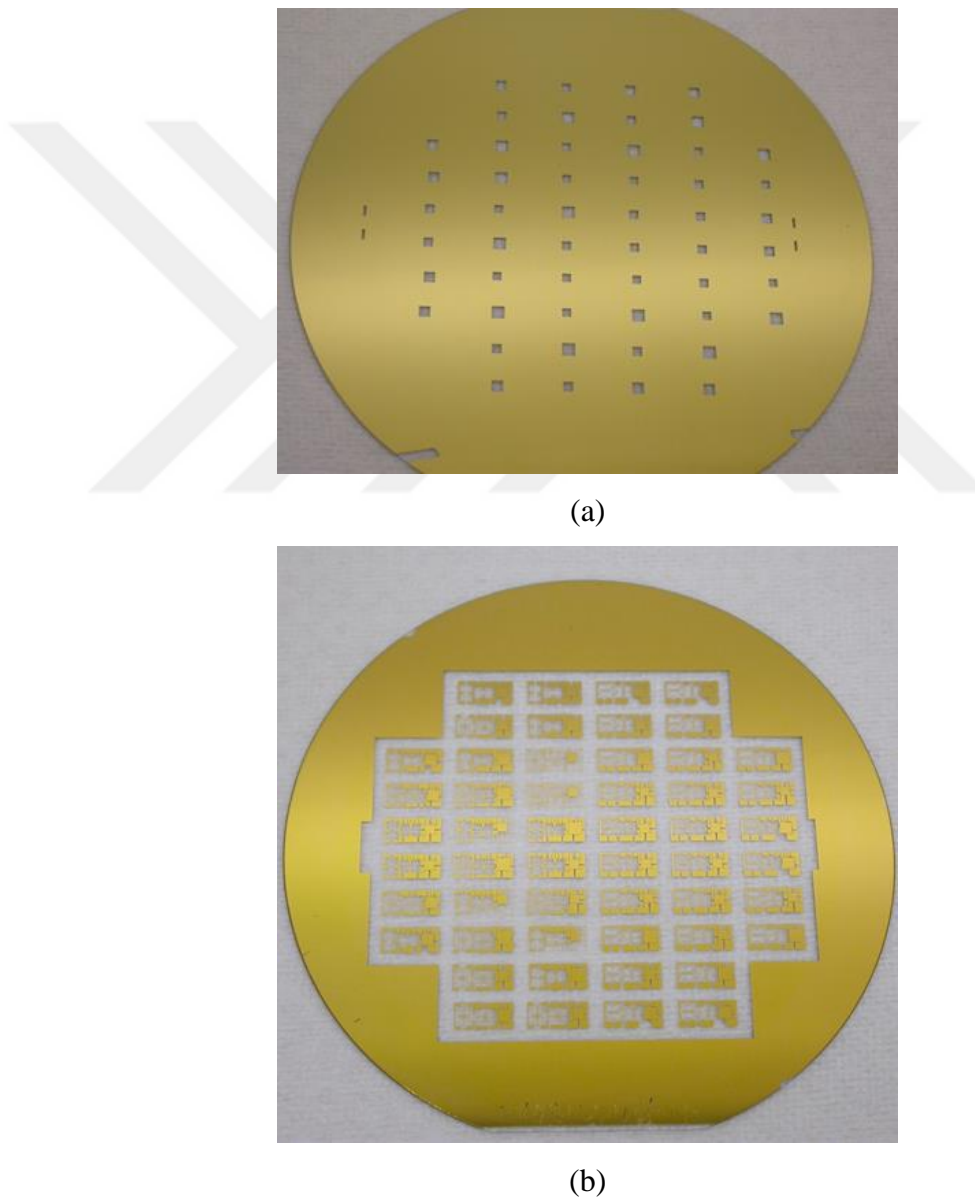
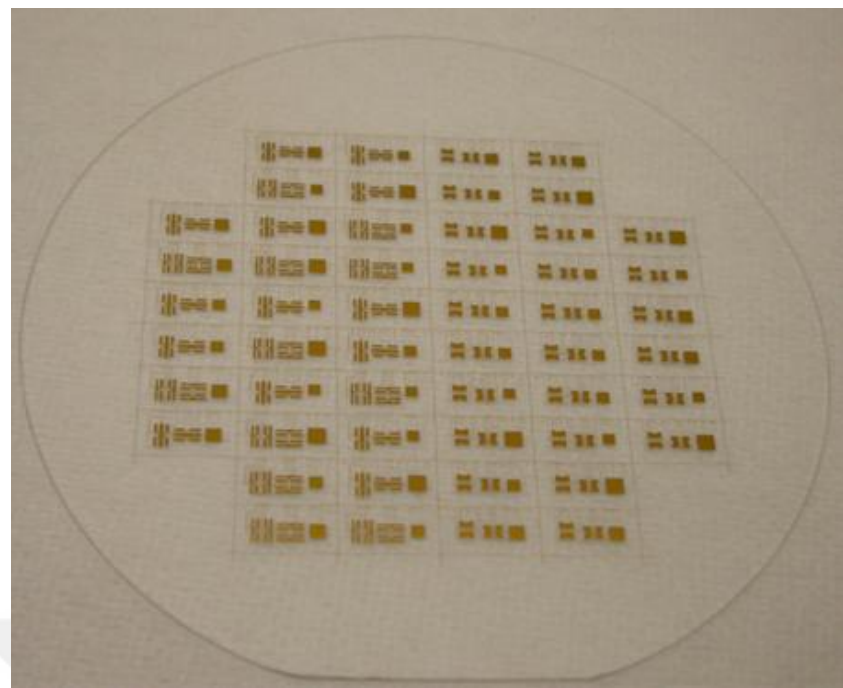
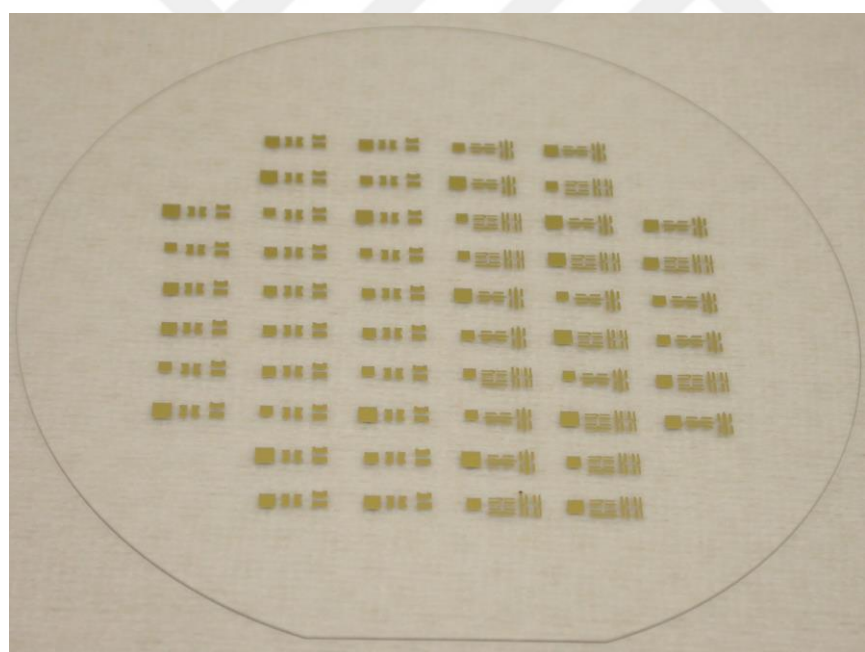


Figure 4.58: The fabricated glass wafers (a) the vertical gap etch (b) the anchor formation.

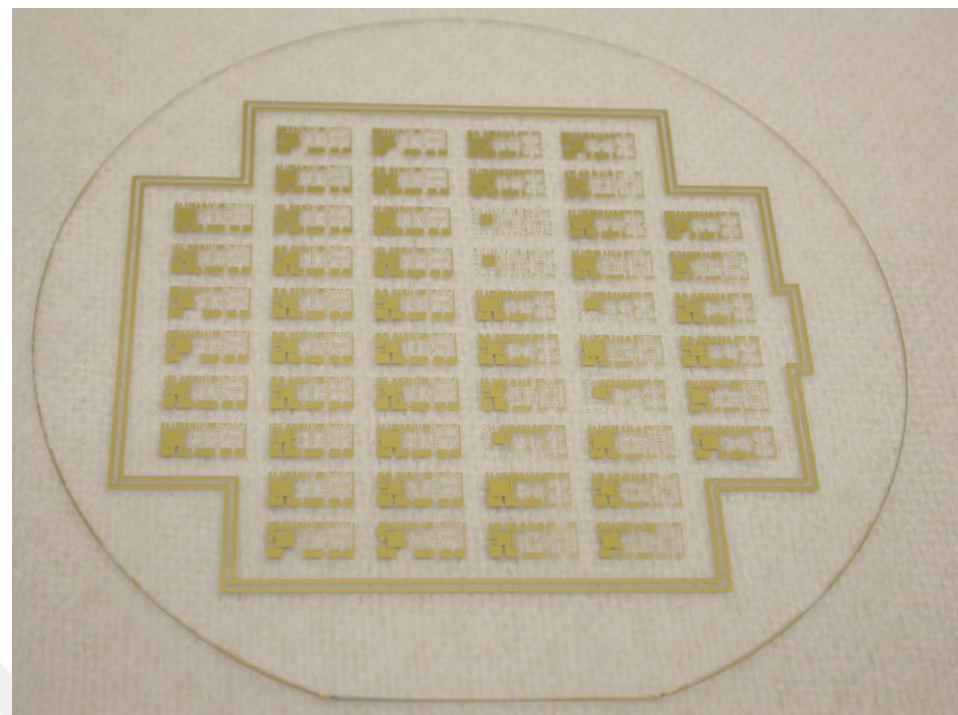


(a)

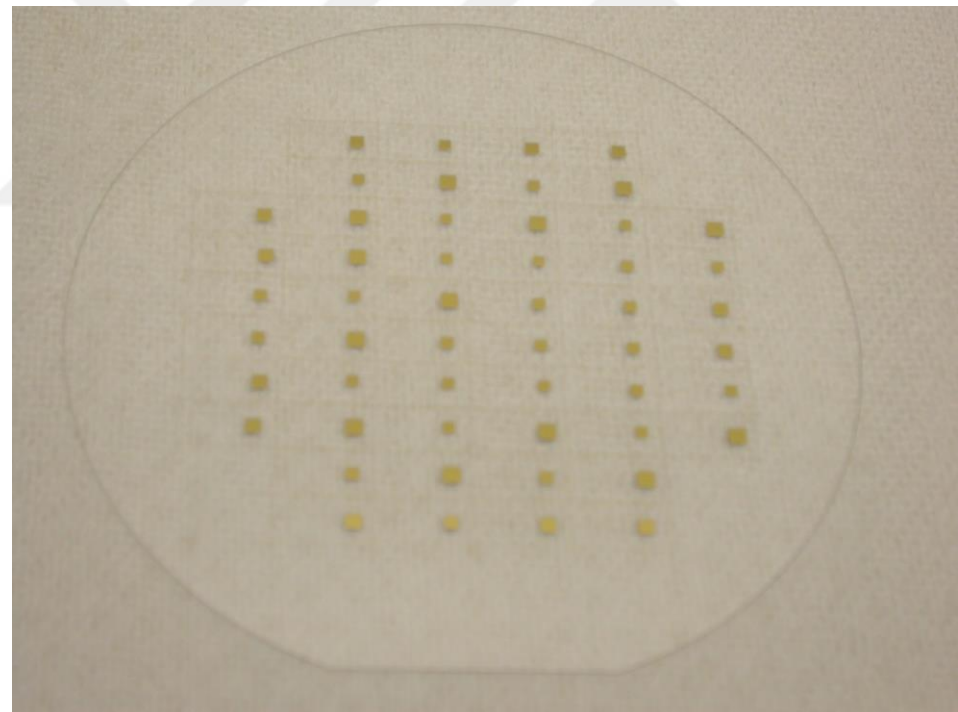


(b)

Figure 4.59: The fabricated glass wafer for the two-step anodic bonding process (a) the bottom glass wafer (b) the top glass wafer



(a)



(b)

Figure 4.60: The fabricated glass wafers for the anodic bonding and then the Au-Si eutectic bonding.

4.2.3. Structural DRIE

The SOI wafer is patterned by using DRIE. Process parameters for DRIE are already optimized in the previous section. The structure pattern is easily transferred to the SOI wafer. Figure 4.61 shows the prepared SOI wafer for three axis accelerometer fabrication process.



Figure 4.61: Structures are patterned on the SOI wafer by using DRIE.

4.2.4. Bonding Optimization

The most important part of the fabrication process is to form the glass-silicon-glass structure without any problem. The formation of the glass-silicon-glass structure is completed two different bonding methods: the two-step anodic bonding and the anodic bonding-the Au-Si eutectic bonding. In the first part, the two-step anodic bonding with the two-electrode method is explained. However, it is observed that there is a strong interaction between the chuck of the bonder and sandwich structure. To eliminate this problem, the three-electrode bonding is also optimized in the current part. Furthermore, the formation of the glass-silicon-glass multi-stack is performed for the anodic bonding and then the Au-Si eutectic bonding.

4.2.5. The First Anodic Bonding

The first anodic bonding recipe optimized for DGM-DWP process is applied for SOI and glass wafers. After the anodic bonding the bottom glass silicon-stack is observed, Figure 4.62 shows the bonded bottom glass-SOI stack.

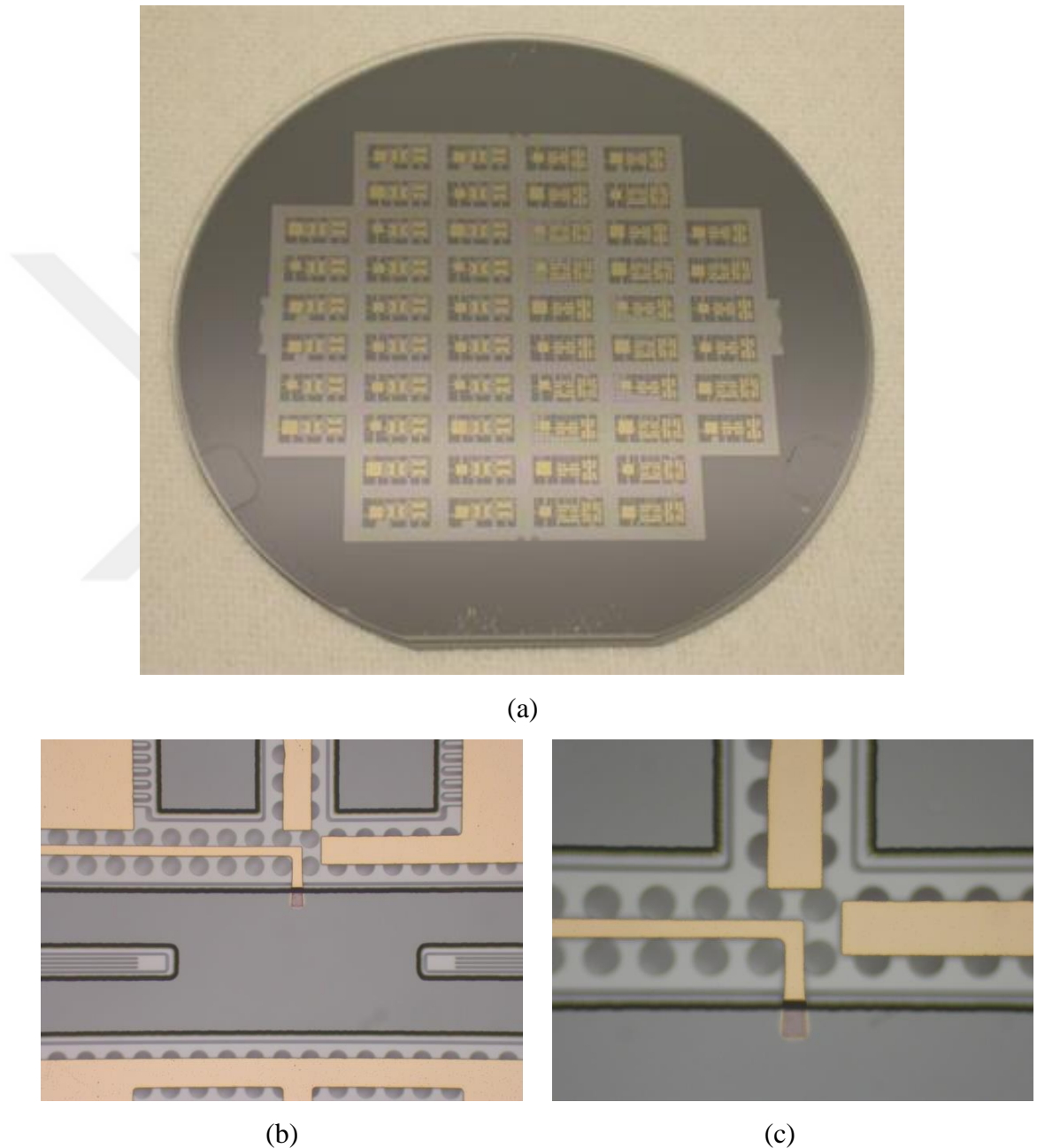


Figure 4.62: The first anodic bonding recipe optimized for the bonding of glass and SiGeB wafers is applied for glass and SOI wafers.

After the first anodic bonding, the handle layer is completely removed by using the DRIE, and the buried oxide is etched in the BHF. However, it is observed that the anchor region is also damaged in this step. As the type of the silicon wafer is changed, it is necessary to repeat the optimization for the first bonding. The SOI wafer is composed of 35 μm thick silicon structure layer, a thin buried oxide layer (0.5-2 μm) and 300 μm handle layer. As the SOI wafer includes a thin oxide layer, the first optimized bonding recipe of SiGeB is no more useful. The detailed investigation about bonding of the SOI to the glass wafer is given in [67].

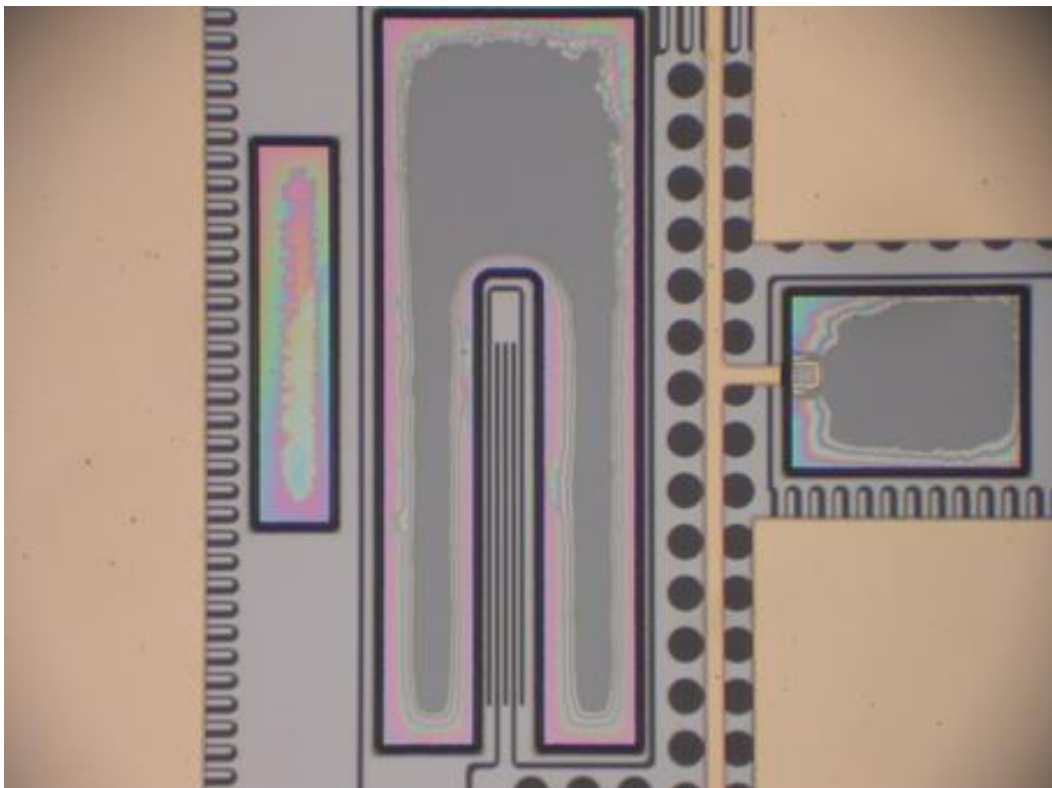
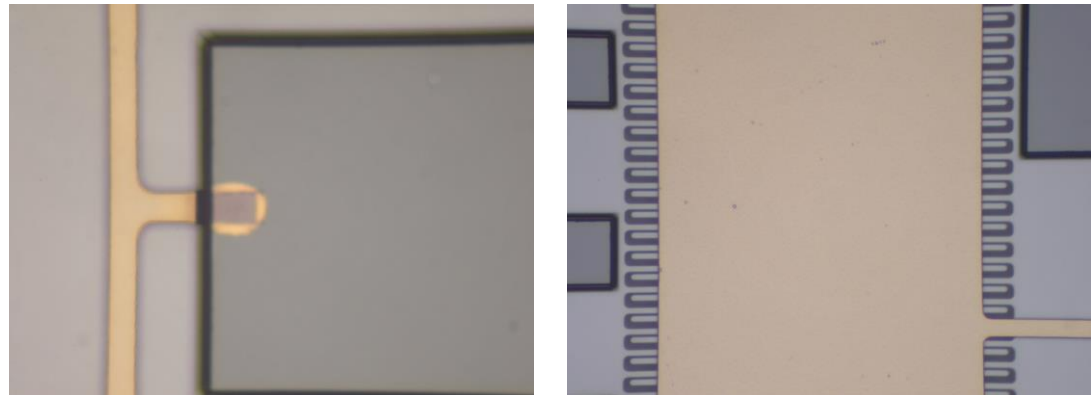


Figure 4.63: The anchor region, which is anodically bonded to the bottom glass in the first bonding fabrication step, is damaged after etching of the buried oxide layer.

To improve the anodic bonding quality, the bonding temperature and bonding voltage are increased. The temperature is increased from 350°C to 355°C, and the voltage is set to 1400V instead of 1200V. These changes help to the improvement of the bonding quality. Figure 4.64 shows the contact region and anchor regions after

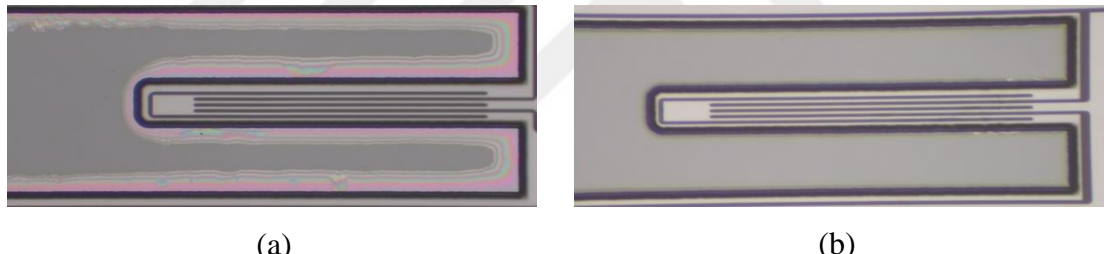
the first anodic bonding. Figure 4.65 shows the comparison of the previous and modified bonding recipe results.



(a)

(b)

Figure 4.64: (a) The contact region and (b) anchor regions after the modified anodic bonding.



(a)

(b)

Figure 4.65: The modified first anodic bonding recipe improves the bonding quality (a) the previous attempt (b) the modified recipe result.

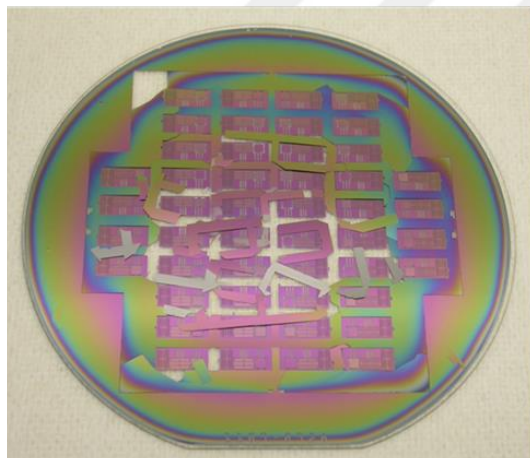
4.2.6. Handle Layer Removing

The next step is to remove the handle layer until the buried oxide region. Two different SOI wafer is used during the fabrication process, where the buried oxide thickness is 0.5 μm and 2 μm , respectively. Therefore, the different process result is obtained. If the SOI wafer having 0.5 μm thick buried oxide layers is used, the frame around the sensor region is completely damaged, and broken frame parts shadow the etching of the handle layer. This is probably related with the stress of the buried oxide layer. When the handle layer removing process is repeated the SOI wafer

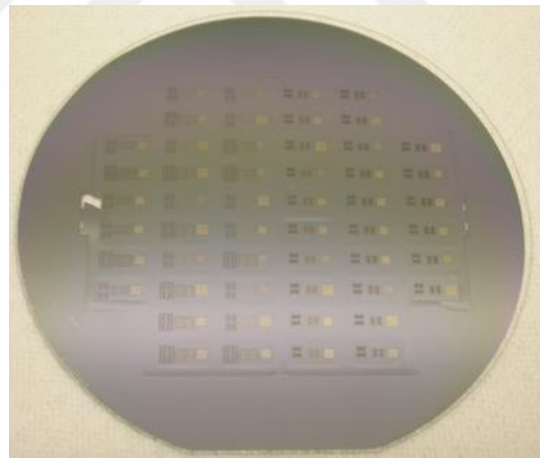
having 2 μm thick buried oxide layer, the problem observed in the fabrication process is solved. Table 4.3 shows the DRIE recipe used during the handle layer removing process. Figure 4.66 shows SOI wafers having 0.5 μm and 2 μm thick buried oxide layers, respectively. After the handle layer removing process, suspended structures are successfully released with the recipe defined in the first fabrication section. Figure 4.67 shows the bottom glass silicon stack after the releasing process.

Table 4.3: The DRIE recipe used for the handle layer removing.

| Etch Step | |
|---------------------|--|
| Gas Flows | SF ₆ : 900 sccm, O ₂ : 90 sccm |
| Pressure | 100 mTorr |
| Coil Power | 2200 W |
| Platen Power | 0 W |
| Temperature | 0°C |

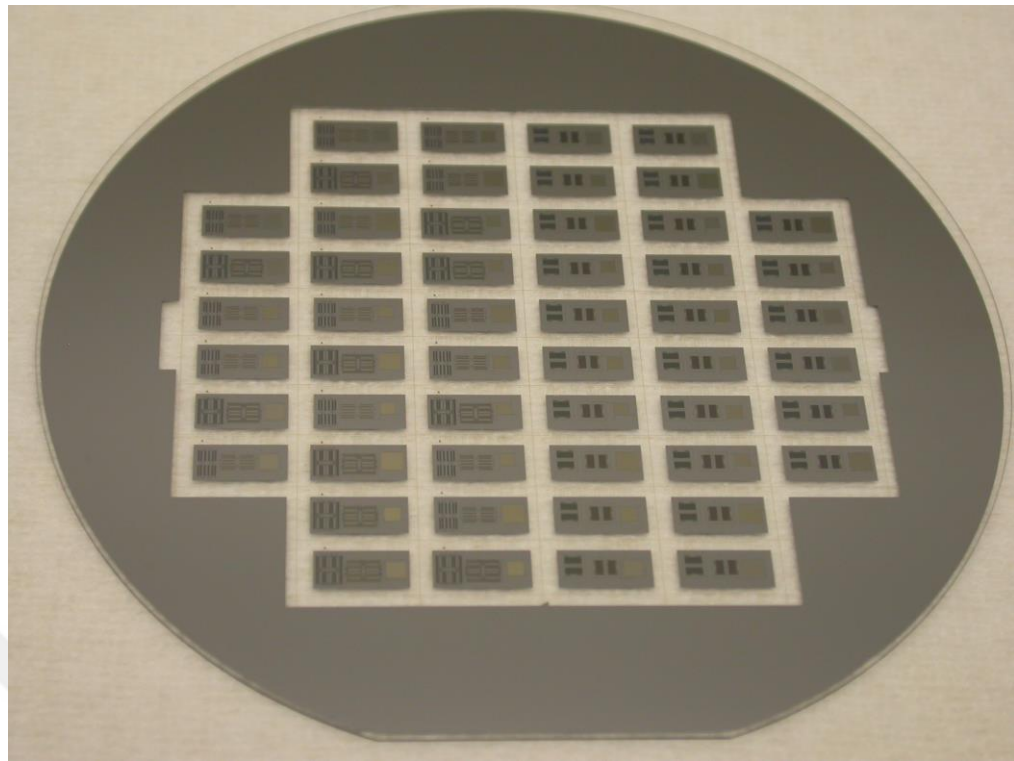


(a)

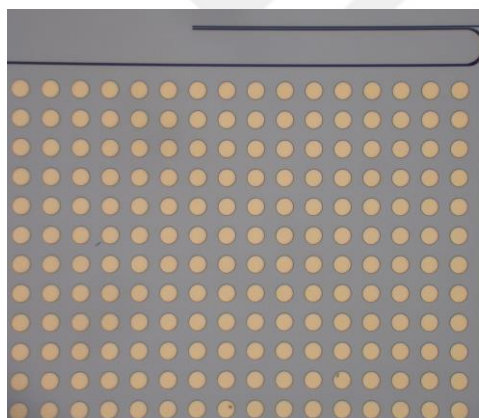


(b)

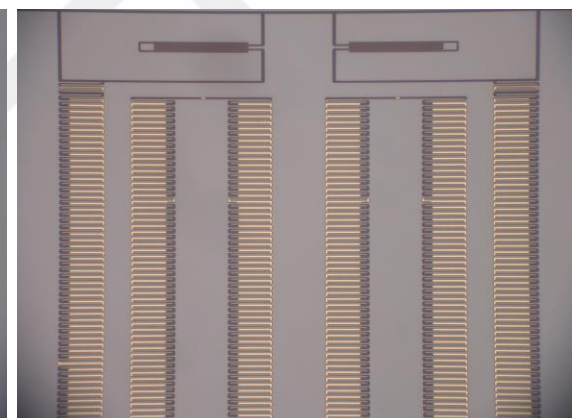
Figure 4.66: The handle layer removing process results (a) for the SOI wafer having 0.5 μm thick buried oxide layer (b) for the SOI wafer having 2 μm thick buried oxide layer.



(a)



(b)



(c)

Figure 4.67: The optical images of (a) the bottom glass-the silicon stack (b) the vertical accelerometer design-4 (c) the lateral accelerometer design-3 after releasing process.

4.2.7. Three-Electrode Anodic Bonding Optimization

It is crucial to fabricate the glass-silicon-glass sandwich structure without any problem for proper fabrication of the three axis accelerometer. One of the proposed

fabrication processes is the two-step anodic bonding for the formation of the sandwich structure. In terms of fabrication process flow, the handle layer is removed, and the devices are released after the handle layer thinning. The bottom glass-the silicon stack including the suspended structure is anodically bonded to the top glass by using the second anodic bonding. There are two challenges. The first one is to form the sandwich structure, and the second one prevents the bonding of the suspended structure to the top glass during the second anodic bonding. In the first fabrication part, the two-electrode anodic bonding optimization is explained. However, it is observed that there is a strong interaction between the chuck of the bonder and the sandwich structure. The main reason of this is related with not being grounded the silicon region between glass wafers. As the silicon is not grounded during the second bonding, there is charge storage, and this most probably causes to the interaction of the triple stack with the chuck of the bonder. Therefore, the bonding process optimization is repeated for three-electrode anodic bonding represented in [65].

As the silicon is placed between glass wafers, three flags of the chuck of the bonder are used for grounding purposes. Figure 4.68 shows the illustration of the second anodic bonding.

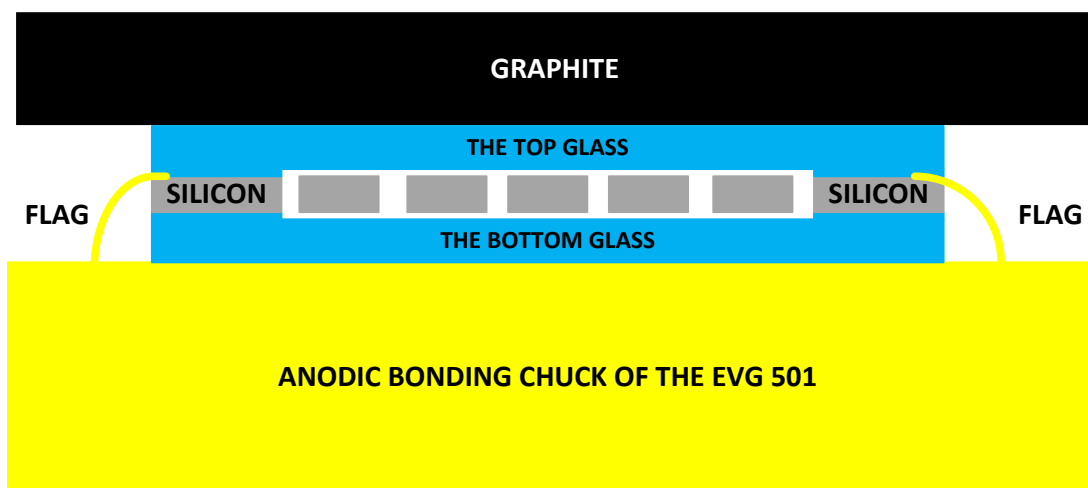


Figure 4.68: The illustration of the second anodic bonding.

The second anodic bonding is performed by using three flags of the chuck of the bonder. As flags are used, small cracks around flags region are expected as a result of height difference in these regions. However, the glass-silicon-glass sandwich structure completely broken. Figure 4.69 shows the triple stack after the second anodic bonding.

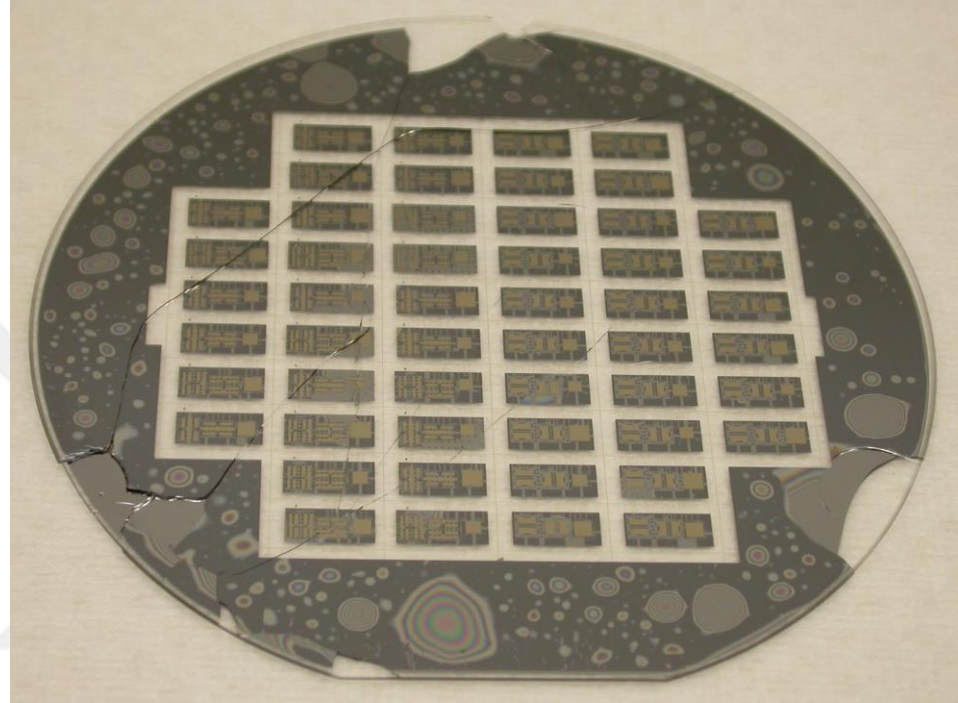


Figure 4.69: The triple stack is broken after the second anodic bonding.

In the first attempt, three flags are used. The thickness of flags is nearly $30 \mu\text{m}$. This thickness creates a step height during the second anodic bonding. Therefore, it is decided to decrease the number of flags used during the second anodic bonding. Furthermore, the second anodic bonding recipe is modified. In the first attempt using three flags, the piston of the bonder is directly applied 1000 N to the triple stack. In the modified recipe, only one flag is used, and the piston force is increased step by step up to 800 N . After applying the voltage, the piston is moved to up position. Furthermore, the applied voltage duration is increased to 15 minutes. Figure 4.70 shows the triple stack fabricated in the second attempt with the modified bonding recipe. As expected, there is a small crack in the flag region.

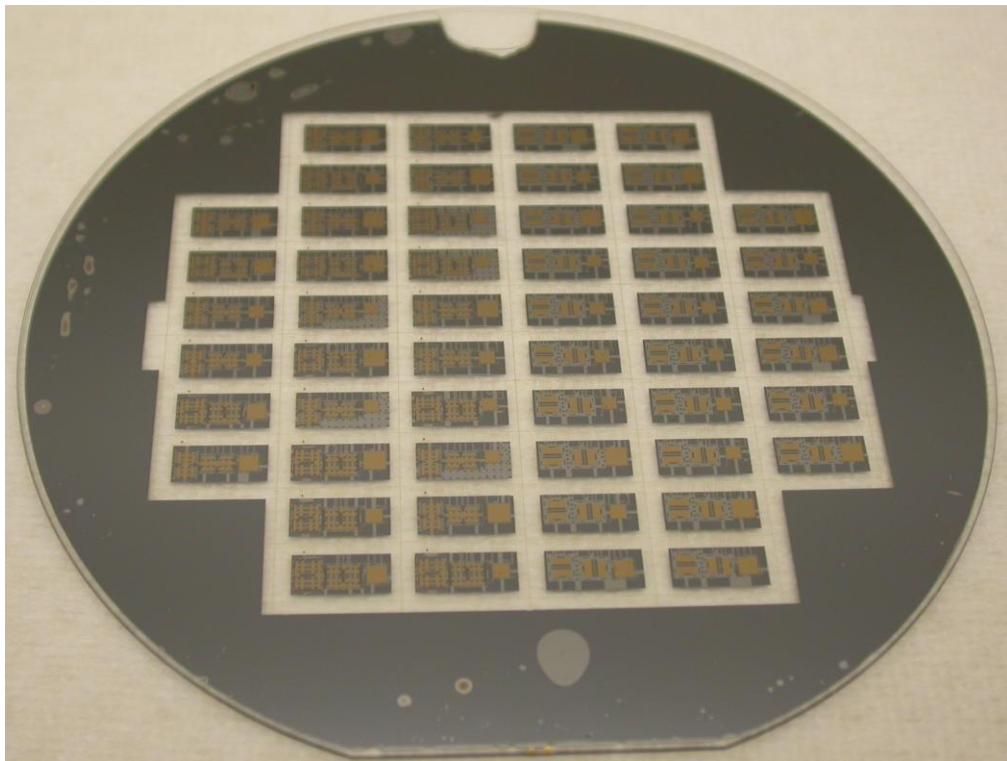
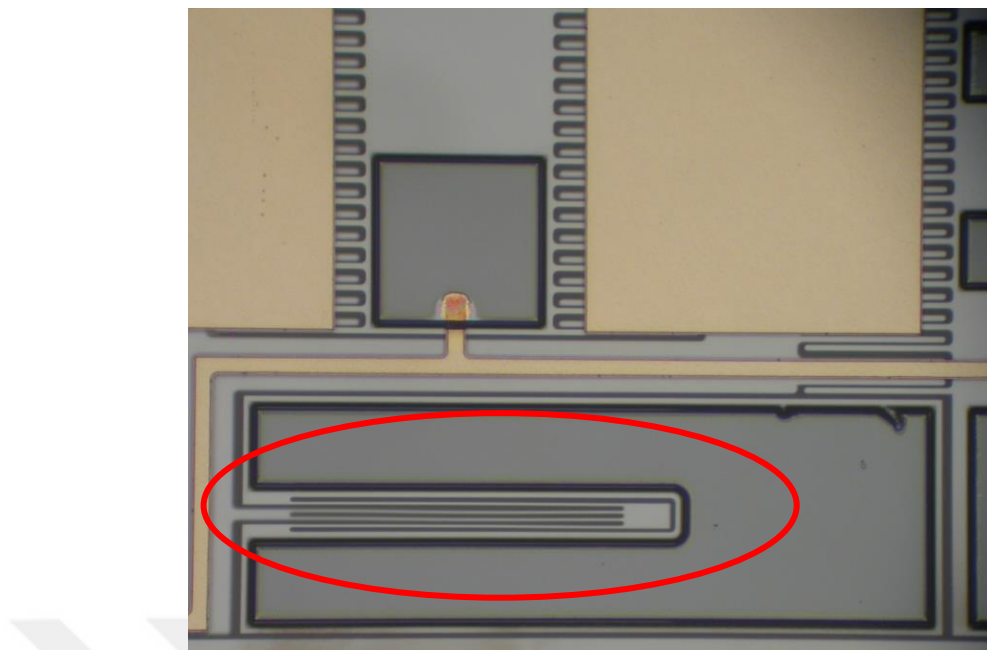
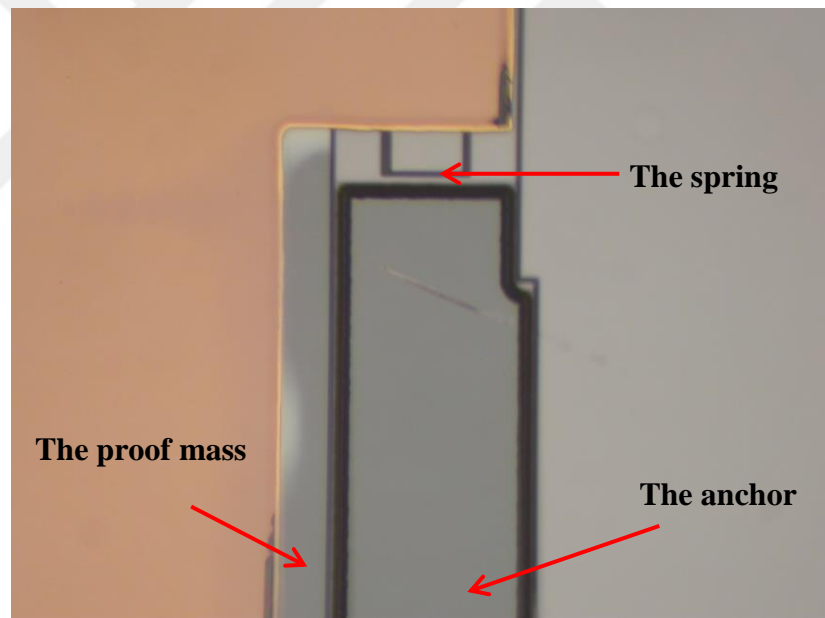


Figure 4.70: The fabricated triple stack in the second attempt. There is small crack in the flag region.

The problem is solved with the modified recipe. However, when sensors are observed under the microscope, it is recognized that the lateral accelerometer is completely damaged. Figure 4.71 shows different designs of the lateral accelerometer after the second anodic bonding. It is observed that the spring region of the lateral accelerometer design-1 and design-3 is exposed to the potential difference during the second anodic bonding as the shield metallization is not placed under the spring region. However, the structural damage looks less for the lateral accelerometer design-2 whose shield metallization almost corresponds to the entire suspended region of the accelerometer. Moreover, vertical accelerometer designs survive after the second anodic bonding as capacitive electrodes also behaves like the shield metallization for them. Therefore, the metal mask is updated for lateral accelerometers, and the shield metallization is expanded as much as possible to solve this problem. Figure 4.72 shows the modified the metal mask for lateral accelerometer designs.



(a)



(b)

Figure 4.71: (a) The spring region and (b) the proof mass of the lateral accelerometer are damaged during the second anodic bonding.

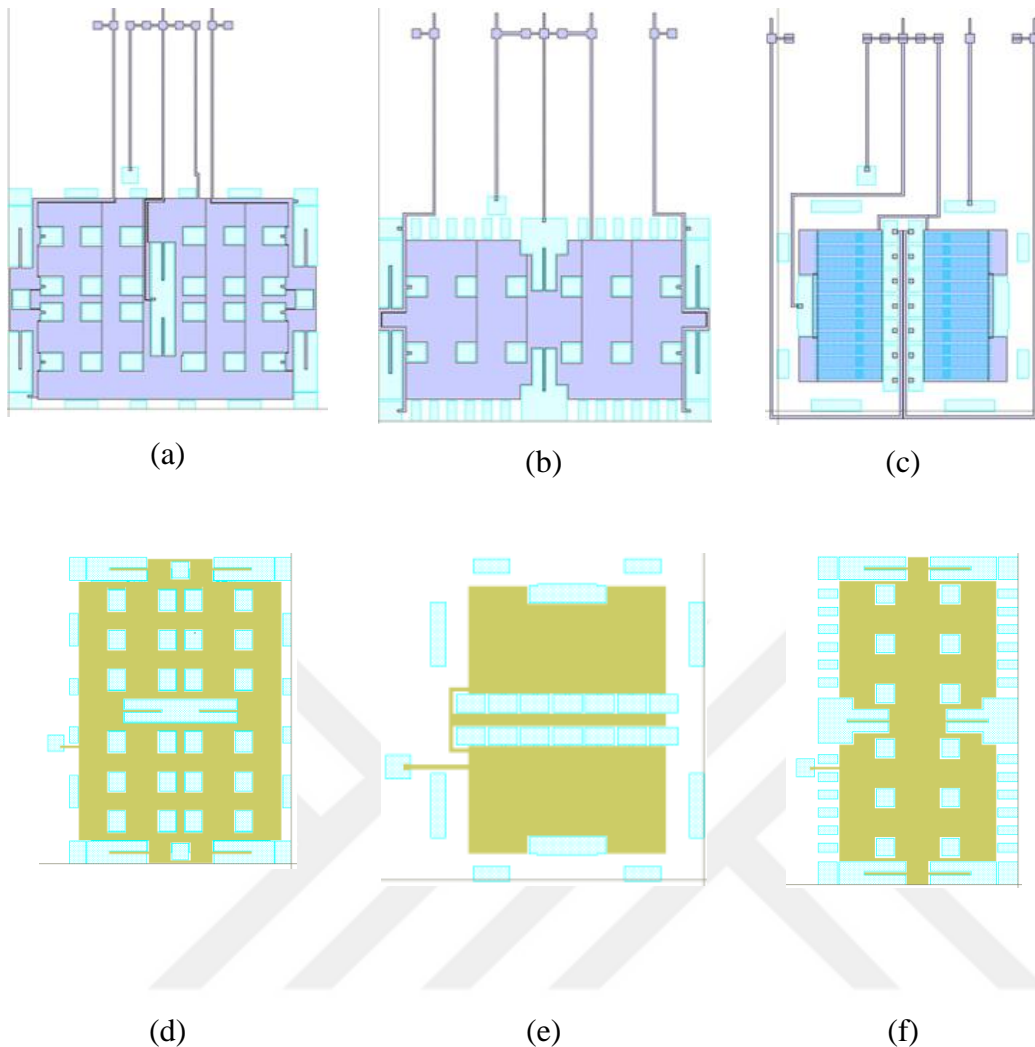
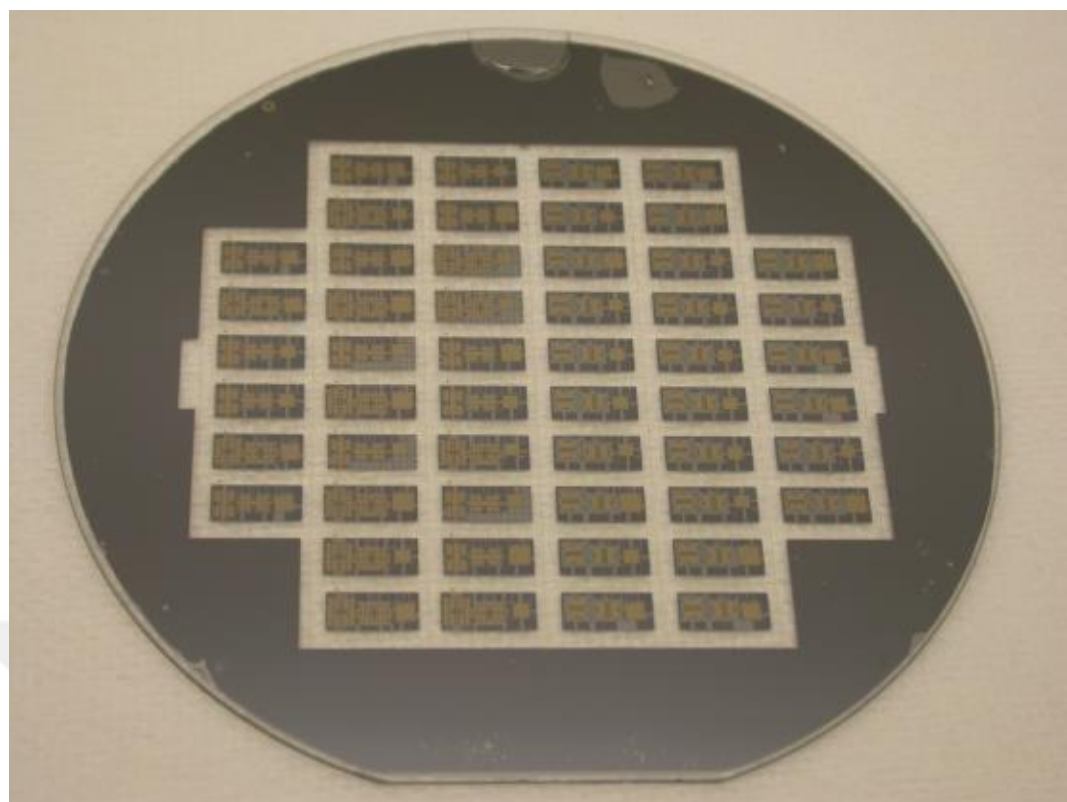
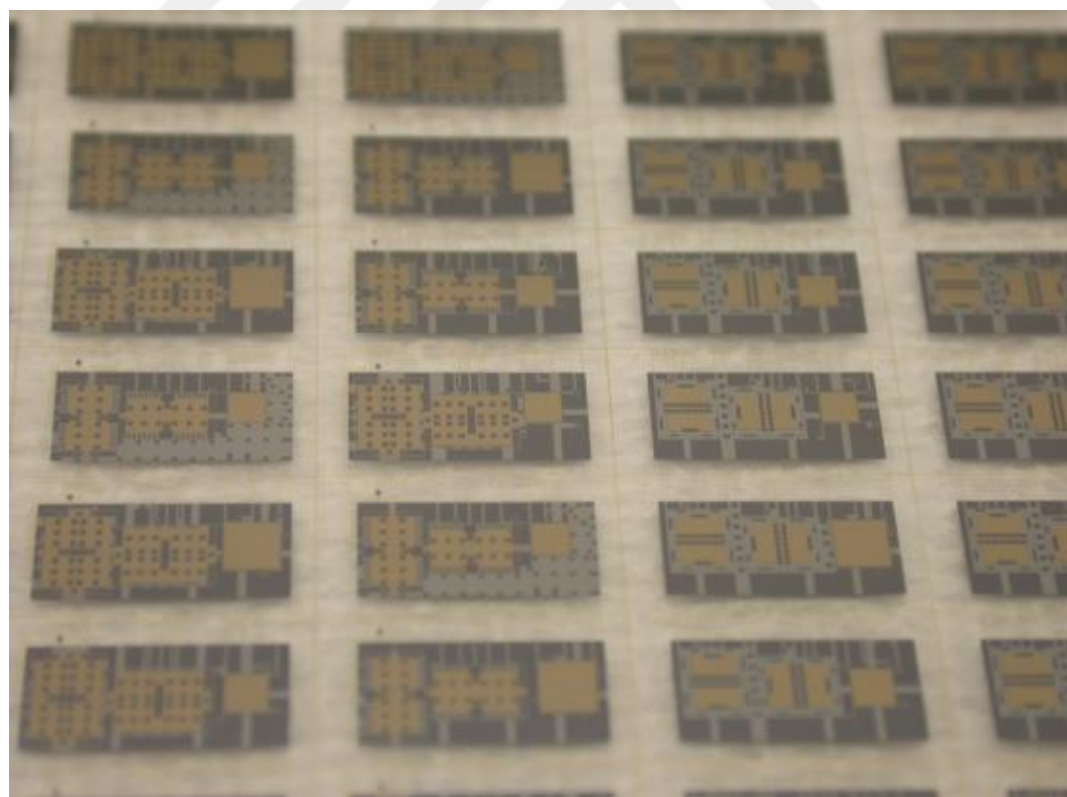


Figure 4.72: Modified metal masks for lateral accelerometer designs (a-b-c) modified bottom electrode masks (d-e-f) modified top electrode masks

After the fabrication of the new shield metallization mask, the three axis accelerometer sensor wafer fabrication is completed without any crack except one in the flag region by using the modified second anodic bonding recipe. Figure 4.73 shows the fabricated three axis accelerometer sensor wafer.



(a)



(b)

Figure 4.73: The fabricated sensor wafer. (a) Wafer level image (b) close view image of the sensor region.

When sensors are examined under the microscope, it is recognized that there is slightly misalignment. However, this is not a major problem as the misalignment is in the mask tolerance range. Figure 4.74 shows an optical image of the lateral accelerometer. The modified shield metallization mask eliminates the problem of the bonding of the suspended structure to the top glass during the second anodic bonding. Figure 4.75 shows the comparison of the previous and current fabrication results. The glass-silicon-glass sandwich structure is successfully formed, and three axis accelerometers are fabricated without any damage by using two-step anodic bonding process. The fabricated sensor wafer is hermetically sealed in the wafer level. The fabricated sensor die level and the system level result will be given in the following die level and system level test part.

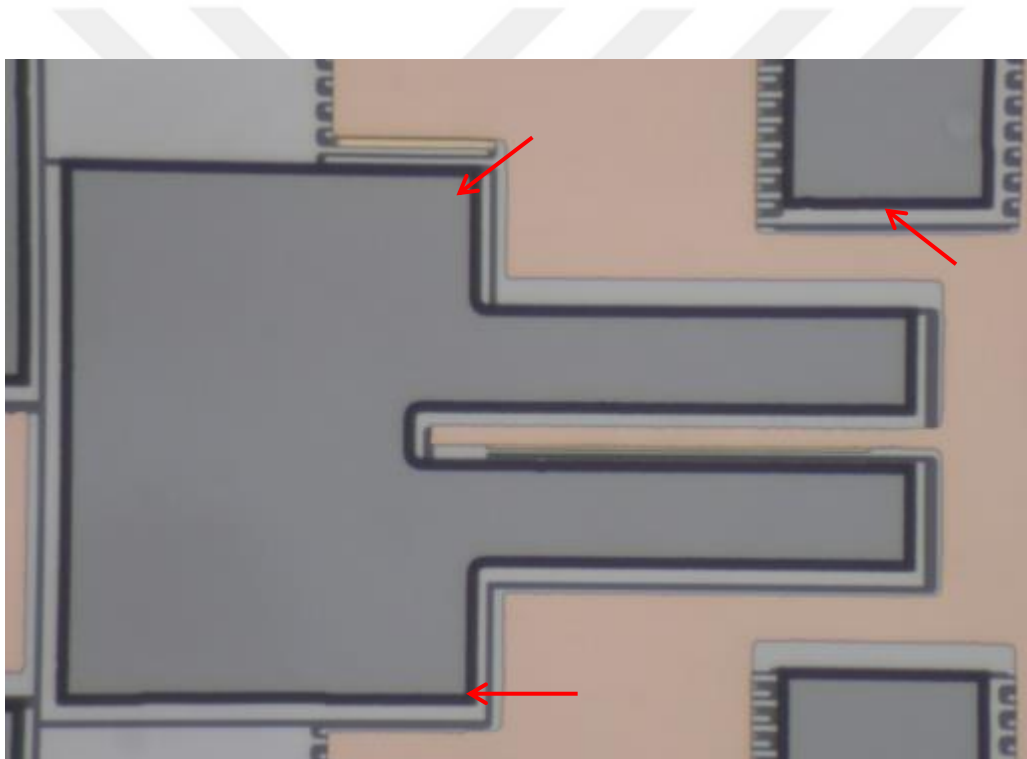


Figure 4.74: There is slightly misalignment observed after the second anodic bonding. However, this is in the mask tolerance range.

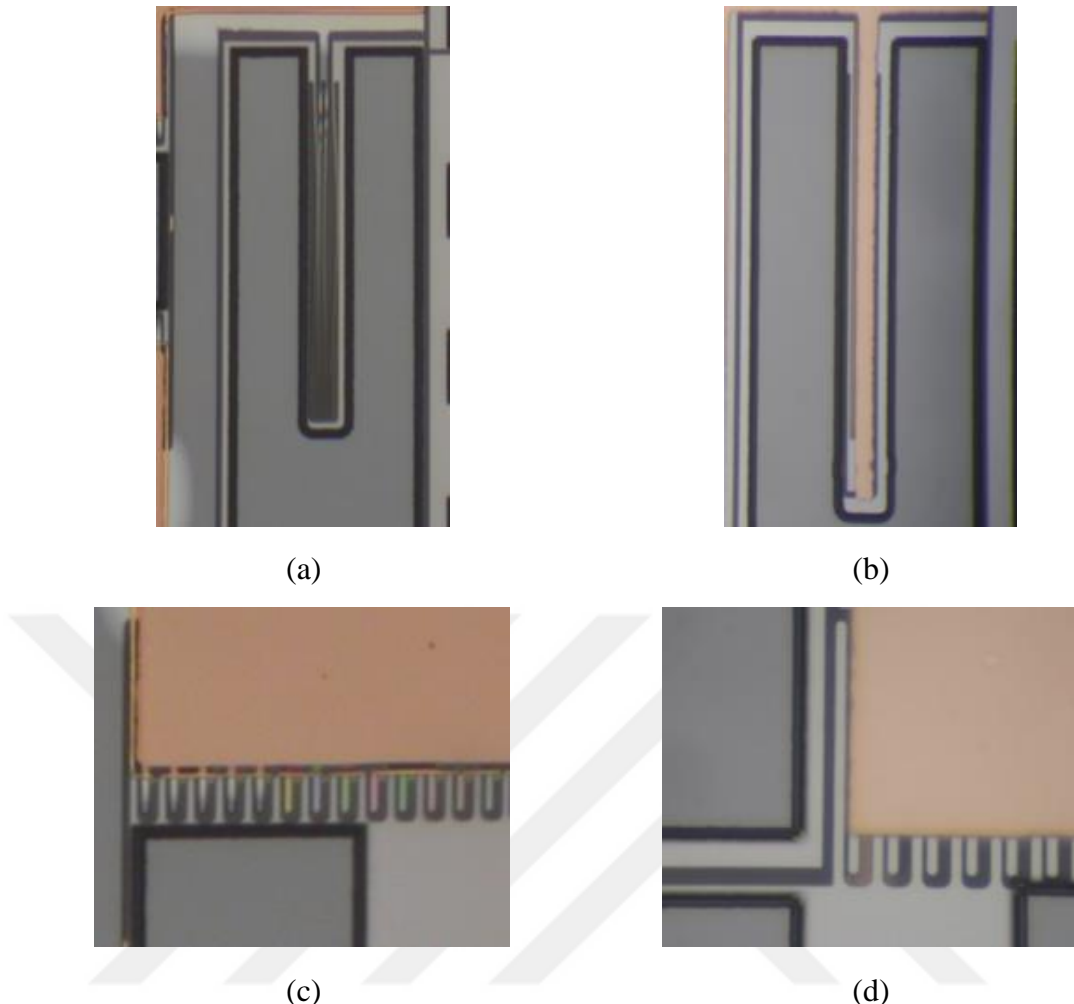


Figure 4.75: The comparison of previous (a-c) and last (b-d) fabrication runs. The damage given the suspended structure during the second anodic bonding is eliminated by modifying the shield metallization mask.

4.2.8. Anodic and then Au-Si Eutectic Bonding Optimization

The other alternative method to form the glass-silicon-glass multi-stack is to use the Au-the silicon eutectic bonding defined in [68]. The Au-Si eutectic bonding is a vital technique for microfabrication. It is possible to provide high bonding strength and good stability at a temperature (about 363°C) [69]. However, the bonding temperature of 363°C can be harmful for the temperature sensitive materials and integrated circuit [70].

The the Au-Si eutectic bonding fabrication method is a good choice to use in the last step of the formation of the glass-silicon-glass multi-stack. Furthermore, the anodic bonding and the Au-Si eutectic bonding fabrication method has some advantages in terms of the two-step anodic bonding process for the formation of the glass-silicon-glass sandwich structure. One of the advantages is related with preventing the parasitic capacitance. The two-step anodic bonding process includes shield metal region to provide same potential not only the structure but also the top and the bottom glass side. However, the shield electrode causes undesired parasitic capacitances. In the Au-Si eutectic bonding process, this can be prevented. On the other hand, the eutectic bonding is formed between gold and silicon region under condition of suitable temperature and piston force; this eliminates the risk of the bonding of the suspended structure to the top glass observed in the two-step anodic bonding.

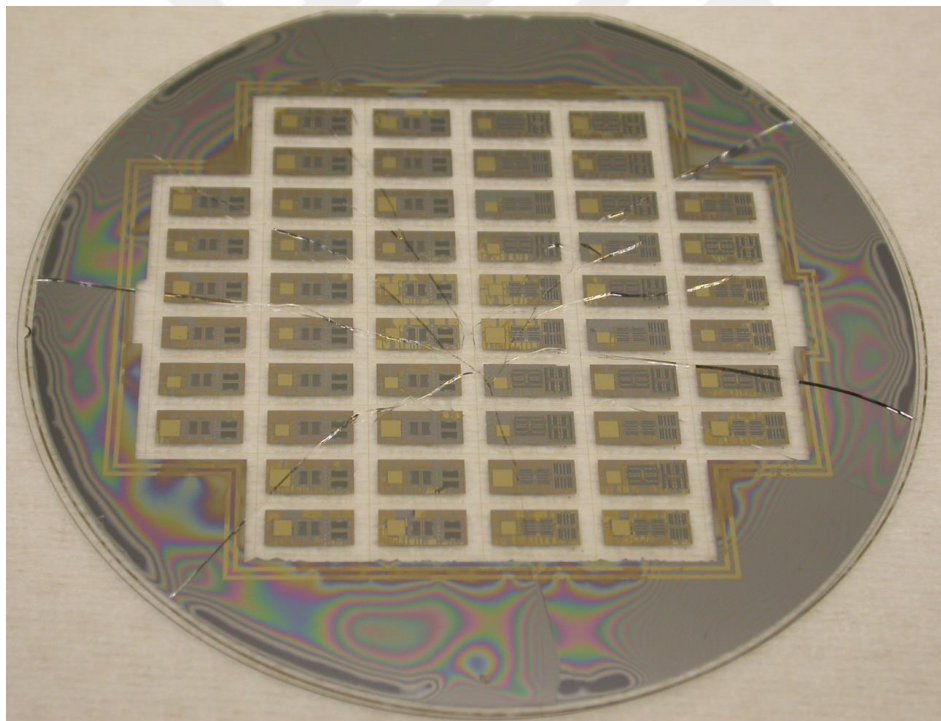


Figure 4.76: The result of the first attempt for the anodic bonding and then the Au-Si eutectic bonding. The bonding temperature and force are 390°C, 3000 N, respectively.

For the first eutectic bonding attempt, the process flow will be same with the two-step anodic bonding process except the Au-Si eutectic bonding, where the bonding temperature is 390°C applied 17 minutes, and the piston force is 3000 N. Figure 4.76 shows the fabricated sensor wafer by using the anodic bonding and then the Au-Si eutectic bonding.

After observing the crack problem, the Au-Si eutectic bonding recipe parameters are modified. In the modified bonding recipe, the temperature is increased to 300°C. Then, there is a waiting step for 30 minutes to stabilize the temperature. Next, the piston moves down position, where 1500 N force is applied to the triple stack. Then, the temperature is increased 390°C and the triple stack is exposed to this temperature for 15 minutes. Afterwards, the temperature is decreased to 300°C and the piston is lifted up position in this temperature. The modified Au-Si eutectic bonding recipe solves the observed problem. Figure 4.77 shows the fabricated triple stack after the eutectic bonding.

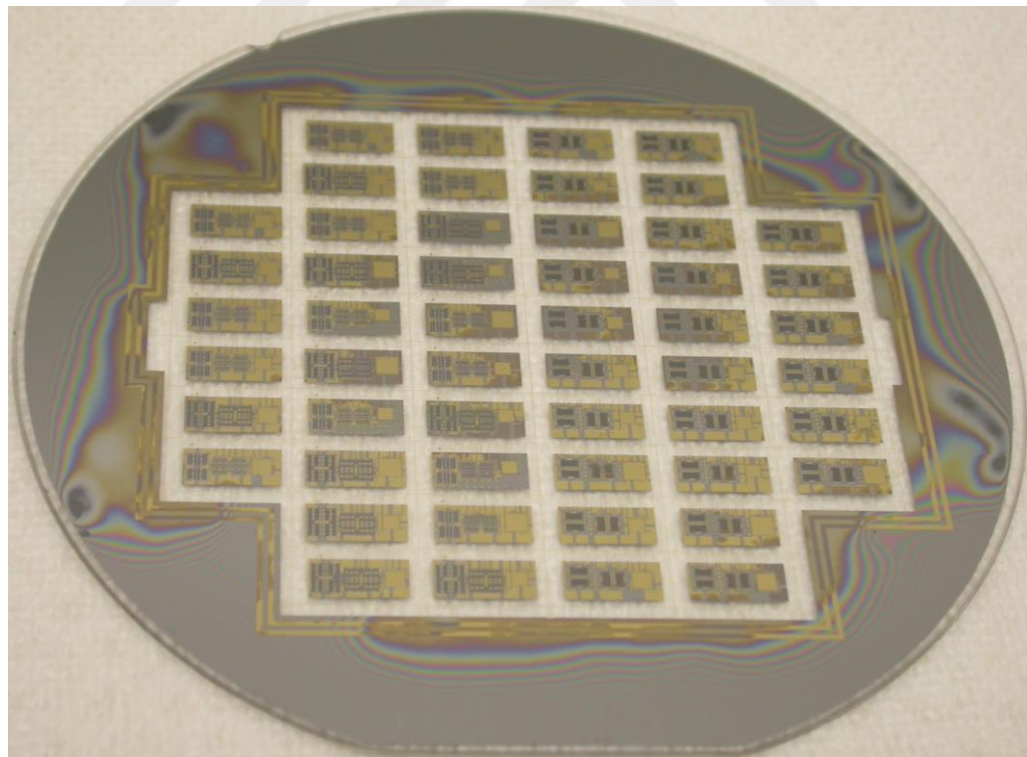


Figure 4.77: The fabricated glass-silicon-glass sandwich structure by using the Au-Si eutectic bonding.

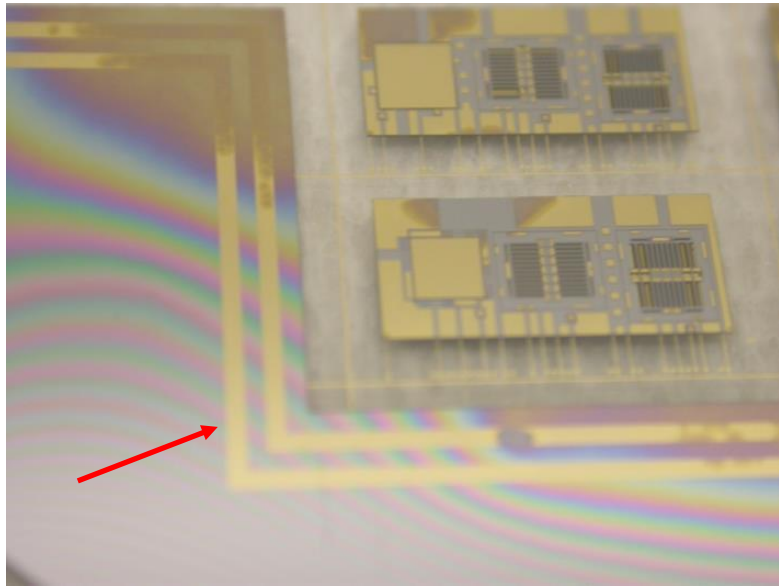


Figure 4.78: The color of the gold frame around the sensor region is not uniform.

Although the Au-Si eutectic bonding is completed without any problem, the gold frame around the sensors seems having unbounded areas. Figure 4.78 shows the gold frame around the sensor region. It is seen that the color of the gold frame is not uniform. As mentioned in the previous section, the sandwich structure is exposed to the water flow during the dicing step. Therefore, it is necessary to provide wafer level sealing after the Au-Si eutectic bonding. Therefore, by using the current recipe, the bonding temperature is increased from 390°C to 400°C . The same triple stack shown Figure 4.77 is used with the modified bonding recipe. However, the gold ring around the sensors again is not properly bonded although there is an improvement in the eutectic bonding.

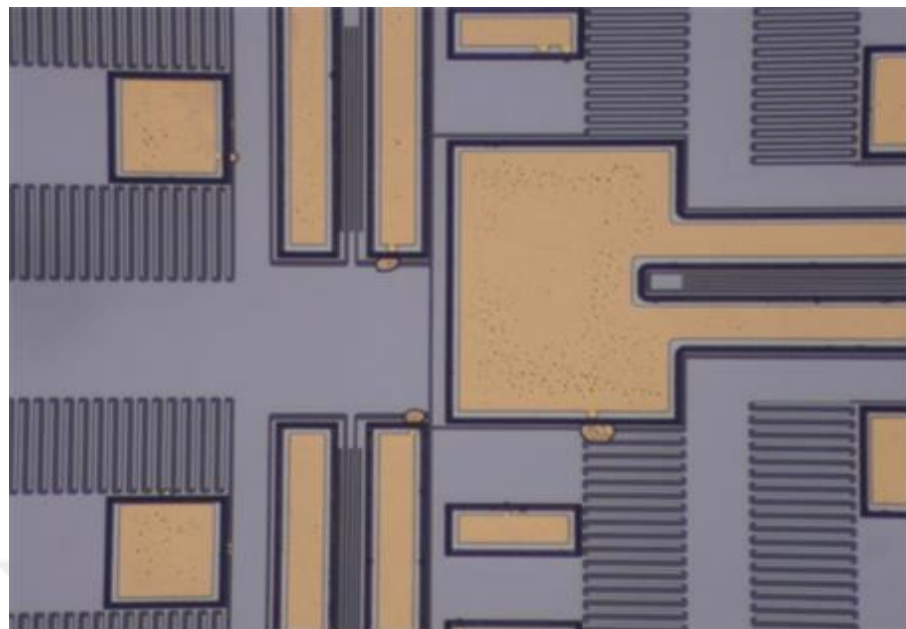
After these results, the optimization of the Au-Si eutectic bonding recipe is continued to improve the bonding quality and to provide hermetically sealing in the wafer level. Therefore, not only the temperature but also piston force values are changed in the modified the Au-Si eutectic bonding recipe. The temperature and piston force are set 410°C , 2500 N, respectively in the second attempt. However, it is observed that the gold is melted and spreads around. Furthermore, contact regions seem damaged after applying 410°C , 2500 N. Figure 4.79 shows the result of the second attempt. The temperature and piston values are too high to obtain functional three axis

accelerometer with these recipes. Therefore, these parameters are accepted as upper limits for the eutectic bonding.

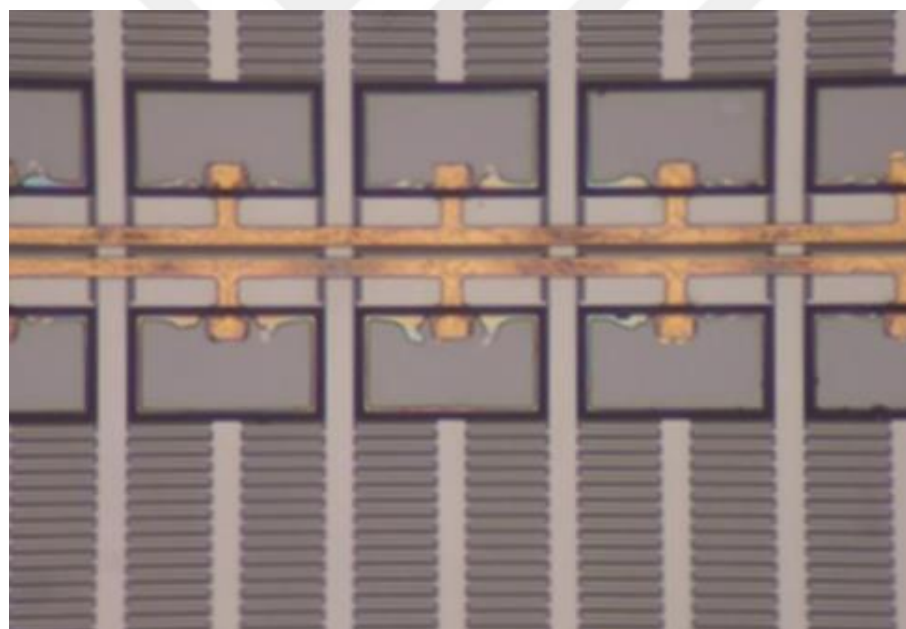
In fabrication run# 3, the temperature is decreased 400°C and the piston force is set 2500 N. The metal contacts look good. However, the gold frame around the sensor region is not properly bonded. The metallization used in the fabrication process is sputtered by using sputtering system in all of these attempts. Therefore, in the last attempt, the metallization of the bottom glass is deposited by using sputtering system, and the top glass metallization is deposited by using the evaporator. The temperature is decreased 390°C and the piston force is set 2500 N. The bonding result looks quite good with this configuration. The color of the gold frame is almost same except small region located in the edge of the wafer. Figure 4.80 and Figure 4.81 shows all of the fabricated wafers by using the modified eutectic bonding with different temperature and piston values. Figure 4.82 shows close view image of the fabricated sensors. Figure 4.83 shows the comparison of the Au-Si eutectic regions for different recipes. Figure 4.84 shows the contact regions of the fabricated sensor with the recipe 390°C and 2500 N. Table 4.4 shows different temperature and piston values used in the modified Au-Si bonding recipe.

Table 4.4: Temperature and piston values used during the optimization of the Au-Si eutectic bonding recipe.

| Run# | Bottom glass metallization | Top glass metallization | Temperature (°C) | Piston Force (N) | Contact Region | Sealing |
|------|----------------------------|-------------------------|------------------|------------------|----------------|---------|
| 1 | Sputtering | Sputtering | 390 | 1500 | Good | ✗ |
| 2 | Sputtering | Sputtering | 400 | 1500 | Good | ✗ |
| 3 | Sputtering | Sputtering | 410 | 2500 | Damaged | ✗ |
| 4 | Sputtering | Sputtering | 400 | 2500 | Good | ✗ |
| 5 | Sputtering | Evaporation | 390 | 2500 | Good | ✓ |

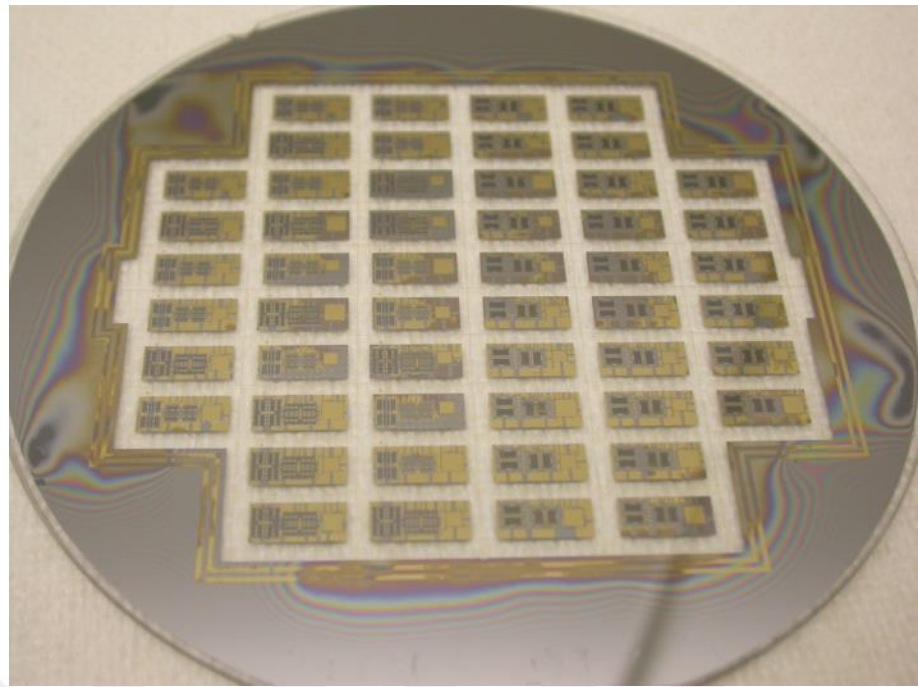


(a)

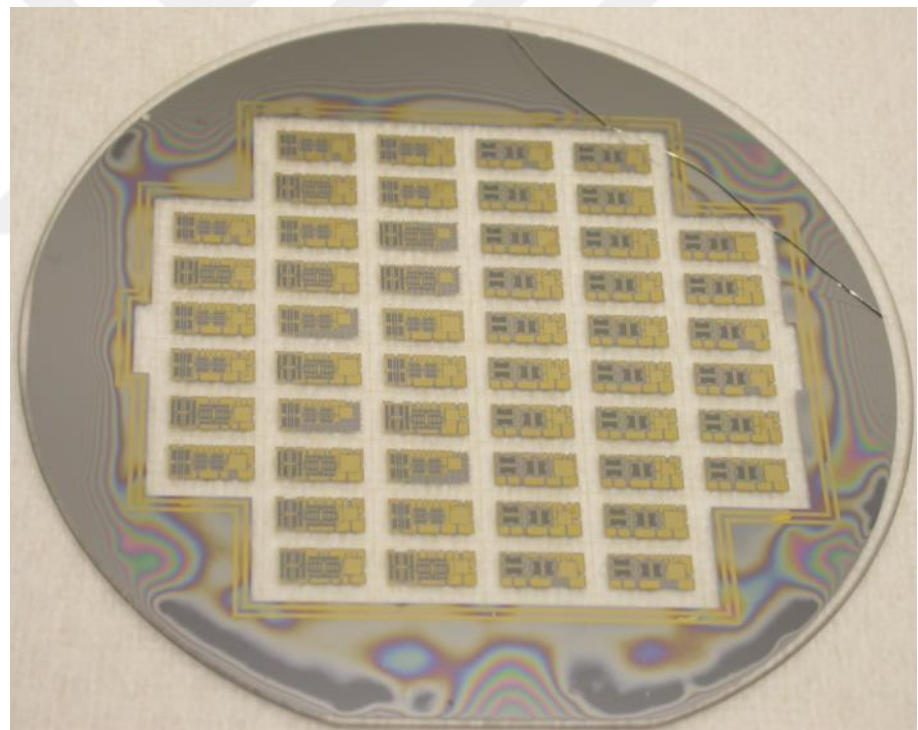


(b)

Figure 4.79: The result of the Au-Si eutectic bonding for 410°C and 2500 N. (a) The gold is melted and spreads around. (b) Contacts regions are damaged after the eutectic bonding.

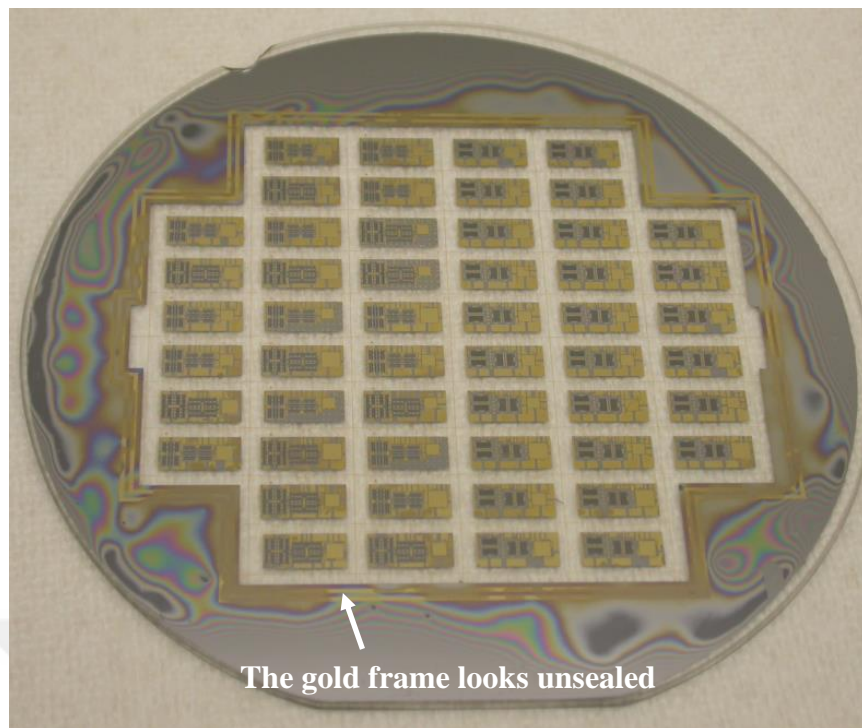


(a) Fabrication run#1 and run#2

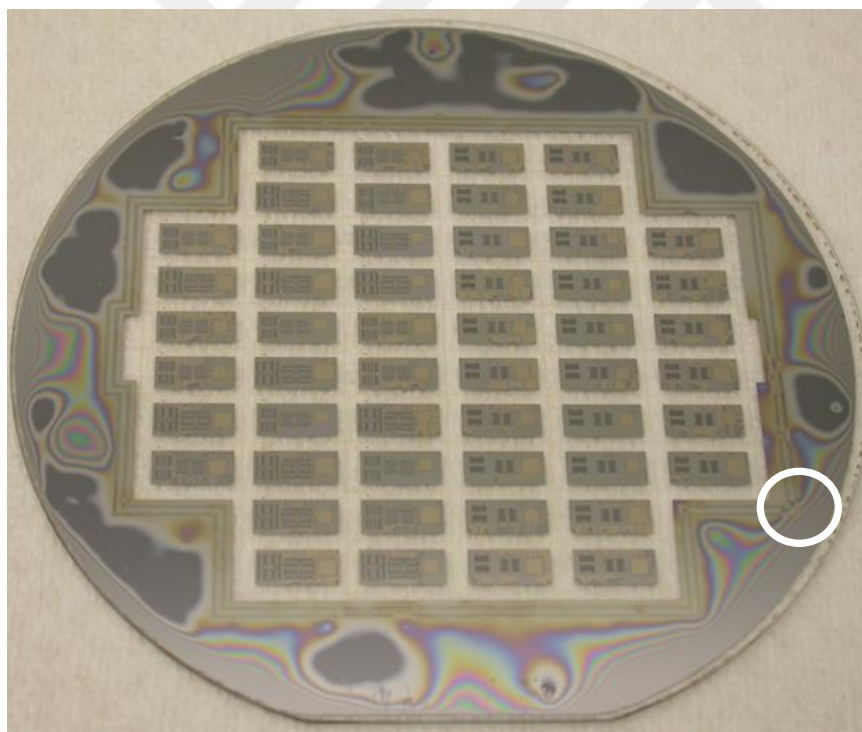


(b) Fabrication run#3

Figure 4.80: The fabricated wafer during the optimization process of the Au-Si eutectic bonding. The temperature and the piston value (a) 390°C and 1500 N and 400°C and 1500 N (b) 410°C and 2500 N.



(c) Fabrication run#4



(d) Fabrication run#5

Figure 4.81: The fabricated wafer during the optimization process of the Au-Si eutectic bonding. The temperature and the piston value (a) 400°C and 2500 N (b) 390°C and 2500 N.

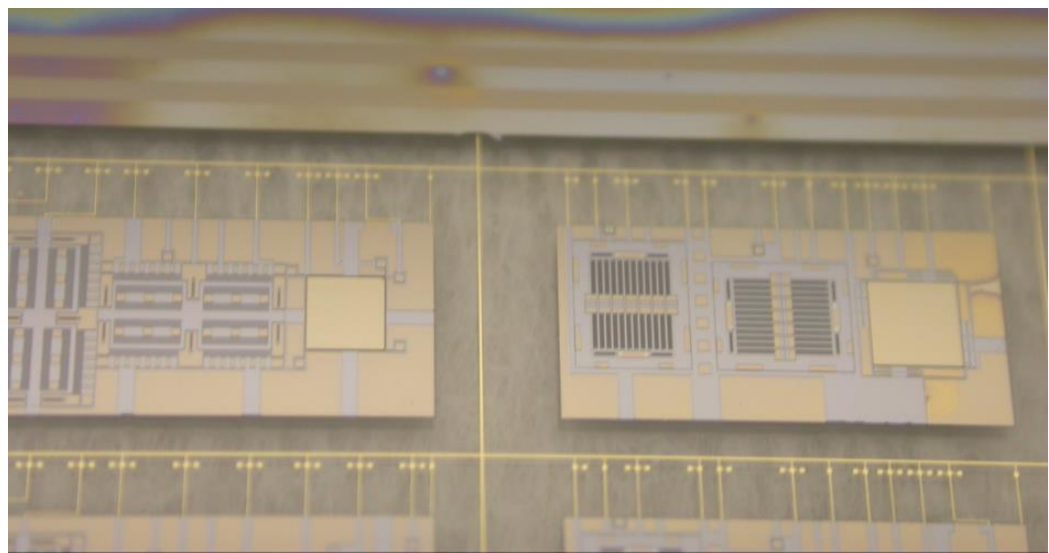


Figure 4.82: Close view of sensor region after the Au-Si eutectic bonding (390°C and 2500 N).

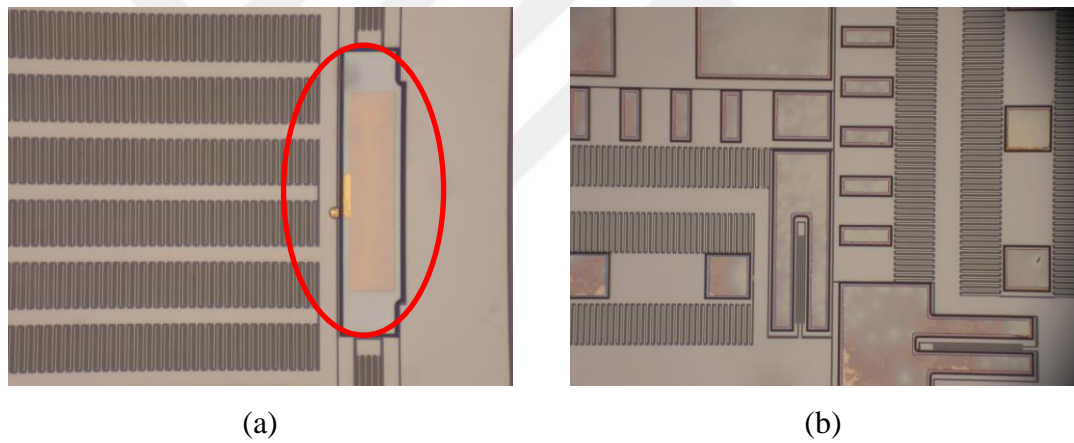


Figure 4.83: The comparison of the Au-Si eutectic bonding (a) 400°C and 2500 N (b) 390°C and 2500 N.

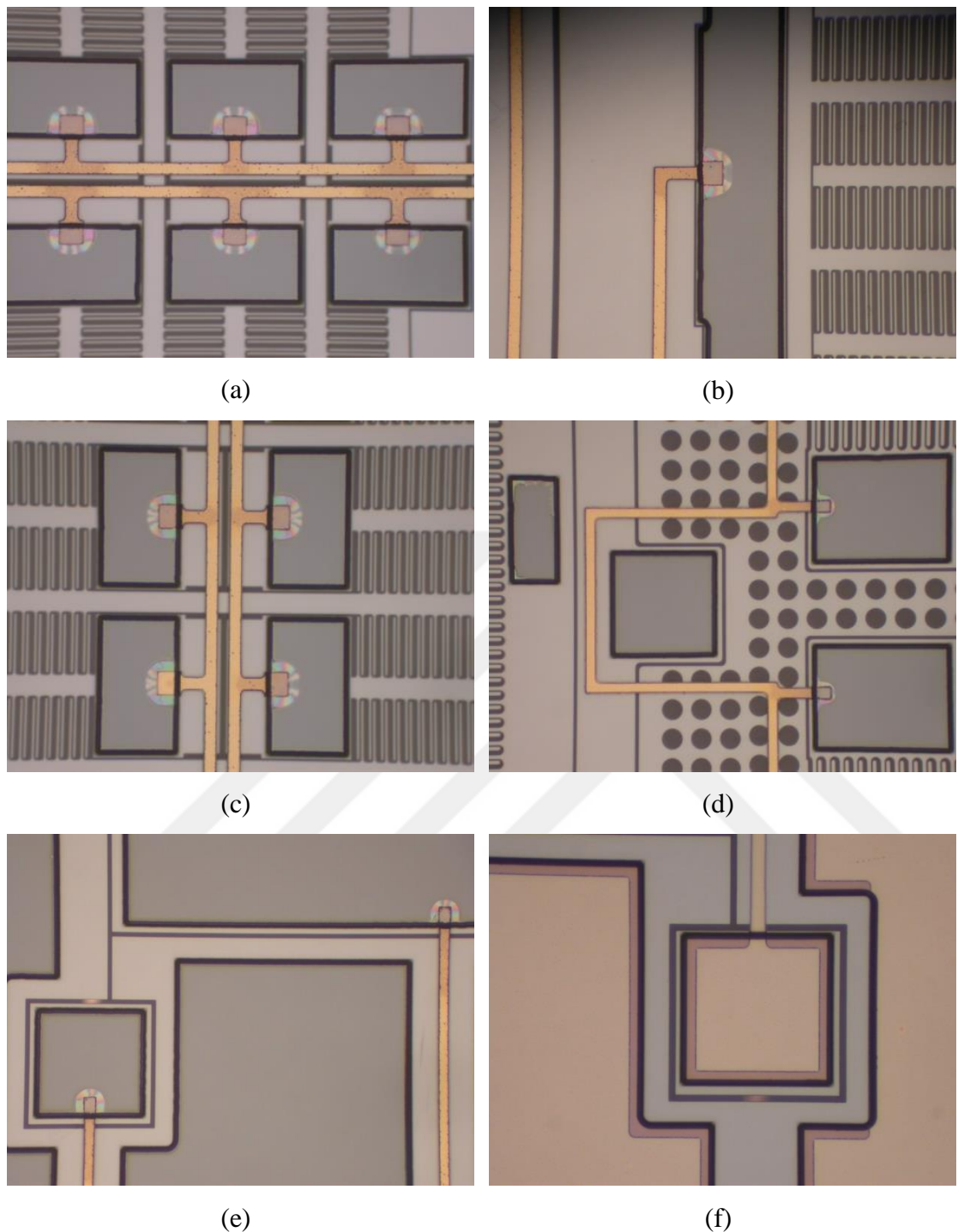


Figure 4.84: (a-d) Contacts regions of lateral accelerometers. (e) The bottom electrode contact region of the vertical accelerometer. (f) The top electrode contact region of the vertical accelerometer.

4.2.9. Two-Step Dicing Process

The two-step dicing process, which is explained in 4.1.7, is applied for fabricated wafers. The wafer-level sealing of the sensor wafer, which is fabricated with the two step-anodic bonding, is spontaneously provided as a result of the fabrication process feature. Therefore, there is not a risk of leaking water inside to the sensor region during the dicing process for the wafer shown in Figure 4.73 (a). However, there is a risk of leaking the water inside to the triple stack for the wafer shown in Figure 4.85 as the color of the gold frame in the right edge of the wafer is not uniform. Therefore, the photoresist is spilled between the sandwich structures to eliminate this risk. Then, sensor wafers are successfully diced, and pad metals are uncovered. However, the top glass of some of sensors detaches from the bottom-glass silicon stack while they are being manually separated from each other. Figure 4.86 shows one of sensors of which the top glass detaches from the bottom glass silicon stack. Figure 4.87 shows an SEM image of the glass-silicon-glass sandwich structure. Figure 4.88 shows diced sensors.

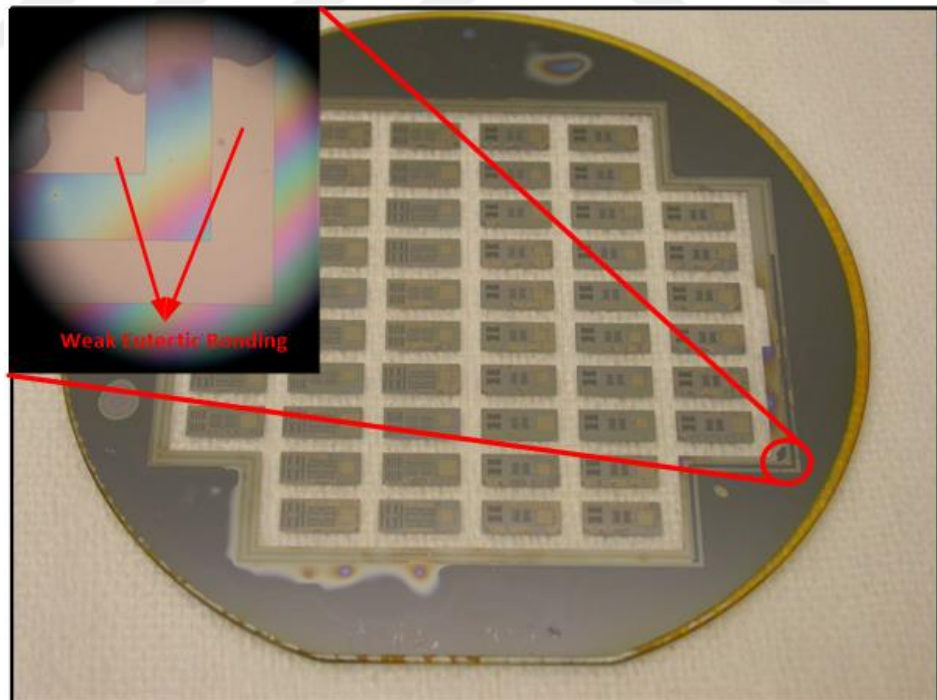


Figure 4.85: The photoresist is spilled into the glass-silicon-glass sandwich structure to eliminate the risk of leaking water during the dicing process.

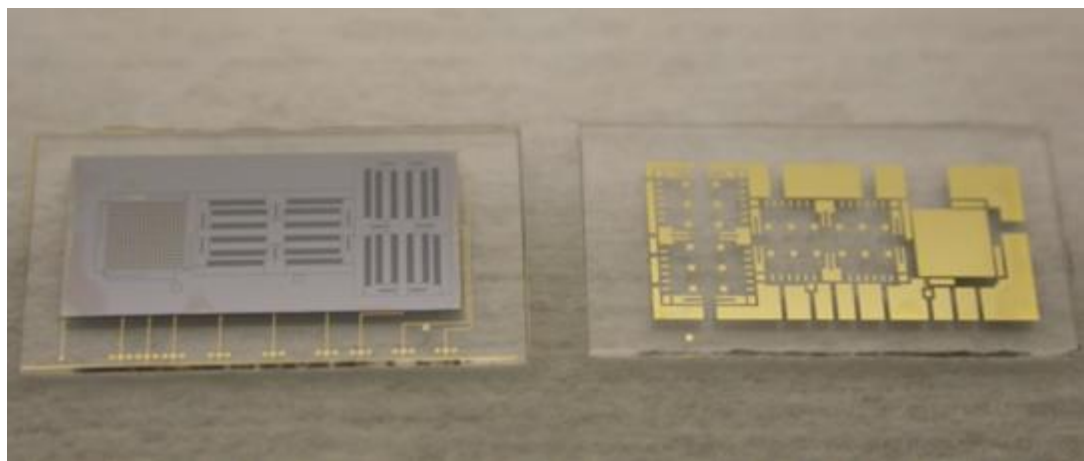


Figure 4.86: The top glass of some of sensors, which is fabricated by using the anodic bonding and then Au-Si eutectic bonding, detaches from the bottom glass-silicon stack

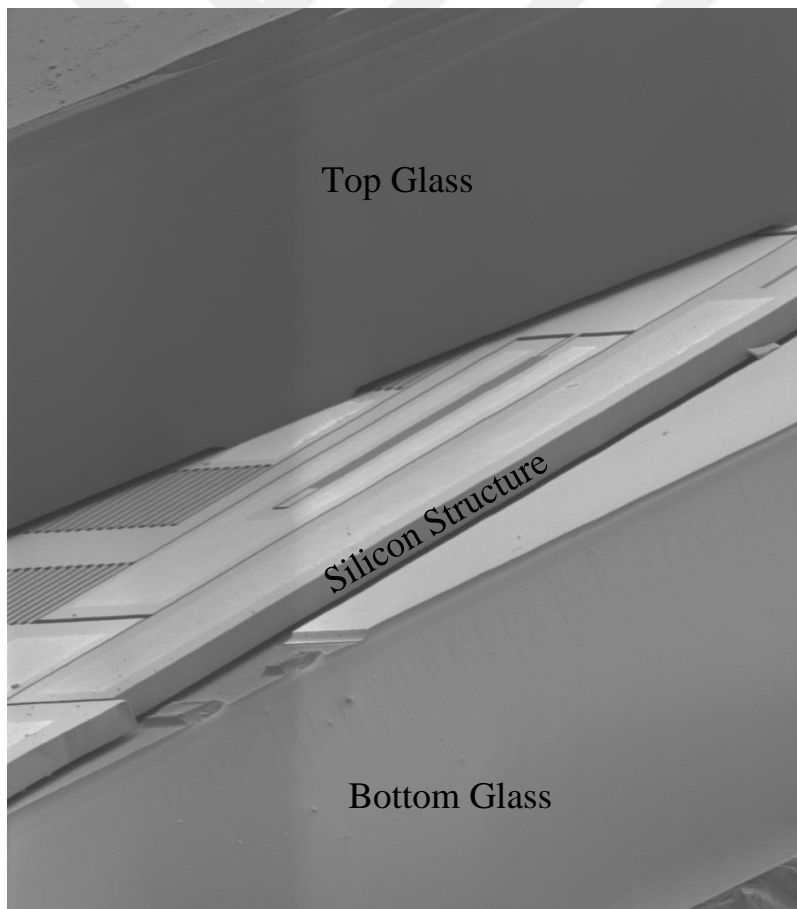
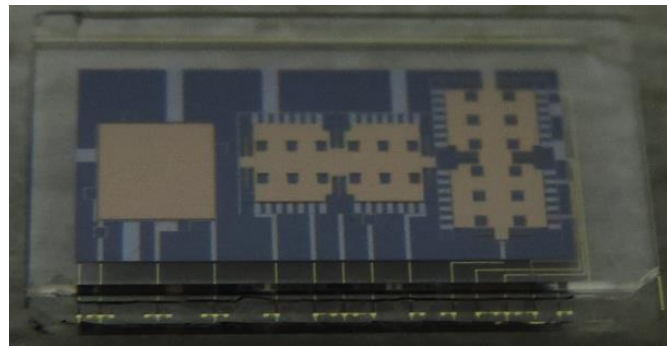
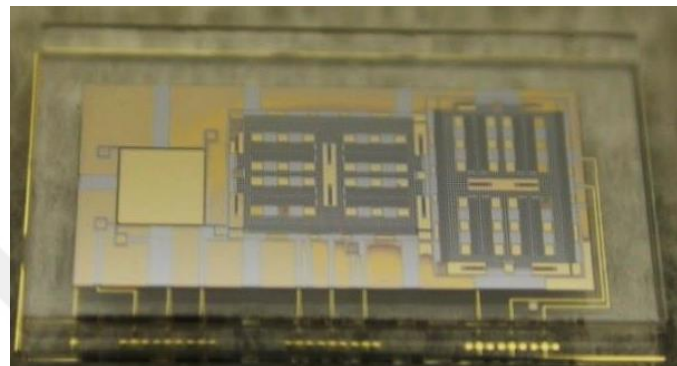


Figure 4.87: An SEM image of the glass-silicon-glass sandwich structure fabricated by using the anodic and then the Au-Si eutectic bonding.



(a)



(b)

Figure 4.88: Diced sensor for (a) fabricated with the two-step anodic bonding (b) fabricated with the anodic bonding and then the Au-Si eutectic bonding.

4.3. Summary of the Chapter

The formation of the glass-silicon-glass sandwich structure is summarized with two different fabrication methods: the two-step anodic bonding and the anodic bonding and then Au-Si eutectic bonding. Problems observed during the fabrication process, and solutions are comprehensively explained in this section.

The vertical gap optimization, the deposition of an insulator layer on silicon, the structural DRIE, the first anodic bonding, the thinning of the handle layer of SiGeB and SOI wafers, the two step anodic bonding by using the two-electrode method, the two-step dicing process optimization are given in this section for the fabrication mask set-1. The first fabrication masks set shows the feasibility of the proposed fabrication process. Then, in the second mask set, performance parameters of there-

axis accelerometers are mainly considered. To solve interaction problem observed between the chuck of the bonder and the glass-silicon-glass multi-stack, the three-electrode method optimization is performed. Furthermore, the anodic bonding and then the Au-Si eutectic bonding is optimized as an alternative method for the formation of the triple stack.

Figure 4.89 shows the summary of the fabrication process for the formation of the glass-silicon-glass multi stack. Figure 4.90 shows process steps of the final optimized process.

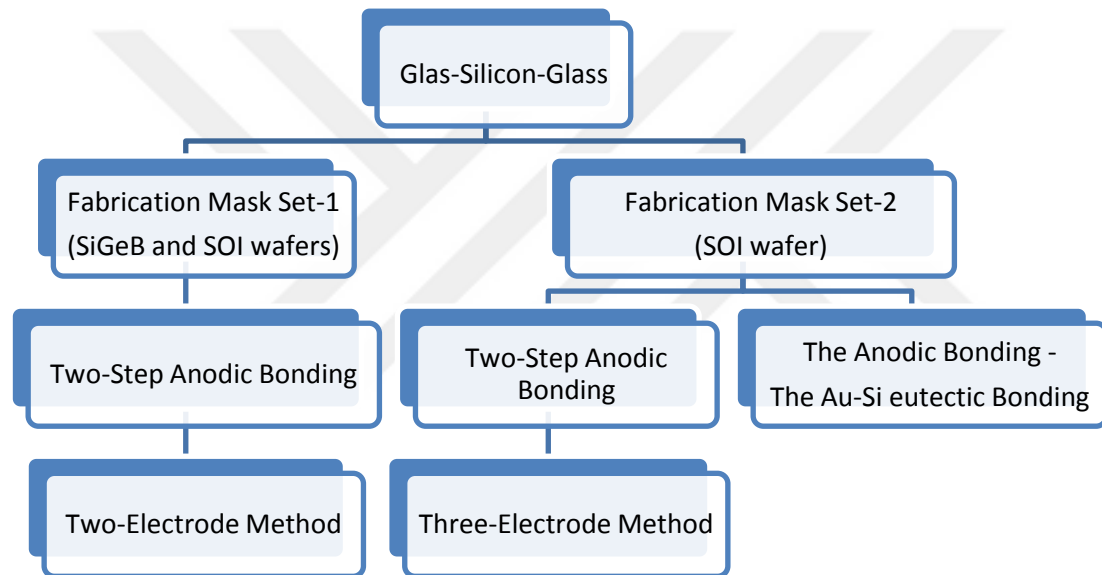


Figure 4.89: The summary of the fabrication optimization for the three-axis accelerometer implemented with the glass-silicon-glass multi-stack.

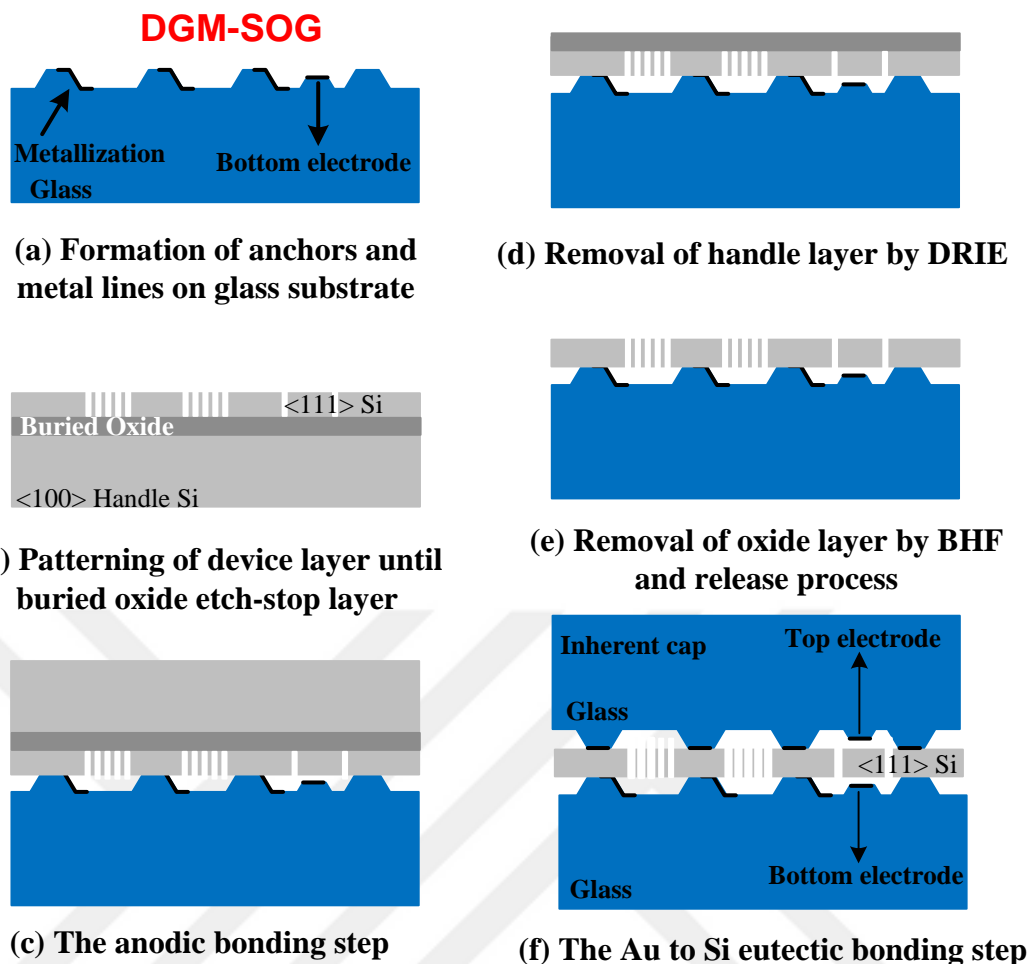


Figure 4.90: Optimized process steps for the fabrication of the three-axis accelerometer.



CHAPTER 5

THE DIE LEVEL AND SYSTEM LEVEL TEST

This chapter presents die level and system level test results of the three-axis accelerometer fabricated by using DGM-SOG process with the two-step anodic bonding as well as the anodic bonding and then the Au-Si eutectic bonding methods. The rest capacitance and the capacitance change with respect to the applied voltage (C-V) are determined for individual lateral and vertical accelerometers. Moreover, the resonance frequency of the lateral and the vertical accelerometer are measured. The test result is compared with theoretical calculations of design parameters. The system level test is performed by the functional three-axis accelerometer. Then, three-axis accelerometer is connected to a readout circuit presented in [71]. The noise level, the bias instability and the expected dynamic range are determined.

5.1. Die Level C-V Test

The die level test is performed in order to verify the functionality of the three-axis accelerometer. Therefore, lateral and vertical accelerometers are individually tested to observe the rest capacitance and the C-V change characteristics. Moreover, resonance frequencies of the fabricated sensors are measured by using the automatic probe station.

5.1.1. C-V Measurement Test

The C-V measurement test is performed by using the Agilent Precision Impedance Analyzer 4294A. Figure 5.1 shows the Agilent Precision Impedance Analyzer 4294A

used during the C-V measurement. Three-axis accelerometer sensors are placed under the probe station and fixed by using the vacuum chuck of the probe station (Figure 5.2). The calibration is important step before the C-V measurement. The calibration of the Agilent Precision Impedance Analyzer 4294A is performed with open and short tests. During the open test, the manipulator of the probe station is aligned on metal pads of the three-axis accelerometer. Then, the calibration is performed by pushing open test button on Impedance Analyzer 4294A. Next, when tips of manipulator gets contact from metal pads of three-axis accelerometer, the short test button on the Impedance Analyzer 4294A is pushed. Each of lateral and the vertical accelerometers located in the same die are measured separately by applying DC bias voltages between their proof masses and one of their electrodes while their other electrodes are connected to ground for eliminating the parasitic capacitance during the die level tests.



Figure 5.1: Agilent Precision Impedance Analyzer 4294A used during the C-V test.

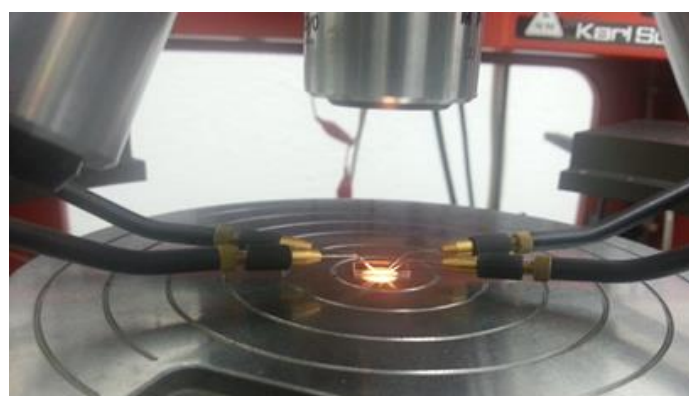


Figure 5.2: The C-V measurement test setup for the three-axis accelerometer.

5.1.2. The Resonance Frequency Test

The resonance test of the three axis accelerometer is performed under the vacuum environment (approximately 10 mTorr) by using the automatic probe station (Figure 5.3). Three-axis accelerometer sensors are fixed on a dummy wafer as the chuck of the automatic probe station is in the wafer level. Then, the proof mass voltage and AC source are provided by using the power supply and the dynamic signal analyzer, respectively. The dynamic signal analyzer is capable of sweeping the desired frequency and gives the resonance frequency characteristic of sensors.



Figure 5.3: The resonance frequency test is performed by using the automatic probe station.

5.2. The System Level Test

It is necessary to integrate the three-axis accelerometer with the readout circuit reported in [71] into a 16 pin package to take the system level result from three-axis accelerometers of which functionality is verified with the C-V and resonance measurements. Therefore, a glass substrate is designed and fabricated. One of the challenges is to fit the glass substrate in the 16 pin package. Therefore, a proper design of the glass substrate is important. The clock line is intentionally drawn as large as possible during the design and tried to isolate by drawing an additional

ground line from other metal lines. Figure 5.4 shows the designed glass substrate and the wire bonding diagram for the integration of the three-axis accelerometer with the readout circuit. Figure 5.5 shows the fabricated glass substrate. After the fabrication, the three-axis accelerometer and readouts are placed on the glass substrate, and then the glass substrate is stacked to the 16 pin package. Figure 5.6 shows the 16 pin package used during the system level test. Figure 5.7 shows the prepared package of the three-axis accelerometer.

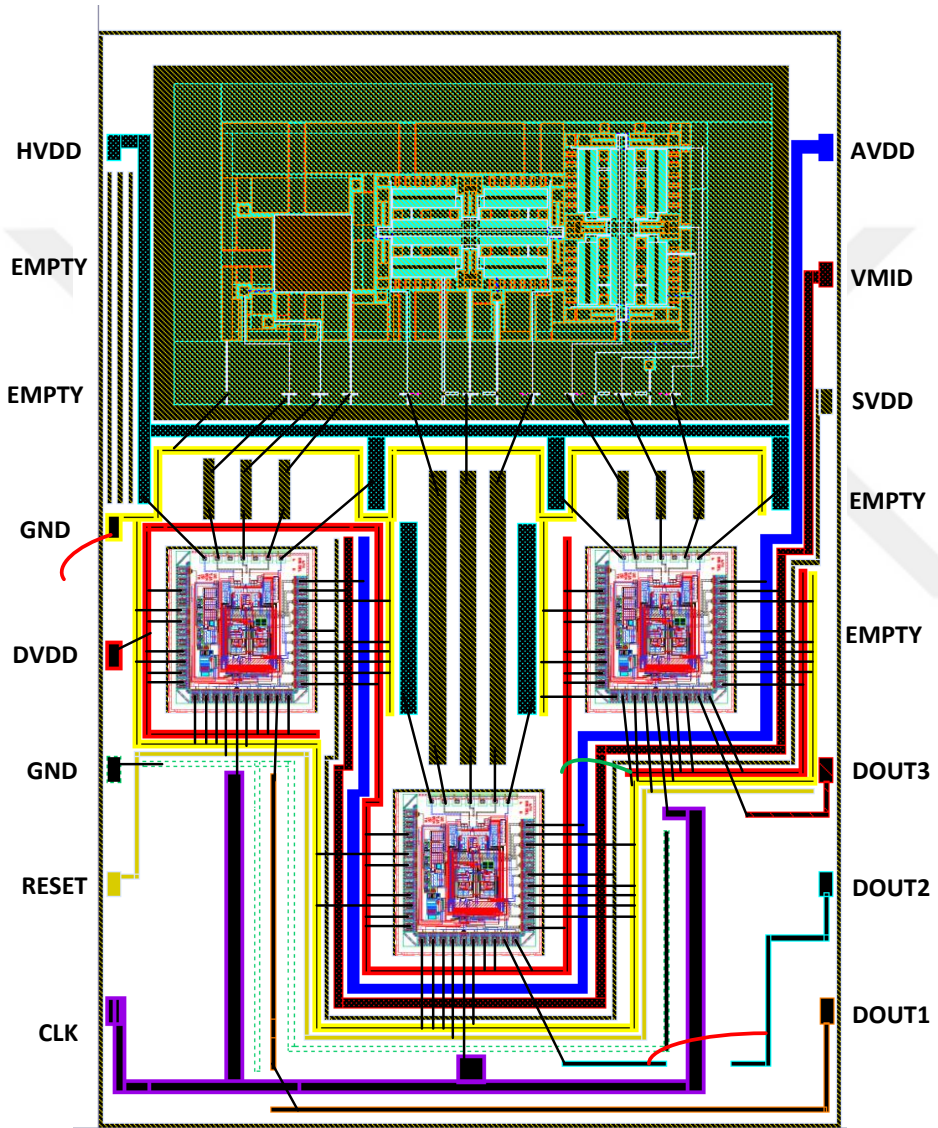
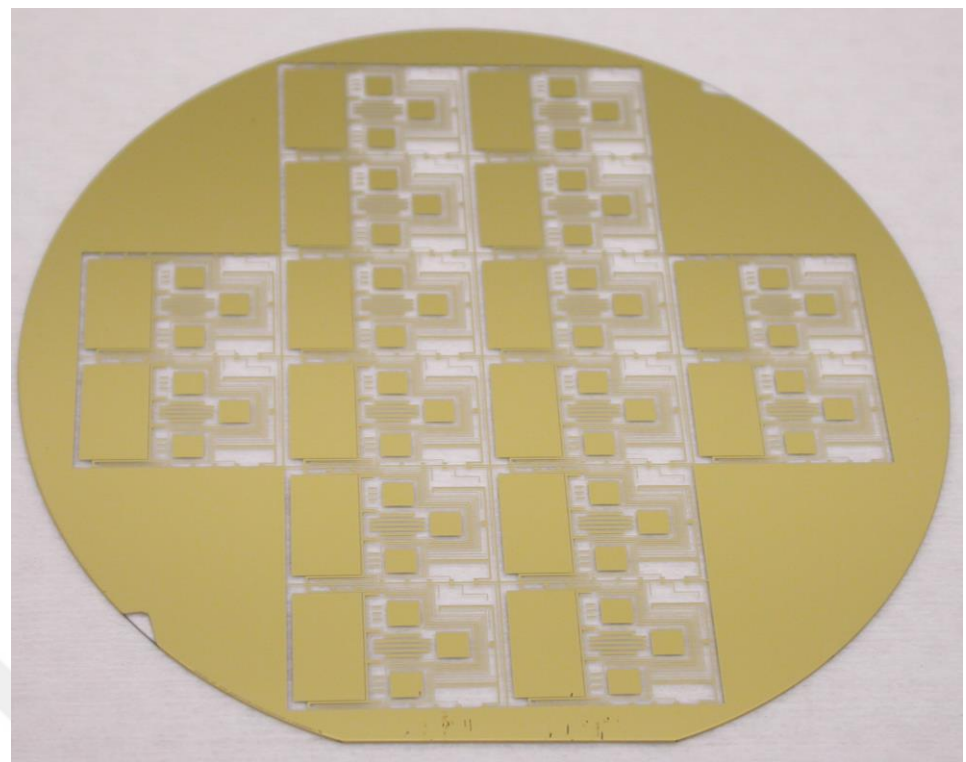
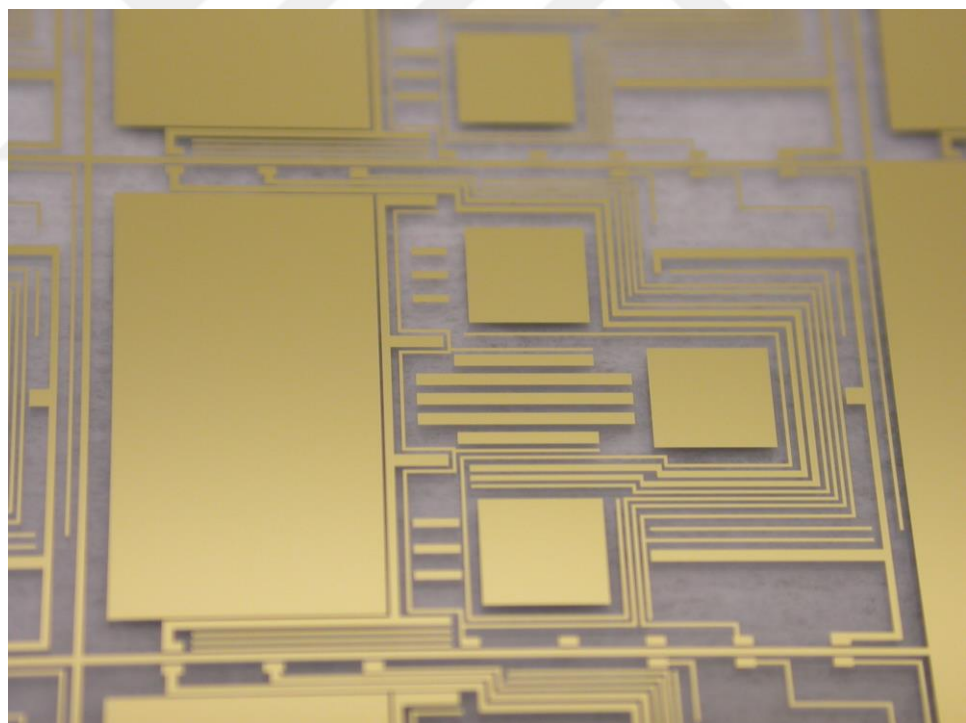


Figure 5.4: The layout of the glass substrate designed for integration of the three axis accelerometer with readout circuit.



(a)



(b)

Figure 5.5: The fabricated glass substrate for integration of the three-axis accelerometer with the readout circuit. (a) The wafer level image (b) close view image of the glass substrate.



Figure 5.6: The 16 pin package used during the system level test.

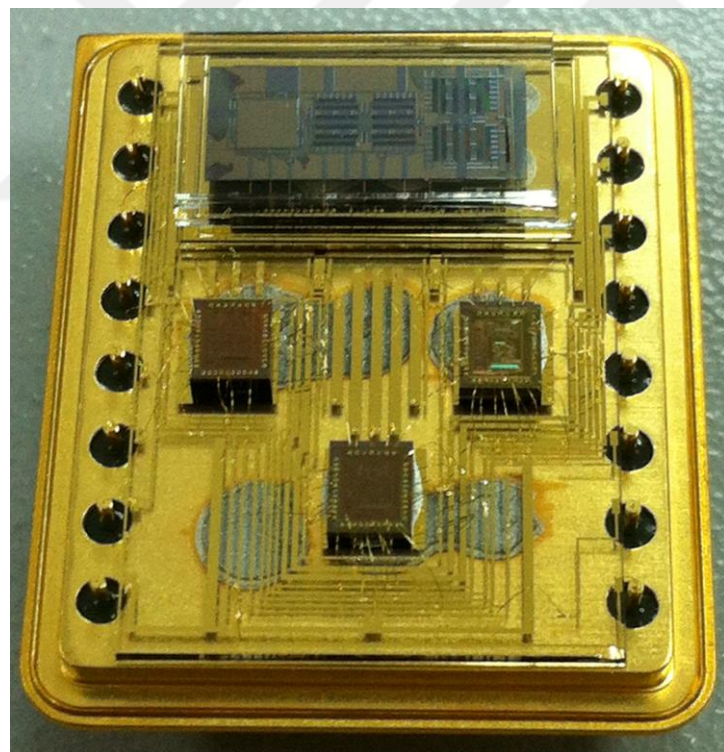


Figure 5.7: The prepared three-axis accelerometer package. The three-axis accelerometer die is integrated with three individual readout circuit, and the wire-bonding is performed.

5.2.1. Allan-Variance Noise and Bias Instability Measurement Technique

According to ANSI verified IEEE Standard 1293 - 1998 (R2008), noise and bias drift tests of accelerometers should be evaluated by the power spectral density (PSD) and Allan Variance graphs by performing the measurement at zero-g conditions. [72]. Allan variance, which is developed to study the frequency stability of oscillator, is a technique depending on a time domain analysis. It can help to determine of underlying random process that cause to the data noise. Therefore, it can also be elucidated the source of a given noise term in the data. Figure 5.8 shows a typical Allan variance plot. The Allan variance method can be used to determine the noise and the bias instability values of the accelerometer [73]. One can assume that there are N samples with a sample time τ_0 . Thus, n consecutive data clusters whose lengths $\tau_0, 2\tau_0, \dots, k\tau_0$ can be formed with $n < N/2$ and obtained averages of the sum of the data points contained in each cluster over the length of that cluster. The Allan variance is defined as a function of cluster time [74].

$$\theta(T) = \int_0^T \Omega(t') dt' \quad (5.1)$$

The lower integration limit is not specified only angle or velocities differences are employed in the definitions. The Allan variance can be estimated as:

$$\theta(T) = \frac{1}{2\tau^2(N-2n)} \sum_{k=1}^{N-2n} (\theta_{k+2n} - 2\theta_{k+2n} + \theta_k)^2 \quad (5.2)$$

There are six regions in Figure 5.8 which determine the performance of an accelerometer. These regions are explained in the following parts.

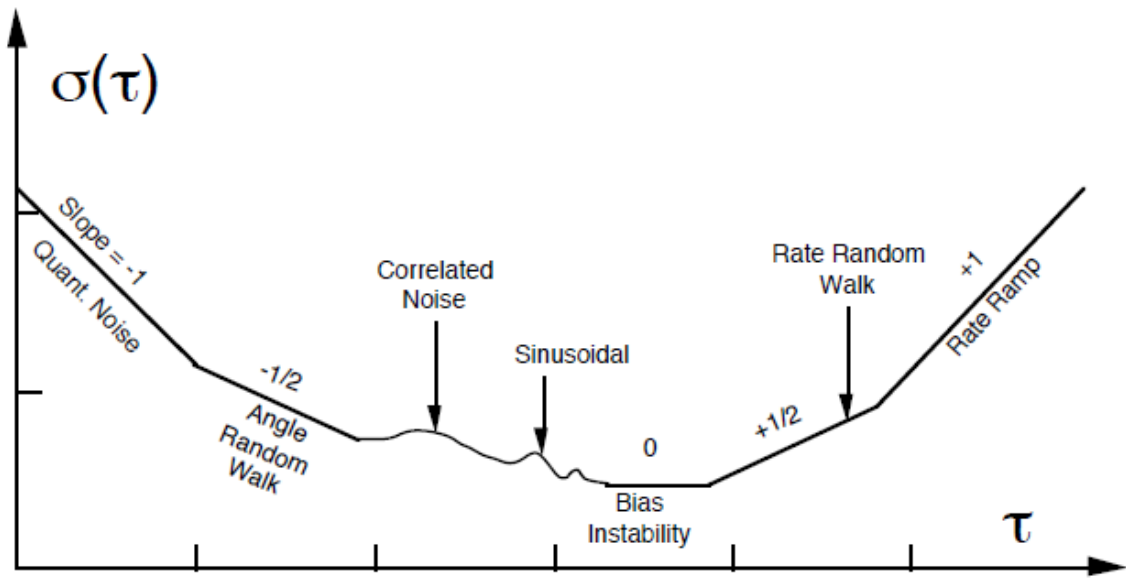


Figure 5.8: $\sigma(\tau)$ Sample plot of Allan variance analysis results [73].

5.2.1.1. Quantization Noise

The quantization noise can be described as the errors that introduced into an analog signal by encoding its digital form. The small differences between the actual amplitudes of the points being sampled and the bit resolution of analog-to-digital converter causes that noise. The quantization noise is determined by a slope of -1 in a logarithmic plot of $\sigma(\tau)$ versus τ [74].

5.2.1.2. Angle (Velocity) Random Walk

The high frequency noise terms that have correlation time much shorter than the sample time make a contribution to the angle (velocity) random walk. The velocity random walk is denoted by a slope of -1/2 in a logarithmic plot of $\sigma(\tau)$ versus τ [74].

5.2.1.3. Bias Instability

The electronics or other components, which are susceptible to random flickering, are the origin of this noise. Due to its low-frequency nature, it is denoted as the bias fluctuations in the data. The bias instability is specified by a slope of 0 in a logarithmic plot of $\sigma(\tau)$ versus τ [73].

5.2.1.4. Rate Random Walk

Rate random walk can be described as a random process of uncertain origin, possibly a limiting case of an exponentially correlated noise with a very long correlation time. The rate random walk is represented by a slope of $+1/2$ in a logarithmic plot of $\sigma(\tau)$ versus τ [73].

5.2.1.5. Rate Ramp

Rate ramp is more of a deterministic error rather than a random noise for long, but finite time intervals. The rate ramp is displayed by a slope of $+1$ in a logarithmic plot of $\sigma(\tau)$ versus τ [73].

5.2.1.6. Exponentially Correlated (Markov) Noise

The noise is characterized by an exponential decaying function with a finite correlation time. Figure 5.8 shows exponentially correlated (Markov) noise [73].

5.2.2. System Level Test Procedure

Figure 5.9 shows the system level test setup. The accelerometer is connected to the FPGA, where the data coming from the readout is registered to be as either 1 or 0. Under the ideal condition, the bias of the decimated data is exactly half full scale range of decimation filters. However, the bias point can be different for various accelerometers as a result of the electronic and the mechanical offset coming from fabrication mismatches and environmental conditions. The bias output, which is the mean output value under zero-g condition, can be extracted from the Allan variance analysis.

The bias point of the accelerometer under the acceleration is different value with respect to zero-g environment. Scale factor is a constant value which can be calculated by subtracting bias values obtained for zero-g and 1-g acceleration. When

the bias point and scale factor are determined, the output of the accelerometer can be easily mapped into real acceleration values. The bias point and the scale factor of the accelerometer can be determined by using freeware software like Alavar. After obtained the bias point and the scale factor, the full scale range and the dynamic range of the accelerometer can be estimated with the following equation:

$$\text{Full Scale Range (FSR)} = \pm \frac{\text{Bias Point}}{\text{Scale Factor}} \quad (5.3)$$

$$\text{Dynamic Range} = 20 \log\left(\frac{\text{FSR}}{\sqrt{2} \times \text{Velocity Random Walk (VRW)}}\right) \quad (5.4)$$



Figure 5.9: The test setup used during the system level test of the three-axis accelerometer.

5.2.3. Non-Linearity Measurement

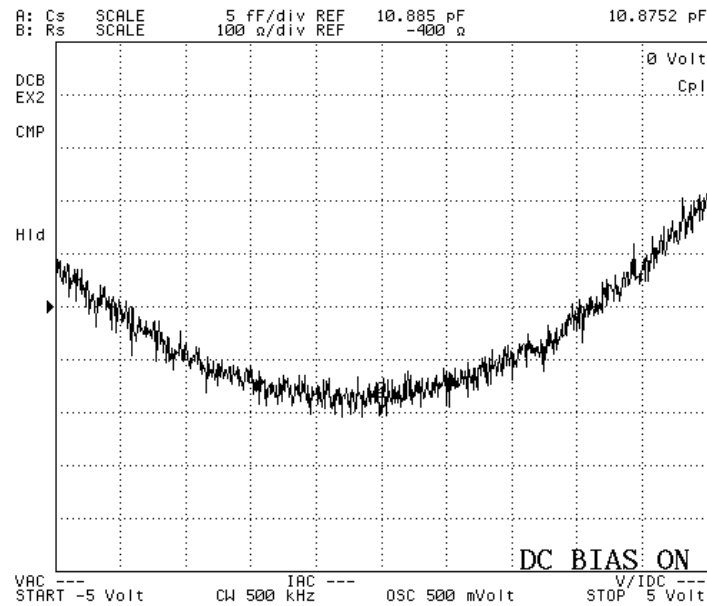
The non-linearity measurement test of sensors is performed by using centrifuge. The accelerometer package is placed on the centrifuge, where the sensitive axis of accelerometers is aligned to the centripetal acceleration. Then, sensors are exposed to the different accelerations. Thus, the mean value of the output is calculated for different accelerations. A graph is formed in terms of the mean value of the data collected for different acceleration to the input acceleration. The non-linearity is determined by fitting a first order line to the graph.

5.3. Test Performed on Sensors Fabricated by Using Mask Set-1

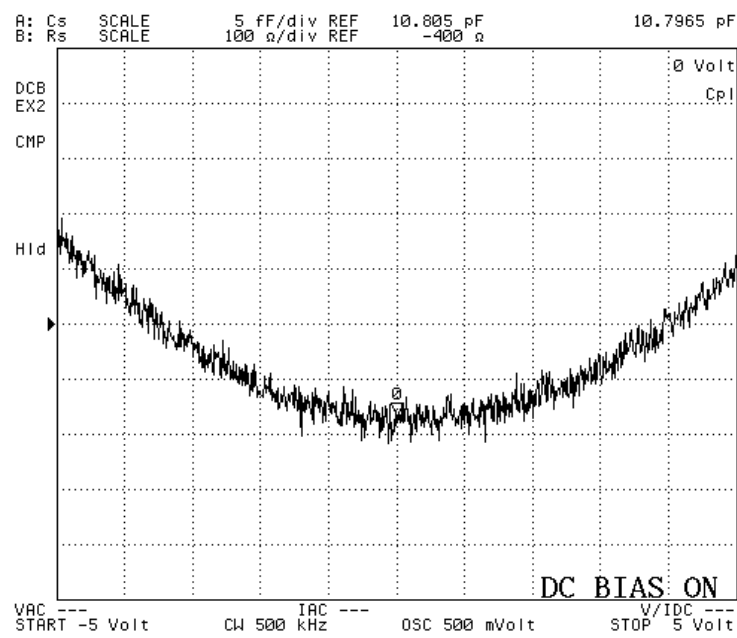
The first fabrication mask set is an optimization mask, where sensor performance parameters are not taken into consideration. The main aim of the first mask set is to show the feasibility of the fabrication process. As the two-step anodic bonding approach is considered in the first mask set, the spring constant of the lateral and vertical accelerometer is designed as much as possible. Therefore, the measured capacitance change of the lateral and the vertical accelerometer is quite low. Moreover, the fabricated sensor wafer is used during the optimization process of the two-electrode anodic bonding and the two-stage dicing process. Therefore, the yield is low, and a sensor whose three-axis is functional is not fabricated. Therefore, only the C-V test is performed for the lateral and vertical accelerometer.

After the functionality of sensors is verified by the C-V test result, and a new mask set is designed to eliminate problems observed in the fabrication of the first mask set and improve performance of the accelerometer.

Figure 5.10 and Figure 5.11 shows the C-V measurement result of the lateral and the vertical accelerometer, respectively. The applied voltage is 5 V for the lateral and the vertical accelerometer since the spring constant is high. Table 5.1 shows the lateral and the vertical accelerometer test result fabricated by using the first mask set.

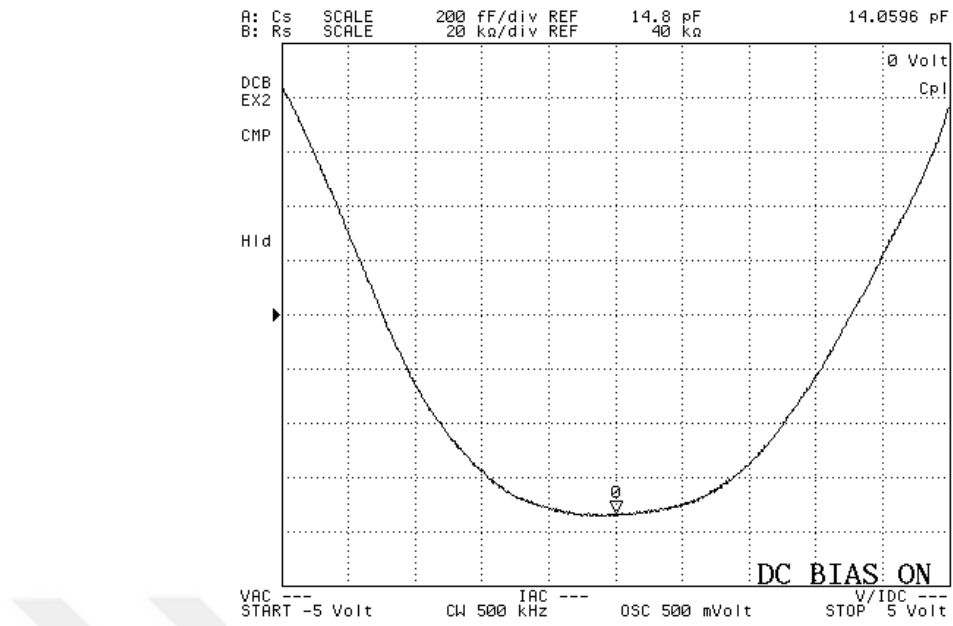


(a)

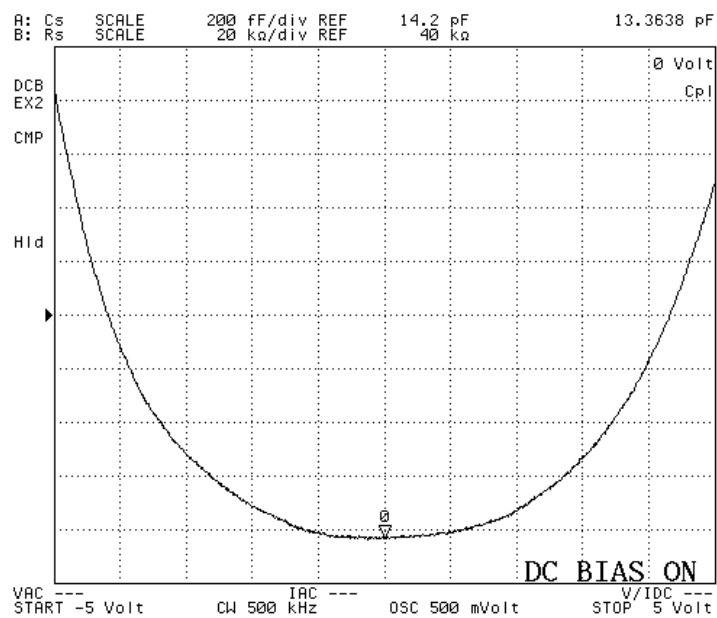


(b)

Figure 5.10: The lateral accelerometer test result designed for the fabrication mask set-1. (a) The C-V change for the left electrode. (b) The C-V change for the right electrode.



(a)



(b)

Figure 5.11: The vertical accelerometer test result designed for the fabrication mask set-1. (a) The C-V change for the bottom electrode. (b) The C-V for the top electrode.

Table 5.1: The lateral and the vertical accelerometer test result for the fabrication mask set-1.

| Lateral Accelerometers | | | | |
|--------------------------------|--------------------------------|-----------------------------|---------------------------------|------------------------------|
| Code | C_{LEFT} | C_{RIGHT} | Δ C_{LEFT} | ΔC_{RIGHT} |
| C04 | 10.87 | 10.79 | 20 | 20 |
| A06 | 11.04 | 10.99 | 20 | 20 |
| B03 | 11.26 | 11.39 | 20 | 20 |
| Vertical Accelerometers | | | | |
| Code | C_{BOTTOM} (pF) | C_{TOP} (pF) | ΔC_{BOTTOM} (fF) | ΔC_{TOP} (fF) |
| B03 | 13.12 | 13.91 | 90 | 140 |
| C02 | 14.05 | 13.36 | 1500 | 1600 |
| B01 | 13.73 | 15.99 | 1400 | 825 |
| B01 | 15.96 | 15.80 | 800 | 1450 |

5.4. Test Performed on Sensors Fabricated by Using Mask Set-2

The second mask set is drawn not only to increase the device performance but also eliminate problems observed in the first mask set. In the first mask set, the spring constant of the lateral axis accelerometer is quite high in the vertical direction to prevent damaging of sensors during the two-electrode anodic bonding. However, in this case, the sensitivity of the lateral accelerometer is quite low. Therefore, in the second mask, three different lateral accelerometers, which are comprehensively explained in the design part, are placed in the mask set. Furthermore, the vertical accelerometer is modified with respect to the proof mass area and the spring constant. The C-V test, the resonance frequency measurement and the system level test are performed for the fabricated three axis accelerometer.

5.4.1. C-V Test Results

5.4.1.1. Sensors Fabricated by Using the Three-Electrode Anodic Bonding Method

Figure 5.12 shows a wafer map which represents die level results for the three-axis accelerometers shown in Figure 4.73 (a). Figure 5.13 shows the C-V measurement result for the lateral accelerometer design-3. After the fabrication, the rest capacitance is compared with the design value since the top and bottom shield electrode is short to the proof mass. So, a parasitic capacitance is formed as result of existence of the top and the bottom shield metallization. However, once the top and bottom shield electrode connection are grounded during the C-V test, the rest capacitance value is similar to the design value. The same situation is also valid for the lateral accelerometer design-1 and design-2. Figure 5.14 shows C-V measurement results for the vertical accelerometer design-2 and design-4. Table 5.2 shows test results.

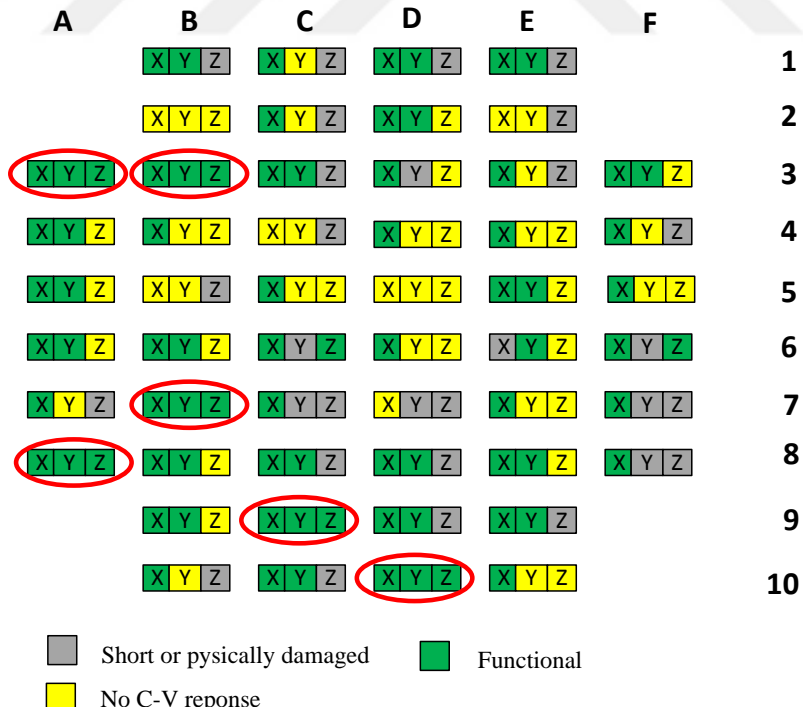
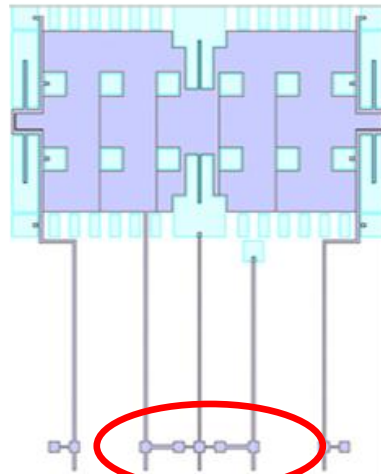
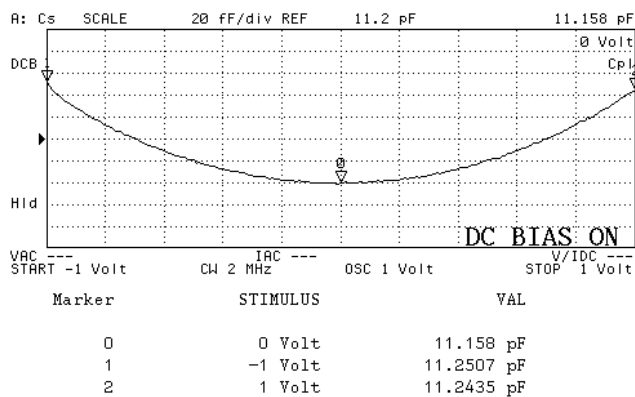
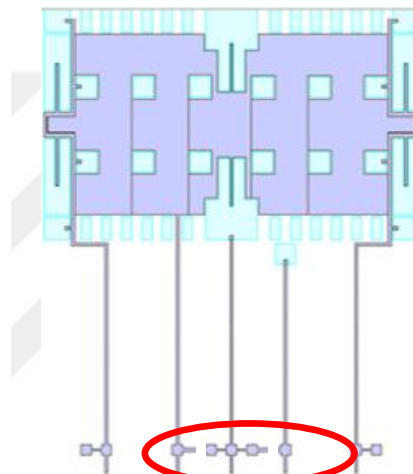
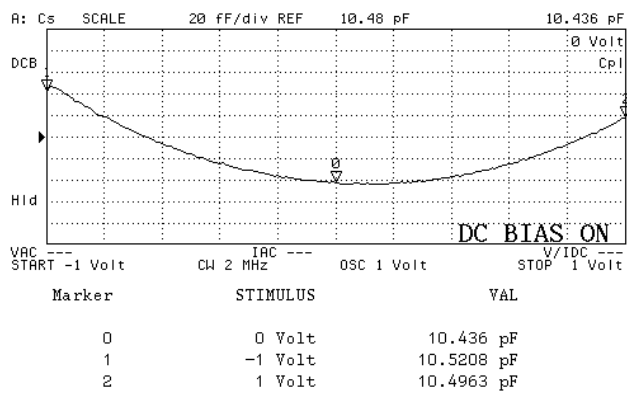


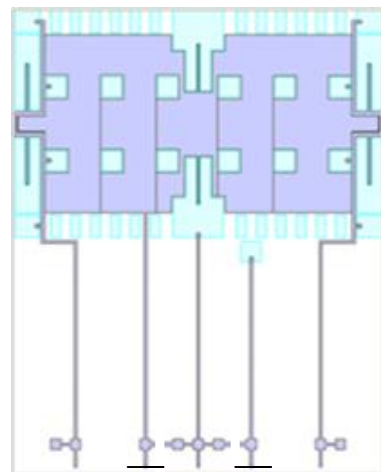
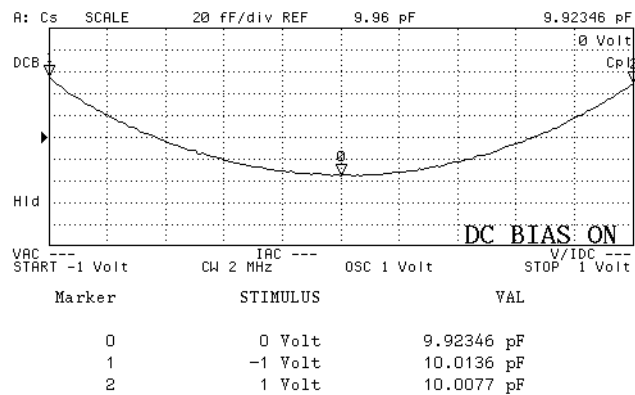
Figure 5.12: The wafer map for sensors fabricated the three-electrode anodic bonding method.



(a) The bottom and the top shield metalization are short to the proof mass.

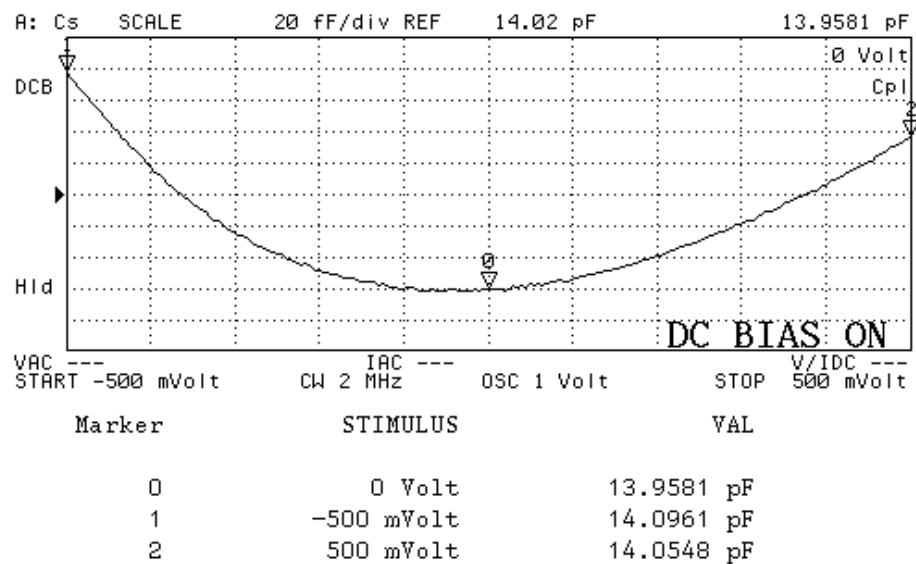


(b) Bottom and top shield metalization connections are cutted.

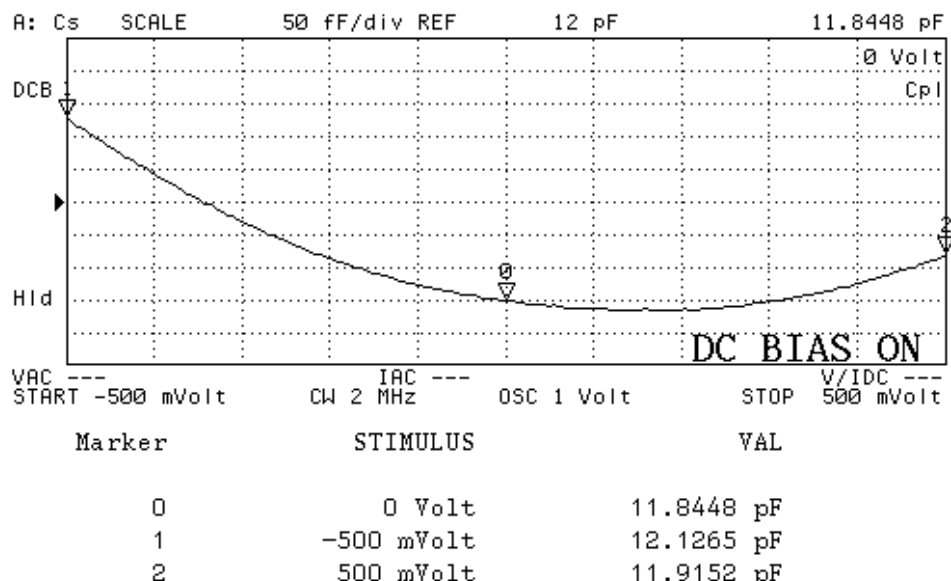


(c) The bottom and the top shield metalization connection is grounded.

Figure 5.13: The rest capacitance of the lateral accelerometer design-3 for different pad diagram of the shield metallization.



(a)



(b)

Figure 5.14: The C-V characteristic of the vertical accelerometer design-4 (a) for the bottom electrode (b) for the bottom electrode.

Table 5.2: Test results of the three axis accelerometer designed for the fabrication mask set-2 fabricated by two-step anodic bonding.

| Three-Axis Accelerometers | | | | | | |
|---------------------------|------|-----------------------|-----------------------|-----------------------------------|-----------------------------------|------------|
| Code | Axis | $C_{ELEC\#1}$ (pF) | $C_{ELEC\#2}$ (pF) | Average | | Design# |
| | | | | Δ $C_{ELEC\#1}$ (fF) | Δ $C_{ELEC\#2}$ (fF) | |
| A01 | X | 9.92 | 9.73 | 85 | 85 | Lateral#3 |
| A01 | Y | 9.98 | 9.95 | 85 | 85 | Lateral#3 |
| A01 | Z | 11.46 | 13.85 | 140 | 85 | Vertical#4 |
| A06 | X | 9.71 | 9.89 | 85 | 80 | Lateral#3 |
| A06 | Y | 9.74 | 9.01 | 80 | 90 | Lateral#3 |
| A06 | Z | 11.77 | 14.84 | 170 | 605 | Vertical#4 |
| B03 | X | 9.33 | 9.45 | 75 | 80 | Lateral#3 |
| B03 | Y | 9.33 | 9.43 | 90 | 85 | Lateral#3 |
| B03 | Z | 15.68 | 14.16 | 600 | 225 | Vertical#2 |
| C09 | X | 9.79 | 8.96 | 91 | 90 | Lateral#3 |
| C09 | Y | 9.74 | 8.95 | 90 | 90 | Lateral#3 |
| C09 | Z | 13.95 | 16.05 | 120 | 225 | Vertical#2 |
| D10 | X | 6.28 | 6.09 | 50 | 50 | Lateral#2 |
| D10 | Y | 6.19 | 6.37 | 50 | 42 | Lateral#2 |
| D10 | Z | 11.84 | 13.94 | 170 | 220 | Vertical#4 |

5.4.1.2. Sensors Fabricated the Anodic Bonding and then the Au-Si Eutectic Bonding

Table 5.3 shows the measurement result of the vertical accelerometer design-5 fabricated in the first attempt of the anodic bonding and then the Au-Si shown in Figure 4.76.

Table 5.3: The rest capacitance value for the vertical accelerometer design 5 fabricated in the first attempt of the anodic bonding and then the Au-Si shown in Figure 4.76.

| Design# | C _{ELEC#1} (pF) | C _{ELEC#2} (pF) | ΔC _{BOTTOM} (fF) | ΔC _{TOP} (fF) |
|-------------|--------------------------|--------------------------|---------------------------|------------------------|
| Vertical -5 | 11.64 | 12.33 | 390 | 370 |

Figure 5.15 represents a wafer map which shows die level results for the three-axis accelerometer shown in Figure 4.81 (d). Table 5.4 shows test results of sensors fabricated by using the anodic bonding and then the Au-Si eutectic bonding in fabrication run#5 shown in Figure 4.81 (d). Figure 5.16 shows some example of C-V measurement results for the lateral accelerometer deisgn-1, design-2, and design-3, respectively. Figure 5.17 shows some example of C-V measurement result for vertical accelerometer design-1 and design-2. Figure 5.18 demonstrates some example of C-V measurement results for vertical accelerometer design-3 and design-4.

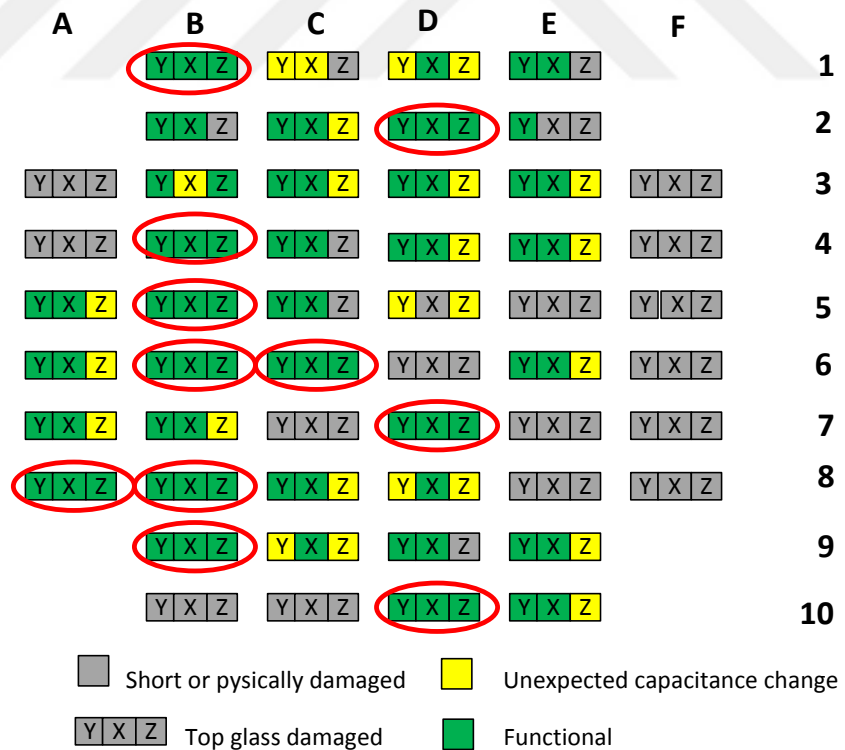
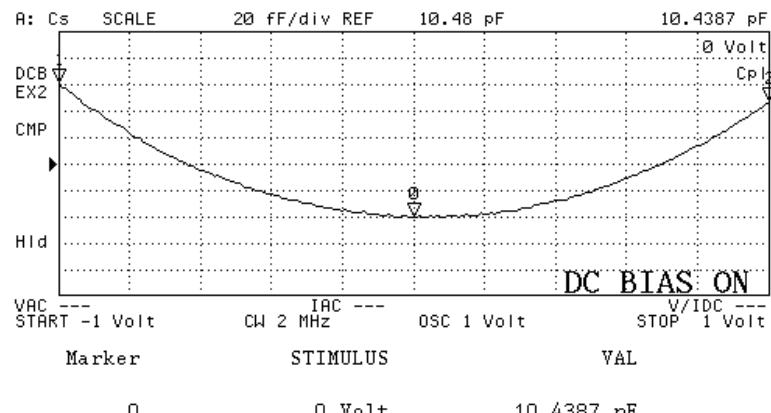


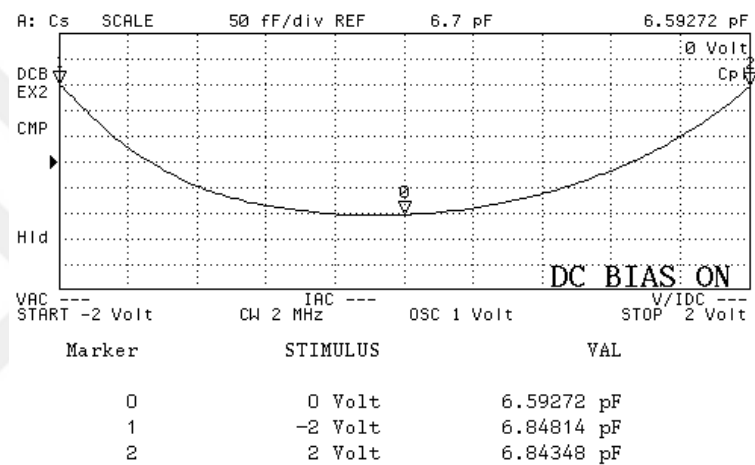
Figure 5.15: The wafer level map for sensors fabricated the anodic bonding and then the Au-Si eutectic bonding in fabrication run#5 shown in Figure 4.81 (b).

Table 5.4: Sensors test results for the fabrication run#5 shown in Figure 4.81 (b). .

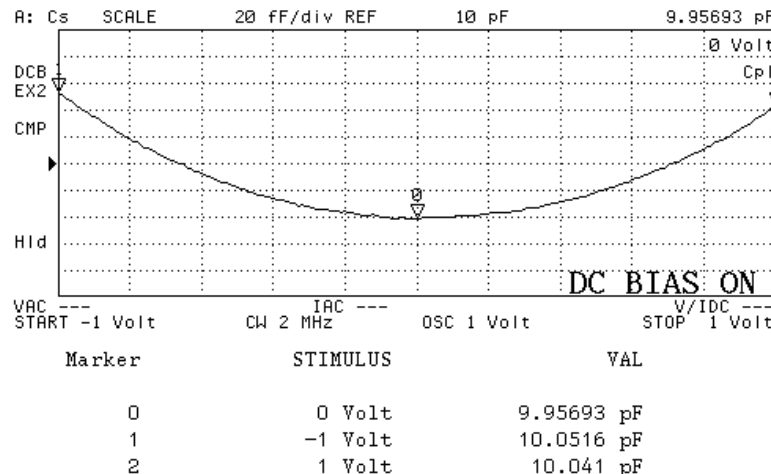
| Three-Axis Accelerometers | | | | | | |
|---------------------------|------|-----------------------------|-----------------------------|------------------------------|------------------------------|------------|
| Code | Axis | C _{ELEC#1} (pF) | C _{ELEC#2} (pF) | Average | | Design# |
| | | | | ΔC _{ELEC#1} (fF) | ΔC _{ELEC#2} (fF) | |
| A06 | X | 9.75 | 9.95 | 100 | 80 | Lateral#3 |
| A06 | Y | 9.91 | 9.89 | 90 | 100 | Lateral#3 |
| A06 | Z | 11.69 | 12.96 | 140 | 210 | Vertical#4 |
| B01 | X | 9.69 | 9.56 | 90 | 80 | Lateral#3 |
| B01 | Y | 9.63 | 9.61 | 100 | 80 | Lateral#3 |
| B01 | Z | 12.63 | 13.69 | 380 | 235 | Vertical#4 |
| B04 | X | 10.19 | 10.29 | 80 | 80 | Lateral#1 |
| B04 | Y | 10.41 | 10.26 | 90 | 85 | Lateral#1 |
| B04 | Z | 15.92 | 13.40 | 155 | 115 | Vertical#2 |
| B05 | X | 9.68 | 9.75 | 80 | 80 | Lateral#3 |
| B05 | Y | 9.49 | 9.48 | 100 | 90 | Lateral#3 |
| B05 | Z | 7.45 | 7.47 | 25 | 265 | Vertical#1 |
| B06 | X | 10.25 | 10.27 | 80 | 70 | Lateral#1 |
| B06 | Y | 10.39 | 10.36 | 80 | 70 | Lateral#1 |
| B06 | Z | 16.99 | 13.78 | 25 | 265 | Vertical#2 |
| B08 | X | 10.29 | 10.27 | 80 | 90 | Lateral#1 |
| B08 | Y | 10.31 | 10.36 | 80 | 90 | Lateral#1 |
| B08 | Z | 18.91 | 12.15 | 35 | 135 | Vertical#2 |
| B09 | X | 10.55 | 10.62 | 90 | 80 | Lateral#1 |
| B09 | Y | 10.61 | 10.54 | 80 | 100 | Lateral#1 |
| B09 | X | 8.23 | 8.08 | 65 | 25 | Vertical#3 |
| C06 | X | 9.80 | 9.74 | 90 | 80 | Lateral#1 |
| C06 | Y | 9.67 | 9.67 | 120 | 120 | Lateral#1 |
| C06 | X | 16.91 | 14.90 | 330 | 195 | Vertical#2 |
| D02 | X | 6.76 | 6.73 | 250 | 230 | Lateral#2 |
| D02 | Y | 6.62 | 6.64 | 230 | 260 | Lateral#2 |
| D02 | Z | 16.23 | 13.45 | 290 | 120 | Vertical#2 |



(a)

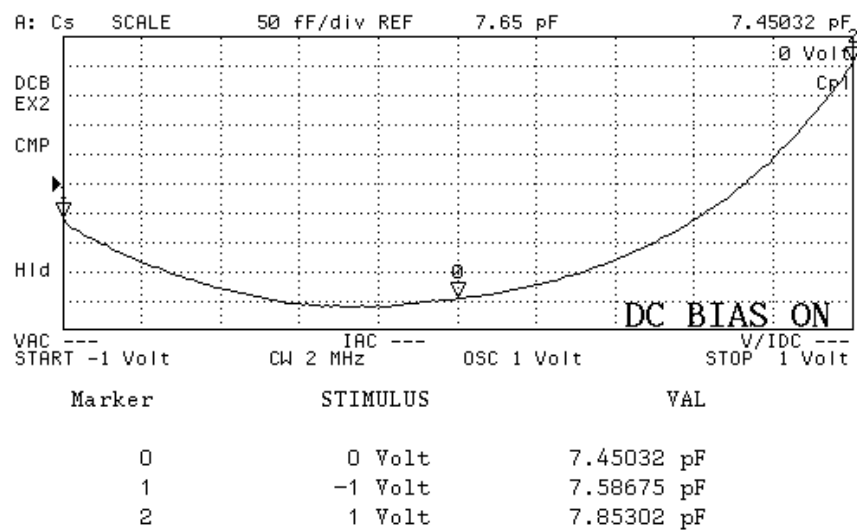


(b)

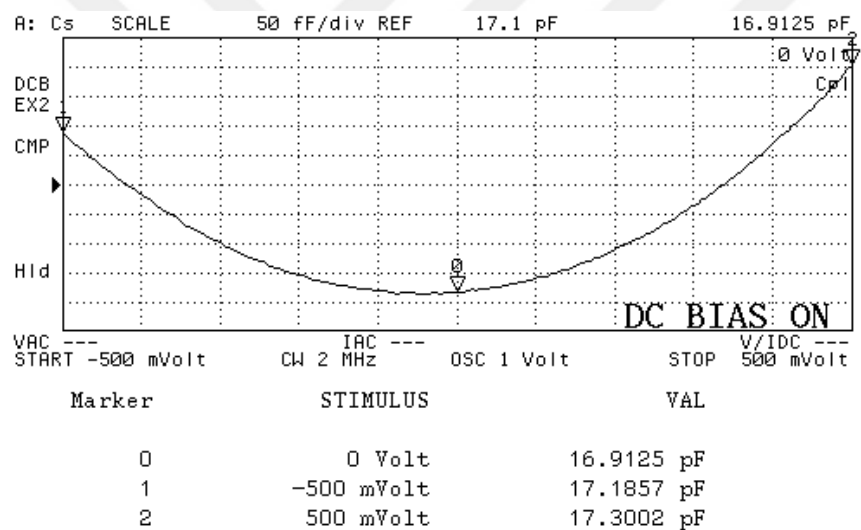


(c)

Figure 5.16: Lateral accelerometer C-V test results (a) design-1 (b) design-2 (c) design-3.

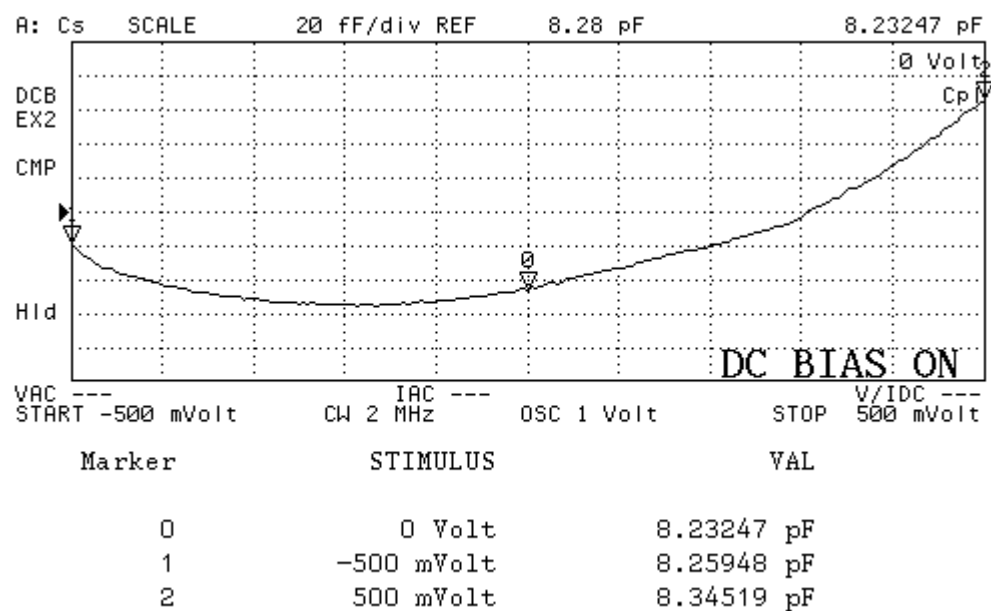


(a)

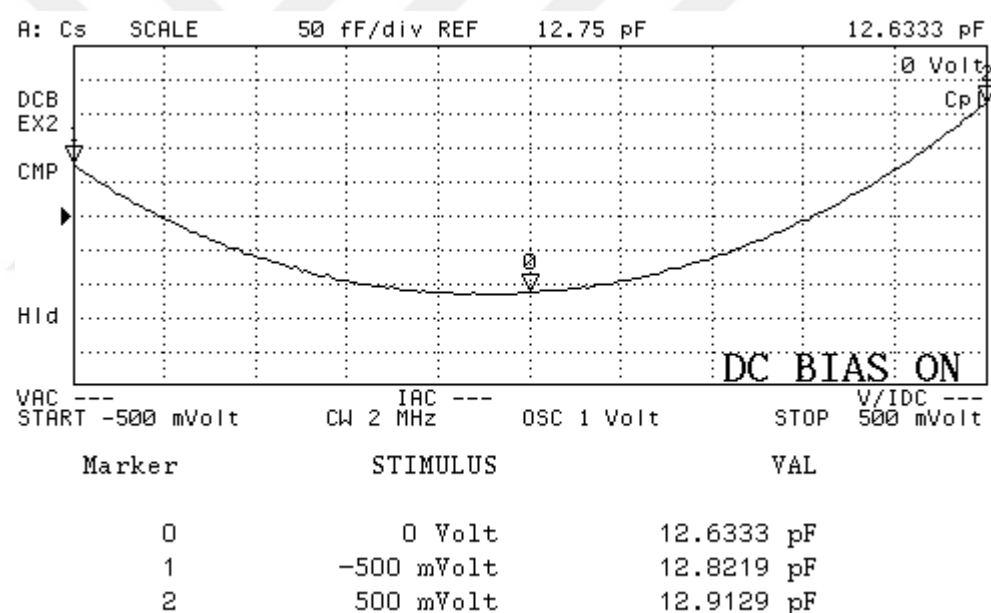


(b)

Figure 5.17: Vertical accelerometer C-V test results (a) design-1 (b) design-2.



(a)



(b)

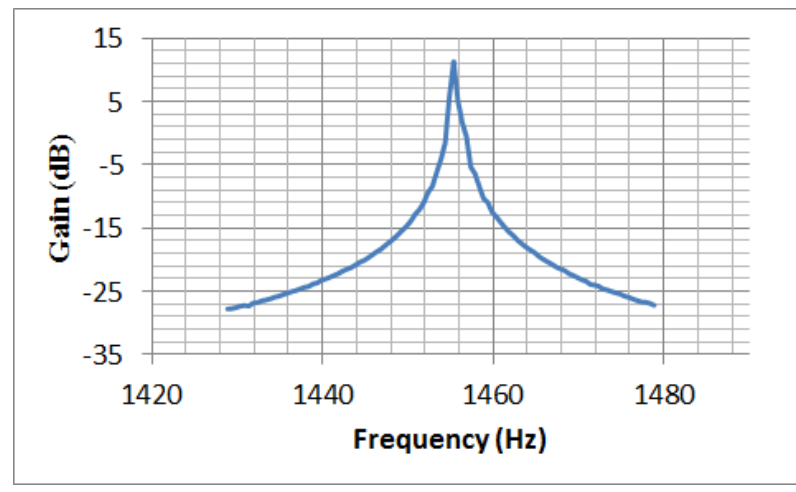
Figure 5.18: Vertical accelerometer C-V test results (a) design-3 (b) design-4.

5.4.2. Resonance Frequency Measurement Test Results

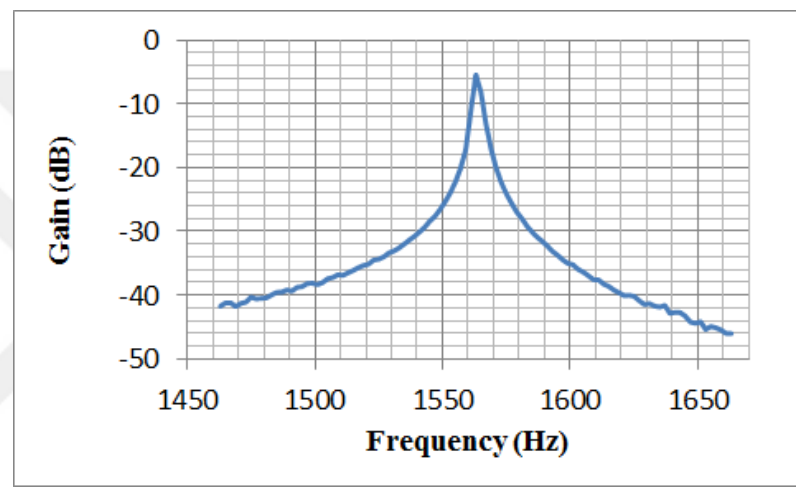
The reason of the mismatch between the design and tested values of the resonance frequency for the lateral and the vertical accelerometer is related with the spring constant. The spring is thinned during the DRIE etch. Therefore, there is a mismatch for the design and tested values of the resonance frequency. However, it can be seen that the resonance frequency of the lateral and vertical accelerometer is close to each other, which is one of the aim of the current study. Figure 5.19 and Figure 5.20 shows test results of the lateral and vertical accelerometer. Table 5.5 shows the comparison of the designed and tested values of the resonance frequency for different sensors.

Table 5.5: The comparison of design and test values of the resonance frequency.

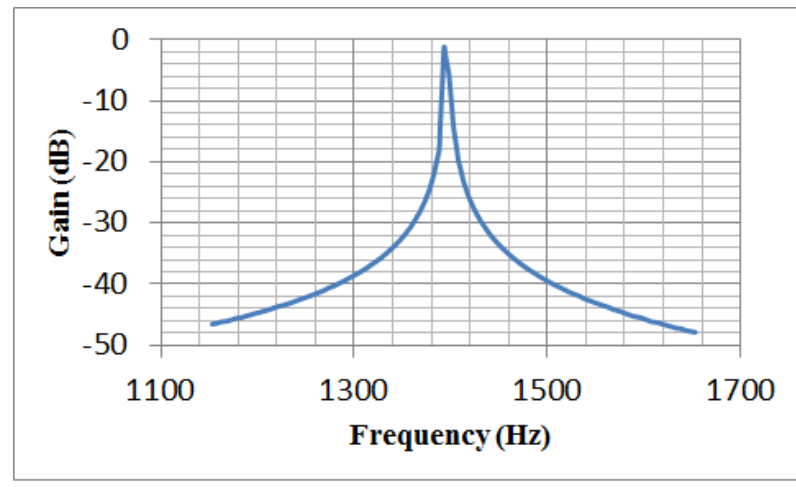
| Resonance Frequency (Hz) | Designed | Tested |
|--------------------------|----------|--------|
| Lateral design_1 | 2549 | 1455 |
| Lateral design_2 | 2481 | 1566 |
| Lateral design_3 | 2495 | 1400 |
| Vertical design_1 | 2275 | - |
| Vertical design_2 | 2278 | 1660 |
| Vertical design_3 | 2505 | 1400 |
| Vertical design_4 | 2221 | 1800 |



(a)

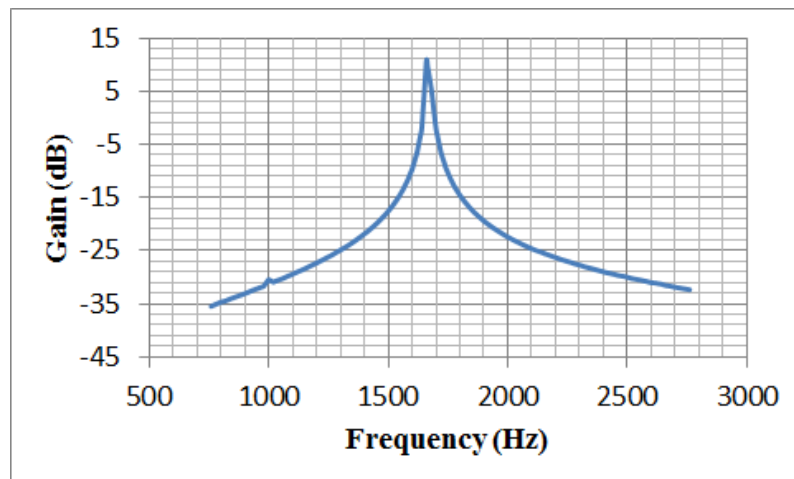


(b)

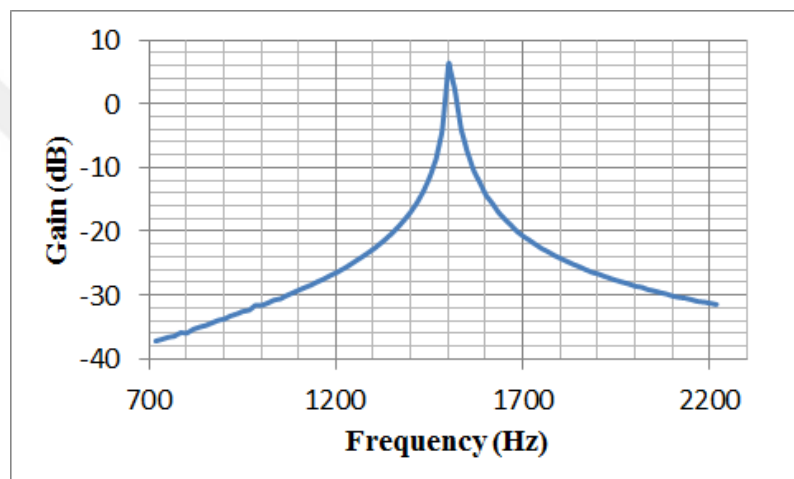


(c)

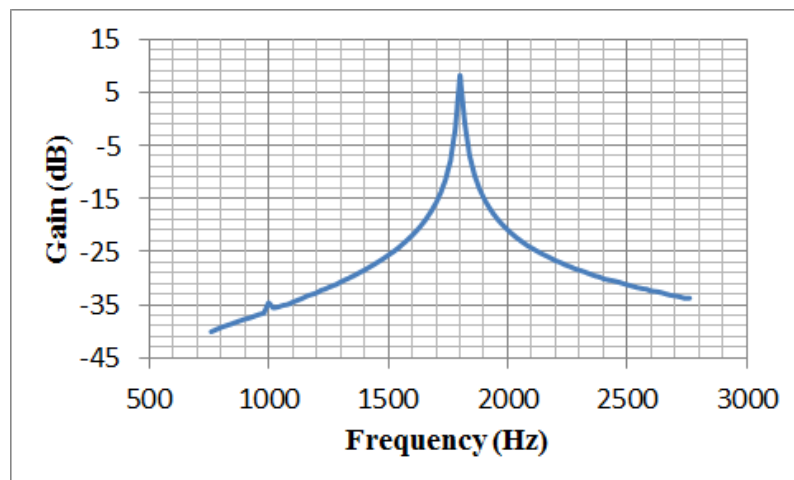
Figure 5.19: The resonance frequency measurement result for lateral accelerometer
(a) design-1 (b) design-2 (c) design-3.



(a)



(b)



(c)

Figure 5.20: The resonance frequency measurement result for vertical accelerometer
(a) design-2 (b) design-3 (c) design-4.

5.4.3. System Level Test Result

After determination of the functional three axis accelerometer, some of them are integrated with a readout circuit reported in [71] to take system level result such as the noise, the bias instability and the dynamic range. The system level test is repeated for two different fabrication processes. Furthermore, the system level results are compared with different accelerometer having same design concept.

5.4.3.1. System Level Results For Sensors by Two-Step Anodic Bonding

Sensors fabricated by using the two-step anodic bonding are tested for the lateral accelerometer design-2 and design-3 as well as the vertical accelerometer design-2 and design-4. Table 5.6 shows system level test results for the lateral accelerometer design-2, the lateral accelerometer design-3 and the vertical accelerometer design-2.

Table 5.6: The system level test results for three-axis accelerometer fabricated by using the two-step anodic bonding.

| Code | Design# | VRW | Bias Instability | Dynamic Range |
|--------------|-------------------|-------------------------------------|------------------------------------|---------------|
| D10-x | Lateral design-2 | 7.2 $\mu\text{g}/\sqrt{\text{Hz}}$ | 9.2 μg | 122 dB |
| D10-y | Lateral design-2 | 6.6 $\mu\text{g}/\sqrt{\text{Hz}}$ | 7.6 $\mu\text{g}/\sqrt{\text{Hz}}$ | 122 dB |
| A01-x | Lateral design-3 | 3.8 $\mu\text{g}/\sqrt{\text{Hz}}$ | 3.1 μg | 128 dB |
| A01-y | Lateral design-3 | 4.1 $\mu\text{g}/\sqrt{\text{Hz}}$ | 3.1 μg | 127 dB |
| A01-z | Vertical design-4 | 17.6 $\mu\text{g}/\sqrt{\text{Hz}}$ | 19 μg | 113 dB |
| B03 | Vertical design-2 | 8.7 $\mu\text{g}/\sqrt{\text{Hz}}$ | 15 μg | 120 dB |
| C09 | Vertical design-2 | 9.4 $\mu\text{g}/\sqrt{\text{Hz}}$ | 17 μg | 119 dB |

Figure 5.21 and Figure 5.22 show the system level result for two different sensors having same design concept (the lateral accelerometer design-2). Figure 5.23 and Figure 5.24 show the system level result for two different sensors having same

design concept (the lateral accelerometer design-3). Figure 5.25 shows the system level result for the vertical accelerometer design-4. Figure 5.26 shows the system level result for the vertical accelerometer design-2. Figure 5.27 shows the comparison of system level results for D10-x-axis and D10-y-axis accelerometers. Figure 5.28 shows the comparison of system level results for A01-x-axis and A01-y-axis accelerometers. Figure 5.29 shows the comparison of system level results for B03 and C09.

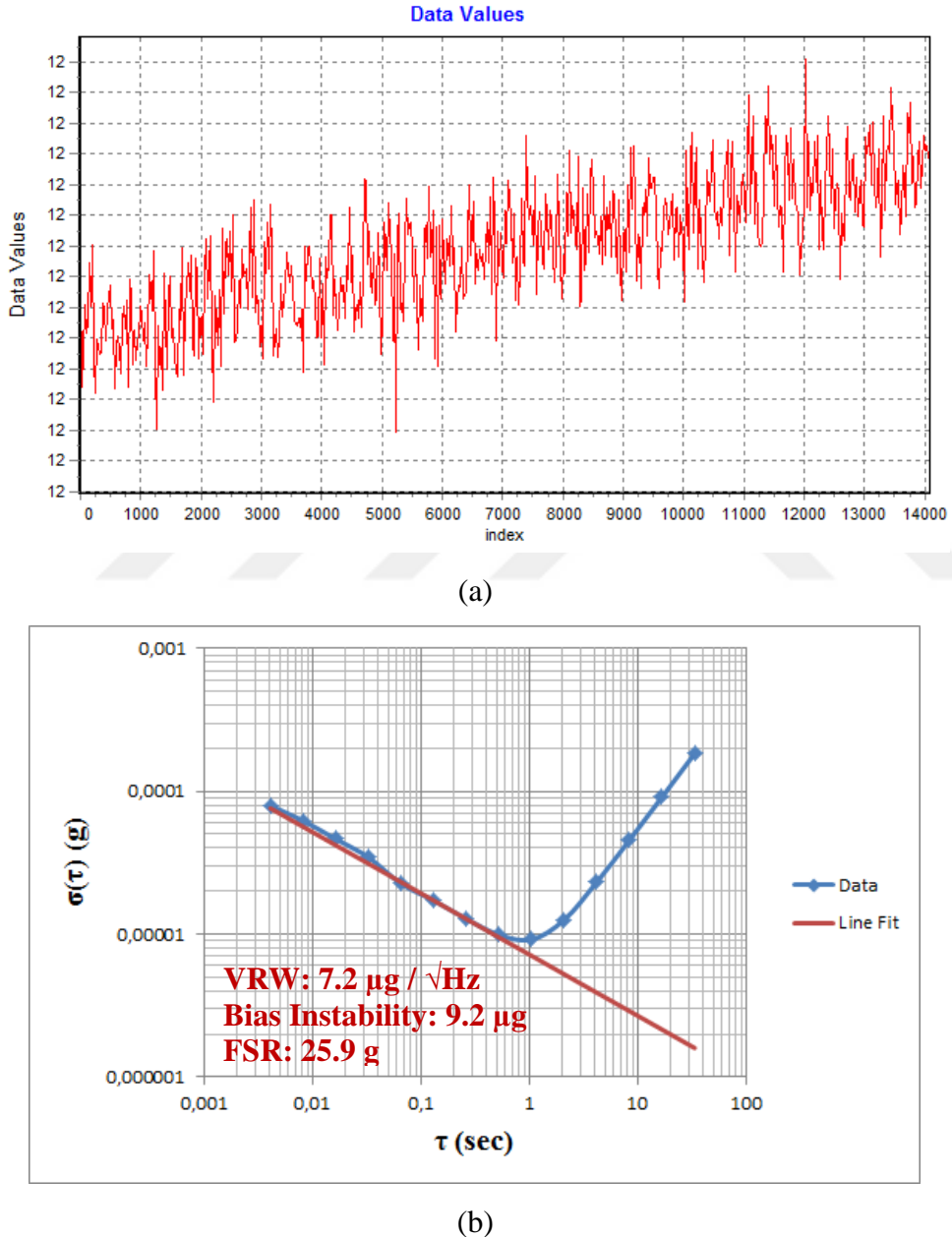
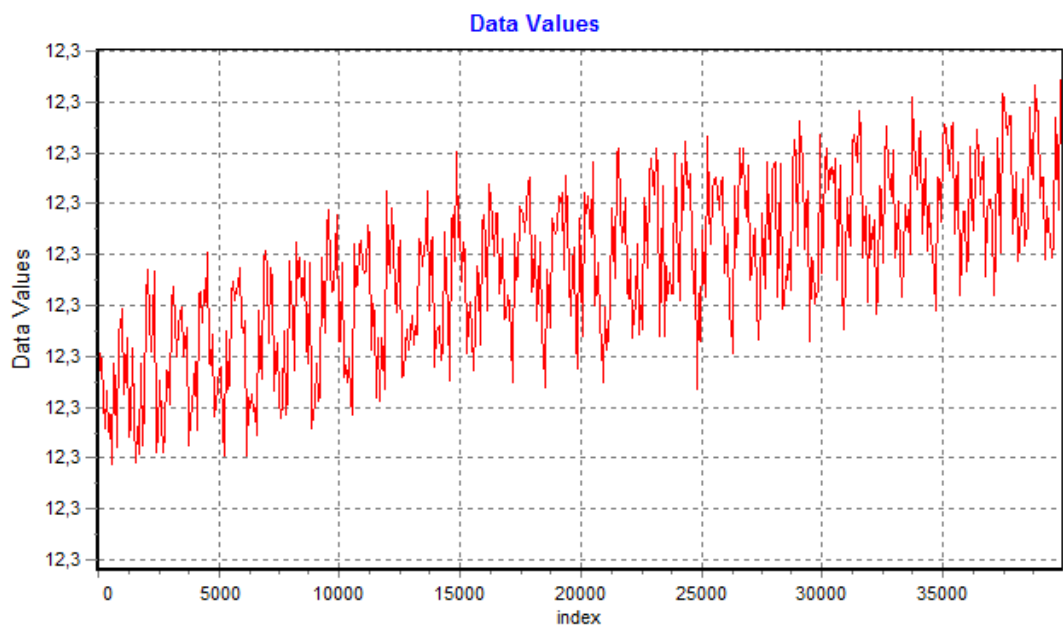
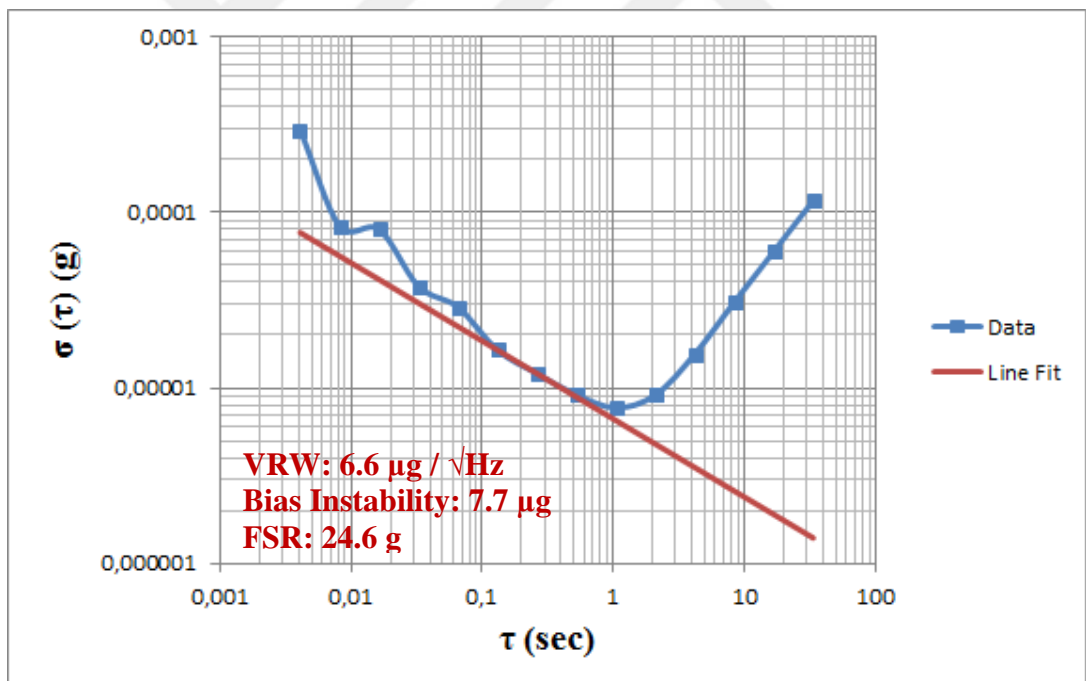


Figure 5.21: (a) The data is collected for 2 minutes at 23 MHz sampling frequency.
 (b) The Allan Variance graph of the lateral accelerometer design-2, D10-x.

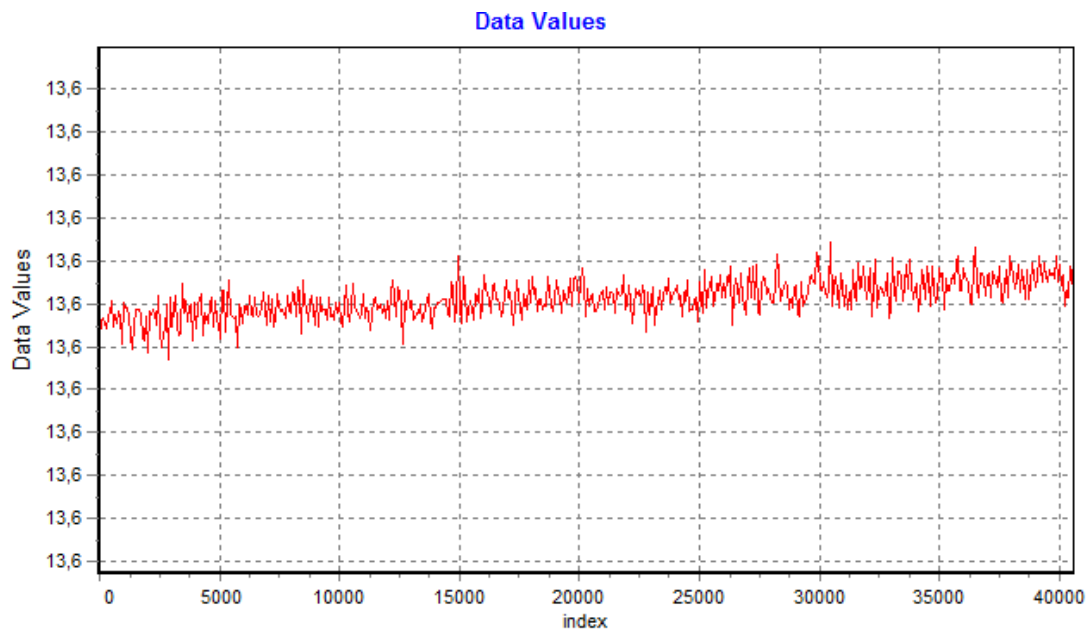


(a)

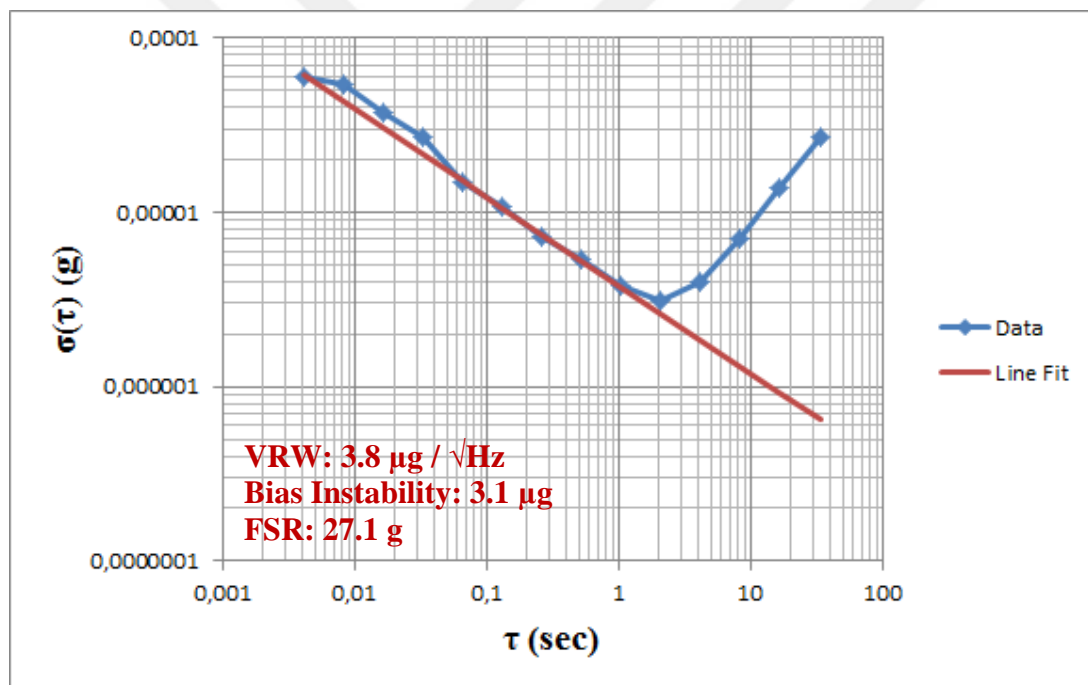


(b)

Figure 5.22: (a) The data is collected for 2 minutes at 23 MHz sampling frequency.
 (b) The Allan Variance graph of the lateral accelerometer design-2, D10-y axis.

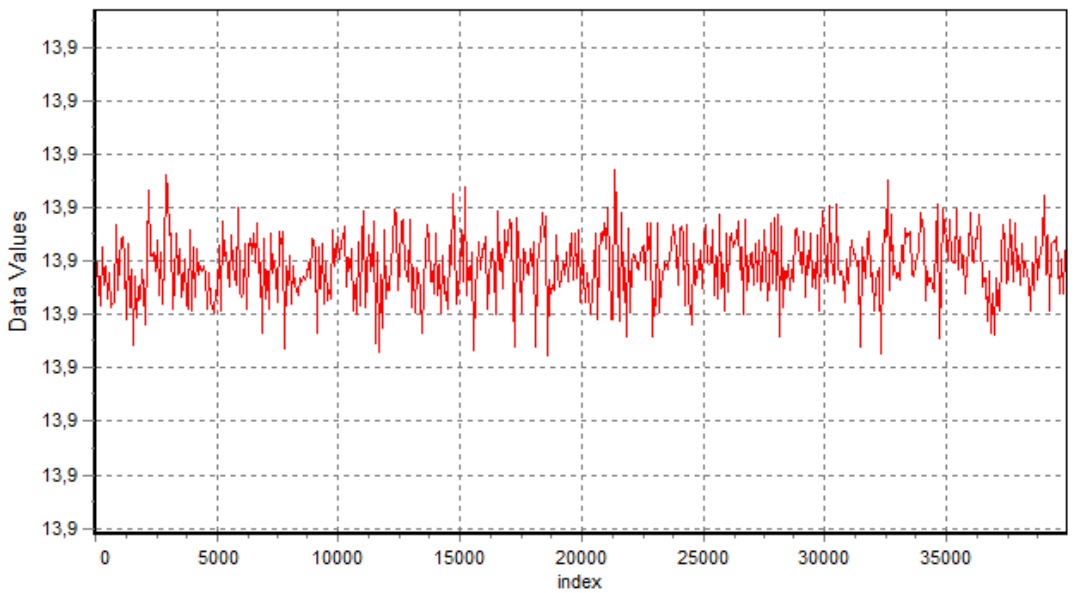


(a)

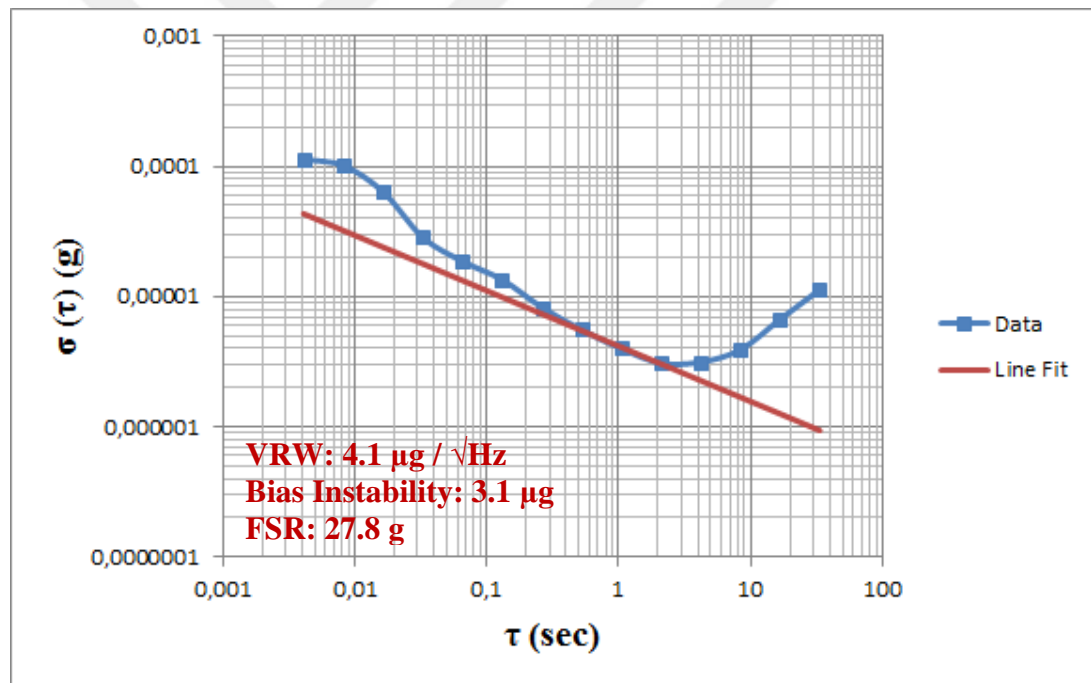


(b)

Figure 5.23: (a) The data is collected for 2 minutes at 23 MHz sampling frequency.
(b) The Allan Variance graph of the lateral accelerometer design-3, A01-x-axis.

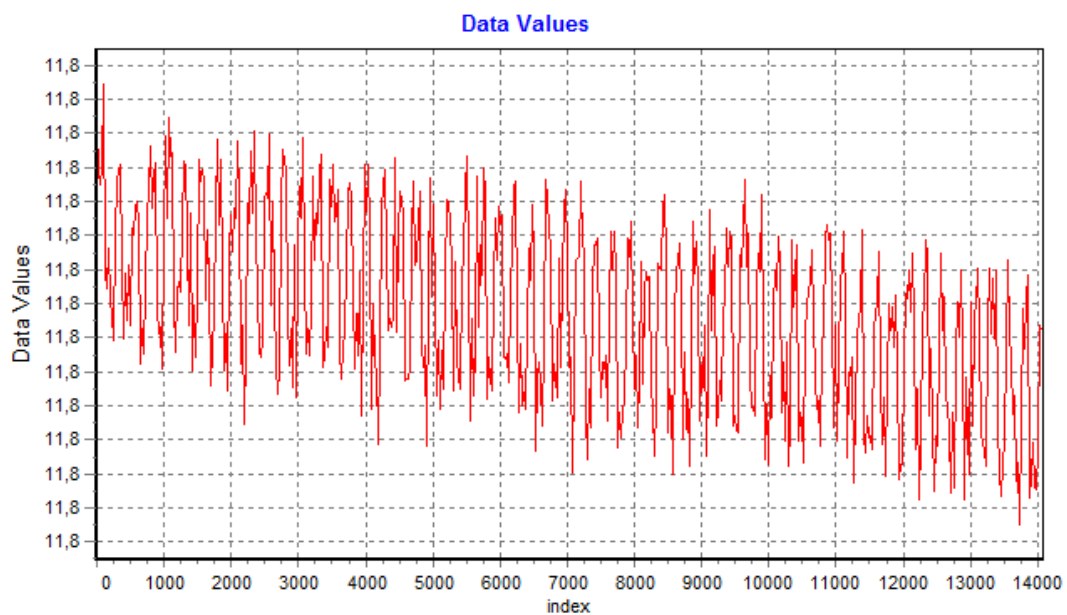


(a)

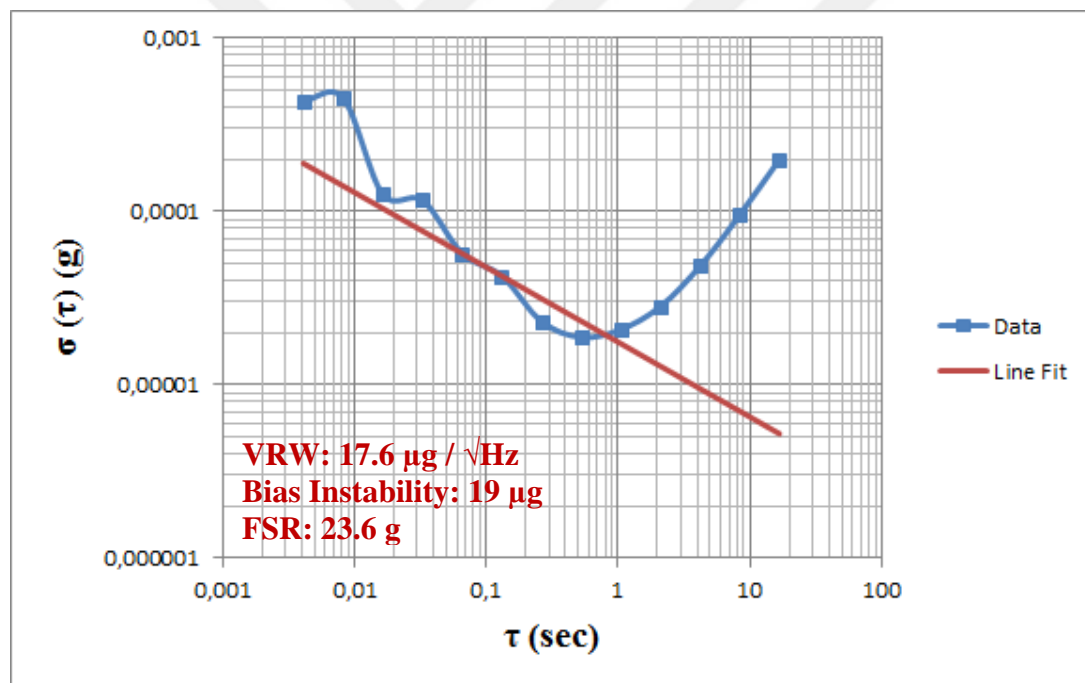


(b)

Figure 5.24: (a) The data is collected for 2 minutes at 23 MHz sampling frequency.
(b) The Allan Variance graph of the lateral accelerometer design-3, A01-y-axis.

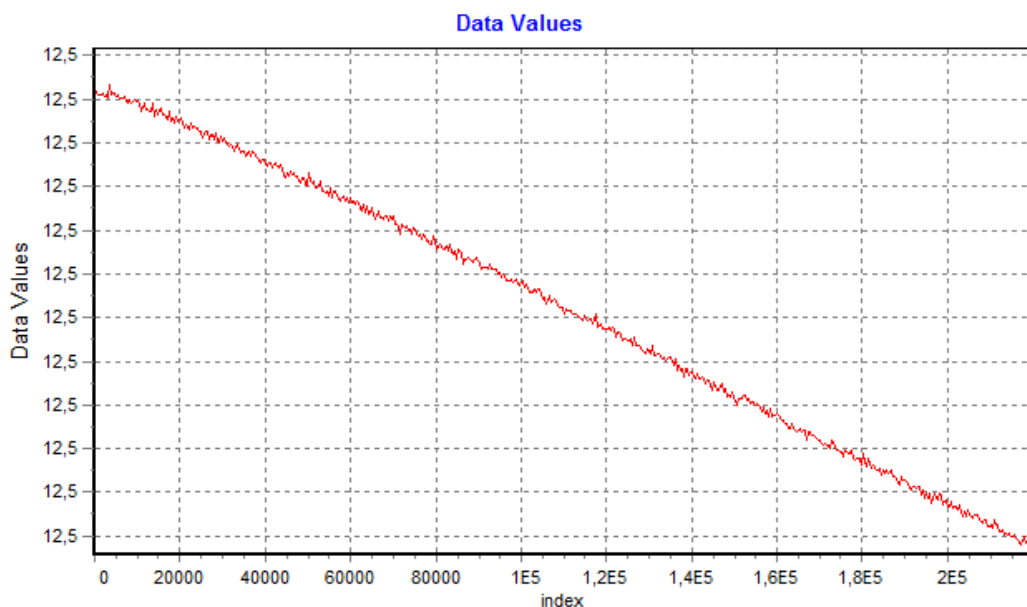


(a)

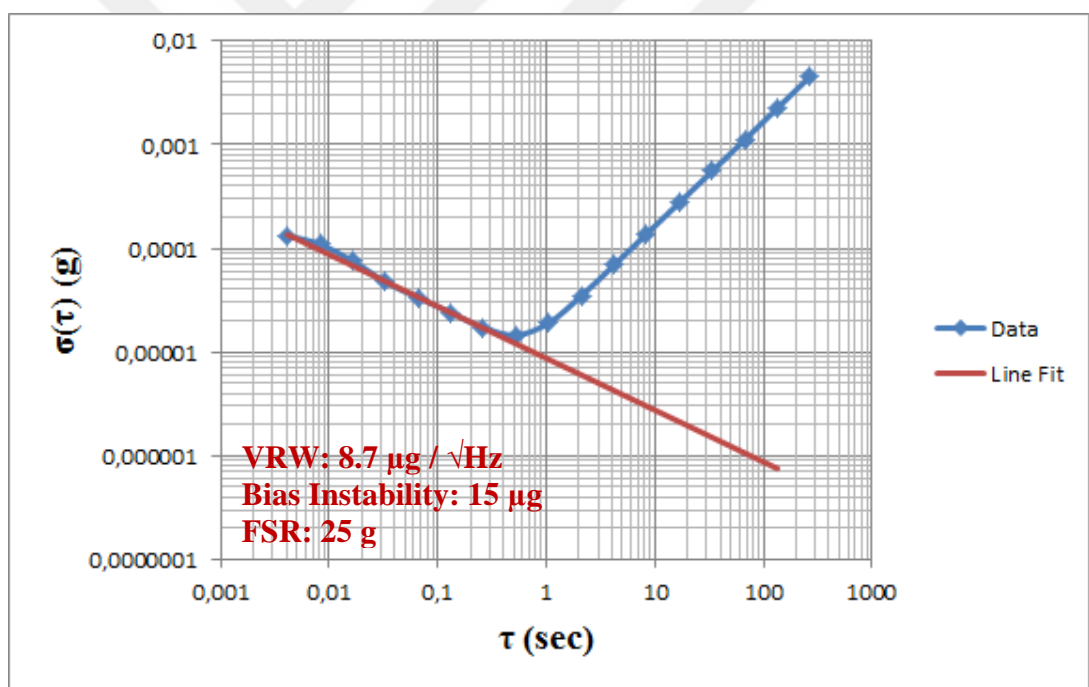


(b)

Figure 5.25: (a) The data is collected for 2 minutes at 23 MHz sampling frequency.
 (b) The Allan Variance graph of the vertical accelerometer design-4, A01-z axis.



(a)



(b)

Figure 5.26: (a) The data is collected for 2 minutes at 23 MHz sampling frequency.
 (b) The Allan Variance graphs for the vertical accelerometer design-2, B03.

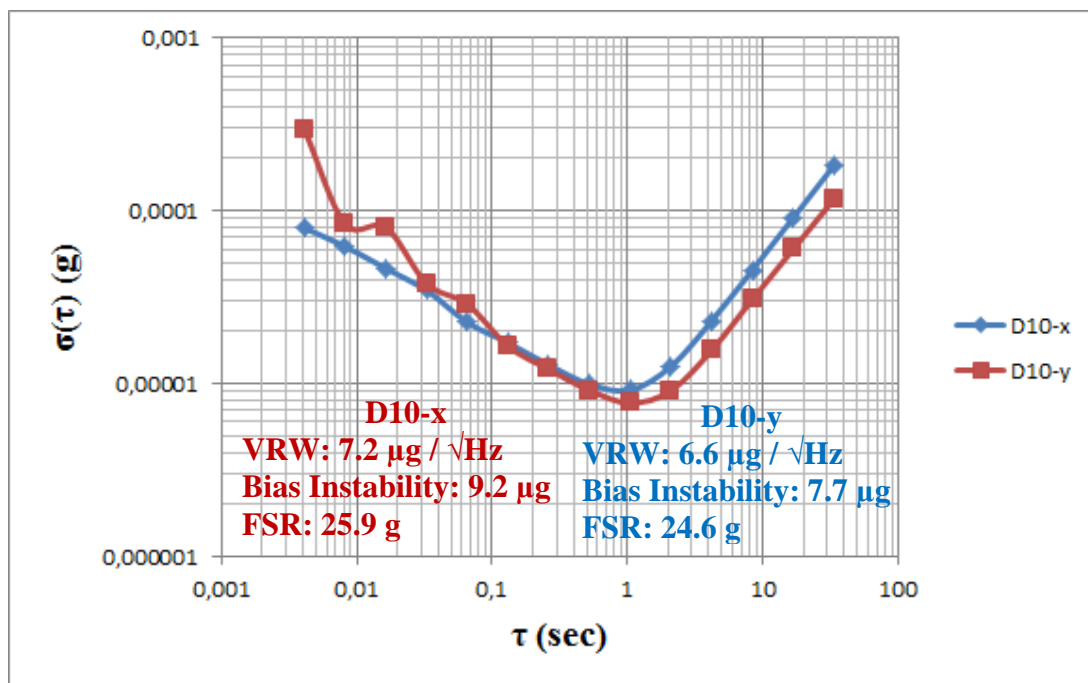


Figure 5.27: The comparison of Allan Variance graphs for D10-x and D10-y for the lateral accelerometer design-2 fabricated by using two-step anodic bonding.

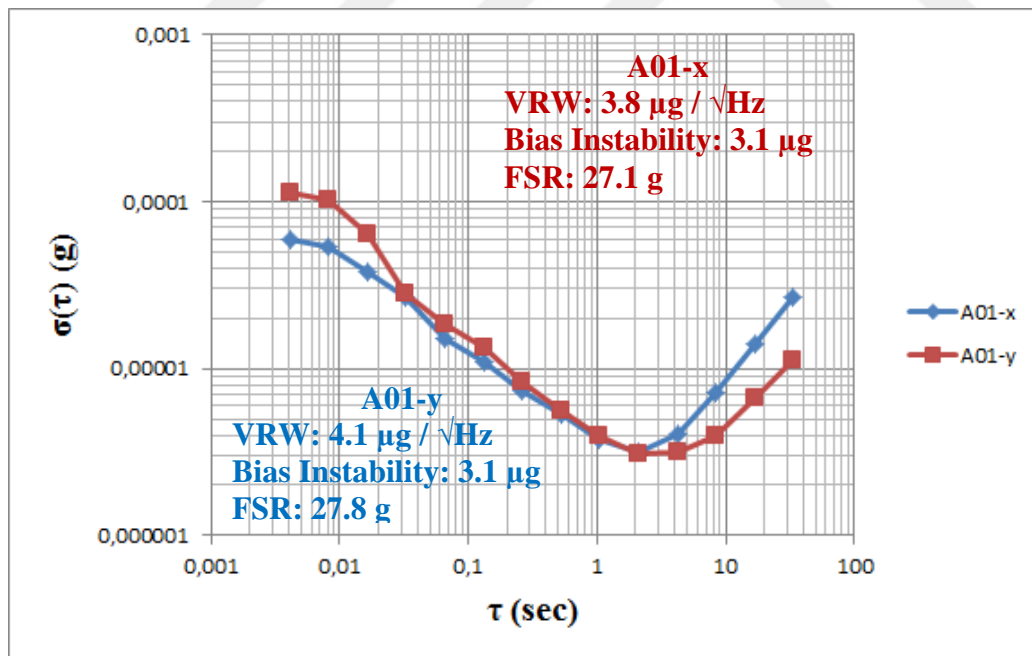


Figure 5.28: The comparison of Allan Variance graphs for A10-x and A10-y for the lateral accelerometer design-3 fabricated by using two-step anodic bonding.

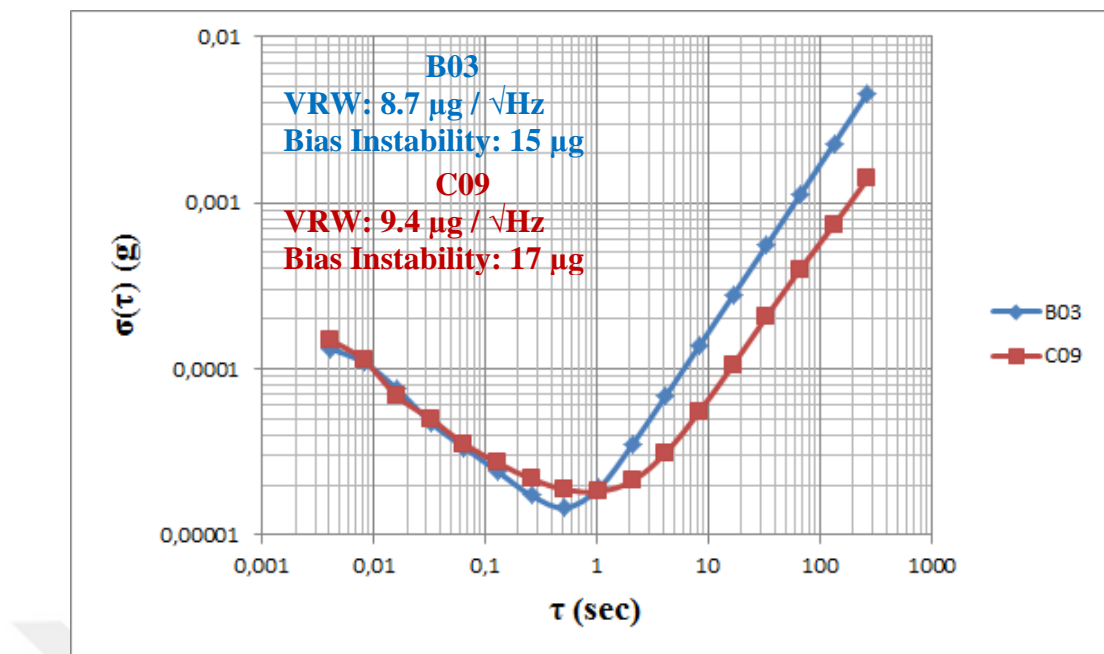


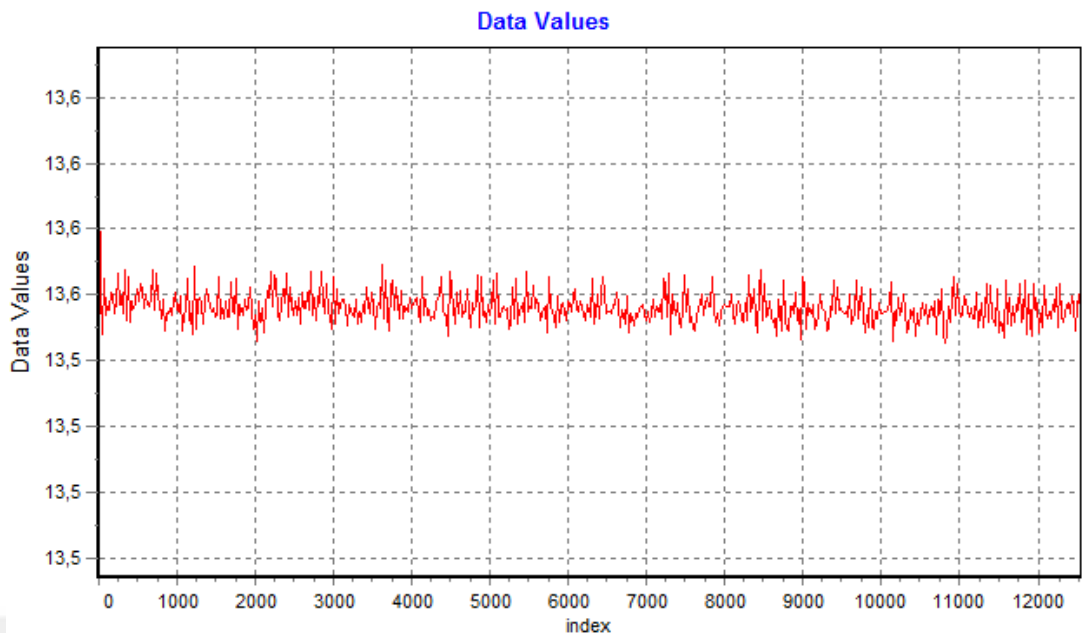
Figure 5.29: The comparison of Allan Variance graphs for B03 and C09 for the vertical accelerometer design-2 fabricated by using two-step anodic bonding.

5.4.3.2. System Level Results For Sensors by The Anodic Bonding and then Au-Si Eutectic Bonding

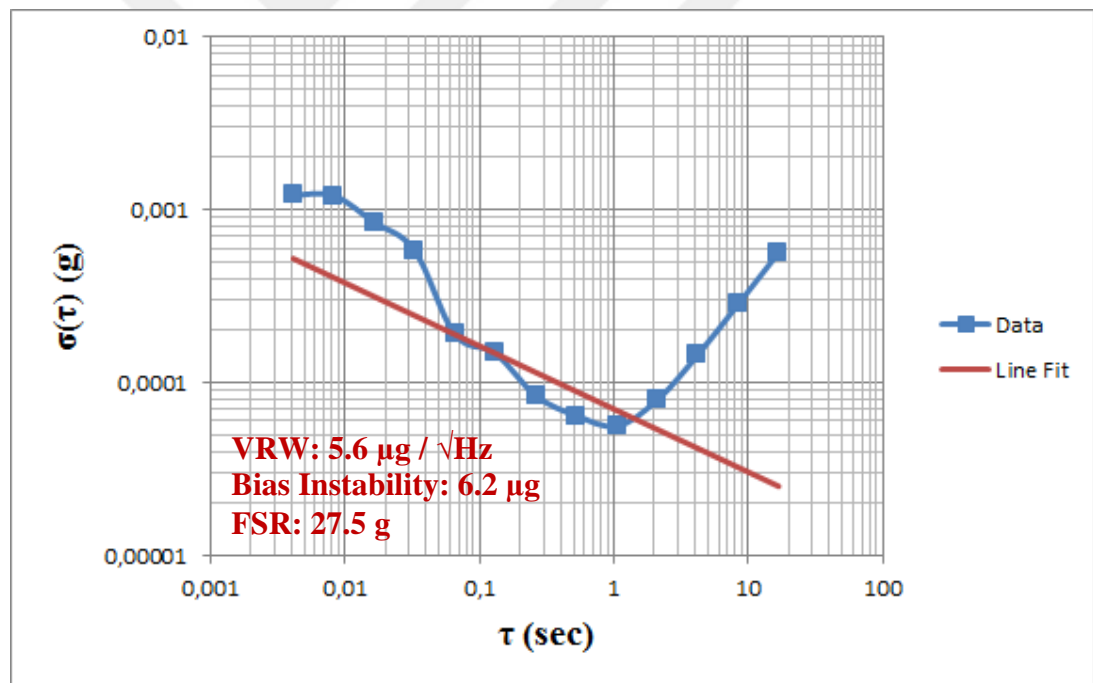
Sensors fabricated by using the anodic bonding and then the Au-Si eutectic bonding are tested for the lateral accelerometer design-1, design-2 and design-3 as well as the vertical accelerometer design-2 and design-4. Table 5.7 shows system level test results for the lateral accelerometer design-1, the lateral accelerometer design-2, the lateral accelerometer design-3 and the vertical accelerometer design-2 and design-4. Figure 5.30 shows the system level result for the lateral accelerometer design-1. Figure 5.31 shows the system level result for the lateral accelerometer design-2. Figure 5.32 and Figure 5.33 show the system level result for two different sensors having same design concept (the lateral accelerometer design-3). Figure 5.34 shows the system level result for the vertical accelerometer design-2. Figure 5.35 shows the system level result for the vertical accelerometer design-4. Figure 5.36 and Figure 5.37 shows the comparison of system level results for accelerometers having same design concept. Figure 5.38 and Figure 5.39 shows the comparison of system level result for accelerometers fabricated by using two different fabrication methods.

Table 5.7: The system level test results for three-axis accelerometers fabricated by using the anodic and then the Au-Si eutectic bonding.

| Code | Design | VRW | Bias Instability | Dynamic Range |
|------------|-------------------|-------------------------------------|-----------------------------------|---------------|
| B09 | Lateral design-1 | 5.6 $\mu\text{g}/\sqrt{\text{Hz}}$ | 6.2 μg | 127 dB |
| D10 | Lateral design-2 | 8.2 $\mu\text{g}/\sqrt{\text{Hz}}$ | 10 μg | 120 dB |
| A06 | Lateral design-3 | 5 $\mu\text{g}/\sqrt{\text{Hz}}$ | 5.6 μg | 125 dB |
| A06 | Lateral design-3 | 4.3 $\mu\text{g}/\sqrt{\text{Hz}}$ | 3.3 μg | 125 dB |
| B04 | Vertical design-2 | 7.85 $\mu\text{g}/\sqrt{\text{Hz}}$ | 9.6 μg | 118 dB |
| B06 | Vertical design-2 | 8.95 $\mu\text{g}/\sqrt{\text{Hz}}$ | 17 μg | 118 dB |
| A06 | Vertical design-4 | 10.5 $\mu\text{g}/\sqrt{\text{Hz}}$ | 12 μg | 122 dB |
| B01 | Vertical design-4 | 11.4 $\mu\text{g}/\sqrt{\text{Hz}}$ | 14 $\mu\text{g}/\sqrt{\text{Hz}}$ | 119 dB |

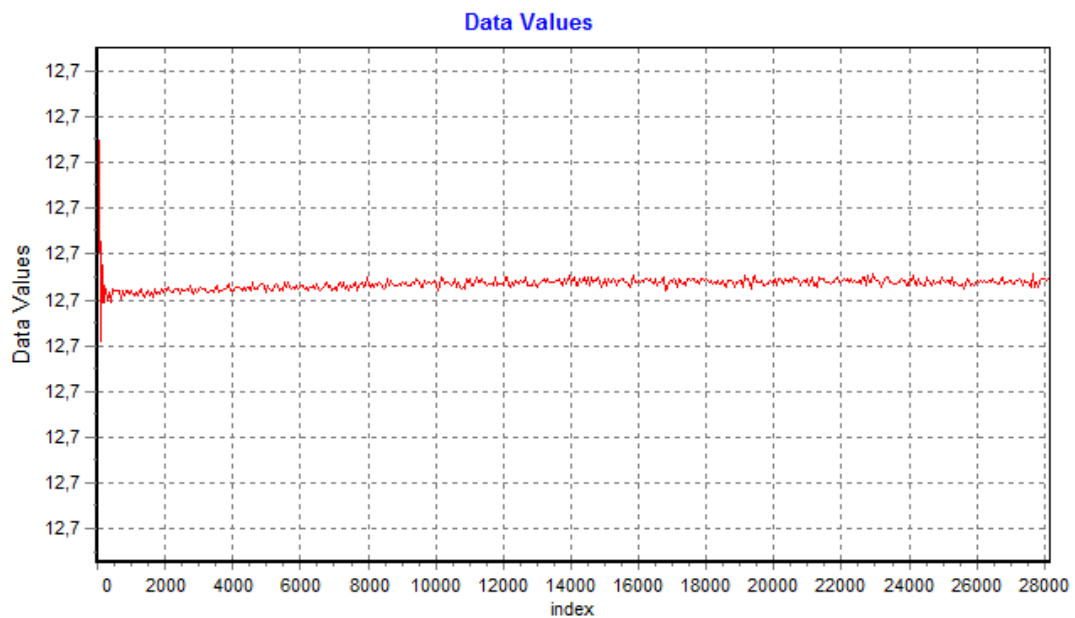


(a)

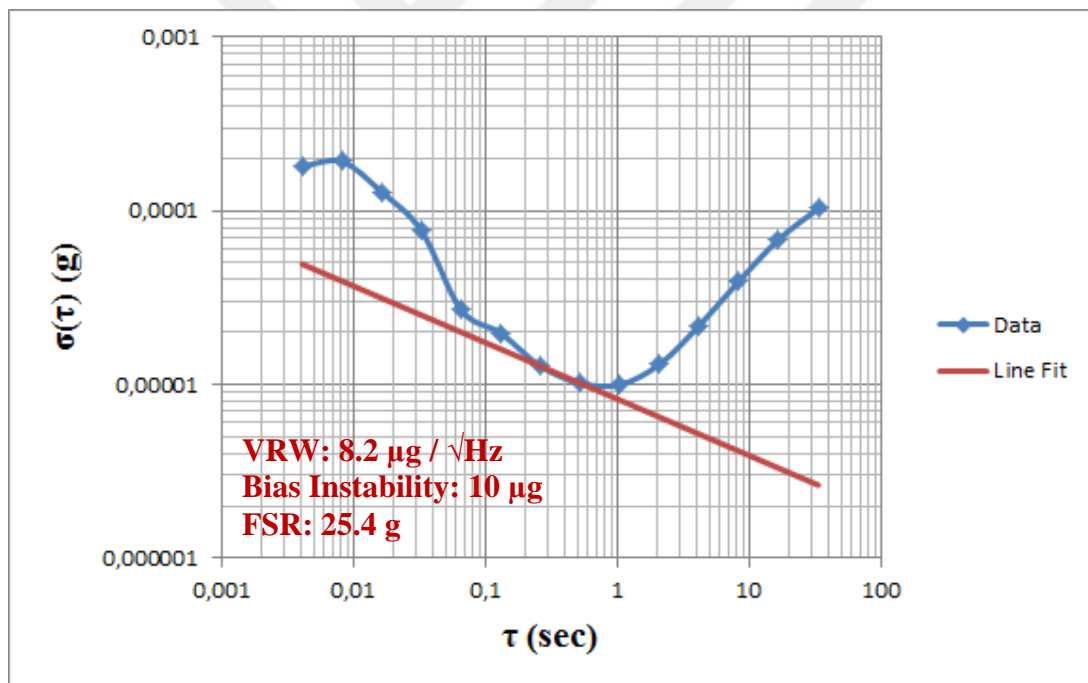


(b)

Figure 5.30: (a) The data is collected for 2 minutes at 46 MHz sampling frequency.
 (b) The Allan Variance graph of the lateral accelerometer design-1, B09.

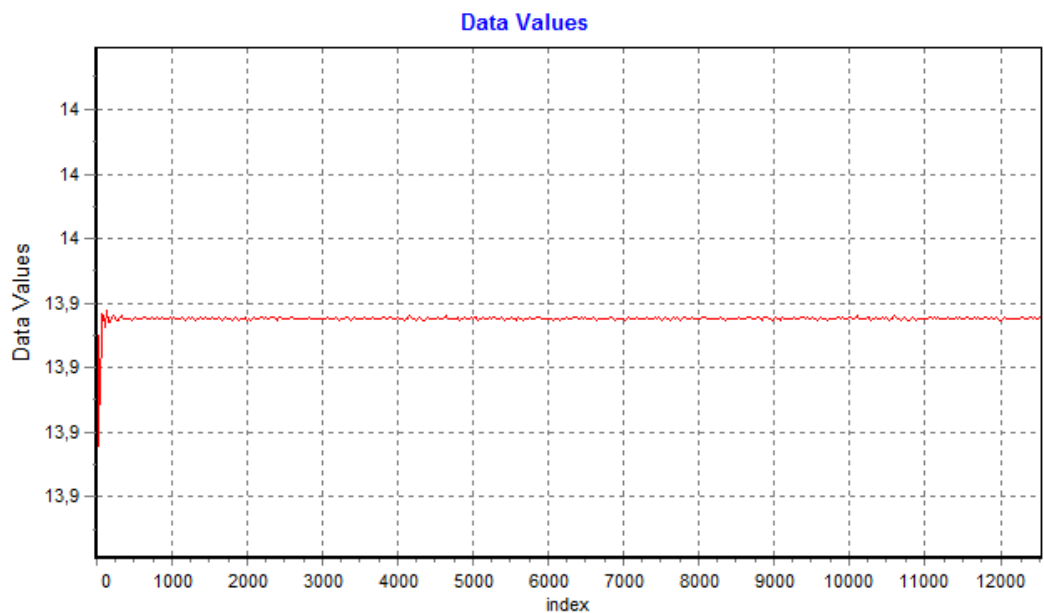


(a)

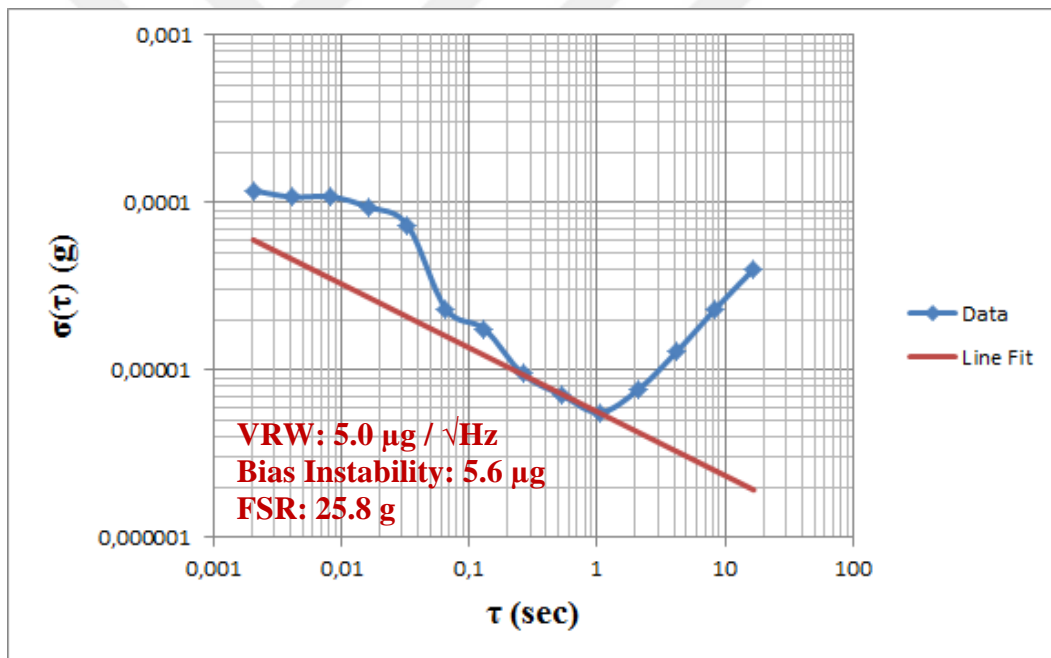


(b)

Figure 5.31 (a) The data is collected for 2 minutes at 46 MHz sampling frequency:
 (b) The Allan Variance graph of the lateral accelerometer design-2, D10.

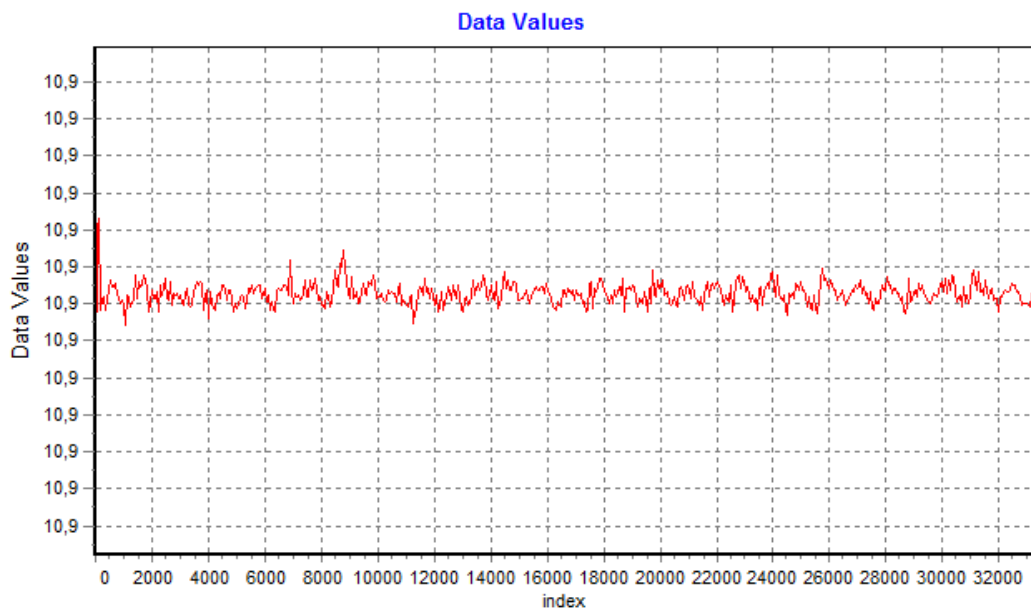


(a)

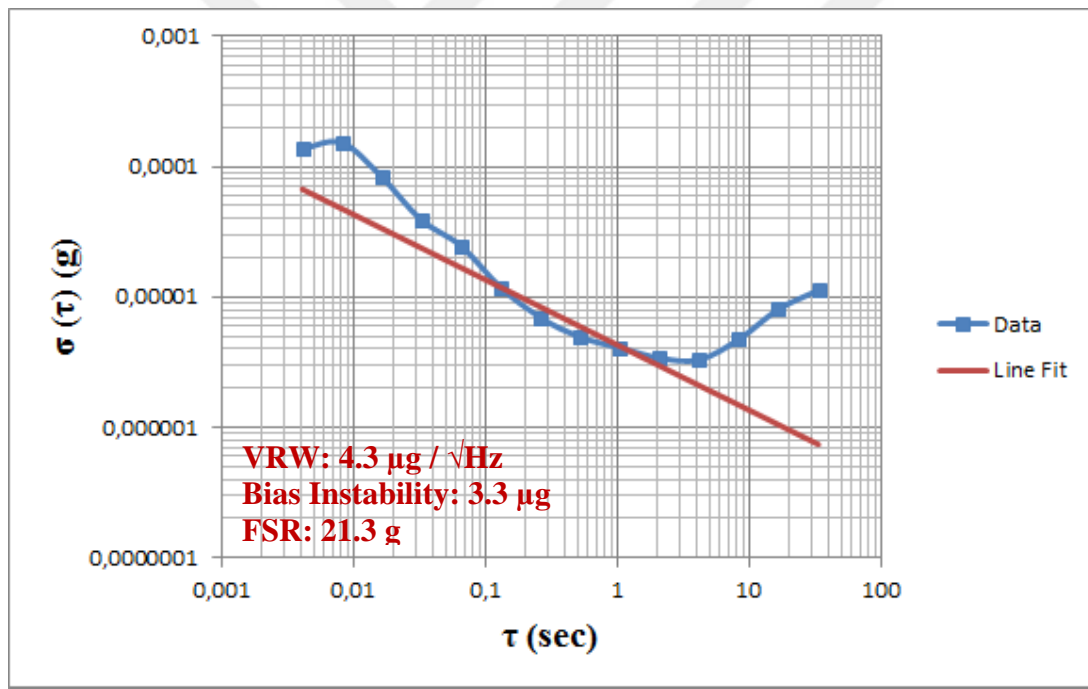


(b)

Figure 5.32: (a) The data is collected for 2 minutes at 46 MHz sampling frequency.
 (b) The Allan Variance graph of the lateral accelerometer design-3, A06-x.

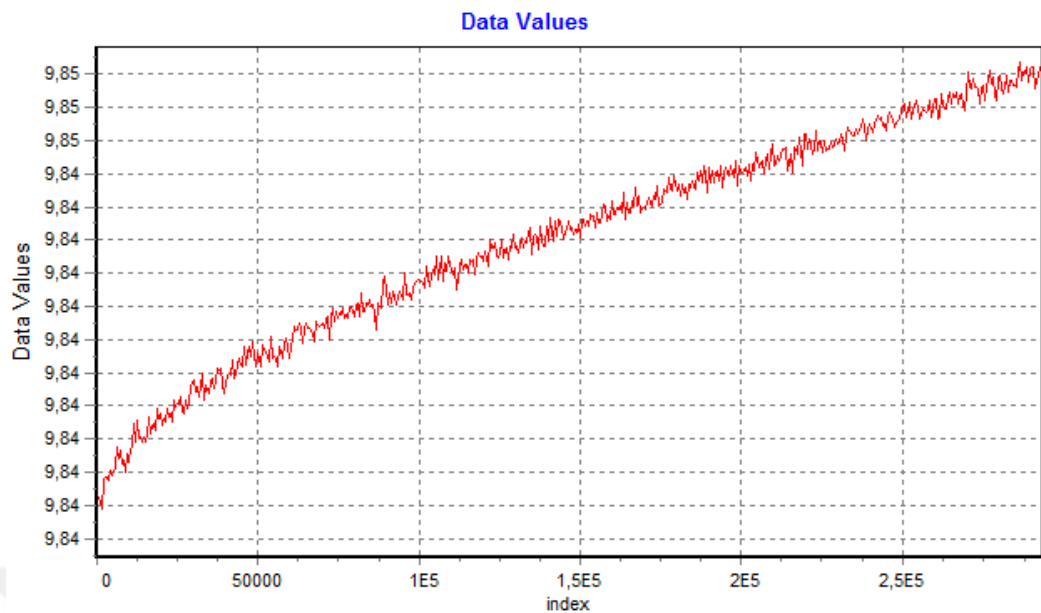


(a)

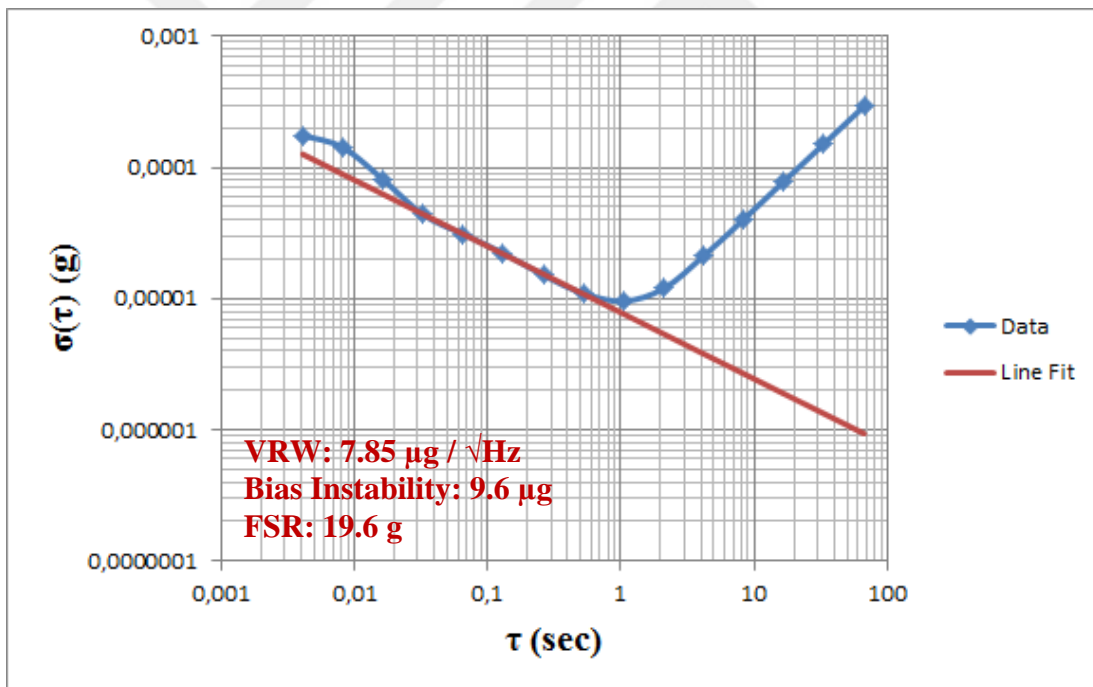


(b)

Figure 5.33: (a) The data is collected for 2 minutes at 46 MHz sampling frequency.
 (b) The Allan Variance graph of the lateral accelerometer design-3, A06-y.

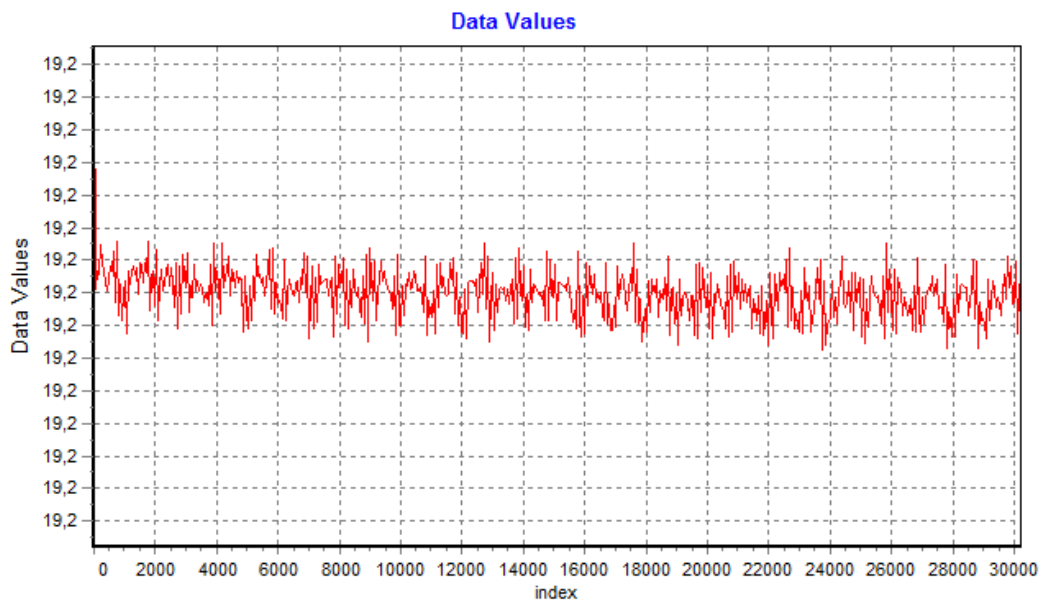


(a)

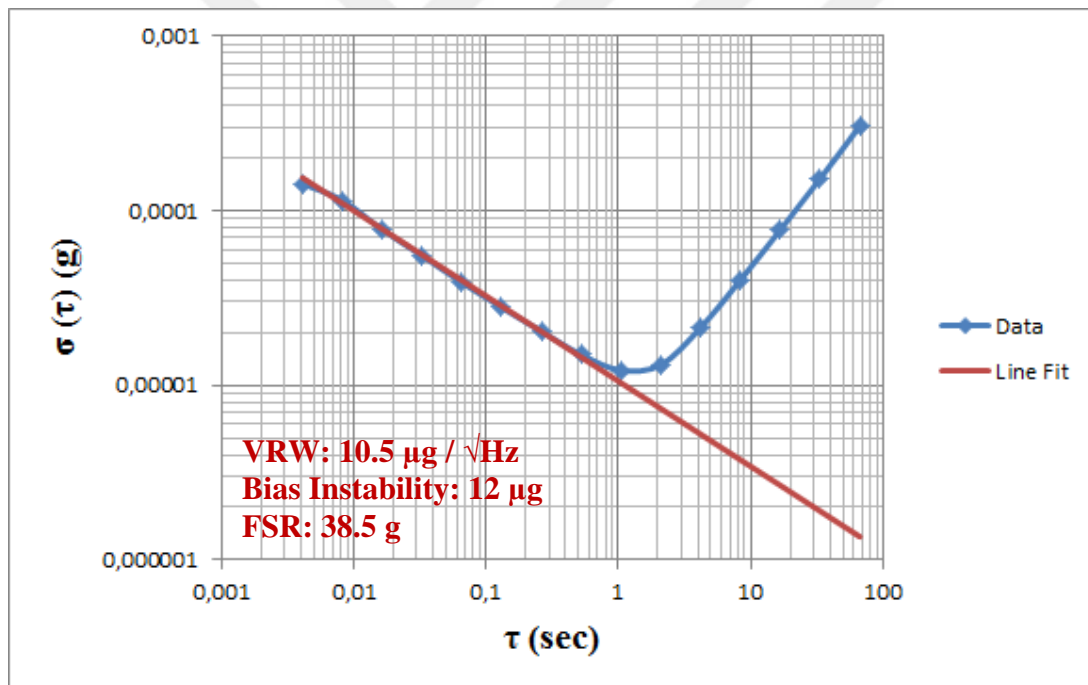


(b)

Figure 5.34: (a) The data is collected for 2 minutes at 46 MHz sampling frequency.
 (b) The Allan Variance of the vertical accelerometer design-2, B04.



(a)



(b)

Figure 5.35: (a) The data is collected for 2 minutes at 46 MHz sampling frequency.
(b) The Allan Variance graph of the vertical accelerometer design-4, A06.

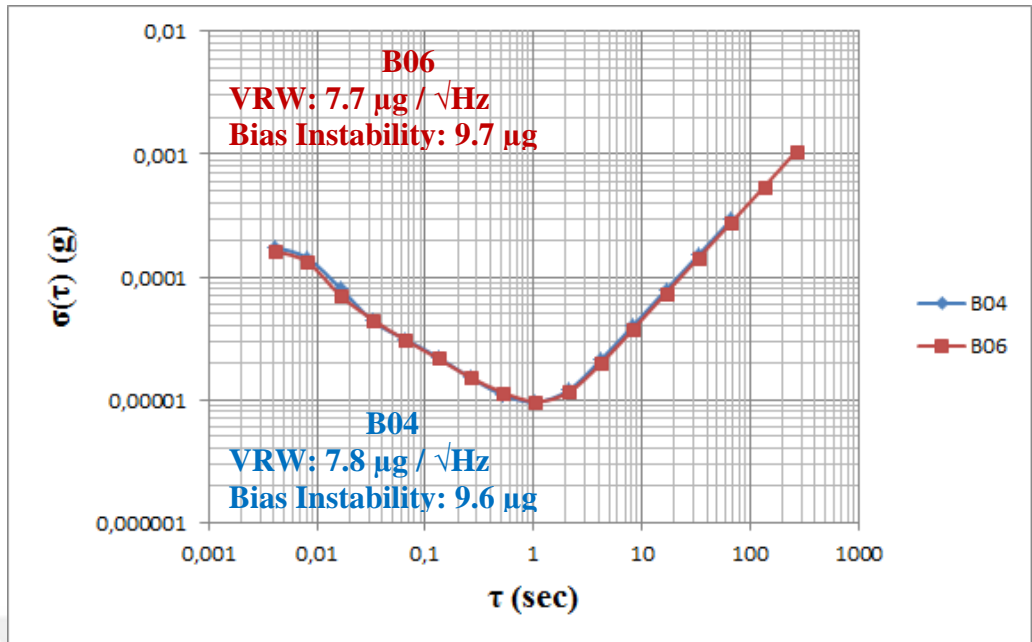


Figure 5.36: The comparison of Allan Variance graphs for B06 and B04 for the vertical accelerometer design-2 fabricated by using the anodic bonding and then Au-Si eutectic bonding.

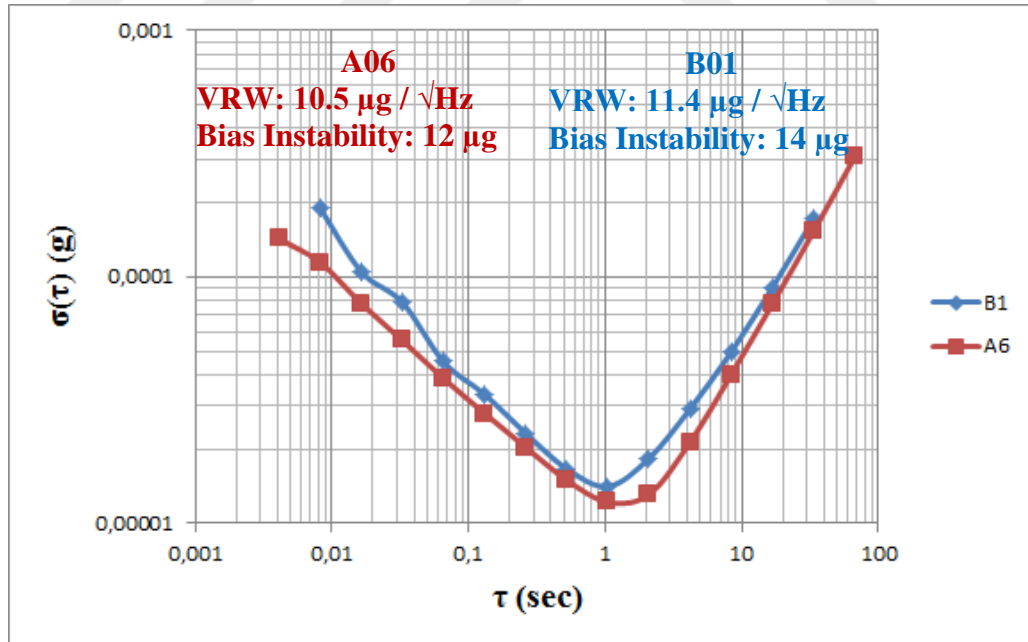


Figure 5.37: The comparison of Allan Variance graphs A06 and B01 for the vertical accelerometer design-4 fabricated by using the anodic bonding and then Au-Si eutectic bonding.

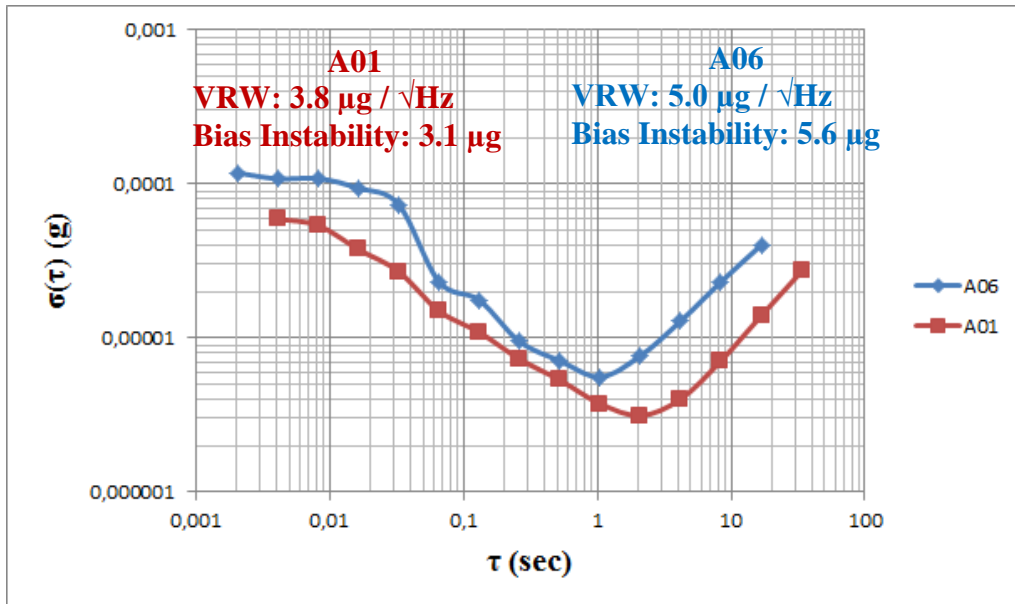


Figure 5.38: Allan Variance graphs of lateral accelerometers A01 versus A06 fabricated by using two-step anodic bonding and the Au-Si eutectic bonding, respectively.

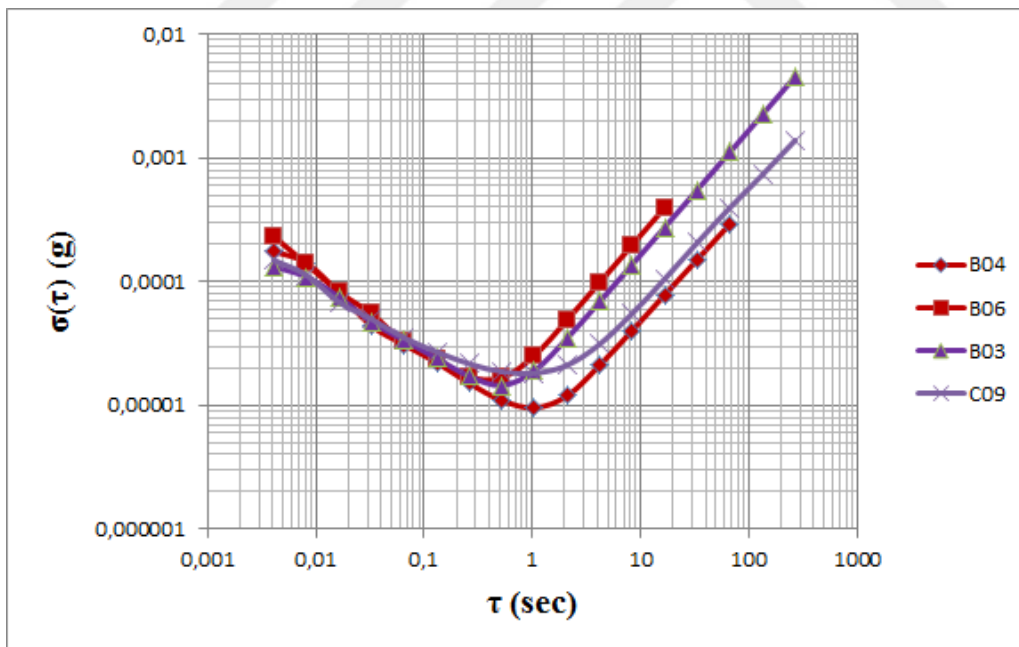


Figure 5.39: The comparison Allan Variance graphs for the vertical accelerometer design-2 fabricated different methods. The red one corresponds to the anodic and then the Au-Si eutectic bonding. The purple one corresponds to the two-step anodic bonding.

The rest capacitance mismatch is highly low for the vertical accelerometer design-5 as a result of high spring constant. However, the system level noise and the bias instability are starting increase for this design like in [53].

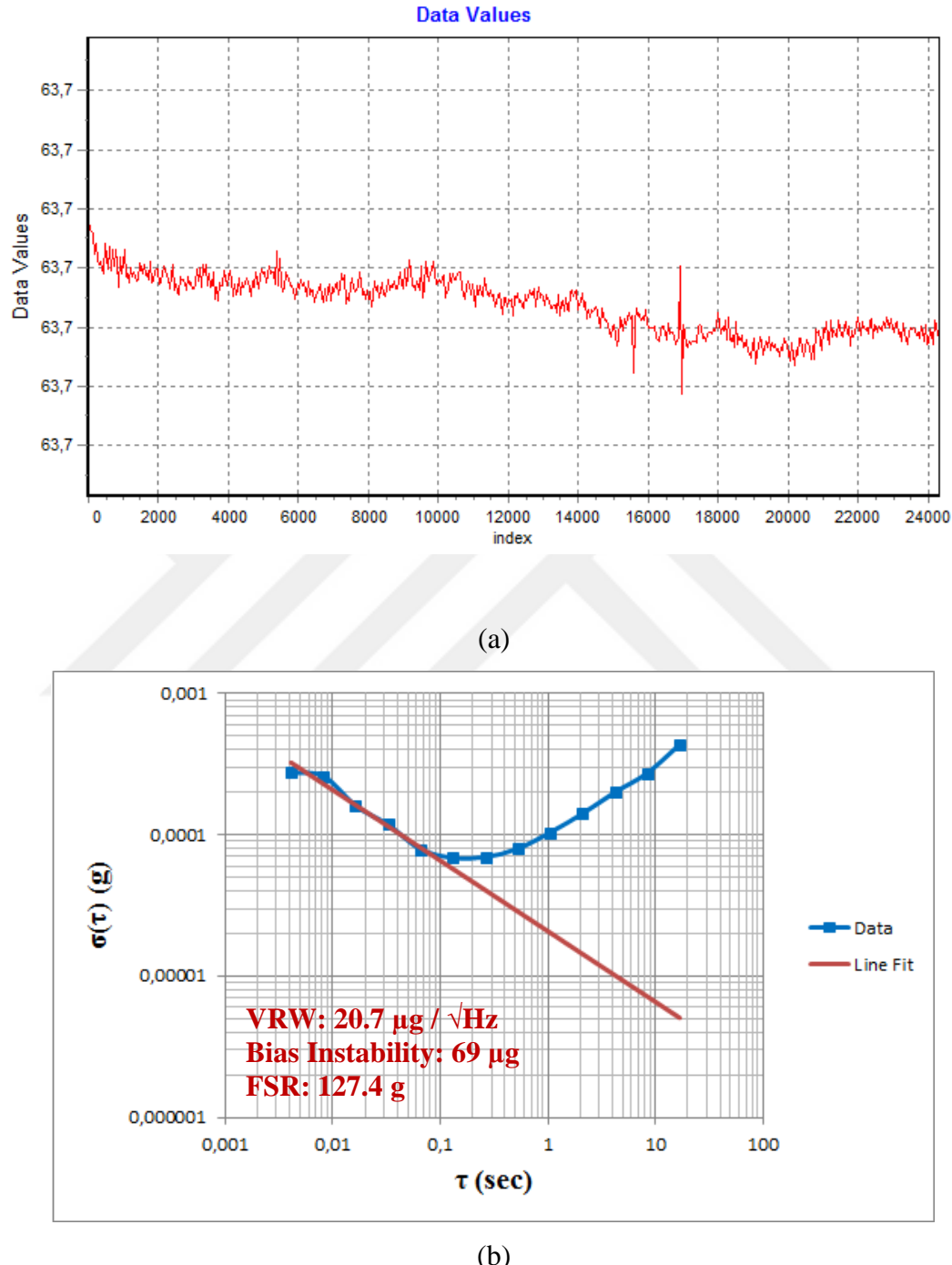


Figure 5.40: (a) The collected data and for 2 minutes at 23 MHz sampling frequency
(b) the Allan Variance graph of the vertical accelerometer design-5.

5.4.4. The Non-Linearity Test Result

The non-linearity of the lateral and the vertical accelerometer is determined. Table 5.8, Table 5.9, Table 5.10 and Table 5.11 shows the non-linearity result for the different vertical accelerometer. Table 5.12 and Table 5.13 shows the non-linearity result for the lateral accelerometer design-3. Figure 5.41 and Figure 5.42 shows non-linearity graphs for lateral accelerometers A04 and B07. Figure 5.43 shows the non-linearity graph for the vertical accelerometer C09.

Table 5.8: Non-linearity test result of the C09 accelerometer for different measurement ranges. Output range is extracted as +16.1 g, -7.5 g from the linearity test.

| Code | Range (g) | Non-linearity (ppm) (Positive direction) | Non-linearity (ppm) (Negative direction) |
|-----------------------------|-----------|---|---|
| Vertical design-2 C09 | 12 | 905 | - |
| | 10 | 446 | - |
| | 7 | 677 | 1793 |
| | 5 | 640 | 1189 |

Table 5.9: Non-linearity test result of the B04 accelerometer for different measurement ranges. Output range is extracted as +13.6 g, -9.4 g from the linearity test.

| Code | Range (g) | Non-linearity (ppm) (Positive direction) | Non-linearity (ppm) (Negative direction) |
|------------------------------|-----------|---|---|
| Vertical- design-2 B04 | 12 | 2298 | - |
| | 10 | 1442 | - |
| | 8 | 810 | 1525 |
| | 5 | 141 | 685 |

Table 5.10: Non-linearity of the B06 accelerometer for different measurement ranges. Output range was extracted as +13.8 g, -9.6 g from the linearity test.

| Code | Range (g) | Non-linearity (ppm) (Positive direction) | Non-linearity (ppm) (Negative direction) |
|--------------------------------------|------------------|---|---|
| Vertical design-2 B06 | 12 | 2259 | - |
| | 10 | 1423 | - |
| | 8 | 502 | 1754 |
| | 5 | 136 | 658 |

Table 5.11: Non-linearity of the A06 accelerometer for different measurement ranges. Output range is extracted as +21.9 g, -16.5 g from the linearity test.

| Code | Range (g) | Non-linearity (ppm) (Positive direction) | Non-linearity (ppm) (Negative direction) |
|--------------------------------------|------------------|---|---|
| Vertical design-4 A06 | 18 | 8516 | - |
| | 14 | 4896 | 8870 |
| | 10 | 2087 | 4994 |
| | 7 | 614 | 2645 |

Table 5.12: Non-linearity of the A04 accelerometer for different measurement ranges. Output range was extracted as +12.0 g, -12.4 g from the linearity test.

| Code | Range (g) | Non-linearity (ppm) (Positive direction) | Non-linearity (ppm) (Negative direction) |
|-------------------------------------|------------------|---|---|
| Lateral design-3 A04 | 10 | 1567 | 1662 |
| | 7 | 786 | 809 |
| | 5 | 377 | 434 |

Table 5.13: Non-linearity of the B07 accelerometer for different measurement ranges. Output range is extracted as +12.1 g, -12.8 g from the linearity test.

| Code | Range (g) | Non-linearity (ppm) (Positive direction) | Non-linearity (ppm) (Negative direction) |
|-----------------|-----------|---|---|
| Lateral | 10 | 1312 | 1185 |
| Design-3 | 7 | 548 | 691 |
| B07 | 5 | 232 | 499 |

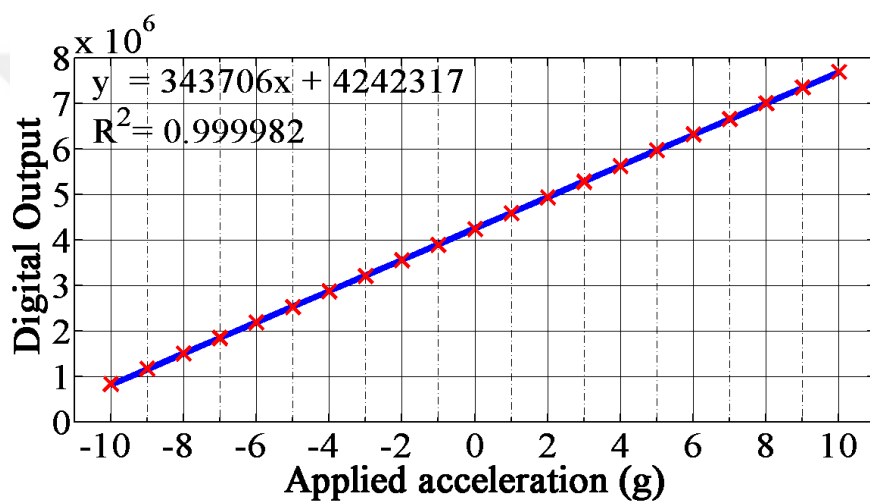


Figure 5.41: Non-linearity result of lateral accelerometer A04 is 0.28 %.

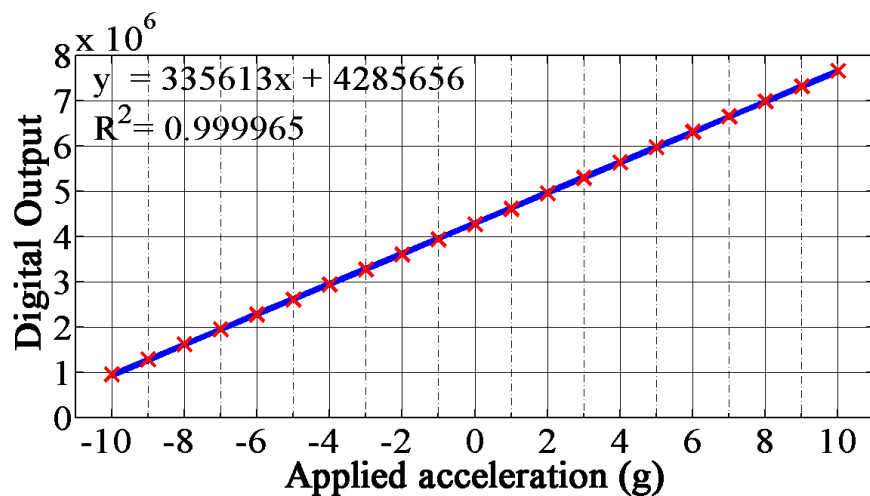


Figure 5.42: Non-linearity result of lateral accelerometer B07 is 0.34 %.

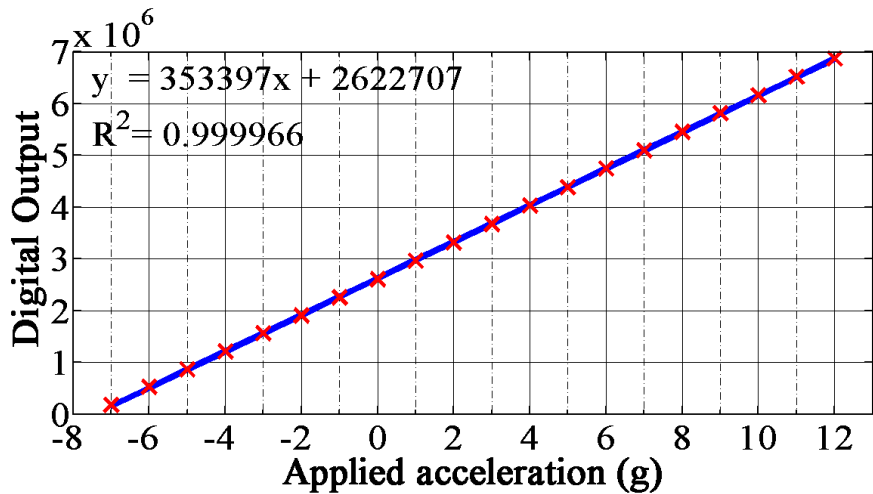


Figure 5.43: Non-linearity result of vertical accelerometer C09 is 0.41 %.

5.5. Summary of the Chapter

This chapter gives information about test equipment and the system level test for the three-axis accelerometer. Then, the functionality and the system level test procedure are comprehensively explained. Finally, the C-V test result, the resonance frequency test result, and the system level test result are presented for the fabricated three axis accelerometer. The system level test result is repeated for different sensors having same design concept. It is observed that the system level results are in good agreement with each other. Furthermore, system level results are compared for the two-alternative fabrication process.



CHAPTER 6

CONCLUSION AND FUTURE WORK

Objective of this thesis is to develop a process enabling the fabrication of the three-axis accelerometer in the same die. Although there are many different accelerometer in the literature, MEMS capacitive type accelerometer is selected as a result of low-cost, low power detection, low noise level as well as its robustness.

Optimized fabrication processes depend on the formation of the glass-silicon-glass structure by using the two-step anodic bonding as well as the anodic bonding and then Au-Si eutectic bonding. Two alternative fabrication processes provide not only an electrode for the vertical accelerometer but also a cap for the entire structure. In the first attempt, the three-axis accelerometer is tried to fabricate by using the highly doped SiGeB wafer and the two-electrode anodic bonding. Two important fabrication results are observed. One of them, as the silicon between glass wafers is not grounded; the triple stack interacts with the chuck of the bonder. The second result is high capacitive mismatched observed for the vertical accelerometer between the top and the bottom electrode after the fabrication. These problems are solved by using the three-electrode anodic bonding and the SOI wafer. Furthermore, as sensors are already released during anodically bonding of the second glass wafer, the shield metallization is required, which introduces the parasitic capacitance to the lateral accelerometer. Therefore, the anodic bonding and then the Au-Si eutectic bonding fabrication methods is also optimized, which eliminates the parasitic capacitance.

During the fabrication process, two mask sets are studied. In the first mask set, sensor performance parameters are not taken into account to show the feasibility of the fabrication process. In the first mask set, there are six vertical accelerometer and

one lateral accelerometer design. Fabrication results of the first mask set is used the optimization of the second mask set, where lateral and vertical accelerometer are designed considering the performance parameters. Furthermore, in the second mask set, the performance parameters of vertical accelerometer is try to fit that of lateral accelerometers.

There are ten different vertical accelerometers and two different lateral accelerometers are designed in this study. The functionality of fabricated sensors is verified with die level results. Furthermore, a three axis accelerometers package is formed by integrating sensor with the readout circuit and a glass substrate for the system level test. Achievements of the study can be summarized as follows:

1. For the first time in the literature, a three-axis accelerometer is fabricated by using a glass-silicon-glass structure.
2. The second glass wafer provides not only a top electrode for the vertical accelerometer but also a cap for the entire structure. Thus, as sensors have cap provided by second glass, they can be easily handled and the top glass can protect sensors from dust and environmental condition.
3. The optimized two-different fabrication process can also be used to provide a cap for different sensor application which does not requires vacuum.
4. The system level test result of the lateral and vertical accelerometers are in good agreement with each other. To match the lateral and vertical accelerometer performance parameters is one of the main challenges for the fabrication of the three axis accelerometer.
5. Performance parameters of lateral and vertical accelerometers fabricated by using the two-different fabrication method are summarized in the following tables.

Table 6.1: The comparison of fabrication results of accelerometers for two-different fabrication process.

| Code | Design | VRW | Bias Instability | Dynamic Range | Fab. Method |
|------------|-------------------|-------------------------------------|-------------------|---------------|--------------------------------------|
| A06 | Lateral desing-3 | 5 $\mu\text{g}/\sqrt{\text{Hz}}$ | 5.6 μg | 125 dB | The Anodic- The Au-Si Eutectic |
| A01 | Lateral desing-3 | 3.8 $\mu\text{g}/\sqrt{\text{Hz}}$ | 3.1 μg | 128 dB | Two-Step Anodic Bonding |
| D10 | Lateral desing-2 | 8.2 $\mu\text{g}/\sqrt{\text{Hz}}$ | 10 μg | 120 dB | The Anodic- The Au-Si Eutectic |
| D10 | Lateral desing-2 | 7.2 $\mu\text{g}/\sqrt{\text{Hz}}$ | 9.2 μg | 122 dB | Two-Step Anodic Bonding |
| A06 | Vertical design-4 | 10.5 $\mu\text{g}/\sqrt{\text{Hz}}$ | 12 μg | 122 dB | The Anodic- The Au-Si Eutectic |
| B01 | Vertical design-4 | 11.4 $\mu\text{g}/\sqrt{\text{Hz}}$ | 14 μg | 119 dB | The Anodic- The Au-Si Eutectic |

Table 6.2: The three-axis accelerometer sensor A06 system level test results fabricated by using the Au-Si eutectic bonding.

| Sensor A06 | Velocity Random Walk | Bias Instability | Dynamic Range |
|--------------------------|-------------------------------------|-------------------|---------------|
| Vertical Design-4 | 10.5 $\mu\text{g}/\sqrt{\text{Hz}}$ | 12 μg | 122 dB |
| Lateral Design-3 | 4.30 $\mu\text{g}/\sqrt{\text{Hz}}$ | 3.3 μg | 125 dB |
| Lateral Design-3 | 5 $\mu\text{g}/\sqrt{\text{Hz}}$ | 5.6 μg | 125 dB |

Table 6.3: The three-axis accelerometer sensor A01 system level test results fabricated by using the two-step anodic bonding.

| Sensor A01 | Velocity Random Walk | Bias Instability | Dynamic Range |
|--------------------------|-------------------------------------|-----------------------------|--------------------------|
| Vertical Design-4 | 17.6 $\mu\text{g}/\sqrt{\text{Hz}}$ | 19 μg | 113 dB |
| Lateral Design-3 | 3.8 $\mu\text{g}/\sqrt{\text{Hz}}$ | 3.1 μg | 128 dB |
| Lateral Design-3 | 4.1 $\mu\text{g}/\sqrt{\text{Hz}}$ | 3.1 μg | 127 dB |

Although the shield metallization leads to the parasitic capacitance observed in the C-V test of sensors, this does not cause a major problem during the system level test as the shield metallization is grounded. Furthermore, system level results obtained from two-step anodic bonding are slightly better than that of the anodic and then the Au-Si eutectic bonding.

Although many goals are achieved within the scope of this thesis, some improvements can also be performed, which are listed below.

1. The capacitance mismatch problem is eliminated by using the SOI wafer for vertical accelerometer with high spring constant. However, as performance parameters of the vertical accelerometer are matched to that of the lateral accelerometer, the spring constant of the vertical accelerometer is designed quite low in the second mask with respect to the first one. Therefore, there is slightly difference in the capacitance formed between the top and the bottom electrode for vertical axis accelerometer fabricated by using the second mask. Different vertical axis accelerometer design and spring structure can also be researched to solve this problem.
2. The Table 5.3 shows the C-V test result of the design-5 whose spring constant is high. Although the capacitance mismatch is considerably decreased by using design-5 accelerometer, the noise and the bias instability results are degraded. Therefore, the more flexible readout circuit which is not affected from sensor parameters can be designed.

3. The fabrication processes provides a cap for entire structure; however, sensors are hermetically not sealed after two fabrication processes. Two fabrication processes can be modified by using a second glass wafer having vertical feed through interconnections. Figure 6.1 shows the proposed fabrication steps. The fabrication step will be same with the current fabrication step except kind of the second glass wafer.

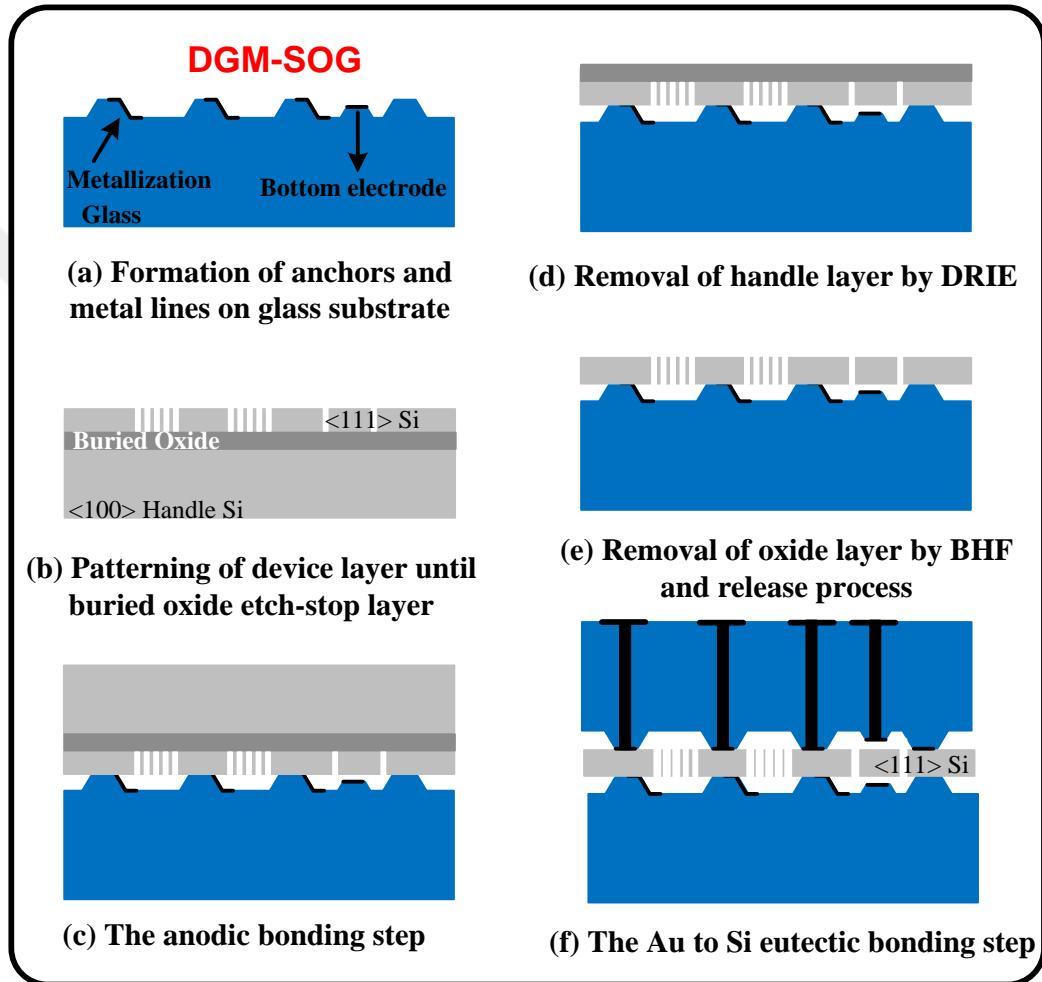


Figure 6.1: The proposed fabrication method to hermetically seal the sensors region.

As a conclusion, two alternative fabrication processes are optimized for the fabrication of the three axis accelerometer, where the second glass provides not only an electrode for the vertical accelerometer but also a cap for entire structure.



REFERENCES

- [1] Robert Bogue, "MEMS Sensors: Past, Present and Future," *Sensor Review*, Vol. 27, no.1, pp. 7-13, 2007.
- [2] S. Y. Yurish, N.V. Kirianaki, I. L. Myshkin, "World Sensors and MEMS Market: Analysis and Trends," *Sensors and Transducers Magazine*, Vol. 62, no. 12, pp. 456-461, December 2005.
- [3] Yunhan Huang, Arind Sai Sarathi Vasan, Ravi Doraiswami, Michael Osterman and Michael Petch, "MEMS Reliability Review," *IEEE Transactions on Device and Materials Reliability*, Vol. 12, no. 2, pp. 482-492, June 2012.
- [4] Derek K. Shaeffer, "MEMS Inertial Sensors: A Tutorial Overview," *IEEE Communications Magazine*, Vol. 51, no.4, pp. 100-109, April 2013.
- [5] Michael Kraft, "Micromachined Inertial Sensors State of the Art and a Look into the Future," *Measurement + Control*, Vol. 33, no.6, pp. 164-168, July 2000.
- [6] Patrick L. Walter, "The History of MEMS Accelerometer: 1920s-1996 – Prolouqe and Epiloque," *Sound and Vibration, Acoustical Publications*, Inc., 2007.
- [7] A. Alvin Barlian, Woo-Tae Park, Joseph R. Mallon, Jr., Ali j., Rastegar, and Beth L. Pruitt, "Review: Semiconductor Piezoresistance for Microsystems," Proceedings of the IEEE, Vol. 97, no. 3, pp. 513-552, March 2009.
- [8] Wen H. Ko, "Trend and Frontiers of MEMS," *Sensor and Actuators A*, Vol 135, pp.62-67, February 2007.
- [9] Terahz, http://terahz.org/_html/22SensorChronology.html, last visited on Janurary 2014.
- [10] Laurent Robin, Yole Development, "New MEMS Opportunities in Cell Phones and Tablets: What will be the New Killer Apps ?," *Micromachine/MEMS 2012-MEMS Market Briefing*, July 2012.
- [11] Karen Lightman, http://www.memsindustrygroup.org/files/resource_library_files/Lightman%20%20Uplinq%20HW%20%20MEMS%20%26%20Sensor%20Trends.pdf, last visited on January 2014.

[12] Navid Yazdi, Farrokh Ayazi, Khalil Najafi, "Micromachined Inertial Sensors," *Proceedings of the IEEE*, Vol. 86, no.8, pp. 1640-1659, August 1998.

[13] Cheng-Hsien Liu and Thomas W. Kenny, "A High-Precision, Wide-Bandwidth Micromachined Tunneling Accelerometer," *Journal of Microelectromechanical Systems*, Vol. 10, no.3, September 2001.

[14] Ashwin A. Seshia, Moorthi Palaniapan, Tery A. Roessig, Roger T. Howe, Roland W. Gooch, Thomas R. Schimert, and Stephen Montague, " A Vacuum Packaged Surface Micromachined Resonant Accelerometer," *Journal of Microelectromechanical Systems*, Vol. 11, no.6, December 2002.

[15] Veljko Milanovi, Edwin Bowen, Nim Tea, John Suehle, Beverly Payne, Mona Zaghloul, and Michael Gaitan, " Convection-based Accelerometers and Tilt Sensor Implemented in Standart CMOS," *Proc. Int. Mech. Eng. Conf. and Exp., MEMS Symposium*, Anaheim, Nov. 1998.

[16] Yu-Chia Liu, Ming-Han Tsai, Sheng-Shian Li, and Weileun Fang, " A fully-differential multiplex-sensing interface circuit monolithically integrated with tri-axis pure oxide capacitive CMOS-MEMS accelerometers," *Proceedings of Transducers*, pp. 610-613, Barcelona, Spain June 2013.

[17] Ming-Han Tsai, Yu-Chia Lui, and Weileun Lang, "A three-axis CMOS-MEMS accelerometer structure with vertically integrated fully differential sensing electrodes," *Journal of MicroEelectromechanical Systems*, Vol.21, no: 6, pp. 1329-1337, December, 2012.

[18] Chih-Ming Sun, Ming-Han Tsai, Yu-Chia Liu, and Weileun Fang, "Implementation of a monolithic single proof-mass tri-axis accelerometer using CMOS-MEMS technique," *IEEE Transactions on Electron Devices*, Vol.57, no:7, pp. 1670-1679, July 2010.

[19] Y. Jeong, D. E. Serrano, V. Keesara, W. K. Sung, and F. Ayazi. "Wafer-level vacuum-packaged tri-axial accelerometer with nano airgaps," *IEEE MEMS 2013*, pp. 3-36, Taipei, Taiwan, January 2013.

[20] Yu-Wen Hsu, Jen-Yi Chen, Hsin-Tang Chien, Sheah Chen, Shih_ting Lin and Lu_Po Liao, " New capacitive low-g triaxial accelerometer with low cross-axis sensitivity," *J. Micromech. Microeng.*, Vol. 20, pp.1-10, February, 2010.

[21] Junseok Cahe, Haluk Kulah and Khalil Najafi, “A monolithic three-axis micro-g micromachined silicon capacitive accelerometer,” *Journal of Microelectromechanical Systems*, Vol.14, no: 2, pp. 235-242, April, 2005.

[22] Henrik Rödjestad, Christer Johansson, Peter Enoksson, Gert Andersson, “A monolithic three-axis SOI-accelerometer with uniform sensitivity,” *Sensors and Actuators A*, Vol.123-124, pp.50-53, February, 2005.

[23] Yangxi Zhang, Gang Yang, Chengchen Gao, Yilong Hao, “A MEMS sandwich differential capacitive silicon-on-insulator accelerometer,” *Microsyst. Technol.*, Vol. 19, pp.1249-1254, January, 2013.

[24] Qifang Hu, Chengchen Gao, Yilong Hao, Dacheng Zhang, Guizhen Yan, Yangxi Zhang, “Design and fabrication of a MEMS capacitive accelerometer based on double-device-layers SOI wafer,” *Proceedings of 5th IEEE International Conference on Nano/Micro and Molecular Systems*, pp.1036-1039, Xiamen, China, January, 2010.

[25] Chia-Pao Hsu, Ming-Chuen Yip, Weileun Fang, “Implementation of a gap-closing differential capacitive sensing z-axis accelerometer on an SOI wafer,” *J. Micromech. Microeng*, Vol.19, pp.1-7, June 2003.

[26] H. Seidel, H. Riedel, R. Kolbeck, G. Mück, W. Kupke and M. Königer, “Capacitive Silicon with Highly Symmetrical Design,” *Sensors and Actuators*, A21-A23 pp.312-314 June 1990.

[27] Eric Peeters, Stef Vegote, Bob Puers and Willy Sansen, “ A highly symmetrical capacitive micro-accelerometer with single degree-of-freedom response,” *J. Micromech. Microeng.*, Vol.2, pp. 104-112, April 1992.

[28] Bweatrice Wenk, J. Ramos-Martos, M. Fehrenbach, P. Lange, Michael Offenberg, Werner Riethmüller, “Thick-polysilicon-based surface micromachined capacitive accelerometers with force-feedback operation,” *Proc. of SPIE 2642*, Micromachined Devices and Components, September 1995.

[29] K.H.-L Chau, S.R. Lewis, Y.Zhao, R.T. Howe, S.F. Bart, R.G. Marcheselli, “An integrated force-balanced capacitive accelerometer for low-g applications,” *Sensors and Actuators A*, Vol.54, pp. 472-474, 1996.

[30] M. Lemkin, Bernhard E. Boser, “A Micromachined Fully Differential Lateral Accelerometer,” *IEEE 1996 Custom Integrated Circuits Conference*, pp.315-318, 5-8 May 1996, San Diego, CA.

- [31] Mar A. Lemkin, Monlco A. Ortiz, Nalyavudhi Wongkomel, Bernhard E. Boser, James H. Smith, “A 3-Axis Surface Micromachined $\Sigma\Delta$ Accelerometer,” *IEEE International Solid-State Circuit Conference*, February 1997.
- [32] B.P. van Drieënhuizen, N.I. Maluf, I. E. Opris and G.T.A Kovacs, “ Force-Balanced Accelerometer with mG Resolution, Fabricated using Silicon Fusion Bonding and Deep Reactive Ion Etching,” *Transducer 97, International Conference on Solid-State Sensors and Actuators*, Chicago, June 16-19, 1997.
- [33] R. Puers, S. Reyntjens, “Design and processing experiments of a new miniaturized capacitive triaxial accelerometer,” *Sensors and Actuators A*, Vol.68, pp.324-32.
- [34] R. Puers and S. Reyntjens, “The charecterization of a miniature silicon micromachined capacitive accelerometer,” *J. Micromech. Microeng.*, Vol. 8, pp.127-133, January 1998.
- [35] Byeoungju Ha, Yongsoo Oh, Byeungleul Lee, K.Y. Park Seogsoon Baek, and Seoungdo Ann, Cimoo Song, “A Area Variable Capacitive Microaccelerometer with Force-Balancing Electrodes,” *IEEE Position Location and Navigation Symposium*, pp.146-151, Palm Springs, CA, April 20-23, 1998.
- [36] Arvind Salian, Haluk Kulah, Navid Yazdi. Guohong He, and Khalil Najafi, “A Hybrid Silicon Microaccelerometer System with CMOS Interface Circuit,” *Circuits and Systems, Proceeedings of the 43rd IEEE Midwest Symposium*, Vol,1, pp.228-231, 08-11Aug, 2000.
- [37] H. Luo, Gary K. Fedder, and L. Richard Carley, “ A 1mg Lateral CMOS-MEMS Accelerometer,” The Thirteenth Annual International Conference on Micro Electro Mechanical Systems, pp. 502-507, Janurary 23-27, 2000, Miyazaki.
- [38] Huikai Xie and Gary K Fedder, “A CMOS Z-Axis Capacitive Accelerometer with Comb-Finger Sensing,” The Thirteenth Annual International Conference on Micro Electro Mechanical Systems, pp. 496-501, Janurary 23-27, 2000, Miyazaki.
- [39] Risaku Toda, Nobuo Takeda, Takao Murakoshi, Shigeru Nakamura and Masayoshi Esashi, The Fifteenth IEEE International Conferencce onMicro Electro Mechanical Systems, pp.710-713, January 24, 2002, Las Legas, NV, USA.

[40] S.H. Ghafari, M.F. Golnaraghi and R. Mansour, "Design and Modeling of a 3D Micromachined Accelerometer" *Technical Proceedings of the 2004 NSTI Nanotechnology Conference*, Vol. 2, pp. 259-262. March 2004.

[41] Hongwei Qu, Deyou Fang, and Huikai Xie, "An Integrated Fully-Differential CMOS-MEMS Z-Axis Accelerometer Utilizing a Torsional Suspension," *Proceeding of the 3 rd IEEE International Conference on Nano/Micro Engineered and Molecular System*, Janurary 2008.

[42] Hongwei Qu, Deyou Fang, Huikai Xie, "A Monolithic CMOS-MEMS 3-Axis Accelerometer with a Low-Noise, Low-Power Dual Chopper Amplifier," *IEEE Sensors Journal*, Vol.8, no.9, September 2008.

[43] Chia-Pao Hsu, Ming Chuen Yio, and Weileun Fang, "A Novel SOI Z-Axis Accelerometer with Gap Closing Differential Sensing Electrodes," *Transducer 2009*, Denver, CO, USA, June 21-25, 2009.

[44] Ming-Han Tsai, Chih-Ming Sun, Yu-Chia Liu, Chuanwei Wang, and Weileun Fang, "Design and implementation of high performance CMOS-MEMS capacitive sensors," *Transducers 2009*, Denver, CO, USA, June 21-25, 2009.

[45] Qifang Hu, Chengchen Gao, Yilong Hao, Dancheng Zhang, Guizhen Yan, Yangxi Zhang, "Design and Fabrication of a MEMS Capacitive Accelerometer Based on Double-Device Layers SOI Wafer," *Proceedings of the 5th IEEE International Conference on Nano/Micro Engineered and Molecular Systems*, January 20-23, 2010.

[46] Chia-Pao Hsu, Yi-Chang Hsu, Ming-Chuen Yip, and Weileun Fang, "A Novel SOI-Based Single Proof -Mass 3-Axis Accelerometer with Gap-Closing Differential Capacitive Electrodes in All Sensing Directions," *IEEE Sensors Conference*, pp. 1188-1191, 2010.

[47] Yu-Wen Hsu, Jen-Yi Chen, Hsin-Tang Chien, Sheah Chen, Shih-Ting Lin and Lu-Po Liao, "New capacitive low-g triaxial accelerometer with low cross-axis sensitivity," *J Micromech. Microeng.*, Vol. 20 pp.1-10, April 2010.

[48] Y.Dong, P. Zwahlen, A.-M. Nguyen, F. Rudolf, J-M.Stauffer, "High Performance Inertial Navigation Grade Sigma-Delta MEMS Accelerometer," *IEEE Position Location and Navigation Sympaosium (PLANS)*, pp.32, Indian Wells, CA, USA, May 2010.

[49] Uğur Sönmez, Haluk Külah, and Tayfun Akin, “A Fourthorder Unconstrained $\Sigma\Delta$ Capacitive Accelerometer,” *The 16th International Conference on Solid-State Sensors, Actuators and Microsystems (Transucer 11)*, Beijing China, June 5-9, 2011.

[50] Jiankun Wang, Zhenchuan Yang, Guizhen Yan, “A Silicon-on-Glass Z-Axis Accelerometer with Vertical Sensing Comb Capacitors,” *NEMS 2012*, Kyoto, Japan, March 2012.

[51] Fengtian Han, Boqian Sun, Linlin Li and Gaoyin Ma, “A sensitive thee-axis micromachined accelerometer based on an electrostatically suspended proof mass,” *IEEE Sensors Conference*, Baltimore, USA, 2013.

[52] S.-C.Lo, C-K. Chan, W.-C. Lai, M. Wu, Y.C. Lin, and W. Fang, “Design and Implementation of A Novel Poly-Si Single Proof-Mass Differential Capacitive-Sensing 3-Axis Accelerometer,” *Transducer 2013*, pp. 1819-1822, Barcelona, Spain, June 2013.

[53] Akin Aydemir, “A Three Axis Capacitive MEMS Accelerometer on a Single Substrate,” *PhD. Dissertation, Middle East Technical University*, September 2013.

[54] Analog Devices ADXL377, Datasheet, 2012.

[55] Bosch Sensor, http://www.bosch-sensortec.com/en/homepage/products_3/3_axis_sensors/acceleration_sensors/bma355_2/bma355_3, last visited on January 2014

[56] ST H3LIS331DL, Datasheet, 2013.

[57] Freescale Semiconductor, Xtrinsic MMA8452Q 3-Axis, Datasheet, 2013.

[58] İlker Ender Ocak, “A tactical grade MEMS accelerometer,” *PhD. Dissertation, Middle East Technical University*, September 2010.

[59] Jongpal Kim, Dong-il (Dan) Cho, Richard S. Muller, “Why is (111) silicon a better mechanical material for MEMS,” *ASME 2003 International Mechanical Engineering Congress and Exposition*, Washington, DC, USA, November 15-21, 2003

[60] Gabriel M. Rebeiz, “RF MEMS: Theory, Design, and Technology,” *Wiley-Interscience*, 2002.

[61] Minhang Bao, Heng Yang, “Squeeze film air damping in MEMS,” *Sensors and Actuators*, Vol.136, pp. 3-27, January 2007.

- [62] Gary Li and Henry Hughes, "Review of Viscous Damping in Micro-Machined Structures," *Proceedings of SPIE*, Vol.4176, pp.30-46, June 2000.
- [63] Minhang Bao, Heng Yang, Yuancheng Sun, Yuelin Wang, "Squeeze-film air damping of thick hole-plate," *Sensors and Actuators A*, Vol. 108, pp.212-217, May 2003.
- [64] Thomas B. Gabrielson, "Mechanical-Thermal Noise in Micromachined Acoustic and Vibration Sensors," *IEEE Transactions on Electron Devices*, Vol.40, no.5, May 1993.
- [65] M. Harz, "Anodic bonding for the third dimension," *J. Micromech. Microeng.*, Vol.2, pp.161-163, September 1992.
- [66] Zhang Tingkai, Zhang Honghai, Xu Jian, Liu Sheng, Gan Zhiyin, "Study on triple-stack anodic bonding using two electrodes," *Sensors and Actuators A*, Vol. 157, pp. 168-172, July 2010.
- [67] E. Tatar, M. M. Torunbalci, S. E. Alper, and T. Akin, "A Method and Electrical Model for the Anodic Bonding of SOI and Glass Wafers," *The 25th IEEE International Conference on Micro Electro Mechanical Systems (MEMS 2012)*, pp. 68-71, Paris, France, Jan. 29-Feb.2, 2012.
- [68] L. Valero, "The Fundamentals of eutectic die attach," *Semicond. Int.*, Vol.7, pp.236-241, 1984.
- [69] Liwei LIN, Yu-Thing CHENG and Khalil Najafi, "Formation of Silicon-Gold Eutectic Bond Using Localized Heating Method," *Jpn. J. App. Phys.*, Vol. 37, pp. L1412-L1414, October 1998.
- [70] Y.T. Cheng, Liwei Lin, and Khalil Najafi, "Localized Silicon Fusion and Eutectic Bonding for MEMS Fabrication and Packaging," *Journal of Microelectromechanical Systems*, Vol.9, no, 1, pp.3-8, March 2000.
- [71] Uğur Sönmez, "Capacitive CMOS readouts for high performance MEMS accelerometers," *Msc. Thesis, Middle East Technical University*, February 2011.
- [72] Institute of Electrical and Electronics Engineers, "IEEE Standard Specification Format Guide and Test Procedure for Linear Single-Axis, Nongyroscopic Accelerometers," *IEEE Std. 1293-1998 (R22008)*, September 1998, rev. December 2008.

[73] Institute of Electrical and Electronics Engineers, "IEEE Standard Specification Format Guide and Test Procedure for Single-Axis Interferometric Fiber Optic Gyros," *IEEE Std. 952-1997 (R2008)*, September 1997, rev. December 2008.

[74] Naser El-Sheimy, Haiying Hou, and Xiaoji Niu, "Analysis and Modeling of Inertial Sensors Using Allan Variance," *IEEE Transactions on Instrumentation and Measurement*, Vol.57, no.1, January 2008.



CURRICULUM VITAE

PERSONAL INFORMATION

Surname, Name: Tez, Serdar
Nationality: Turkish (TC)
Date and Place of Birth: 1 September 1983, Isparta
Marital Status: Married
Phone: +90 312 210 44 09
Email: stez@metu.edu.tr

EDUCATION

| Degree | Institution | Year of Graduation |
|-------------|-------------------------------------|--------------------|
| MS | Süleyman Demirel University Physics | 2006 |
| BS | Süleyman Demirel University Physics | 2004 |
| High School | Gazi High School, Isparta | 2000 |

WORK EXPERIENCE

| Year | Place | Enrollment |
|--------------|---------------------------------------|--------------------|
| 2007-Present | METU Micro and Nanotechnology Program | Research Assistant |
| 2006-2007 | Süleyman Demirel University | Part-time |
| 2005-2006 | Atılım Private Teaching Institution | Physics Teacher |

FOREIGN LANGUAGES

Advanced English

PUBLICATIONS

1. A.M. Babayev, Ö. Mercan, S. Tez, "Electron Lande g -factor in GaAs/Al_xGa_{1-x}As quantum wires," *Physica E: Low-dimensional Systems and Nanostructures*, Vol. 41, issue 3, pp. 345-348, 2009.
2. F.M. Hashimzade, A.M. Babayev, and S. Tez, "Particle penetration in Kane type semiconductor quantum dots," *Eur. Phys. J. B*, Vol. 72, pp. 127-131, issue 1, 2009.

CONFERENCES

1. S. Tez and T. Akin, "Fabrication of a Sandwich Type Three Axis Capacitive MEMS Accelerometer," *IEEE Sensors Conference*, pp. 1-4, Baltimore, USA, November 03-06, 2013.
2. S. Tez and T. Akin, "Comparison of Two Alternative Fabrication Processes for a Three-Axis Capacitive MEMS Accelerometer" *The 26th European Conference on Solid -State Transducers (Eurosensors 2012)*, Krakow, Poland, September 09-12, 2012.